UNIVERSITÉ DE LORRAINE

École Doctorale "Sciences et Ingénierie des Molécules des Produits des Procédés et L'énergie"

Laboratoire "Laboratoire Énergétique et Mécanique Théorique Appliquée"

THÈSE

Présentée et soutenue publiquement pour l'obtention du titre de

DOCTEUR DE l'UNIVERSITÉ DE LORRAINE

Spécialité : Énergie et Mécanique

Par **Minghao WANG**

Fluorescence Diagnostics for Characterizing Heat and Mass Transfers in Sprays Based on Fluorescence Lifetime and Two-Photon Excitation

Soutenue le 08 Décembre 2023

Membres du jury:

Directeur de thèse :	M. Guillaume Castanet	Directeur de recherche CNRS, Université de Lorraine
Co-directeur de thèse :	M. Fabrice Lemoine	Professeur, Université de Lorraine
Rapporteur et Président du jury :	M. Claude Rozé	Professeur, Université de Rouen
Rapporteur :	M. Frédéric Grisch	Professeur, INSA Rouen Normandie
Examinateur :	M. Mehdi Stiti	Chargé de recherche, CNRS, Laboratoire IMFT, Toulouse
Examinateur :	Mme. Florine Giraud	Maitre de Conférences, Université Savoie Mont-Blanc

ABSTRACT

Heat and mass transfer play an important role in many spray applications (internal combustion engines, spray cooling, spray drying, etc.). Understanding heat and mass transfer phenomena inside the droplets is essential for optimizing these applications. However, experimental studies are faced with many difficulties. One of the most challenging is measuring droplet temperature and composition. This thesis presents a new measurement technique based on the fluorescence lifetime. Its implementation relies on the Time Correlated Single Photon Counting (TCSPC) technique and makes use of a femtosecond laser delivering ultrashort laser pulses at a high repetition rate.

In a first study, the fluorescence lifetime of certain temperature-sensitive dyes, such as rhodamine B, is used to measure the temperature of water droplets in preheated sprays. Two-photon excitation of the fluorescence is used to mitigate the effects of multiple light scattering by the droplets. Thanks to a relatively high signal-to-noise ratio, the technique makes it possible to achieve a measurement accuracy of the order of ±1°C in most cases. The novel measurement technique has several advantages over intensity-based measurement techniques. However, special care must be taken to avoid the pile-up effect that occurs when several fluorescence photons reach the photodetector in the time interval between two laser pulses. The method was then extended to study the mixing of two sprays injected at different temperatures. The characterization of the fluorescence decay in the time domain makes it possible to measure simultaneously the mixing fraction and temperature of each spray. Finally, the thesis addresses the characterization of the chemical composition of evaporating two-component droplets. This is a complex task, as fluorescence lifetime and intensity can be dependent on both temperature and chemical composition. Eosin Y was selected for its lifetime that provides a measurement of the volume fraction in binary mixtures, where the mixed solvents have different polarities. The measurement method remains valid even in the presence of significant temperature variations inside the mixture. The method is applied on evaporating droplets in an acoustic levitator. A good agreement is obtained when measurements are compared with a theoretical model taking into account various factors such as the convective effect of the acoustic streaming, the air humidity, and the non-ideality of the mixture.

Keywords: Heat and Mass Transfer, Laser-induced Fluorescence, Spray, Two-photon Absorption, TCSPC.

RÉSUMÉ

Les transferts de chaleur et de masse jouent un rôle important dans de nombreuses applications des sprays (moteur à combustion interne, refroidissement par spray, etc.). Comprendre les phénomènes de transferts qui se produisent dans les gouttes est essentiel pour optimiser ces applications. Cependant, les études expérimentales se heurtent à de nombreuses difficultés. En particulier, mesurer la température et la composition des gouttes constitue un véritable défi. Cette thèse présente une nouvelle méthode de mesure basée sur la durée de vie de la fluorescence. Elle met en œuvre la technique de comptage de photon unique corrélé en temps (TCSPC) et un laser femtoseconde délivrant des impulsions ultracourtes avec une grande fréquence de répétition. Dans une première étude, la durée de vie de la fluorescence de colorants sensibles à la température, comme la rhodamine B, est utilisée pour mesurer la température de gouttelettes d'eau dans des sprays préchauffés. Une excitation à deux photons de la fluorescence permet de limiter les effets de la diffusion multiple par les gouttes. Un rapport signal sur bruit élevé permet de garantir une précision de mesure de l'ordre de ±1°C dans la plupart des cas. La technique de mesure a de nombreux avantages par rapport aux techniques basées sur l'intensité de la fluorescence. Toutefois, des précautions doivent être prises pour éviter l'effet pile-up qui se manifeste lorsque plusieurs photons de fluorescence parviennent au photodétecteur dans l'intervalle de temps qui sépare deux impulsions laser. La méthode a ensuite été utilisé pour étudier le mélange de deux sprays injectés à des températures différentes. L'analyse du déclin de la fluorescence dans le domaine temporel permet de déterminer en même temps la fraction de mélange et la température de chaque spray. Finalement, la thèse aborde la mesure de la composition de gouttes bicomposantes. Il s'agit d'une tâche complexe, car la durée de vie et l'intensité de la fluorescence peuvent dépendre à la fois de la température et de la composition chimique. L'éosine Y a été sélectionnée car sa durée de vie peut mesurer la fraction volumique dans des mélanges binaires où les deux composants ont des polarités différentes. De plus, cette mesure reste valable en cas de variation de la température. L'approche a été testée sur des gouttes en évaporation dans un lévitateur acoustique. Un bon accord est obtenu avec un modèle qui prend en compte différents facteurs tels que l'effet du champ acoustique et l'humidité ambiante, la non-idéalité du mélange.

Mots clés : Transferts de chaleur et de masse, fluorescence induite par laser, absorption biphotonique, sprays, TCSPC.

ACKNOWLEDGEMENTS

I would like to thank my advisor, Pro. Guillaume, who really helped me a lot. Not only did he teach me a lot of basic theories about fluorescence, but he also personally worked with me to solve a lot of experimental problems. I am sorry that Mr. Guillaume had to take a lot of effort to teach me because I didn't have any knowledge about optics and fluorescence before and I only can go to the lab after 6 months after registering due to the epidemic, which wasted a lot of my time. I still remember at the end of my first year (2020), Mr. Guillaume stayed in the lab until 8 or even 9 p.m. in order to guide me in my experiments. This was very touching to me, and sometimes Mr. Guillaume even drove me home because I was so late with my experiments.

During the following three years of study, I also felt Mr. Guillaume's erudition and love for his career, and was filled with admiration and respect for him. At the same time, I also felt a deep sense of remorse and regret because I felt that I could have done better instead of making troubles. I am very grateful for the opportunity to meet Mr. Guillaume and wish him all the best!

I would also like to thank Pro. Fabrice. Although we spent a short time together, mainly during the first year of my Ph.D. graduation, I get benefit about many revisions and suggestions he made to my report and to my annual CSI report.

After that, I would like to thank Hadrien, Simon and Jamel. Hadrien taught me a lot about the operation of the optical experiments, and whenever I encountered problems with the experimental setup, he would take me to solve the problems. Simon wrote a program to control my entire lab bench from the computer, which impressed me a lot. Jamel can fix all sorts of experimental circuit problems, which is pretty cool! Frank, Eric, Ludovic, I also would like to show my thanks, who helped me a lot with some other minor experimental issues or offered me things to complete the experiment.

Feina and Pascal, are two warm-heated persons who warms my heart. I still remember that I accidentally touched the acid on my hand and they took me to the pharmacy and asked me if I was still okay after that. There are also some professors or administrators, like Giuseppe, Valérie and so on, I also like to thank them for their kindness.

Then, I would like to thank all my colleagues and partners. YangPeng, Mehdi, Romain, Thibaud, Jérémy, Abderrahmane, Raouf and Thomas, it's an honor to work in the same office with all of you, to learn, to talk, to joke. Dat, Adrien, Gagan, Meriem, Bruno, Zarina, Juan, Salah, Jean, Gaukhar, Bowen, Aninda, Remi, liudamyla, Nicolo, thanks for all of your companionship, glad to

have dinners together and we had fun ever. Ali, the special one, that I would like to mention, for the reason that you took me to the supermarket by your car to buy an electrical fan, which saved my life from this goddamn hot weather.

There are many other people I would like to thank, such as the two people who got me started in France, Regis and Gongling, and the UT-INSA program. Because at first, I didn't plan to come to France. It was a beautiful accident that made me lucky to live here for almost four years.

I am also thankful for my family and myself. I thank my family for supporting me, I would have hoped to share this joy with everyone in my family when I graduate, but I lose my grandfather during the quarantine of the epidemic, and I want to show how much I miss him in the acknowledgments of my dissertation, and sorry I don't get to see him for the last time. And even though there are a lot of things that I regret, I still want to say thanks to myself, otherwise I would have given up a long time ago because when the epidemic hit, I was really scared to come to a strange place, to be alone and isolated for three months, with a language barrier, but luckily, I persevered.

It is time to say goodbye and it is just so hard to say goodbye to all of these people and things.

Maybe in a decade or so, these memories will be gone.

But at least, I had those beautiful ghosts here once.

Minghao WANG
Nancy
September

CONTENTS

LIST OF TABLES

LIST OF FIGURES

GENERAL INTRODUCTION

Spray applications, whose process is that liquid is turned into extremely fine particles, have been widely used in a wide variety of industries in all aspects. Many spray technologies heavily depend on transport processes and phase change phenomena occurring in droplets. By atomizing a liquid into fine droplets, the contact area between the liquid and a gas or solid surface is greatly enhanced, which promotes heat and mass transfers. Sprays are widely used in the cooling of hot surfaces and in the combustion of liquid fuels. Some examples include spray cooling for heat management, fuel injectors for gasoline, and atomizers for injecting heavy fuel oil steam, boiler injectors. Sprays also play a predominant role in industrial processes like spray drying, spray coating and many other things. A common objective for these spray technologies is to optimize performance by tuning the spray characteristics. However, this requires a deep understanding of the phenomena involved in the sprays. In these applications, it is therefore of significant importance to gain quantitative information about the droplets' size, velocity, composition, and temperature. The determination and clarification of those parameters are beneficial and decisive when spray applications are employed. Droplet systems are generally characterized through the measurement of droplet sizes and velocities, but quantities like the temperature and chemical composition of the droplets were probably not given the same level of attention. This is all the more detrimental for the research community that the modelling of heat and mass transfer is extremely complex since the dynamic behavior of droplets and transfer phenomena are usually strongly interconnected. It is also necessary to consider phase change phenomena and many length scales in a spray.

Over the years, several phenomena have been proposed for measuring the parameters mentioned above as shown in Figure 1. As far as the temperature and the composition are concerned, it is possible to make a distinction between measurement techniques based on elastic (e.g. rainbow refractometry) or inelastic (Raman scattering) light scattering, and techniques based on spontaneous photon emission, of which laser-induced fluorescence is one.

However, the techniques have some comparative limitations like susceptibility to environmental effects, the strength of the light signal, the need for droplets to be spherical. Therefore, there is still a need for the development of measurements techniques specifically dedicated to non-intrusive optical measurements in sprays.

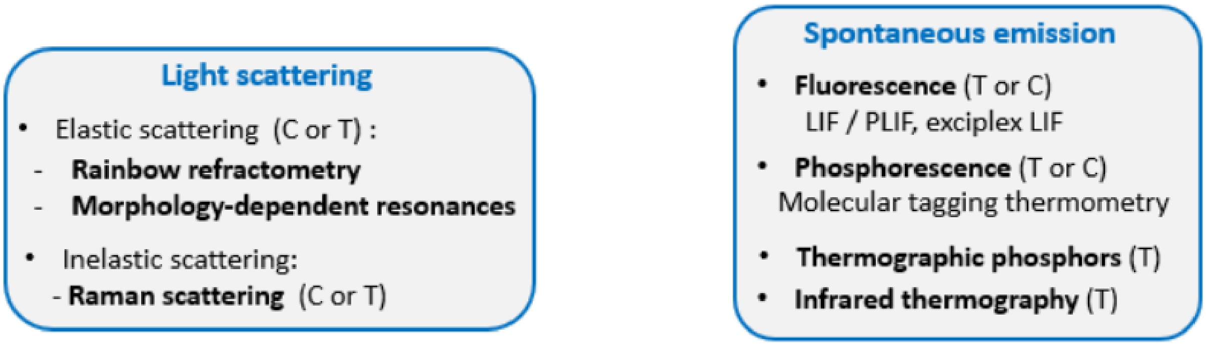

Light scattering

- Elastic scattering (C or T) :
  - **Rainbow refractometry**
  - **Morphology-dependent resonances**
- Inelastic scattering:
  - **Raman scattering** (C or T)

Spontaneous emission

- **Fluorescence** (T or C)
  LIF / PLIF, exciplex LIF
- **Phosphorescence** (T or C)
  Molecular tagging thermometry
- **Thermographic phosphors** (T)
- **Infrared thermography** (T)

Figure 1: A non-exhaustive list of physical phenomena used to measure drop temperature and composition in the literature. For more details, see Lemoine and Castanet, 2013.

Among the proposed measurement methods, Laser-Induced Fluorescence (LIF) has several advantages which has led us to its selection. Many fluorescent dyes are known to be very sensitive to the temperature and the composition of their chemical environment. Some of them are also very efficient at delivering a strong signal. Contrary to several methods, LIF measurements can be made independent to the droplet shape. The time spent in the excited state is called fluorescence time, the number of emitted photons over the number of absorbed photons is called fluorescence quantum yield. Both quantities are dependent on the molecule’s nature, temperature, and chemical composition of the liquid solvent.

In most LIF applications to fluid mechanics, measurements are generally based on the intensity of the fluorescence signal, which is proportional to the quantum yield, and for this reason can be dependent on temperature and chemical composition. However, in sprays and in multiphase flows more generally, the intensity of the signal from the droplet is also function of many other parameters. Fluorescence excitation and detection are affected by optical effects like light refraction and reflection when light crosses a liquid/gas interface. It is always an issue that the signal intensity is difficult to control in a spray where droplet have random size and position relative to the optics. A solution commonly adopted consist of detecting fluorescence in two spectral bands. Assuming that these bands are affected to the same extend by the perturbating optical effects, these can be eliminated by doing the ratio of the intensities detected in two spectral bands. This approach has been widely used at LEMTA over the past 20 years. However, it's not always that simple to implement. It requires considerable care in the selection of the detection bands, which must be as sensitive as possible to the parameters of interest (temperature, composition). The use of two dyes can sometimes improve measurement sensitivity and the balance of signal level between the two detection bands, but finding suitable dye pairs whose emission spectra are shifted in wavelength for optical separation of their signal using bandpass filters, can be difficult. Another issue lies in the fluorescence intensity of droplet which is roughly proportional to the droplet volume. This strong variation to the droplet size makes it extremely challenging to measure the intensity for all the droplets of a spray due to the limited dynamic range of conventional detectors. Another difficulty arises from multiple light scattering by the droplets. In dense spray regions, droplets that are not directly exposed to the laser beam, eventually receive laser light and emit fluorescence in return. Because of this effect, a significant part of the fluorescence signal now comes from regions outside the depth of field of the receiving optics. Consequences are a background noise that is difficult to get rid of and of the impossibility to precisely localize the fluorescence emission to get spatially resolved measurements.

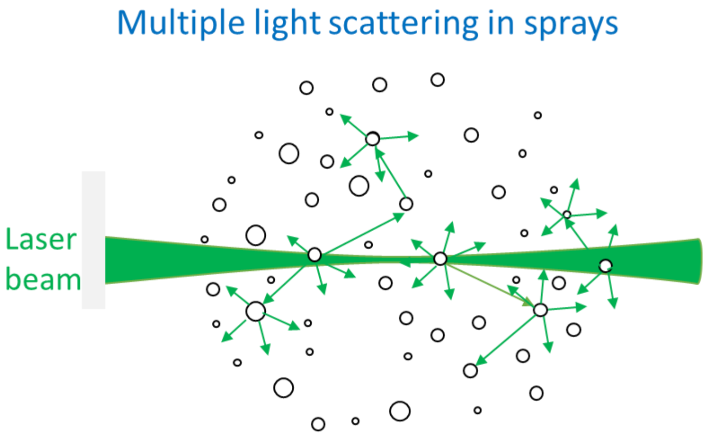

Figure 2: Out-of-field fluorescence is induced by laser light scattering

As an alternative, measurement can be based on the fluorescence lifetime, which corresponds to the time fluorescent molecules remain in the excited state before returning to the ground state. The excitation can be achieved by means of an ultra-short light pulse produced by a femtosecond or a picosecond laser. The fluorescence emission follows an exponential decay and the lifetime can be evaluated simply by fitting this decay curve. In contrast to fluorescence intensity, fluorescence lifetime is an absolute quantity, which means that any interference with optical transmission will change the value of fluorescence intensity, but not the value of fluorescence lifetime. One of the primary goals of this report is to explore the advantages and identify the inconveniences of measurement methods applied to temperature and composition measurements. In order to solve, or at least effectively limit, the problem of multiple light scattering by droplets in sprays, two-photon absorption (TPA), a fluorescent molecule that absorbs two photons at the same time, is also a method to consider. Since two-photon absorption is a nonlinear process in which the absorption rate increases with the square of the incident excitation fluence, this effect can be limited to a small spot around the focal point of the focused laser beam. However, the fluorescence signal of TPA is low compared to conventional single-photon absorption. Therefore, it is worthwhile to develop it specifically for implementation and testing under real spray conditions.

This manuscript is composed of five main chapters.

Chapter 1 focuses on the principle of fluorescence. Meanwhile, the relevant factors that affect the fluorescence lifetime are analyzed in detail. The merits and drawbacks of single and two-photon techniques are discussed in this chapter and the importance of two-photon absorption for droplet measurement is illustrated.

Chapter 2 mainly explains the necessity of summarizes and analyzes the advantages and disadvantages of existing spray measurement techniques for measuring the temperature and composition in sprays. On this basis, it presents several measurement techniques that were used in the literature to measure the temperature and composition of droplets. Regarding Laser-Induced Fluorescence (LIF), the advantages and disadvantages of measurement based on fluorescence intensity or lifetime are discussed.

Chapter 3 is dedicated to the experiment apparatus, including the femtosecond laser, the photomultiplier detector which are used for implementing the time-correlated single-photon counting (TCSPC) method to measure the fluorescence lifetime. In addition, the operating principle of TCSPC and the factors which may affect the results of TCSPC have been emphasized.

Chapter 4 is devoted to a relevant application of combined lifetime-based measurement and two-photon absorptions in a spray environment. A scanning method is developed to reconstruct the temperature field in the mixing region of a hot spray with a cold spray. By mounting two identical nozzles at a certain angle, injecting fluorescent dye and spraying each other to form a staggered area, the fluorescence information of each point in the area can be collected by moving the spraying system relatively to the optics. The purpose of the whole experiment is to estimate the temperature of droplets located at different locations by analyzing their fluorescence lifetimes. The measurement approach is extended by considering the possibility of exploiting the time decay of fluorescence to estimate the amount of liquid coming from each spray that passes through the two-photon fluorescence spot. A multi-exponential analysis of the lifetime decay is therefore proposed to determine the temperature of the two sprays separately and their volume fraction in the mixing.

Chapter 5 focus on a second experiment, which concerns the mass transfer in evaporating multicomponent droplets. When a droplet containing species of different volatilizes evaporates, its composition evolves over time. This change in composition can be tracked, provided that the fluorescence lifetime varies with the type of species contained in the solvent. An important requirement is that the fluorescence lifetime should be insensitive to temperature, so that measurements are not affected by an ambiguity. Vaporization also comes with a change in the liquid temperature. A two-component droplet is inserted into an acoustic levitator. During the experiment, the variation of shape and size of droplets is observed and the change in fluorescence lifetime is analyzed by TCSPC. The composition of droplet can be inferred by analyzing the variation of the fluorescence lifetime and the mass transfer to the droplet is characterized. The details are also concluded in this chapter, which are the selection of fluorescent dye and the variation of their lifetimes under the influence of the temperature. Finally, measurements are compared with an evaporation model that takes into account the enhanced transfer rate in the gas phase due to the acoustic field, and the non-ideal nature of the mixtures.

INTRODUCTION GÉNÉRALE

Les applications de pulvérisation, qui consistent à transformer des liquides en particules très fines, ont été utilisées dans un grand nombre d'industries et de diverses manières. En atomisant un liquide en fines gouttelettes, la zone de contact entre le liquide et la surface d'un gaz ou d'un solide est considérablement améliorée, ce qui crée un nouveau processus de pulvérisation plus efficace. En atomisant le liquide en fines gouttelettes, la zone de contact entre le liquide et la surface du gaz ou du solide est considérablement améliorée, ce qui facilite le transfert de chaleur et de masse. La pulvérisation est largement utilisée pour le refroidissement des surfaces chaudes et la combustion des combustibles liquides, comme le refroidissement par pulvérisation pour la gestion thermique, les injecteurs d'essence et les atomiseurs. Les exemples incluent le refroidissement par pulvérisation pour la gestion thermique, les injecteurs d'essence et les atomiseurs pour l'injection de pétrole lourd dans les chaudières à vapeur. La pulvérisation joue également un rôle important dans les processus industriels tels que le séchage par pulvérisation et le revêtement par pulvérisation. L'objectif commun de ces technologies de pulvérisation est d'optimiser les performances en réglant les caractéristiques de la pulvérisation. Ces applications, il est donc très important d'obtenir des informations quantitatives sur la taille, la vitesse, la composition et la température des gouttelettes. La détermination et la clarification de ces paramètres sont bénéfiques et décisives pour les applications de pulvérisation. Les systèmes de gouttelettes sont généralement caractérisés par la mesure de la taille et de la vitesse des gouttelettes, mais des grandeurs telles que la température et la composition chimique des gouttelettes n'ont probablement pas fait l'objet du même niveau d'attention. Ceci est d'autant plus dommageable pour la communauté des chercheurs que la modélisation du transfert de chaleur et de masse est extrêmement complexe puisque le comportement dynamique des gouttelettes et les phénomènes de transfert sont généralement fortement interconnectés. Il est également nécessaire de prendre en compte les phénomènes de changement de phase et de nombreuses échelles de longueur dans un spray.

Au fil des années, plusieurs phénomènes ont été proposés pour mesurer les paramètres mentionnés ci-dessus. En ce qui concerne la température et la composition, il est possible de faire une distinction entre les techniques de mesure basées sur la diffusion élastique (réfractométrie arc-en-ciel, par exemple) ou inélastique (diffusion Raman) de la lumière et les techniques basées sur l'émission spontanée de photons, dont la fluorescence induite par laser fait partie.

Toutefois, ces techniques présentent certaines limites comparatives, telles que la susceptibilité aux effets environnementaux, l'intensité du signal lumineux et la nécessité d'avoir des gouttelettes sphériques. Par conséquent, il est encore nécessaire de développer des techniques de mesure spécifiquement dédiées aux mesures optiques non intrusives dans les sprays.

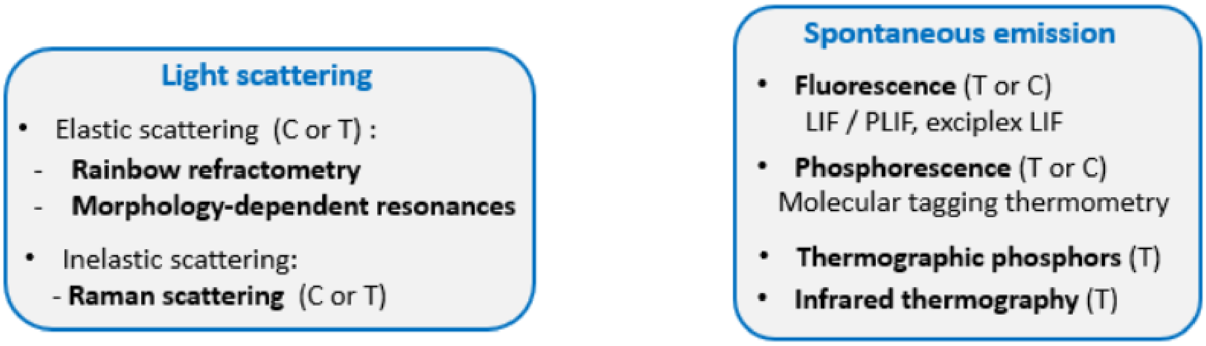

Light scattering

- Elastic scattering (C or T) :
  - **Rainbow refractometry**
  - **Morphology-dependent resonances**
- Inelastic scattering:
  - **Raman scattering** (C or T)

Spontaneous emission

- **Fluorescence** (T or C)
  LIF / PLIF, exciplex LIF
- **Phosphorescence** (T or C)
  Molecular tagging thermometry
- **Thermographic phosphors** (T)
- **Infrared thermography** (T)

Figure 1: A non exhaustive list de phénomènes physiques utilisés pour mesurer la température et la composition de gouttes dans la littérature. Pour plus de détails on pourra se rapporter à l'article Lemoine et Castanet, 2013.

Parmi les méthodes de mesure proposées, la fluorescence induite par laser (LIF) présente plusieurs avantages qui nous ont conduits à la sélectionner. De nombreux colorants fluorescents sont connus pour être très sensibles à la température et à la composition de leur environnement chimique. Certains d'entre eux sont également très efficaces pour délivrer un signal fort. Contrairement à plusieurs méthodes, les mesures LIF peuvent être effectuées indépendamment de la forme des gouttelettes. Le temps passé dans l'état excité est appelé temps de fluorescence, le nombre de photons émis par rapport au nombre de photons absorbés est appelé rendement quantique de fluorescence. Ces deux quantités dépendent de la nature de la molécule, de la température et de la composition chimique du solvant liquide.

Dans la plupart des applications de la LIF à la mécanique des fluides, les mesures sont généralement basées sur l'intensité du signal de fluorescence, qui est proportionnelle au rendement quantique et qui, pour cette raison, peut dépendre de la température et de la composition chimique. Cependant, dans les sprays et, plus généralement, dans les écoulements multiphasiques, l'intensité du signal provenant de la gouttelette est également fonction de nombreux autres paramètres. L'excitation et la détection de la fluorescence sont affectées par des effets optiques tels que la réfraction et la réflexion de la lumière lorsque celle-ci traverse une interface liquide/gaz. Il est toujours difficile de contrôler l'intensité du signal dans un spray où les gouttelettes ont une taille et une position aléatoires par rapport à l'optique. Une solution couramment adoptée consiste à détecter la fluorescence dans deux bandes spectrales. En supposant que ces bandes sont affectées dans la même mesure par les effets optiques perturbateurs, ceux-ci peuvent être éliminés en faisant le rapport des intensités détectées dans les deux bandes spectrales. Cette approche a été largement utilisée au LEMTA au cours des 20 dernières années. Cependant, elle n'est pas toujours aussi simple à mettre en œuvre. Elle nécessite une grande attention dans la sélection des bandes de détection, qui doivent être aussi sensibles que possible aux paramètres d'intérêt (température, composition). L'utilisation de deux colorants peut parfois améliorer la sensibilité de la mesure et l'équilibre du niveau de signal entre les deux bandes de détection, mais il peut être difficile de trouver des paires de colorants appropriés dont les spectres d'émission sont décalés en longueur d'onde pour la séparation optique de leur signal à l'aide de filtres passe-bande. Un autre problème réside dans l'intensité de fluorescence de la gouttelette qui est grossièrement proportionnelle au volume de la gouttelette. Cette forte variation de la taille des gouttelettes rend extrêmement difficile la mesure de l'intensité pour toutes les gouttelettes d'un spray en raison de la plage dynamique limitée des détecteurs conventionnels.

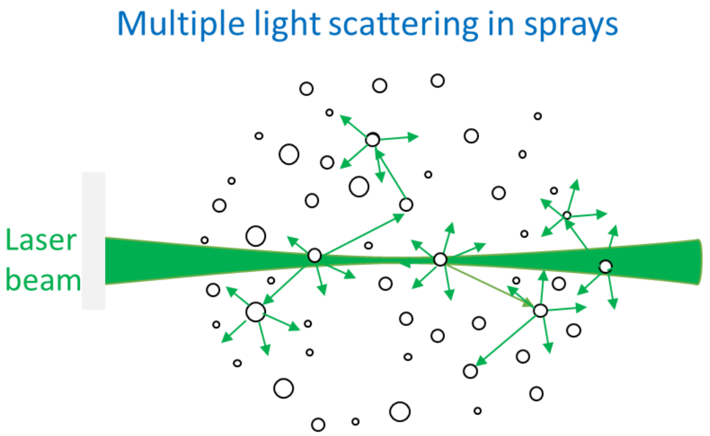

Figure 2 : La fluorescence hors champ est induite par la diffusion de la lumière laser.

Une autre difficulté provient de la diffusion multiple de la lumière par les gouttelettes. Dans les zones de pulvérisation denses, les gouttelettes qui ne sont pas directement exposées au faisceau laser finissent par recevoir la lumière laser et émettent de la fluorescence en retour. En raison de cet effet, une part importante du signal de fluorescence provient désormais de régions situées en dehors de la profondeur de champ de l'optique de réception. Il en résulte un bruit de fond dont il est difficile de se débarrasser et l'impossibilité de localiser précisément l'émission de fluorescence pour obtenir des mesures résolues dans l'espace.

La mesure peut également être basée sur la durée de vie de la fluorescence, qui correspond au temps pendant lequel les molécules fluorescentes restent dans l'état excité avant de retourner à l'état fondamental. L'excitation peut être réalisée au moyen d'une impulsion lumineuse ultra-courte produite par un laser femtoseconde ou picoseconde. L'émission de fluorescence suit une décroissance exponentielle et la durée de vie peut être évaluée simplement en ajustant cette courbe de décroissance. Contrairement à l'intensité de la fluorescence, la durée de vie de la fluorescence est une quantité absolue, ce qui signifie que toute interférence avec la transmission optique modifiera la valeur de l'intensité de la fluorescence, mais pas la valeur de la durée de vie de la fluorescence. L'un des principaux objectifs de ce rapport est d'explorer les avantages et d'identifier les inconvénients des méthodes de mesure appliquées aux mesures de température et de composition. Afin de résoudre, ou du moins de limiter efficacement, le problème de la diffusion multiple de la lumière par les gouttelettes dans les sprays, l'absorption à deux photons (APT), une molécule fluorescente qui absorbe deux photons en même temps, est également une méthode à envisager. L'absorption à deux photons (TPA) étant un processus non linéaire dans lequel le taux d'absorption augmente avec le carré de la fluence d'excitation incidente, cet effet peut être limité à une petite tache autour du point focal du faisceau laser focalisé. Cependant, le signal de fluorescence de l'APT est faible par rapport à l'absorption mono-photonique conventionnelle. Il vaut donc la peine de le développer spécifiquement pour le mettre en œuvre et le tester dans des conditions de pulvérisation réelles.

Ce manuscrit est composé de cinq chapitres principaux.

Le chapitre 1 porte sur le principe de la fluorescence. Parallèlement, les facteurs pertinents qui affectent la durée de vie de la fluorescence sont analysés en détail. Les mérites et les inconvénients des techniques à un et à deux photons sont discutés dans ce chapitre et l'importance de l'absorption à deux photons pour la mesure des gouttelettes est illustrée.

Le chapitre 2 explique principalement la nécessité de résumer et d'analyser les avantages et les inconvénients des techniques de mesure existantes pour mesurer la température et la composition des sprays. Sur cette base, il présente plusieurs techniques de mesure qui ont été utilisées dans la littérature pour mesurer la température et la composition des gouttelettes. En ce qui concerne la fluorescence induite par laser (LIF), les avantages et les inconvénients des mesures basées sur l'intensité ou la durée de vie de la fluorescence sont discutés.

Le chapitre 3 est consacré à l'appareillage expérimental, y compris le laser femtoseconde et le détecteur photomultiplicateur qui sont utilisés pour mettre en œuvre la méthode de comptage des photons uniques corrélés dans le temps (TCSPC) afin de mesurer la durée de vie de la fluorescence. En outre, le principe de fonctionnement du TCSPC et les facteurs qui peuvent affecter les résultats du TCSPC ont été soulignés.

Le chapitre 4 est consacré à une application pertinente de la mesure combinée de la durée de vie et des absorptions à deux photons dans un environnement de pulvérisation. Une méthode de balayage est développée pour reconstruire le champ de température dans la région de mélange d'un spray chaud avec un spray froid. En montant deux buses identiques à un certain angle, en injectant un colorant fluorescent et en les pulvérisant l'une contre l'autre pour former une zone décalée, les informations de fluorescence de chaque point de la zone peuvent être collectées en déplaçant le système de pulvérisation par rapport à l'optique. Le but de l'expérience est d'estimer la température des gouttelettes situées à différents endroits en analysant leur durée de vie de fluorescence. L'approche de mesure est étendue en considérant la possibilité d'exploiter la décroissance temporelle de la fluorescence pour estimer la quantité de liquide provenant de chaque pulvérisation qui passe à travers le spot de fluorescence à deux photons. Une analyse multi-exponentielle de la décroissance de la durée de vie est donc proposée pour déterminer la température des deux sprays séparément et leur fraction de volume dans le mélange.

Le chapitre 5 se concentre sur une deuxième expérience, qui concerne le transfert de masse dans l'évaporation de gouttelettes multi-composantes. Lorsqu'une gouttelette contenant des espèces de volatilisations différentes s'évapore, sa composition évolue au cours du temps. Ce changement de composition peut être suivi, à condition que la durée de vie de la fluorescence varie en fonction du type d'espèces contenues dans le solvant. Une condition importante est que la durée de vie de la fluorescence soit insensible à la température, afin que les mesures ne soient pas affectées par une ambiguïté. La vaporisation s'accompagne également d'un changement de la température du liquide. Une gouttelette à deux composants est insérée dans un lévitateur acoustique. Au cours de l'expérience, la variation de la forme et de la taille des gouttelettes est observée et le changement de la durée de vie de la fluorescence est analysé par le TCSPC. La composition des gouttelettes peut être déduite en analysant la variation de la durée de vie de la fluorescence et le transfert de masse vers les gouttelettes est caractérisé. Les détails sont également conclus dans ce chapitre, à savoir la sélection des colorants fluorescents et la variation de leur durée de vie sous l'influence de la température. Enfin, les mesures sont comparées à un modèle d'évaporation qui prend en compte l'augmentation du taux de transfert dans la phase gazeuse due au champ acoustique, et la nature non idéale des mélanges.

CONTENT 1

Chapter 1 Introduction of Fluorescence

Fluorescence is a form of luminescence which results from molecule excitation via photon absorption (another one is phosphorescence). The phenomenon was first observed and reported by Sir John Frederick William Herschel in 1845. He observed a blue light emitted from a transparent quinine solution in sunlight. This peculiar behavior intrigued researchers, and as time passed, they began to delve deeper into understanding the underlying mechanisms. One key advancement came with the discovery of the Stokes shift, which explained that the emitted fluorescent light had a longer wavelength than the absorbed light, indicating that the molecule had absorbed energy and then released it in the form of fluorescence. As for the development of Laser-induced fluorescence, it can date back when lasers were advent.

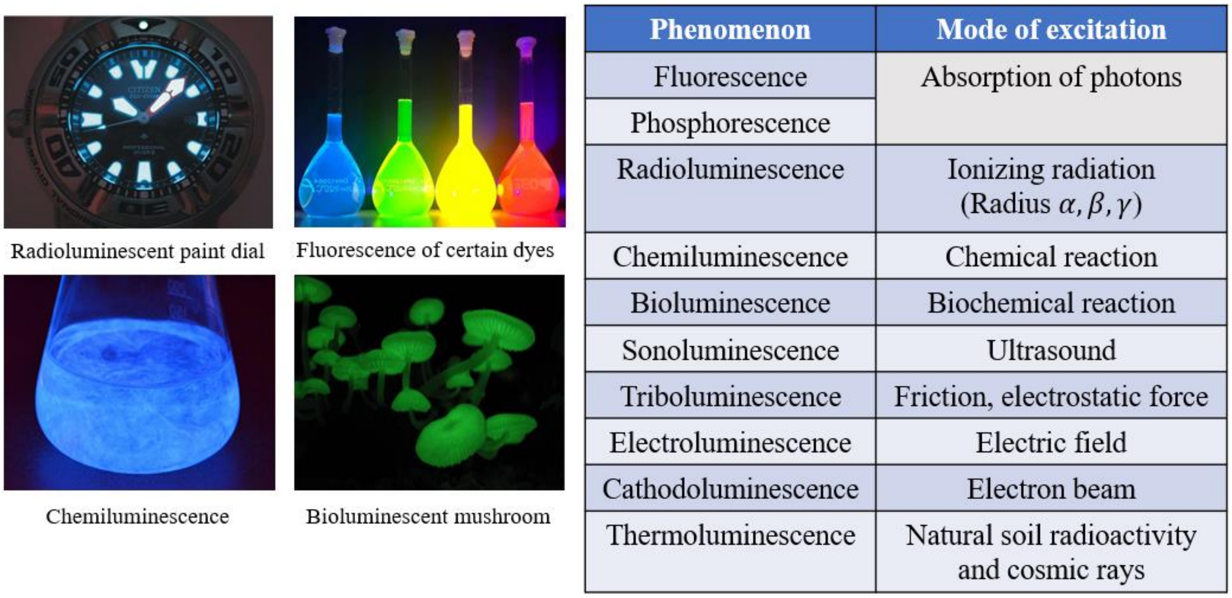

Radioluminescent paint dial

Fluorescence of certain dyes

Chemiluminescence

Bioluminescent mushroom

Phenomenon	Mode of excitation
Fluorescence	Absorption of photons
Phosphorescence	
Radioluminescence	Ionizing radiation (Radius α, β, γ)
Chemiluminescence	Chemical reaction
Bioluminescence	Biochemical reaction
Sonoluminescence	Ultrasound
Triboluminescence	Friction, electrostatic force
Electroluminescence	Electric field
Cathodoluminescence	Electron beam
Thermoluminescence	Natural soil radioactivity and cosmic rays

Figure 1-1 Common luminescence phenomena and corresponding mechanisms

Several phenomena can result in the spontaneous emission of photons, known as luminescence. All these forms of luminescence have a few common features. They are also due to the spontaneous emission of photons but involve different mechanisms to excite the luminescent molecules and give rise to luminescence. The excitation can be obtained by a chemical reaction, in which case the process is known as chemiluminescence. In case of radioluminescence, excitation is achieved through an ionizing radiation. **Figure 1-1** shows the common luminescence phenomena and various forms of spontaneous luminescence. In the case of fluorescence, fluorescent molecules are excited by the absorption of incident photons. The principle of LIF is when a sample containing fluorescent molecules is exposed to the laser light, some of the incident laser photons will be absorbed and the molecules will be excited to a higher-energy electronic state. Then molecules rapidly return to the lower-energy, stable electronic state because of the instability of the molecules in the excited state. During this process, a part of the absorbed energy is released in the form of light which is called fluorescence, and the rest is dissipated in a way or another by heat.

One advantage of fluorescence is that it can be induced very easily and efficiently using laser beams. The use of a laser is by far the most practical way to carry out measurements in a localized and non-intrusive way, and to select the species to be excited by adjusting the excitation wavelength. Laser-induced Fluorescence (LIF) has been extensively used in various fields, such as biochemistry, medical diagnostics, materials science. In these fields, fluorescence can be used to label specific molecules in biological systems so that the whole process of cellular flow can be traced. Fluorescence reveals the localization of labeled molecules and allow high-resolution imaging samples with favorable contrast and sensitivity.

In the aera of fluid mechanics, fluorescent dyes typically are used for particle tracking and flow visualization. When a fluorescent dye is added to a fluid flow, the fluorescence can be captured and tracked if the particle is illuminated by a specific wavelength of the laser. Information such as velocity, acceleration, and trajectory, can be obtained, which offers the possibility of exploring the underlying fluid dynamics. The flow patterns become visible, allowing for the visualization and analysis of complex flow fields, which is particularly useful for studying turbulent flows of fluid. For all these applications, fluorescence is a versatile tool providing a non-intrusive and highly sensitive means of visualizing complex fluid flows.

In addition, fluorescence can also be applied to measure fluid properties. Fluorescence emission is sensitive to a wide range of parameters, shown in **Figure 1-2**. Fluorescence can be dependent on temperature, pressure, viscosity and chemical environment. The intensity and wavelength of fluorescence emission are usually sensitive to the solvent in which the fluorescent molecules are dispersed. Although these effects are not always easy to explain, they can be related to the presence of polar molecules, ionic species and hydrogen bonds. The dependence of the fluorescence signal on numerous parameters is a major advantage. Numerous measurement methods can be developed to measure one of the above-mentioned parameters on which fluorescence depends. But dependence on many parameters can become a problem and a source of ambiguity. If the fluorescence signal is affected by several parameters, all of which vary at the same time, it can be difficult to separate these effects to obtain a quantitative measurement. Here, also, the ability to provide both temporal and spatial information is also a key feature for LIF applications.

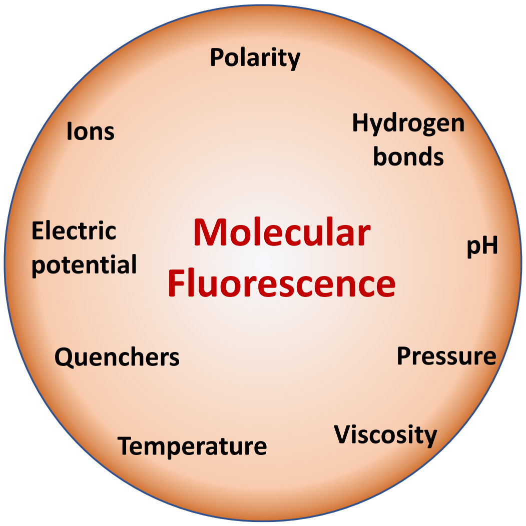

Figure 1-2 Relevant parameters affecting fluorescence

In this chapter, the concept of fluorescence and some of the physical processes which explain its dependence on physical parameters and chemical environment are introduced. Meanwhile, we also present the notion of quantum yield and fluorescence lifetime and describe some phenomena and theories that lead to variation in fluorescence signal, thus laying the theoretical foundation for the subsequent chapters.

1.1 Formation and Rules of Fluorescence

1.1.1 Phenomena of Fluorescence

Fluorescence, in simple terms, is a luminescent phenomenon that occurs when a fluorescent dye is exposed to a specific wavelength of light, causing it to absorb the energy and emit light of a different wavelength. In essence, fluorescence is actually produced by the movement of electrons from an excited state to a lower energy state, which results in the emission of light.

This movement of electrons is caused by the absorption of energy, usually in the form of light, which excites the electrons to a higher energy state. And when the electrons return to their original lower energy state (ground state), they release energy through light, which is what we observe as fluorescence. And those molecules that can fluoresce are defined as fluorophores.

In liquids, fluorescence dyes are usually aromatic molecules like rhodamine, fluorescein. Because of their molecular structures, they are capable of effectively capture the light energy and retain it sufficiently long to release it as fluorescence. An area of delocalized electrons is formed above and below the molecular plane in aromatic molecules like benzene, naphthalene, and anthracene due to the presence of conjugated double bonds that are planar organized. This delocalization of electrons enables the molecule to receive light energy in the ultraviolet or visible region, which excites the electrons to higher energy levels. The rigid structure of the benzene cycles prevents the molecule from losing the captured energy to the neighboring solvent molecules.

1.1.2 Jablonski Diagram

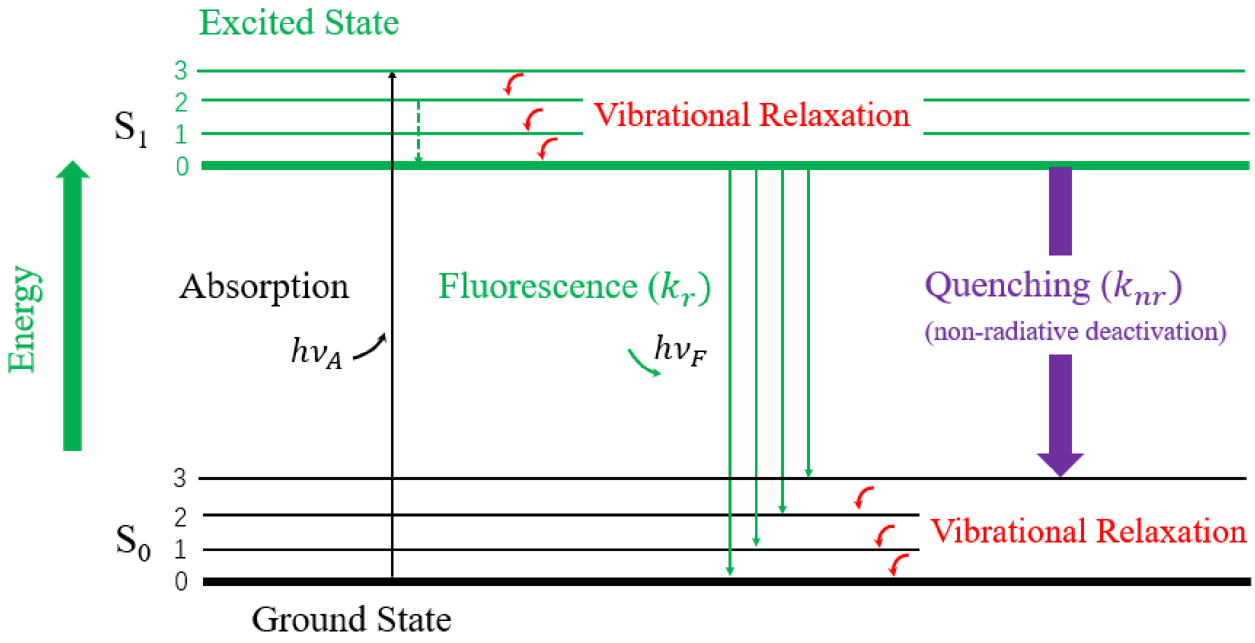

Figure 1-3 Jablonski Diagram

To depict visually how the energy changes when a molecule absorbs and emits light, the Jablonski Diagram assists in clarifying (**Figure 1-3**). S_0 and S_1 correspondingly represent the ground and the excited state. Fluorophores can exist at each of these electrical energy levels in a variety of vibrational energy levels, which are represented by 0,1, 2, 3 etc.

Initially, fluorescent molecules are in the fundamental S_0 state. After absorbing a photon, the molecule passes into a singlet electronic state S_1. Each fluorescent molecule is surrounded by other molecules. In the liquid phase, solvent molecules in particular are located at a very short distance from each fluorescent molecule. When a molecule is placed in a high vibrational level, it tends naturally to lose this energy of vibration to come back to a lower mode of vibration. This excess of vibrational energy is transmitted to solvent molecule through molecular agitation. In other words, the excess vibration is released as heat into the molecule's environment. The above process is called vibrational relaxation. Molecules tend towards thermal equilibrium [1][2].

After having reached one of the lowest vibrational levels of the excited state, fluorescent molecules emit spontaneously a fluorescence photon to return into one of the vibrational levels of the ground state, where vibrational relaxation may also take place. The emitted photons have a random direction of propagation. Therefore, only a few of them actually reach the detector to contribute to the measurement signal.

However, fluorescence is not the only deactivation pathway. An excited molecule also has the possibility to give up by other means that are non-radiative. This process which is usually referred as “quenching” has a rate of occurrence denoted k_{nr} (s^{-1}). To describe this competition between fluorescence and non-radiative pathways, a rate constant Γ (s^{-1}) is also introduced for the rate of emission of fluorescence.

1.1.3 Stokes Shift and Kasha’s rule

Due to vibrational relaxation in the excited state, the energy release is usually less than the total energy received by the molecule by absorption. As a result, the emission wavelength is expected to be in general greater than the absorption wavelength. Stokes Shift is what describes the difference between the absorption and emission spectrum, defined as the difference between the two spectral maxima **(Figure 1-4)**.

Another feature of fluorescence is that the shape of the emission spectrum is usually independent of the excitation of wavelength. As long as fluorescent molecules are excited with an acceptable excitation wavelength, the distribution of emission wavelength will remain the same regardless of its intensity, this is Kasha’s rule. It's conceivable that if the return to the ground state is always from the same vibrational level, and preferably the lowest one (due to vibrational relaxation), the fluorescence emission spectra will be totally independent of the energy absorbed. In addition, for some fluorescence dyes (especially for polynuclear aromatic hydrocarbons), the mirror rule is respected, which shows the geometric symmetric between absorption and emission spectrum. The mirror rule is fulfilled when similar levels of vibrational energy are populated in the ground state and the excited state. For some dyes (like pyrene, perylene or quinine sulfate), the deviations from the mirror symmetry rule are evident [3].

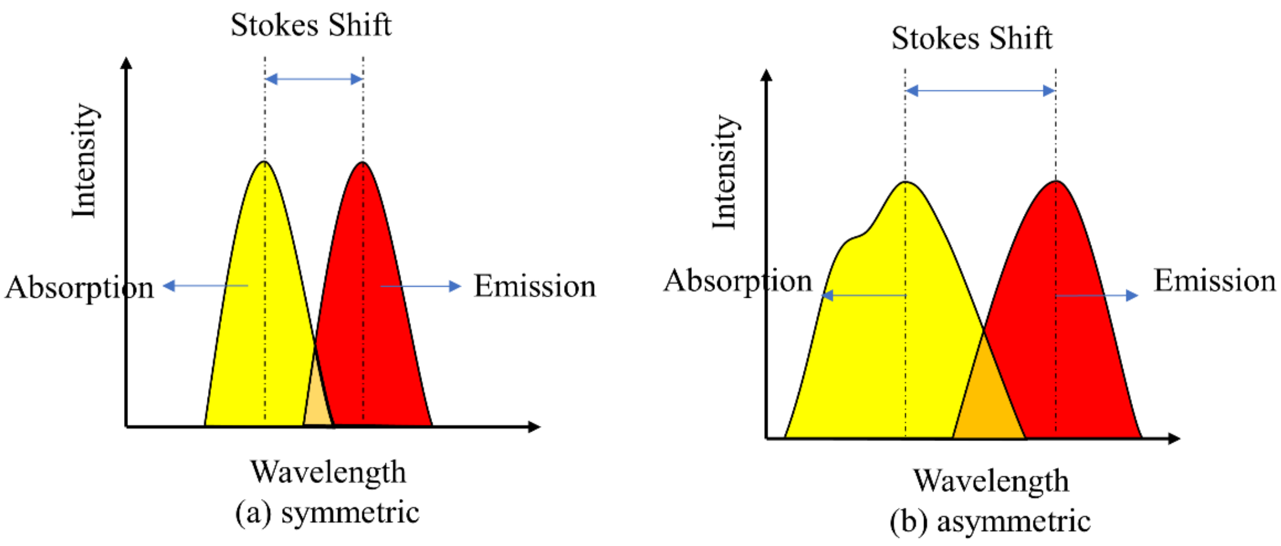

Figure 1-4 Stokes Shift

1.2 Fluorescence Lifetime

The fluorescence lifetime corresponds to the time fluorescent molecules remain in average in the excited state before returning to the ground state. To better define this quantity, we can assume a population of n_0 fluorescent molecules excited by means of an ultra-short light pulse, for example produced by a femtosecond or a picosecond laser. The excited molecules will return to the ground state through radiative and non-radiative pathways, the decay rates of which are Γ and K_{n_r}. The radiative pathways represent the emission of fluorescence photons while the non-radiation pathway correspond to the energy dissipated in the quenching in various processes that we will be clarified later in this chapter. The evolution of the number of molecules can be determined by solving the following equation:

$$\frac{\mathrm{d}n(t)}{\mathrm{d}t} = -(\Gamma + k_{nr})\, n(t) \qquad (1-1)$$

where $n(t)$ denotes the number of excited atoms at the time t, and $(\Gamma + k_{nr})$ represents the rate of transition to the ground state per unit of time. The lifetime is defined as the reciprocal of the transition rate:

$$\tau = \frac{1}{\Gamma + k_{nr}} \qquad (1-2)$$

by simultaneously integrating both sides of the equation $(1-2)$, it can be expressed as:

$$n(t) = n_0\, exp(-t\,/\,\tau) \qquad (1-3)$$

due to that fluorescence intensity is proportional to the number of decaying excited molecules, then:

$$I(t) = I_0\, exp(-t\,/\,\tau) \qquad (1-4)$$

taking the logarithm of both sides of the equation simultaneously, then:

$$In[I(t)] = In(I_0) - t\,/\,\tau \qquad (1-5)$$

thus, the slope is the negative of the inverse of the fluorescence lifetime.

Fluorescence decay is depicted in **Figure 1-5**. The fluorescence lifetime is the amount of time that has elapsed since the intensity of the fluorescence peaked at 1/e of its highest level. In the logarithmic coordinate system, it can be represented by the negative of the inverse of the slope of the corresponding curve.

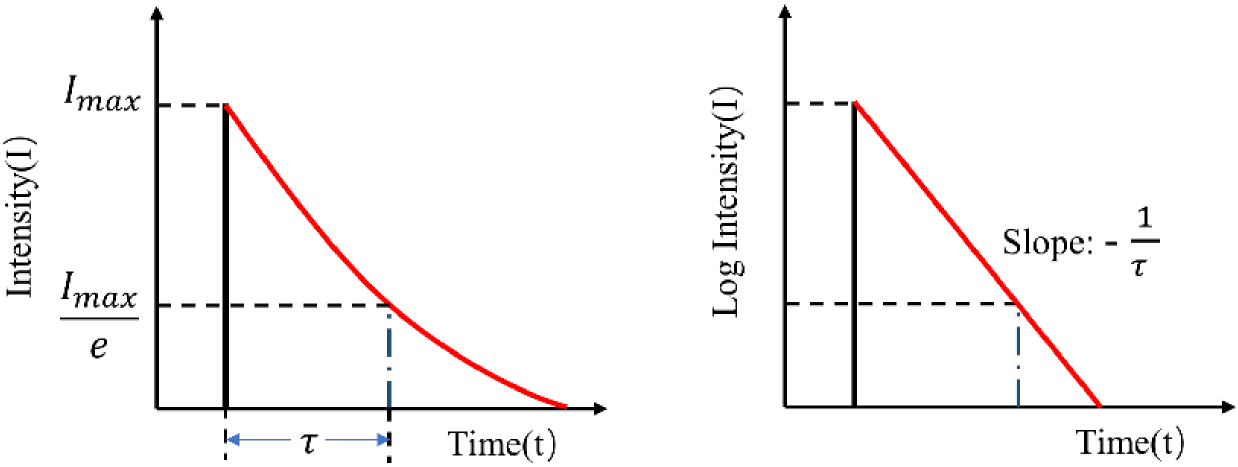

Figure 1-5 Fluorescence lifetime decay curve

Fluorescence lifetime is the average value of time spent that molecules transfer from the excited state to the ground state. In fact, around 63% of molecules decay prior to τ while 37% are later than τ[4].

The emission rates of fluorescence are typically $10^8 s^{-1}$, so that a typical fluorescence lifetime is near 10ns, while lifetimes of phosphorescence are around 1ms~1s. If we neglect the process of non-radiative and assume all the energy is emitted by light, then it can be called natural lifetime $(1-6)$:

$$\tau_n = \frac{1}{\Gamma} \qquad (1-6)$$

Fluorescence lifetimes can vary from nanoseconds to picoseconds, **Table 1-1** lists several commonly used fluorescent dyes and their lifetimes. The minimum fluorescence lifetime (cyanine-3 in the phosphate-buffered saline) is about 0.3ns, whereas the pyrene fluorophore (in water) can have a lifetime of 100ns or even longer. The excitation wavelengths of fluorescent dyes in the corresponding solvents are also given. It is worth noting that the excitation and emission spectra change in various solvents due to the fact that the properties of solvents, such as polarity, dielectric constant and refractive index, affect the electronic structure and molecular conformation of the fluorescent dyes, which in turn affect their absorption, emission bands and fluorescence lifetime.

Table 1-1 Commonly used fluorophores and their lifetimes[5]

Fluorophore	Lifetime[ns]	Excitation Max[nm]	Emission Max[nm]	Solvent
CY3	0.3	548	562	PBS
CY5	1.0	646	664	PBS
CY3B	2.8	558	572	PBS
Pyrene	>100	341	376	Water
ATTO 655	3.6	655	690	Water
Coumarin 6	2.5	460	505	Ethanol
BODIPY FL	5.7	502	510	Methanol
Fluorescein	4.0	495	517	PB (pH=7.5)
Rhodamine B	1.68	562	583	PB (pH=7.8)
Alexa Fluor 647	1.0	651	672	Water
Alexa Fluor 488	4.1	494	519	PB (pH=7.4)
Acridine Orange	2.0	500	530	PB (pH=7.8)
Oregon Green 488	4.1	493	520	PB (pH=9)
Indocyanine Green	0.52	780	820	Water

Note: PBS (phosphate-buffered saline), PB (Phosphate buffer), CY3(Cyanine-3)

It should be noted that real lifetimes of given fluorescent dyes vary in temperature, solvent conditions, pH, concentration and other factors like quenching, in contrast to the wavelength, intensity of excitation of light and various setups of instruments. For example, the excitation wavelength of a fluorescent dye in water is more bluish than in a solvent such as n-heptane, because the water molecules interact more strongly with the fluorescent dye molecules, resulting in a more compact molecular structure and leading to an increase in the amount of energy required for the electronic transition.

In the overall processes of emission, the quantum yield (ϕ) of molecules can be expressed as $(1-7)$, which represents the proportion of the total energy radiated in the form of light:

$$\phi = \frac{\Gamma}{\Gamma + k_{nr}} \qquad (1-7)$$

when $k_{nr} \ll \Gamma$, then ϕ is close to 1, natural lifetime can be acquired, thus the relation between natural lifetime and the quantum yield can be explained as:

$$\phi = \frac{\tau}{\tau_n} \qquad (1-8)$$

Table 1-2 lists quantum yields of common fluorescent dyes. For example, the yield of Rhodamine B and Rhodamine 3B are respectively 0.65 and 0.45, while some fluorescent dyes use in liquid solutions have a fluorescence quantum yield very close to 1, like fluorescein in Rhodamine 101 is around 0.96, and Rhodamine 6G in ethanol is 0.95, according to the literature[6][7].

Table 1-2 Quantum yields of common fluorescent dyes[6][7]

Compound	$C(\times 10^{-7} mol/L)$	$\lambda_E(nm)$	$\lambda_F(nm)Peak$	Quantum yield
Rhodamine B	1.58	259-542	568	0.65
Rhodamine 3B	2.48	257-556	580	0.45
Rhodamine 6G	1.05	248-528	558	0.95
Rhodamine 19	1.47	245-516	544	0.95
Rhodamine 101	1.34	265-563	588	0.96
Rhodamine 110	1.85	267-501	524	0.92
Rhodamine 123	1.76	245-510	534	0.90

1.3 Fluorescence Quenching and Resonance Energy Transfer

1.3.1 Fluorescence Quenching

Fluorescence quenching [8] is one of the most critical phenomena in fluorescence, which depicts the process of reducing the intensity of fluorescence. In essence, any non-radiative process such as collisional energy transfer which decreases energy in the form of light leads to fluorescence quenching (**Figure 1-6**). The physic-chemical processes by which a fluorescent molecule can become de-excited are numerous. Fluorescence is only one of them. The complexity of the interactions between the fluorescent species and its chemical environment is such that it is impossible to give a general description of quenching. A case-by-case analysis is necessary to identify the de-excitation mechanisms at play for a given fluorescent species in its environmental conditions. In the following paragraph, we will simply give an overview of some of the main quenching mechanism. For more details, the reader could refer to [9].

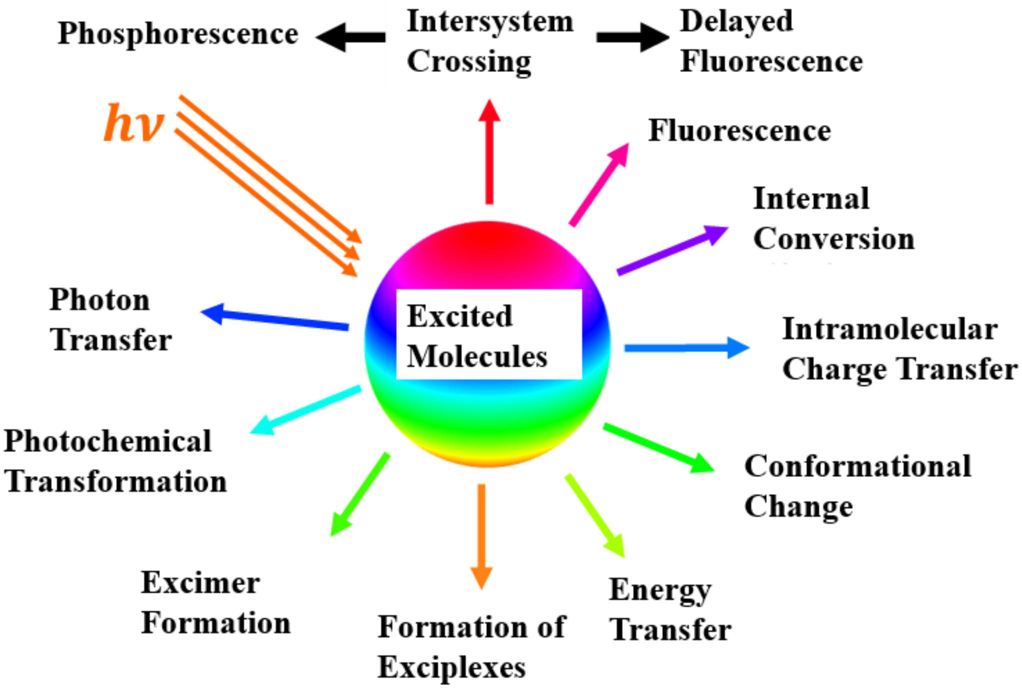

Figure 1-6 Various de-excitation pathways

A) Intersystem Conversion and Phosphorescence

Most stable molecules have complete electron shells with no unpaired electrons and therefore have singlet ground states. The total spin angular momentum S is equal to +1/2-1/2=0, 1/2 being the angular momentum or spin of an electron as in (**Figure 1-7 a)**.

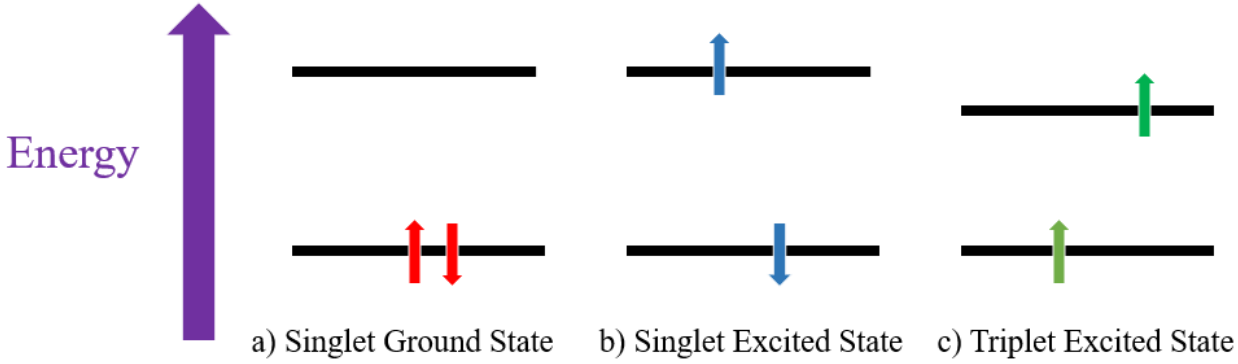

a) Singlet Ground State b) Singlet Excited State c) Triplet Excited State

Figure 1-7 Singlet State VS Triplet State

The multiplicity of the ground state energy level, defined as 2S+1=1, and as such this state is referred as a singlet state. In the case of fluorescence, when an electron transits from the ground state to the excited state, its spin retains the same orientation as depicted in **(Figure 1-7 b).** The multiplicity S remains equal to 0 and thus the excited state can be labelled as singlet as for the ground state. Fluorescence emission always takes place from a singlet state. Phosphorescence, on the other hand, is a transition between two states of different multiplicity. An intersystem crossing occurs with the electron changing of spin orientation **(Figure 1-7 c)**. The total spin angular momentum of the molecules is now equal to S=+1/2+1/2=1, and the state multiplicity 2S+1=3, which means that the excited is referred as a triplet.

According to the Laporte Rule, the transition from triplet state to the singlet ground state is prohibited, therefore the rate constants for triplet emission are much lower than those for fluorescence. Hence, the distinction between fluorescence and phosphorescence **(Figure 1-8)** is that the glow of fluorescence ends immediately after the source of excitatory radiation is turned off, whereas phosphorescence can have afterglows lasting a second to hours.

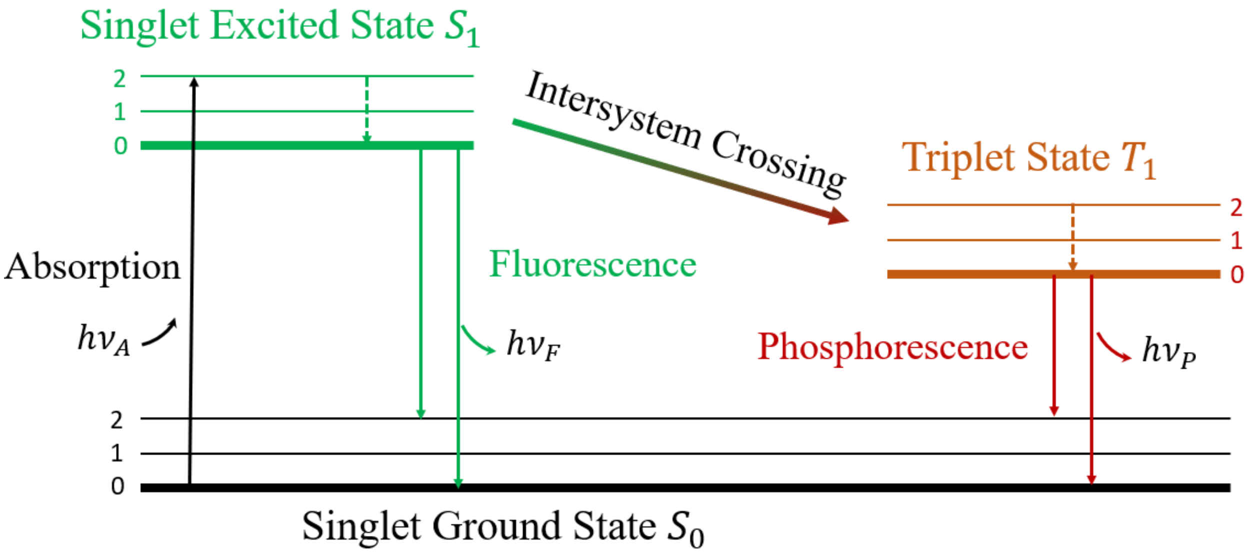

Figure 1-8 Jablonski Diagram involving fluorescence and phosphorescence

B) Internal Conversion

Figure 1-9 shows the process of internal conversion between the singlet excited state and triplet state in Jablonski Diagram. In internal conversion, the molecular spin state remains the same contrary to intersystem crossing. When the energy gap between two electronic states is quite small, vibrational levels of the two electronic states may partially overlap. This overlap means that a molecule is able to return to the state of lower energy without emitting photons through a succession of vibrational relaxations and internal rearrangements. At the end, the excess of energy is dissipated in the form of heat. The smaller the energy gap between the two electronic states, the greater the efficiency of internal conversion. Notably, the internal transition typically occurs around 10^{-12}s, whereas the fluorescence lifetime is close to 10^{-8}s, implying that the internal transition is usually completed before the emission[1].

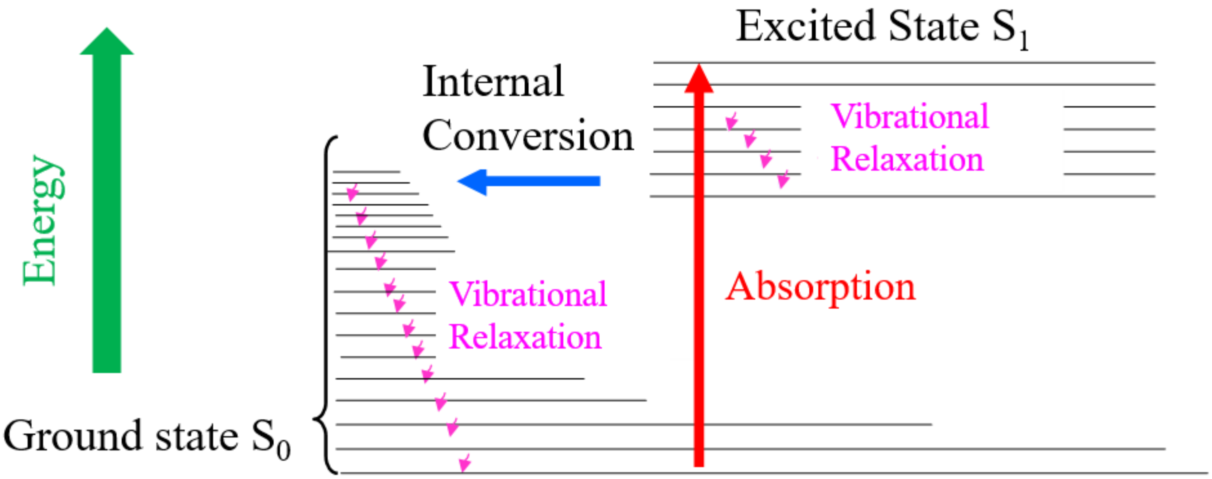

Figure 1-9 Jablonski Diagram indicating internal conversion

C) Collisional quenching

Collisional quenching is an energy transfer from an excited fluorescent molecule to a non-fluorescent molecule. It is thus an intermolecular deactivation process which can be summarized as:

$$\mathrm{A}^{*} + \mathrm{Q} \rightarrow \mathrm{A} + \mathrm{Q}^{*} \qquad (1-9)$$

A is the fluorescent specie, and * designates an excited state. Q is the quencher (the other chemical species accepting the energy). In this reaction, the quencher changes to an excited state, but does not emit light because it has no fluorescence capabilities. The kinetics of collisional quenching follows the Stern–Volmer relationship:

$$\frac{F^0}{F} = 1 + k_q\,\tau_0 \cdot [Q] \qquad (1-10)$$

where F^0 is the intensity of fluorescence without collisional quenching. F is the intensity of the fluorescence in the presence of the quencher. The parameter k_q is the quencher rate coefficient and is the fluorescence lifetime without the quencher species present. $[Q]$ is the concentration of the quencher species.

There are a variety of chemicals that can act as fluorescence quenchers. Molecular oxygen is one of these substances that effectively quenches fluorescence and phosphorescence in gaseous and liquid media. More generally, solvent molecules play the role of the quencher. Even though the quenching rate k_q is not very high, the concentration $[Q]$is so high thatcollisional quenching can become predominant.

For collisional quenching to occur, quencher molecules must diffuse toward and collide the excited fluorescent molecules. If diffusion is the only limiting process, the quenching rate coefficient can be approximated by:

$$k_q = \frac{8RT}{3\eta} \qquad (1-11)$$

where R is the ideal gas constant, T is temperature in Kelvins and η is the viscosity of the solution. In principle, this formula derived from the Stokes–Einstein relation is valid for perfect gas and atom molecules.

However, the collisions with the quencher may be effective at quenching fluorescence when the temperature is sufficiently high because a sufficiently high energy is required in the collision.

$$k_q \sim e^{\frac{E_a}{kT}} \qquad (1-12)$$

E_a is an activation energy for the reaction of quenching.

Due to collisional quenching, the fluorescence yield is expected to decrease with temperature and increase with viscosity, as there is less mobility of the molecules and therefore less collision between them according to equation $(1-12)$.

D) Excimer/Exciplex

An excited molecule can react chemically with a neighbouring molecule. Photochemistry can take many forms. The absorption of a photon can provide the required activation energy for a chemical reaction, but also induces the necessary changes in molecular configuration. Several types of photochemical reactions can affect fluorescence. A fluorescent molecule in the excited state can react with a stable molecule to form an exciplex or excimer. Heteronuclear molecules and molecules that have more than two species are called exciplex molecules. The term excimer (excited state dimer) is limited to cases in which both components of the dimer are the same molecule:

$$\mathrm{M}^* + \mathrm{M} \leftrightarrow (\mathrm{MM})^* \qquad (1-13)$$

Where M is the monomer in the stable ground state of energy. The excimer $(MM)^*$ is only formed when one of the dimer components is in the excited state. When the excimer returns to the ground state, its components dissociate. In general, the emission wavelength of an excimer is longer than that of the excited monomer, since the excimer has a lower level of energy than the excited monomer as shown in the **Figure 1-10**.

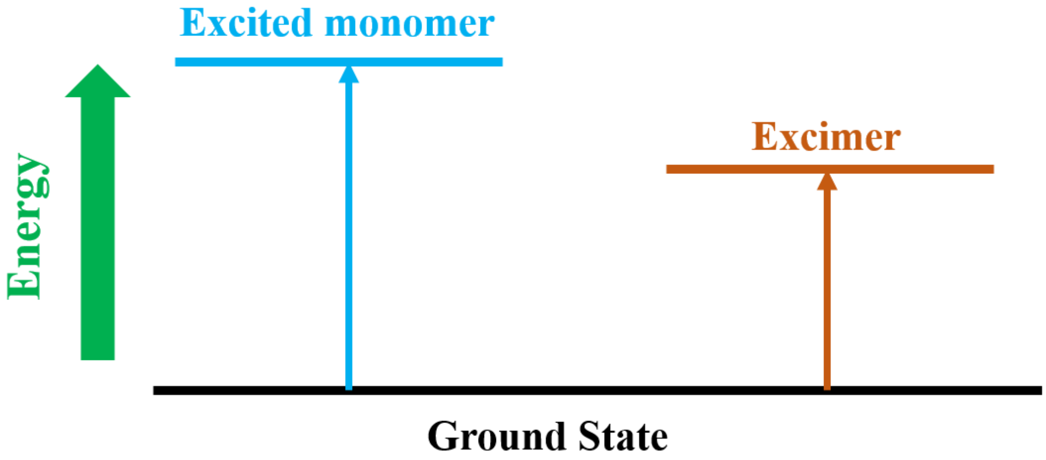

Figure 1-10 Jablonski diagram indicating the formation of an excited monomer and an excimer

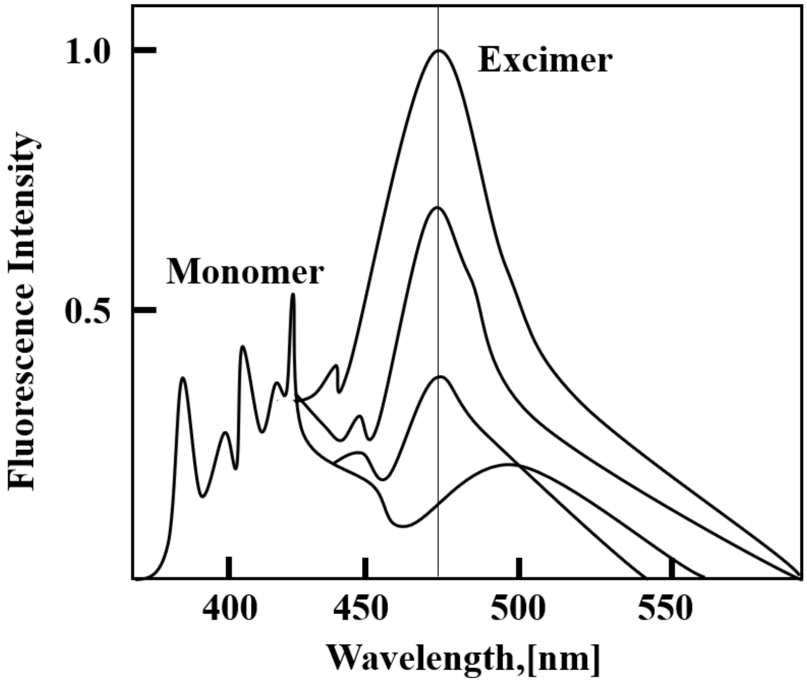

Figure 1-11 Emission spectra of pyrene and its excimer. The relative intensity of the excimer peak (470 nm) decreases as the total concentration of pyrene is decreased from 6 x 10^{-3} M (top) to 0.9×10^{-4} M (bottom). Deprived from [1].

The phenomenon is illustrated in **Figure 1-11** in the case of pyrene. The excimer has a peak of emission around 470 nm, whereas the range of emission is situated around 400 nm for the monomer in the same condition. Increasing the initial concentration in pyrene, moves the chemical equilibrium (Eq $(1-13)$) in the direction of the excimer formation. However, the excimer emission is not always predominant, as in the case of pyrene. Monomer and excimer do not have the same fluorescence yields. They do not behave in the same way to other deactivation pathways like collisional quenching. As a result, the excimer emission can be so low that its emission remains difficult to detect.

E) Static Quenching

Fluorescence quenching can be caused by a chemical reaction in the ground state. Static quenching is caused by the formation of a complex between a fluorescent molecule in the ground state and a quenching molecule. The complex, once formed, is non-fluorescent. Formation of the complex takes place before any photon absorption occurs.

F) Photobleaching

Photobleaching is a chemical alteration of the fluorescent dye. It occurs when a photochemical reaction irreversibly blocks recovery to an excitable state from which the fluorescent species can radiatively de-excite. It is a problem for many measurement methods, especially in microscopy where the same molecules are repeatedly illuminated.

G) Solvent Polarity

Solvent molecules can affect fluorescence in many ways. One of this effect is referred to as solvent relaxation and is dependent on the degree of solvent polarity. Strictly speaking, this effect does not lead to a quenching of the fluorescence but a shift in wavelength of the fluorescence emission (stokes shift). A molecule is polar when it has a polar moment. This can be either as a result of polar bonds due to differences in electronegativity, or as a result of an asymmetric arrangement of nonpolar covalent bonds and non-bonding pairs of electrons. The polarity of solvent has many practical consequences, starting with its effect on solubility. For example, most nonpolar molecules are water-insoluble, while polar molecules are generally able to dissolve in water.

To describe the effect of solvent polarity on fluorescence, we can consider the Jablonsky diagram presented in the figure below **(Figure 1-12)**.

Solvent molecules surrounding a fluorescent molecule in the ground state have dipole moments interacting with the dipole moment of the fluorescent molecule. This interaction yields an ordered arrangement of solvent molecules around the fluorescent molecule. Solvent molecules are aligned with the dipole moment of the fluorescent molecule.

As absorption takes place, the electron changes its orbital, modifying the dipole moment of the fluorescent molecule. Generally, fluorescent molecules have a much larger dipole moment in the excited state than in the ground state[1].

The Franck-Condon principle states that the electronic transition is almost instantaneous. Therefore, the fluorescent molecule is excited to a higher electronic energy level in a far shorter timeframe than it takes for the solvent molecules to re-orient themselves within the interactive environment of the neighboring fluorescent molecule.

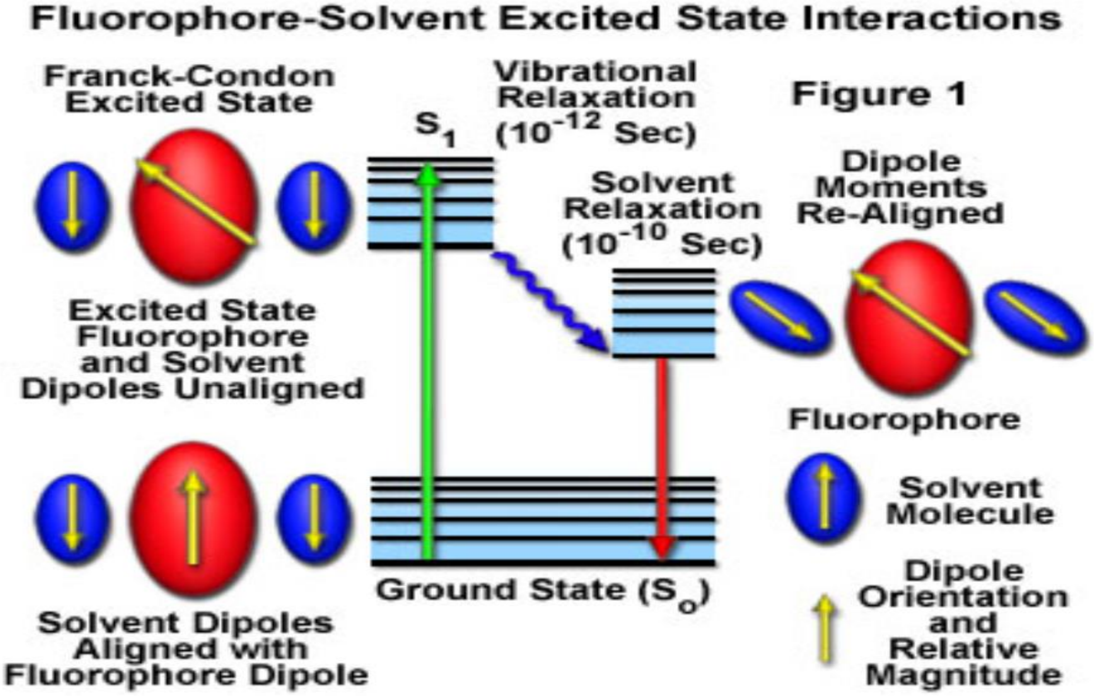

Figure 1-12 Fluorophore-Solvent Excited State Interactions[10]

Once the fluorescence molecule is excited, its excess vibrational energy is rapidly lost by vibrational relaxation on the picosecond time scale. Then, the solvent molecules reorient progressively around the excited fluorophore in a slower process (referred to as solvent relaxation) that takes between 10 and 100 picoseconds. This has the effect of reducing the energy gap between the ground and excited states. As a result, fluorescence emission is red shifted compared to the situation where there is no solvent relaxation.

Increasing solvent polarity produces a greater reduction in the excited state energy level, while decreasing solvent polarity reduces the effect of the solvent on the excited state energy level. The polarity of the fluorescent molecule also determines the sensitivity of the excited state to solvent effects. Charged and polar fluorescent molecules exhibit a greater effect than non-polar molecules.

Solvent relaxation effects on fluorescence can result in a dramatic effect on the size of Stokes shifts. This is for example the case of 6-anilino-2-naphthalene sulfonic acid in **Figure 1-13**.

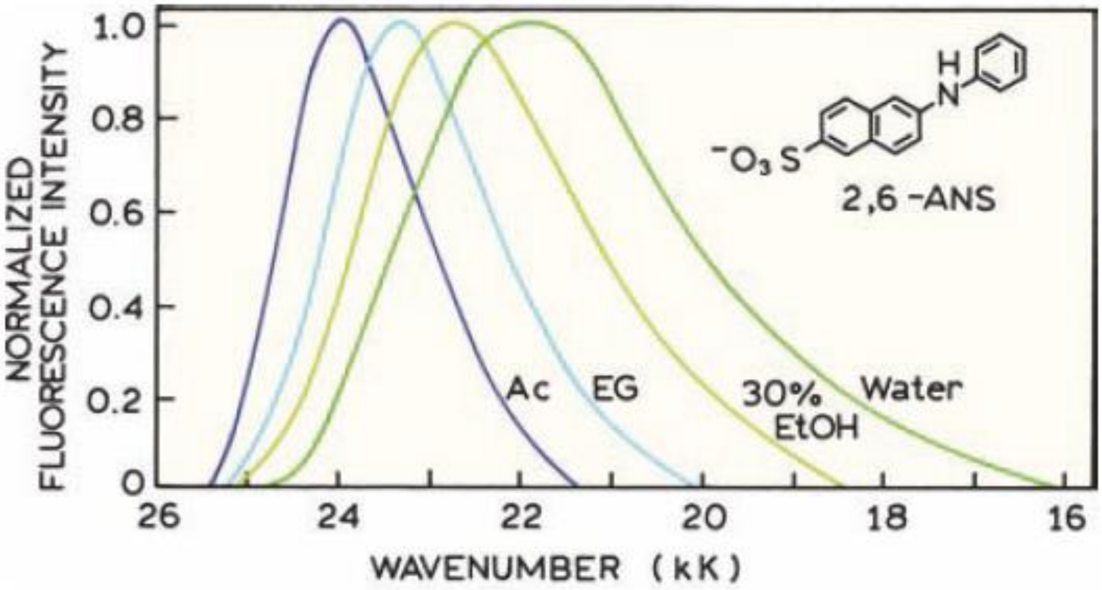

Figure 1-13 Normalized emission spectra for 6-anilino-2-naphthalene sulfonic acid (ANS). The solvents are acetonitrile (Ac), ethylene glycol (EG), 30% ethanol/ 70% water (30% EtOH), and water. 1kK=1000cm^{-1}. Revised from[1].

1.3.2 Fluorescence Resonance Energy Transfer (FRET)

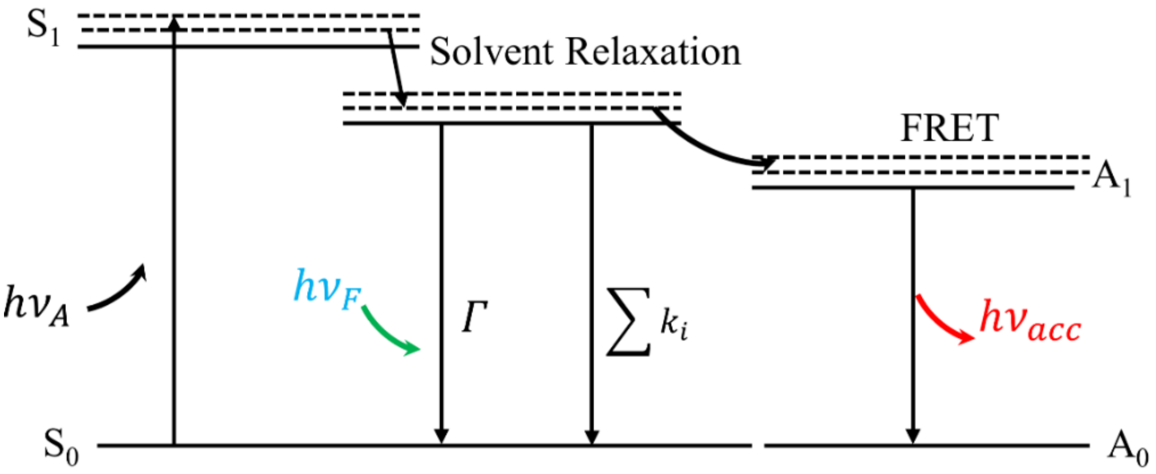

Figure 1-14 Jablonski diagram and fluorescence resonance energy transfer (FRET)

When the concentration of fluorescent molecules is high, energy transfers can take place between fluorescent molecules that are less than a few nm apart. This process has several names in the literature: Förster Resonance Energy Transfer (FRET), Fluorescence Resonance Energy transfer (FRET), Resonance Energy Transfer (RET). FRET explains the energy transfer among the fluorophore molecules as the **Figure 1-14** shows. **Figure 1-15** shows the difference with FRET and without FRET, it can be seen lifetimes of molecules decrease with FRET because of the energy losses..

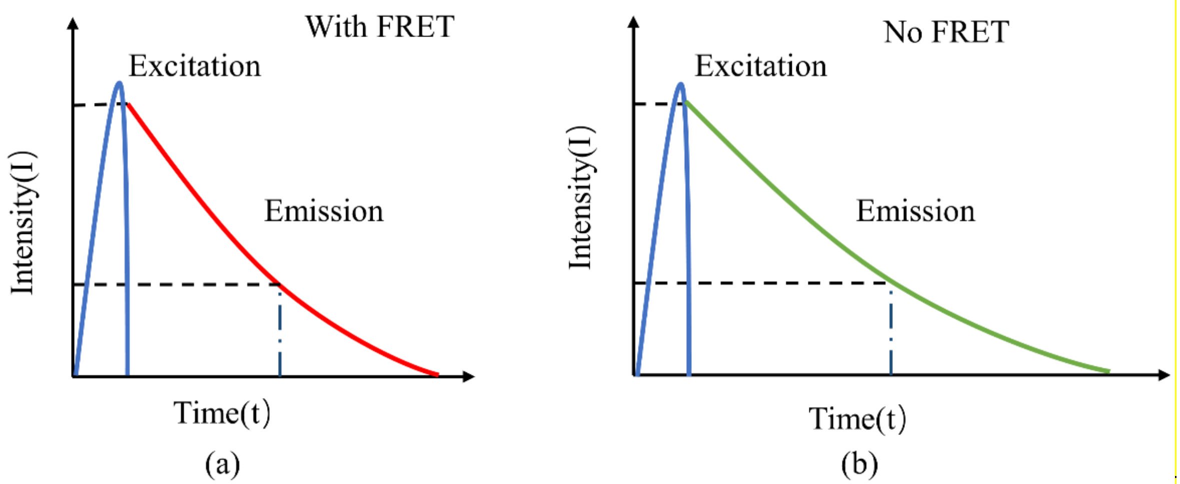

Figure 1-15 With or without fluorescence resonance energy transfer (FRET)

In fact, FRET is a distance-dependent physical process by which energy is transferred non-radiatively from an excited fluorescent molecule (the donor) to another fluorescent molecule (the acceptor) by means of long-range dipole–dipole coupling[9]. The efficiency of FRET denoted E, can be defined as the rate of energy transfer by FRET on the rate of all forms of deactivation pathways. It can also be defined from the fluorescence lifetimes of the donor in the absence of acceptor (τ_0) and that of the donor in presence of acceptor (τ) as:

$$E = 1 - \frac{\tau}{\tau_0} \qquad (1-14)$$

The rate of energy transfer (k_{ET}) is inversely proportional to the sixth power of the distance r between donor and acceptor:

$$k_{ET} = \left(\frac{R_0}{r}\right)^6 \frac{1}{\tau_0} \qquad (1-15)$$

In this expression, R_0 is the Förster distance of this pair of donor and acceptor, i.e., the distance at which the energy transfer efficiency is 50%. This make FRET extremely sensitive to small changes in distance, as it can be demonstrated that FRET efficiency is given by:

$$E = \frac{R_0^6}{r^6 + R_0^6} \qquad (1-16)$$

The distance between the donor and the acceptor is typically in the range of 1–10nm when FRET is usually observed in most fluorescent solutions **(Figure 1-16)**.

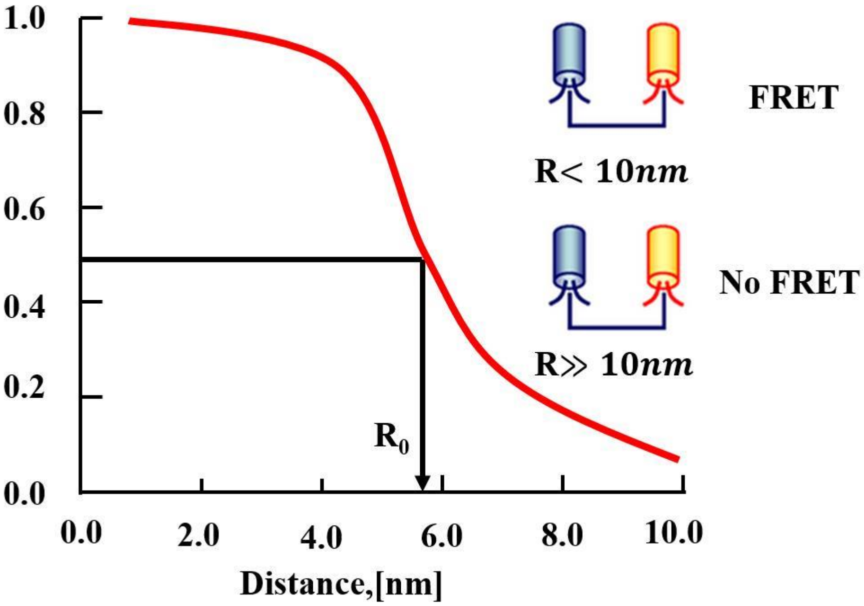

Figure 1-16 Effect of acceptor-donor distance on FRET efficiency

For a FRET to take place, the donor and acceptor must show a certain compatibility. In particular, the emission spectrum of the donor must overlap the absorption spectrum of the acceptor. This overlap is quantified by the overlap integral J:

$$J = \frac{\int_0^\infty F_D(\lambda)\,\varepsilon_A(\lambda)\,\lambda^4\,d\lambda}{\int_0^\infty F_D(\lambda)\,\,d\lambda} \qquad (1-17)$$

$F_D(\lambda)$ is the emission spectrum of the donor in the absence of FRET. $\varepsilon_A(\lambda)$ is the absorption spectrum of the acceptor. A spectral overlap between the donor emission and the acceptor absorption is required **(Figure 1-17)**, although the energy transfer does not involve an emission of photon by the donor and an absorption by the acceptor.

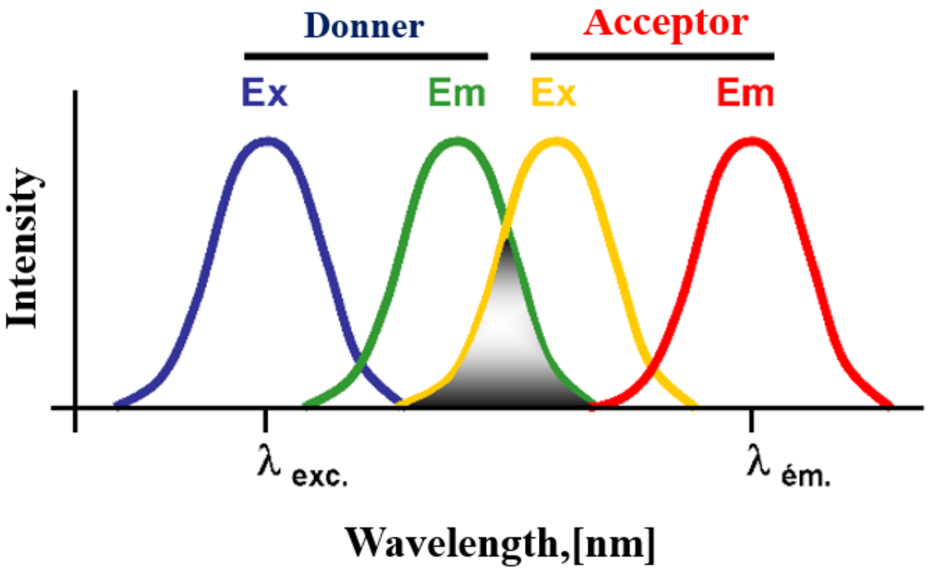

Figure 1-17 Effect of acceptor-donor distance on FRET efficiency

The calculation of the overlap integral J allows to evaluate the Förster distance R_0. If the wavelength is expressed in cm and J(λ) is in units of M^{-1} cm^3, the Förster distance is given by:

$$R_0 = 9.78 \times 10^3 \left(K^2 n^{-4} Q_D J(\lambda)\right)^{1/6} \ (in\ A) \qquad (1-18)$$

The illustrating Jablonski diagram of a FRET is presented in **Figure 1-18**.

There are several examples of couples of dyes that can undergo energy exchange by FRET. An example among others is the pair Rhodamine 6G/Fluorescein which has been studied in detail by Saha[11].

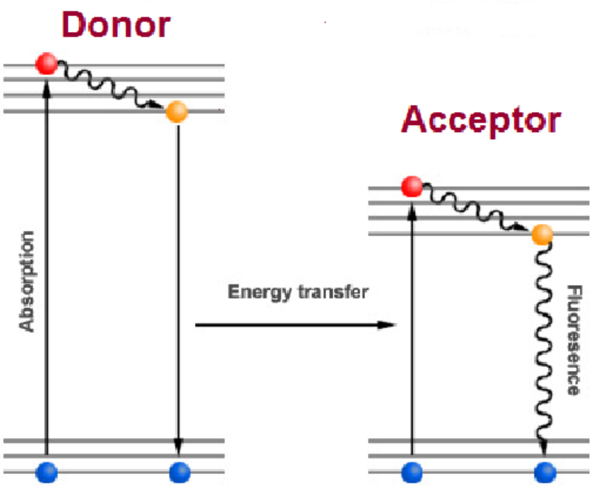

Figure 1-18 Jablonski diagram illustrating the FRET process

Figure 1-19(a) shows the normalized emission and absorption spectra of the two dyes. **Figure 1-19 (b)** compares the emission spectra of the two dyes in solutions where fluorescein is alone as a fluorescent dye (1); rhodamine 6G is alone (2) and in a 1:1 mixture of the two solutions (3). It's obvious that some energy has been transmitted to rhodamine 6G, giving rise to a much higher level of emission, while fluorescein emission is reduced.

FRET can involve fluorescent molecules of two different species, as in the previous example, or fluorescent molecules of the same species. This is known as self-quenching or auto FRET.

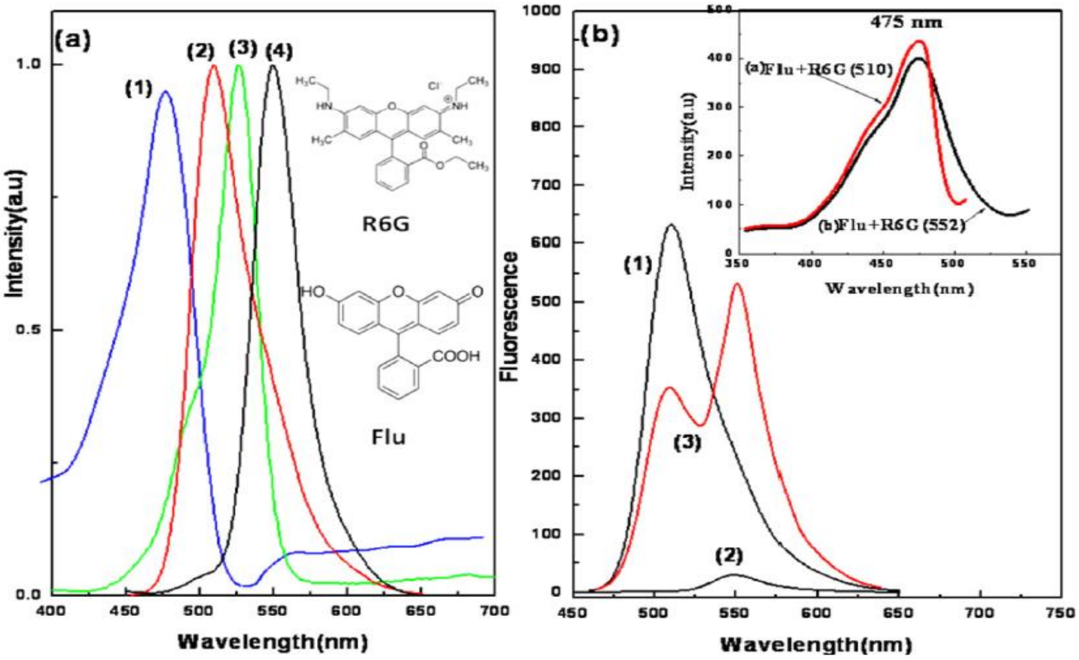

Figure 1-19 (a) Normalized absorption (curve 1 and 3) and emission (curve 2 and 4) spectra of Flu and R6G in aqueous solution. Inset shows molecular structure of Flu and R6G (b)fluorescence spectra of pure Flu (curve 1), pure R6G (curve 2) and Flu–R6G (1:1 volume ratio) mixture in aqueous solution (curve 3). Excitation wavelength was 430 nm. The dye concentration was 10^{-6} M and 0.5×10^{-5} M for Flu and R6G, respectively. Inset shows the excitation spectra for Flu–R6G mixture with monitoring emission wavelengths at (a) 510 nm (Flu emission maximum) and (b) 552 nm (R6G emission maximum).excitation spectra for Flu–R6G mixture with monitoring emission wavelengths at (a) 510 nm (Flu emission maximum) and (b) 552 nm (R6G emission maximum)[11]

1.4 One-Photon Absorption(1PA) and Two-Photon Absorption (2PA)

1.4.1 Absorption Cross-section

Multiple-photon absorption is a non-linear optical process that occurs when fluorescence excitation has a sufficiently high irradiance. The phenomenon was originally predicted by Maria

Goeppert-Mayer in 1931 in her doctoral dissertation. This phenomenon can be illustrated by introducing the Jablonski diagram **(Figure 1-20)**. Multiple-photon absorption is the simultaneous absorption of two or more photons. In two-photon absorption (TPA), two photons combined their energies to produce the same effect as a single photon whose frequency is doubled. In the excited state, the molecule can return to the ground state by the emission of a photon of fluorescence as normally as in the fluorescence induced by the absorption of one photon. Similarly, three photons can be absorbed by a fluorescent molecule at the same time in the three-Photon absorption (3PA). The phenomenon requires an even higher irradiance than for 2PA.

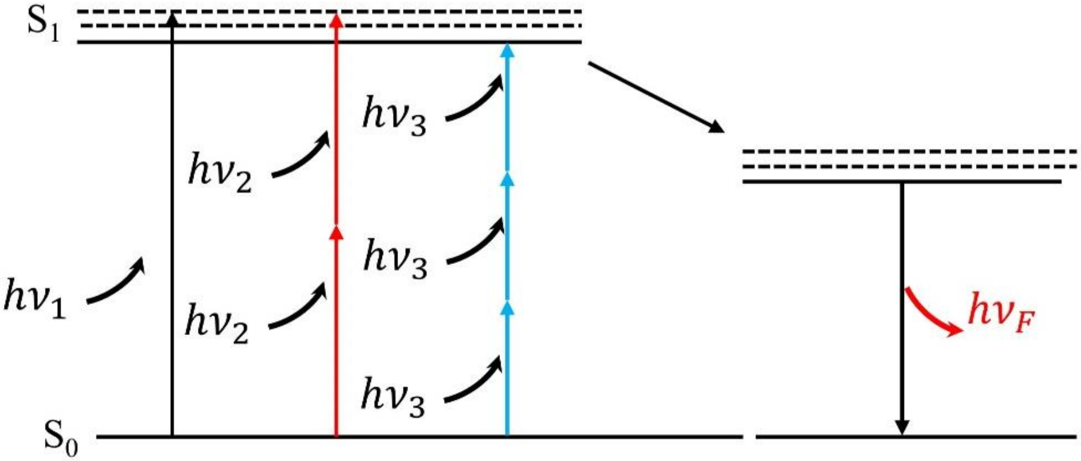

Figure 1-20 Multiphoton Absorption Processes

Absorption cross-section are crucial quantities to compare 1PA, 2PA and 3PA. They are a measurement of the probability that photons interact with fluorescent molecules in the ground state and gives rise to a molecule in the excited state. A beam of incident light travels in the X direction through an absorbing medium of thickness dx. The parameter I denotes the radiance of the beam in W/m^2

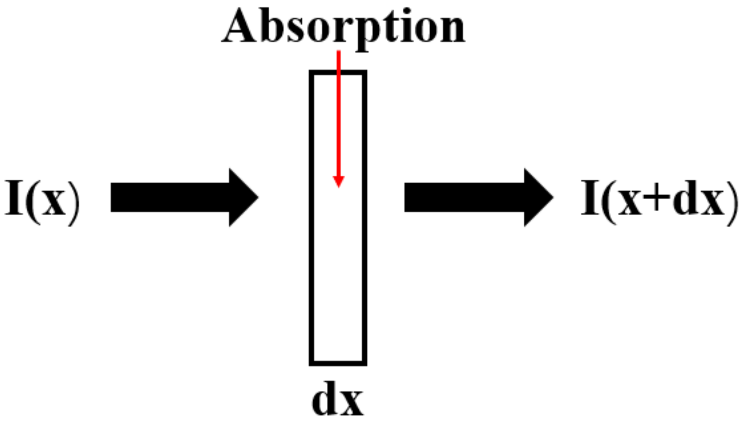

Figure 1-21 Explanation of absorption

As shown in **Figure 1-21**, the process of one-photon absorption can be express as $(1-19)$:

$$(x+dx) = I(x) - \sigma_1\, n\, I(x)\, \mathrm{d}x \qquad (1-19)$$

where n is the number of absorbing molecules in m^{-3}. The molar absorption coefficient ε is frequently used instead:

$$I(x+dx) = I(x) - \varepsilon\, C\, I(x)\, \mathrm{d}x \qquad (1-20)$$

The absorption cross-section σ and the molar absorption coefficient ε $(mol^{-1} \cdot m^2)$ are related through the following equation $(1-21)$:

$$\varepsilon = \sigma \times N_A \qquad (1-21)$$

where, N_A is Avogadro's number (6.022×10^{23} mol^{-1}). Both sides are divided by dx simultaneously, $(1-20)$ can be written as $(1-22)$:

$$\frac{dI}{dx} = -\varepsilon c I(x) \qquad (1-22)$$

Integral both sides, $I(x)$ can be expressed as $(1-23)$:

$$I(x) = I_0 \exp(-\varepsilon c x) \qquad (1-23)$$

The equation$(1-23)$ represents the variation of light intensity with distance in one-photon absorption and is well-known as the Beer-Lambert Law.

For two-photon absorption, since the photons do not interact independently, the probability of two-photon absorption is proportional to the square of the electric field strength, in other words, to the square of intensity of incident light, and thus the process can be express as $(1-24)$:

$$I(x+dx) = I(x) - \sigma_2\, n\, I^2(x)\, dx \qquad (1-24)$$

Here the unit of σ_2 are m^4/W. If one considers instead of the energy, the flux of photons J (photons/m^2 s) along the x direction of the incident beam, $I(x) = h\nu\, J(x)$ with ν the frequency of the incoming photons and h the Planck constant. Eq. $(1-24)$ can be rewritten:

$$J(x+dx) = J(x) - \alpha_2\, n\, J^2(x)\, dx \qquad (1-25)$$

where the molecular two-photon absorption cross section $\alpha_2 = h\nu\, \sigma_2$, has units in m^4 s/photons. It is usually quoted in the units of Goeppert-Mayer (GM), where 1 GM is 10^{-50} cm^4 s photon^{-1}. The large scaling factor (10^{-50}) is introduced to have convenient values with common fluorescent dyes. Example values are given in **Table 1-3** for some common fluorescent dyes. In this table, the wavelength refers to the wavelength of the incident photons, not to the wavelength of the transition, which is two times less.

Table 1-3 Two-Photon cross sections (GM) of the dyes at selected wavelengths(nm). The relative error of numbers shown here is ±15%[12].

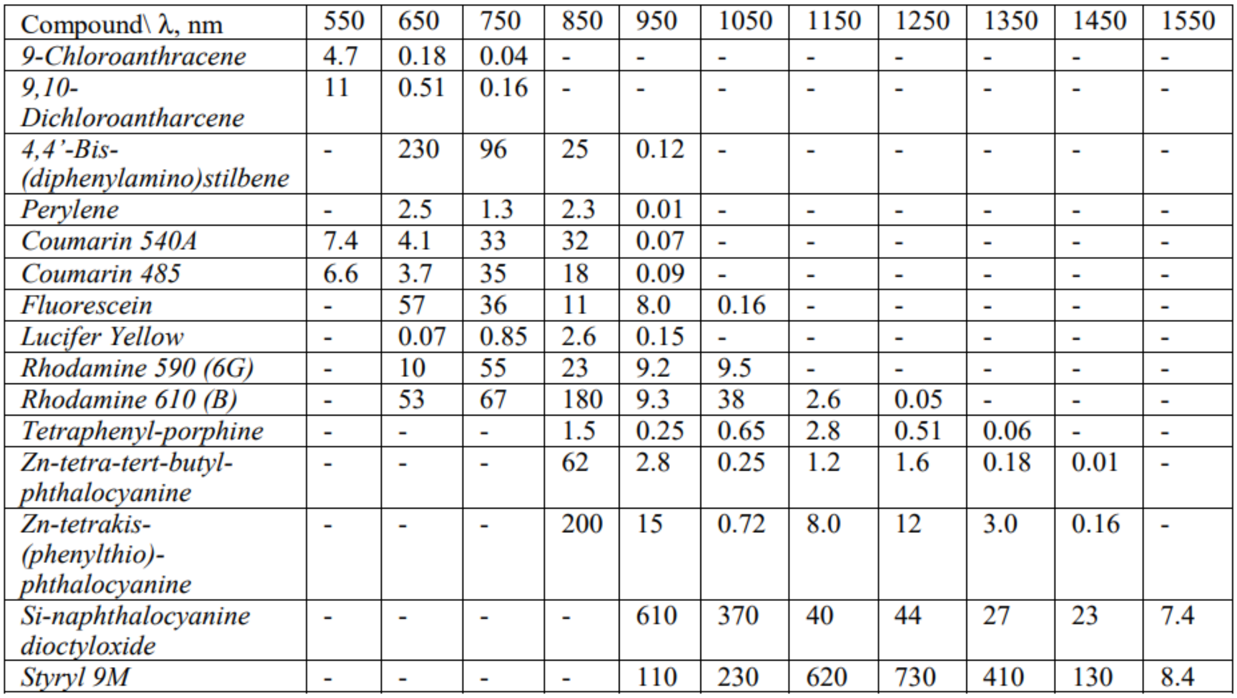

Compound\ λ, nm	550	650	750	850	950	1050	1150	1250	1350	1450	1550
9-Chloroanthracene	4.7	0.18	0.04	-	-	-	-	-	-	-	-
9,10-Dichloroantharcene	11	0.51	0.16	-	-	-	-	-	-	-	-
4,4'-Bis-(diphenylamino)stilbene	-	230	96	25	0.12	-	-	-	-	-	-
Perylene	-	2.5	1.3	2.3	0.01	-	-	-	-	-	-
Coumarin 540A	7.4	4.1	33	32	0.07	-	-	-	-	-	-
Coumarin 485	6.6	3.7	35	18	0.09	-	-	-	-	-	-
Fluorescein	-	57	36	11	8.0	0.16	-	-	-	-	-
Lucifer Yellow	-	0.07	0.85	2.6	0.15	-	-	-	-	-	-
Rhodamine 590 (6G)	-	10	55	23	9.2	9.5	-	-	-	-	-
Rhodamine 610 (B)	-	53	67	180	9.3	38	2.6	0.05	-	-	-
Tetraphenyl-porphine	-	-	-	1.5	0.25	0.65	2.8	0.51	0.06	-	-
Zn-tetra-tert-butyl-phthalocyanine	-	-	-	62	2.8	0.25	1.2	1.6	0.18	0.01	-
Zn-tetrakis-(phenylthio)-phthalocyanine	-	-	-	200	15	0.72	8.0	12	3.0	0.16	-
Si-naphthalocyanine dioctyloxide	-	-	-	-	610	370	40	44	27	23	7.4
Styryl 9M	-	-	-	-	110	230	620	730	410	130	8.4

Figure 1-22 2PA spectra (dark blue circles, left vertical-axis) and molar extinction (magenta line, right vertical axis). Large dark blue circles are absolute cross sections at selected wavelengths measured here. Other symbols are the literature data with corresponding references shown in[12]. shows the 1PA and 2PA spectra of rhodamine B in methanol. The 2PA spectra exhibits several bumps, while the 1PA absorption spectrum shows mainly a single peak around 560 nm. Remarkably, the 2PA cross section is not maximum for an excitation wavelength twice of the 1PA peak (that is 1120 nm). The 2PA spectrum cannot be deduced from the 1PA absorption spectrum.

From Equation $(1-25)$,

$$\frac{dI(x)}{dx} = -n\,\sigma_2\,I^2(x) \qquad (1-26)$$

By introducing $\delta = N_A\,\sigma_2$

$$\frac{dI(x)}{dx} = -c\,\delta\,I^2(x) \qquad (1-27)$$

By integrating both sides of the above equation:

$$I(x) = \frac{1}{\delta\, c\, x + C_1}, \qquad I(x=0) = I_0 = \frac{1}{C_1} \tag{1-28}$$

Then it can be written as $(1-29)$:

$$I(x) = \frac{1}{\delta\, c\, x + C_1} = \frac{I_0}{\delta\, c\, x\, I_0 + 1} \tag{1-29}$$

Thus, in 2PA, the reduction in light intensity is inverse to the optical path when $\delta\, c\, x\, I_0 \gg 1$.

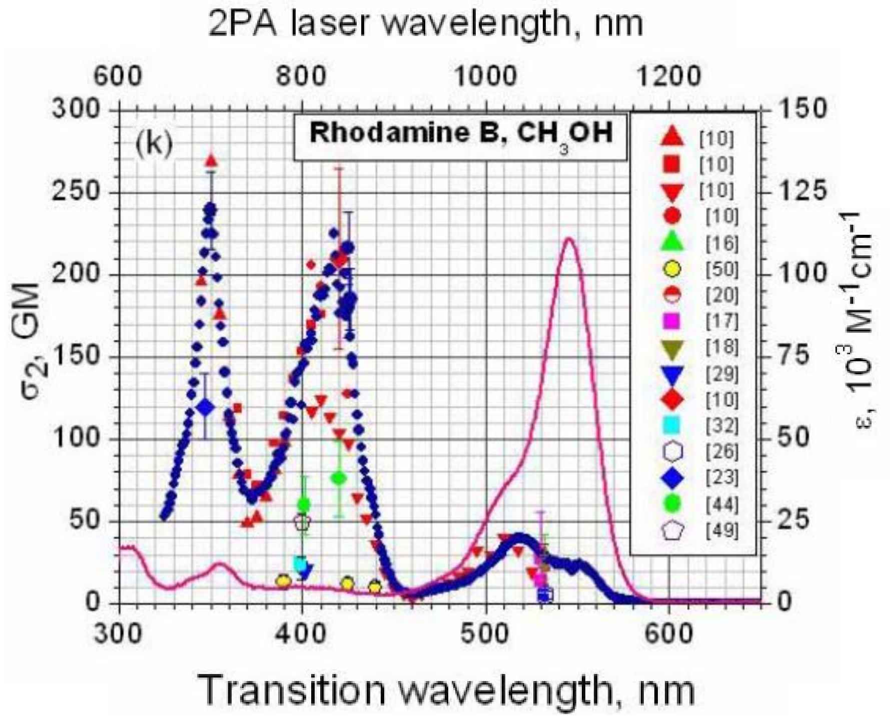

Figure 1-22 2PA spectra (dark blue circles, left vertical-axis) and molar extinction (magenta line, right vertical axis). Large dark blue circles are absolute cross sections at selected wavelengths measured here. Other symbols are the literature data with corresponding references shown in[12].

1.4.2 Intensity of the Fluorescence Signal

The fluorescence dF emitted in a volume dV and collected in a solid angle $d\Omega$ can be expressed as follows:

$$dF(\nu, t) = h\nu\, dn_s(t)\, P(\nu)\, \frac{d\Omega}{4\pi} dV \tag{1-30}$$

In this expression, $dF(\nu)$ is the radiant flux (with unit in W) of emitted fluorescence at frequency ν in the solid angle dΩ and in the volume dV. Parameter $dn_s(t)$ denotes the number of deexcitation by spontaneous emission by unit of volume and time (in $m^{-3} \cdot s^{-1}$). $P(\nu)$ is the probability to emit a fluorescent photon at the frequency ν. It can be determined by:

$$P(\nu) = \frac{S(\nu)}{\int_0^\infty S(\nu)d\nu} \qquad (1-31)$$

where $S(\nu)$ is the emission spectra of the fluorescent species.

In the case of a pulsed excitation by an ultrashort laser, a certain number of molecules dn_0 have time to absorb a photon to get excited after the lasing period. Then, the number of molecules in the excited state progressively decreases since there is no laser excitation anymore. Placing the time origin $t = 0$ just after the end of the laser pulse, the number of molecules in the excited state evolves as:

$$dn(t) = dn_0\, e^{-t/\tau} \qquad (1-32)$$

where τ is the fluorescence lifetime and ϕ is the fluorescence quantum yield. Finally, the number of spontaneous emissions is:

$$dn_s(t) = -\phi \frac{dn}{dt} = \frac{\tau}{\tau_n} e^{-\frac{t}{\tau}}\, dn_0 \qquad (1-33)$$

where τ_n is the natural lifetime of fluorescence. In the case of a long-time excitation by a CW laser or nanosecond pulse laser, a steady state establishes for the distribution of fluorescent molecules between the ground state and the excited state.

Remark: To be valid, Equation $(1-30)$ assumes that the excitation intensity remains small to avoid saturation, when a large proportion of the molecules are in the excited state and are thus no longer able to absorb more energy.

1.4.3 Advantages/Disadvantages of 2PA vs 1PA

1. **Suppression of off-field signal / background signal minimization:**

For 2PA, the excitation process is a non-linear process, with the absorbed intensity is proportional to the square of the incident intensity. The requirement for nearly simultaneous absorption of two photons means that excitation is only achieved near the focal plane. It is because the two-photon absorption cross-section is rather small, and a high photon flux is required to induce a significant absorption in a small volume. Much higher laser fluence can be achieved around the focal point of a microscope objective to meet the conditions of two-photon absorption. As shown in the **Figure 1-23**, A clear distinction is that fluorescence occurs along the entire path of the laser beam in 1PA while it is restricted to a small spot in 2PA. Thus, the fluorescence emitted afore and behind the focal point is suppressed in 2PA. If the same microscope objective is used to collect fluorescence, this leads to a much better spatial resolution along the optical axis to perform an optical slicing.

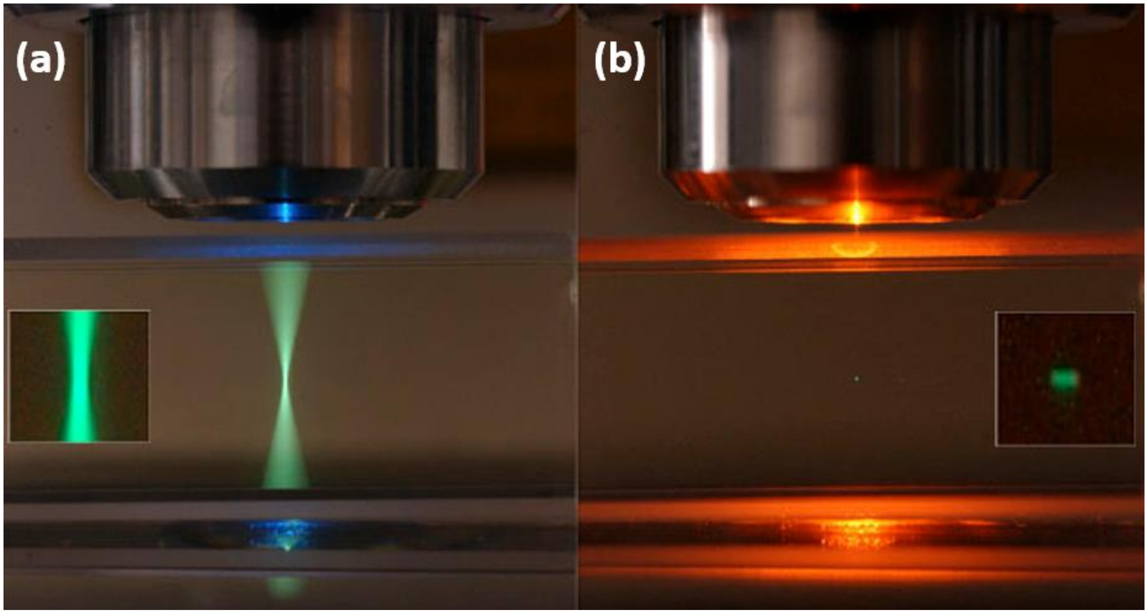

Figure 1-23 (a) one photon absorption VS (b)two-photon absorption, Photos by Steve Ruzin

2. Avoid Multiple Scattering:

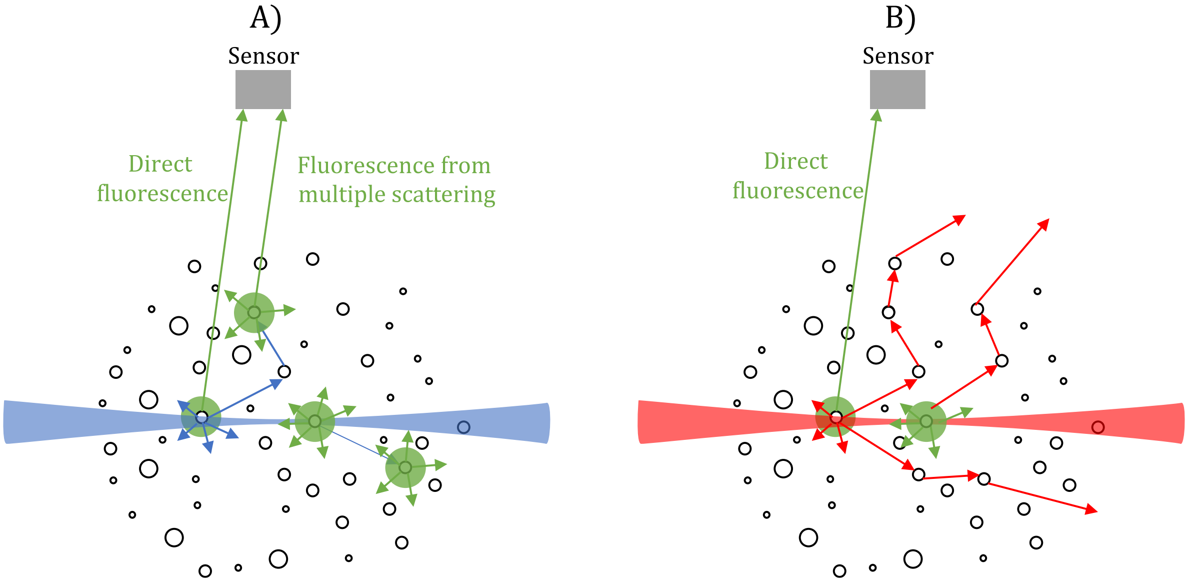

Figure 1-24 Scheme of the fluorescence reaching the sensor after A) one-photon absorption and B) two-photon absorption[13].

Compared to 1PA, 2PA is excited by a longer wavelength. For very small particles, much smaller than the wavelength, Rayleigh scattering is relevant. In that case, the scattering cross section is inversed to λ^4, which causes that for a wavelength multiplied by 2, light scattering is reduced by 16. In the case of particles whose size is close or larger than the wavelength, light scattering is described by Mie theory and geometrical optics. The scattering cross-section is then almost independent of the wavelength. However, it is still very interesting to use 2PA to study scattering media. The approach is therefore widely used in fluorescence microscopy to produce much finer, better-resolved optical sectioning across biological tissues. For studying dense sprays, the suppression of the off-field fluorescence signals mentioned above can be a decisive advantage.

Due to light scattering of the laser, droplets that are not directly exposed to the laser beam, eventually receive laser light. In 1PA, these off field droplets emits fluorescence light in return. This fluorescence light, after being scattered too, can be detected. Hence, multiple light scattering can affect the fluorescence signal by creating a background noise that is difficult to get rid of. In 2PA, a decisive difference is that the laser light scattered by the droplets does not provide sufficiently high intensity to induce a two-photon absorption process. As a result, the emission of fluorescence only takes place at the focal point of the laser beam **(Figure 1-24)**. Still a possibility exists that fluorescence is generated outside the laser focusing region. A secondary fluorescence can be induced by the reabsorption of the primary fluorescence by the surrounding droplets. However, its probabilities to be generated and to reach the receiving optics are very low in most practical situations.

A demonstration of two-photon planar laser induced fluorescence imaging in sprays was presented by Berrocal[14]. **Figure 1-25** shows a comparison of two images, one obtained with 1PA and the other with 2PA. The 2photon-LIF image reveals liquid structures that are hidden in the 1photon-LIF image. 2PA thus provides high fidelity images of ligaments and drops during spray formation since the excitation laser beam does not generate an interfering fluorescence signal.

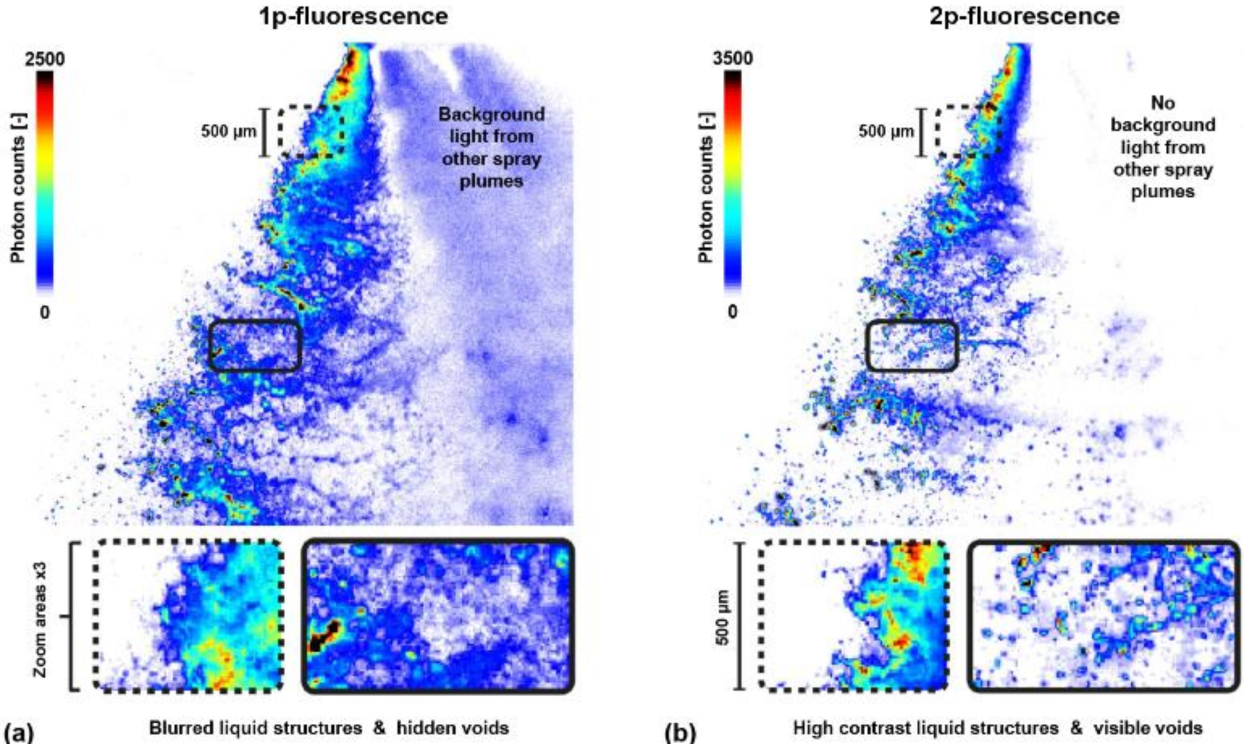

Figure 1-25 Light sheet imaging comparison between 1p-LIF in (a) and 2p-LIF in light sheet imaging in (b) for the 6holes GDI spray injected at 200 bars liquid pressure and recorded at $200\mu s$.The two images have been recorded with the same camera system but corresponds to independent injection events. It is seen from the × 3 zoom areas that 2p-LIF provides images with limited blur allowing the visibility of liquid structures which are not observable with the1p-LIF scheme[14].

3. Finer optical resolution

In 2PA, the size of the fluorescence spot is more restricted. Fluorescence emission evolves with the square of the laser excitation field, it is thus possible to focus sharply the incident laser beam to induce a very locally restricted fluorescence signal. For the same reason, 3PA techniques have emerged in microscopy with an even more delimited fluorescence.

4. Reduction of light extinction and photodamage (mainly for biological cell research)

Another advantage is the possibility to counterbalance the effects of light extinction along the incident path of the laser beam by adequately focusing the incident beam. Furthermore, 2PA enables the use of lower photon energies compared to 1PA. As lower energy photons are less likely to cause photochemical or phototoxic effects, 2PA is well-suitable for imaging delicate or sensitive samples, especially for live cells and tissues.

1.5 Conclusion

In this chapter, a description of fluorescence is made. With the help of the Jablonski diagram, the concepts of quantum yield and fluorescence lifetime are explained, and how fluorescence quenching leads to changes in fluorescence lifetime and intensity are presented. Then we introduced the lifetimes of fluorescence of some commonly used dyes. We have also covered the main phenomena that explain the effect of temperature and the nature of the solvent on fluorescence lifetime and emission spectrum, in particular solvent relaxation and collisional deactivation. This lays the groundwork for the subsequent study of heat and mass transfer phenomena by characterizing the lifetimes of fluorescence dyes in different solvents at different temperatures.

Table 1-4 Difference between One-photon Absorption (1PA) and Two-photon Absorption (2PA)

	One-Photon	Two-Photon
Photodamage	Much	Less
Penetration depth	Shallow	Deep
Background signal	Big	Small
Excitation volume	Big	Small
Fluorescence Imaging	A Laser Beam	A Fluorescence Spot
Excited Wavelength Required	Short	Long

At the end of this chapter, we present the concept of one-photon absorption and two-photon absorption, state the difference between these two absorptions and derive their corresponding molar absorption rates, and illustrate the advantages of two-photon absorption. One of these distinguished benefits is that two-photon absorption can effectively avoid light scattering problems in the sprays, which is important for our subsequent studies. **Table 1-4** lists some of their difference in the photodamage, penetration depth, background noise, excitation volume, and fluorescence imaging.

1.6 Reference

[1]. Lakowicz, J. R. (Ed.). (2006). Principles of fluorescence spectroscopy. Boston, MA: springer US.

[2]. Valeur, B., & Berberan-Santos, M. N. (2011). A brief history of fluorescence and phosphorescence before the emergence of quantum theory. Journal of Chemical Education, 88(6), 731-738.

[3]. Albrecht, C. (2008). Joseph R. Lakowicz: Principles of fluorescence spectroscopy.

[4]. Albani, J. R. (2008). Principles and applications of fluorescence spectroscopy. John Wiley & Sons.

[5]. Ewald Terpetschnig & David M. Jameson. Technical note. ISS. Retrieved March 22, 2023, from https://iss.com/media/Fluorescence_Lifetime.pdf.

[6]. Magde, D., Wong, R., & Seybold, P. G. (2002). Fluorescence quantum yields and their relation to lifetimes of rhodamine 6G and fluorescein in nine solvents: Improved absolute standards for quantum yields. Photochemistry and photobiology, 75(4), 327-334.

[7]. Kubin, R. F., & Fletcher, A. N. (1982). Fluorescence quantum yields of some rhodamine dyes. Journal of Luminescence, 27(4), 455-462.

[8]. Eftink, M. R. (2002). Fluorescence quenching: theory and applications. In Topics in fluorescence spectroscopy: principles (pp. 53-126). Boston, MA: Springer US.

[9]. Valeur, B., & Berberan-Santos, M. N. (2012). Molecular fluorescence: principles and applications. John Wiley & Sons.

[10]. Brian Herman, Joseph R.Lakowicz, Ian D & Davidson M. W. Solvent Effects on Fluorescence Emission. Retrieved March 30, 2023, from https://www.olympus-lifescience.com/en/microscope-resource/primer/java/jablonski/solventeffects/

[11]. Saha, J., Roy, A. D., Dey, D., Chakraborty, S., Bhattacharjee, D., Paul, P. K., & Hussain, S. A. (2015). Investigation of fluorescence resonance energy transfer between fluorescein and rhodamine 6G.Spectrochimica Acta Part A: Molecular and Biomolecular Spectroscopy, 149, 143-149.

[12]. Makarov, N. S., Drobizhev, M., & Rebane, A. (2008). Two-photon absorption standards in the 550–1600 nm excitation wavelength range. Optics express, 16(6), 4029-4047.

[13]. Wang, M., Stiti, M., Chaynes, H., Becker, S., Berrocal, E., Lemoine, F., & Castanet, G. (2022). Two-photon fluorescence lifetime imaging applied to the mixing of two non-isothermal sprays: temperature and mixing fraction measurements. Experiments in Fluids, 63(11), 172.

[14]. Berrocal, E., Conrad, C., Püls, J., Arnold, C. L., Wensing, M., Linne, M., & Miranda, M. (2019). Two-photon fluorescence laser sheet imaging for high contrast visualization of atomizing sprays. OSA Continuum,2(3), 983-993.

CONTENT 2

Chapter 2 State of the Art on the Spray Measurements

Spray technology involves atomizing substances into controlled, minute droplets and finds extensive applications across industries including agriculture, medicine, aerospace, and more. Presently, primary research in the field of sprays revolves around the following areas: Firstly, the investigation of liquid breakup mechanisms into small droplets to enhance spray performance, notably droplet size distribution, is crucial for applications like fuel injection. Secondly, it explores the intricate interactions between sprays and their ambient milieu, encompassing droplet/particle generation, behavior, and the impact of environmental variables on spray dynamics. The significance of this research lies in its potential to enhance comprehension of phenomena such as climate change, air pollution, ocean currents, and, crucially, spray combustion, as well as heat and mass transfer processes. Combustion-based technologies, such as engines and burners, require the elucidation of spray combustion mechanisms to enhance performance, while the clarification of heat and mass transfer processes associated with sprays is vital for enhancing cooling efficiency in various applications. Therefore, the investigation of spray characteristics holds paramount importance and substantial value.

This chapter predominantly delineates some prevalent applications of spray technologies, and contextualizes their significance in research. Subsequently, various spray measurement techniques are expounded, encompassing their merits, drawbacks, and their ability to capture droplet parameters (e.g., temperature, composition). A detailed analysis of the applicability is given for the corresponding techniques. Ultimately, this chapter elaborates extensively on the laser-induced methods, highlighting some of their advantages over alternative approaches.

2.1 Introduction about Spray Applications

The term "spray" refers to the process of transforming a liquid into exceedingly fine particles. These finely dispersed particles often hold greater utility. Primary research in the field of spray evolves around different areas. The investigation of liquid breakup mechanisms into small droplets to enhance spray performance, notably droplet size distribution, is crucial for many applications. The clarification of heat and mass transfer processes associated with sprays holds paramount importance and substantial value. Finely dispersed droplets have a large surface area and volume ratio, which promotes the intensification of heat and mass transfer compared with some other multiphase flow systems. To illustrate this point, a few examples of spray applications are presented below.

Spray Cooling:

spray cooling consists of generating small droplets through a nozzle and directed the spray onto the surface to be cooled. Compared to other cooling technologies such as forced air cooling, liquid immersion, liquid jet cooling, the technique has many advantages. Spraying the liquid coolant allows the dispersed droplets to penetrate small crevices and gaps in the surface being cooled, enabling heat transfer more efficient. The liquid is also more uniformly distributed than in the case of the impact of a liquid jet. By controlling and regulating the size, shape, or flow rate of the droplets, the performance of spray cooling can be optimized. If the solid surface is very hot, cooling is further enhanced by the heat dissipation caused by liquid evaporation and boiling in contact to the surface. Therefore, as a phase change cooling technique with a high cooling efficiency, spray cooling is widely seen a technology of interest in the electronic cooling and other high heat flux applications. As an example, in aerospace industry, it is especially used as a way of thermal protection in engines and electronic components with high heat flow density[1].

Figure 2-1 illustrates the basic heat transfer mechanism of spray cooling. It mainly includes four processes: (1) evaporation of liquid film. A thin liquid film generated will cover the hot surface when the spray cooling starts. (2) forced convection arising from droplet impingement on the heated surface. After these dispersed small droplets collide with the surface and form a liquid film on the surface, subsequent droplets will impinge on that thin liquid film, the force form the incoming droplets produce an enhancement of the forced convection in the liquid film (3) enhancement of nucleation sites on heated surface (4) presence of secondary nucleation sites on the surface of spray droplets[2][3][4]. Although spray cooling has reached a certain maturity, there are still limits to the prediction of cooling performance. Modeling is highly dependent on the distribution and properties of spray-formed particles. The temperature of the injected liquid is also critical for recovering heat from the wall. Research into the impact of individual droplets on hot walls requires measurement of the temperature of the secondary droplets and liquid fragments formed on impact to assess the efficiency of heat transfer to the liquid phase (sensible heating). If droplet temperature can be obtained, it can bring many advantages to all research focusing on spray cooling [5][6][7][8] or impaction cooling [9][10][11][12].

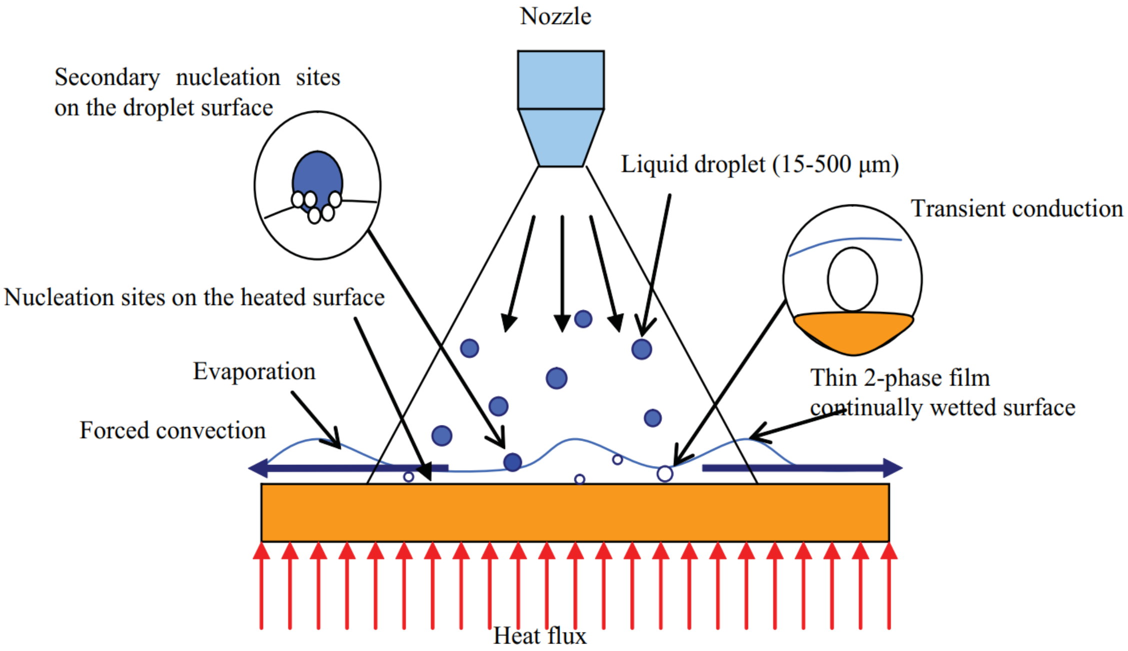

Figure 2-1 Basic heat transfer mechanism of spray cooling[12]

Combustion of fuel sprays:

Spray combustion is also an area of significant application in spray research. It is used to study the combustion of liquid fuels. Atomizing the liquid fuel into tiny droplets leads to increased combustion efficiency and energy utilization due to the increased surface area of the fuel. Spray combustion is extensively used in transportation systems. It finds applications in compression ignition (diesel) engines for road vehicles, ships, and in aviation, marine, or land-based gas turbines[13].

Figure 2-2 shows the process of liquid fuel combustion. The liquid fuel is atomized by a nozzle, producing fine droplets, then these droplets begin to vaporize in the combustor where the temperature is high. Finally, the fuel vapor is auto-ignited and combusted in the sufficiently high temperature[14]. The evolution of the droplets in the chamber, i.e., their size, temperature and composition, largely controls combustion, acting on the flow of steam released around the droplets and the local richness of combustion. In addition, common fuels contain compounds of different volatilities, so that evaporation and heating of the droplets is accompanied by a change in their composition.

In the study[15][16], modeling droplet heating and evaporation, as well as fuel-air mixing necessitates advanced experimentally obtained droplet behavior knowledge, with temperature and composition measurements being particularly important parameters to characterize. In the literature[17][18][19], the kinetics and chemical reactions can be more clarified if we can acquire the composition of the droplets which constitute of many chemical species.

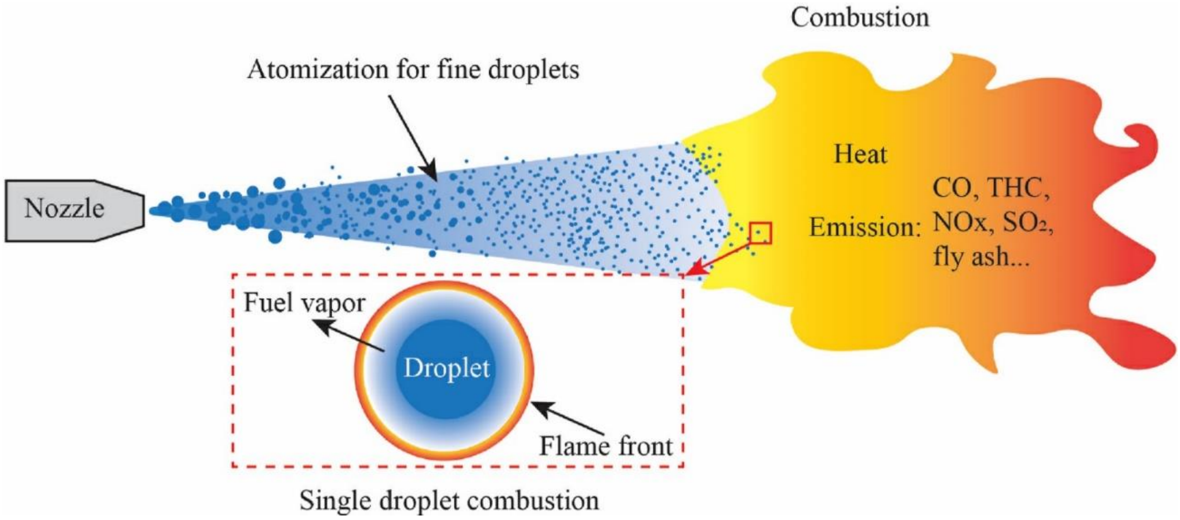

Figure 2-2 Basic heat transfer mechanism of spray cooling[14]

Spray drying:

Another notable application of spraying technology is in spray drying. Within the pharmaceutical sector, spray drying finds application in producing desiccated materials exhibiting specific attributes essential for diverse drug formulations[20]. Similarly, in the food industry, the spray dryer has emerged as a pivotal apparatus for desiccating heat-sensitive fluid products, encompassing foods and biological substances[21][22]. **Figure 2-3** illustrates the traditional process and system of spray drying in the food industry.

The primary principle behind spray drying involves dispersing a liquid solution to be dried into small droplets using a sprayer. Subsequently, the introduction of hot air facilitates the evaporation of internal water content, resulting in the formation of solid particles which are ultimately collected. During the drying process, smaller droplet sizes lead to a greater surface area-to-volume ratio and thus an augmentation of the evaporation and drying rate. In general, droplets are uniformly dispersed within the drying chamber to achieve the drying at the same rate for all the droplets and better control the drying process which is critical for the quality of the final powder (residual moisture, cohesion of the solid grains). The evolution of droplet temperature and composition during the initial phase of droplet evaporation, and the subsequent transformation from a droplet to a solid grain, is critical to gain a deep understanding of heat and mass transfer phenomena.

Beyond the differences between these three examples (spray cooling, spray combustion and spray drying), there are many common features. Analysis of heat and mass transfer is intimately related to droplet dynamics (liquid atomization, turbulent transport, droplet/wall interactions…). The temperature and composition of the droplets are central to describing the processes involved. There is therefore a strong interest in developing measurement techniques capable of obtaining information on these parameters.

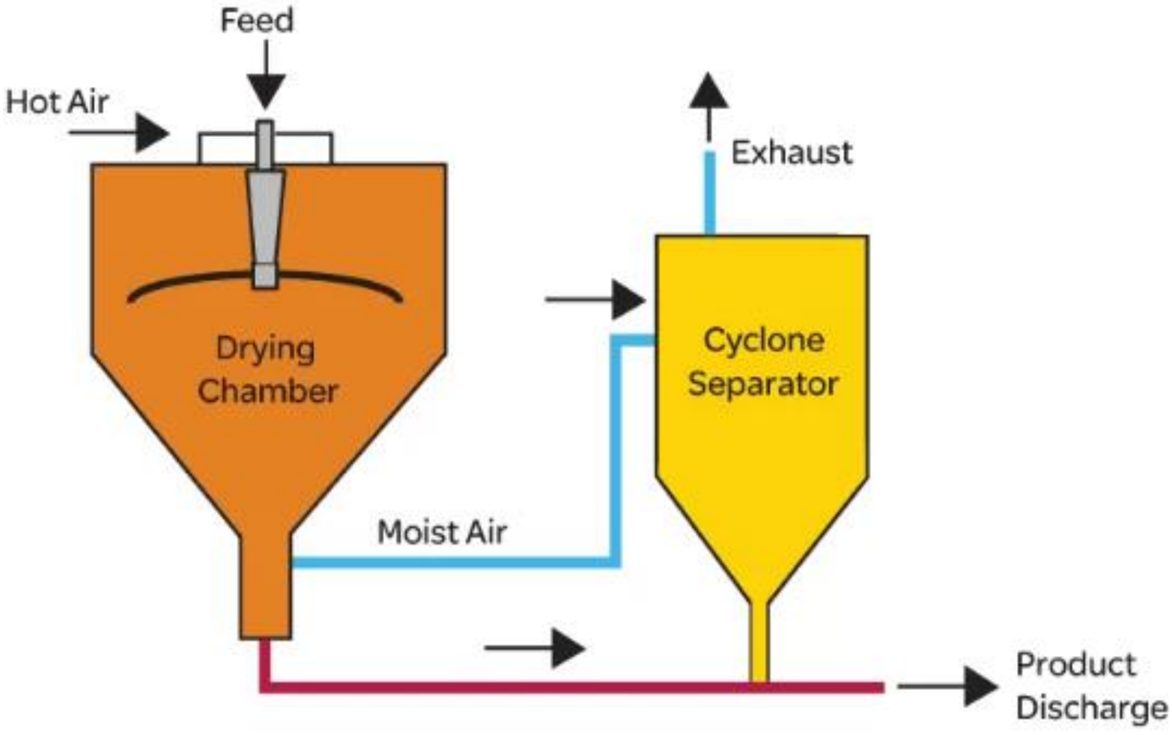

Figure 2-3 Traditional process and system of spray drying in the food industry

2.2 Spray Measurement Techniques

Most of the existing measurement techniques used for sprays are optical techniques, which work with no physical contact with the droplets. Measurement techniques, such as hot-wire anemometry (HWA), resistance temperature detectors (RTD) and thermocouples are designed for measurements in a continuous fluid flow instead of spray. As intrusive techniques, they might affect the spray flow, and are not suitable for the spray conditions.

2.2.1 Droplet Sizing

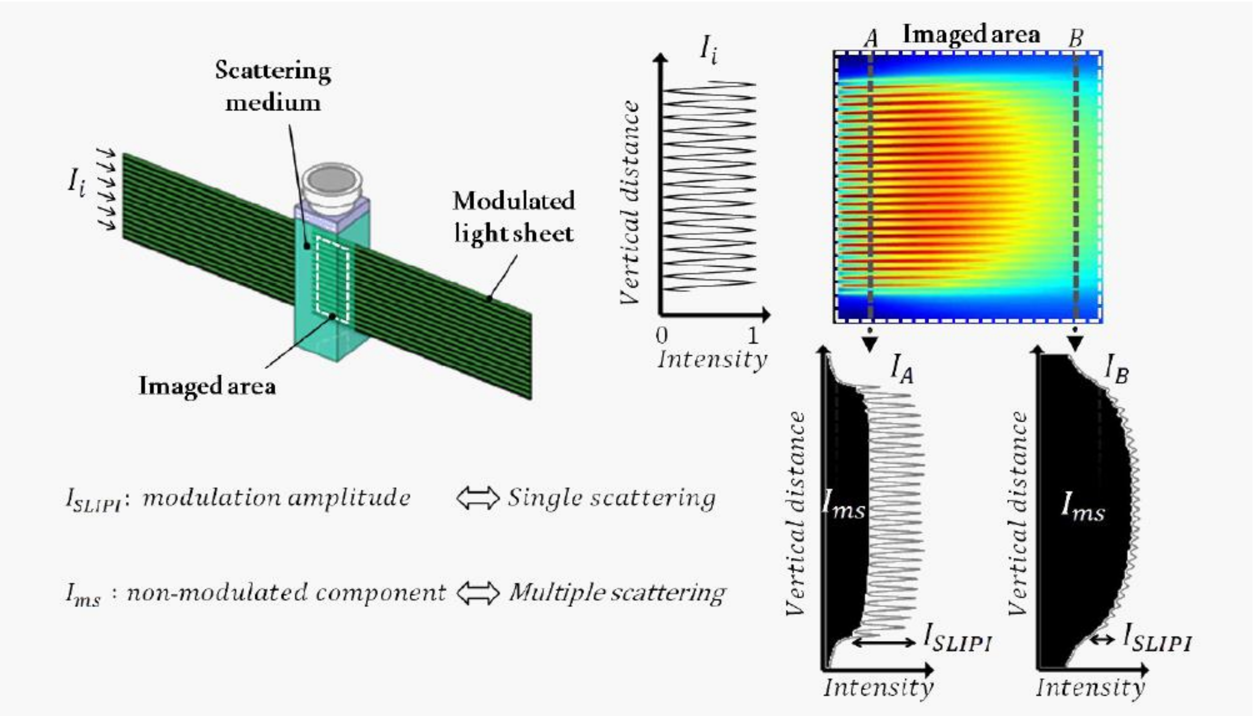

Figure 2-4 Illustration of how the SLIPI technique works. A spatially intensity-modulated laser beam passes through a cuvette containing 15 µm polystyrene spheres suspended in water. Due to multiple scattering, the amplitude of the modulations in the recorded image decreases between positions A and B.

Characterizing the sizes and velocities of droplets relies upon optical measurement techniques which are rather well established despite some minor shortcomings. Among them, Phase Doppler Anemometry (PDA) allows measuring both the velocities and sizes of droplets. It can provide valuable information about the size distribution, and number densities of individual particles. The LIF/Mie droplet sizing technique has been studied for many years. It relies on the assumption that laser-induced fluorescence (LIF) and Mie scattering optical signals from spherical droplets depend on their volume and surface area, respectively. Two cameras are used to observe the Mie scattering and fluorescence of droplets illuminated by a laser sheet. While the fluorescence signal increases with the volume of liquid illuminated, the scattered light is essentially proportional to the surface area of the drops. The ratio between the two images is thus proportional to the definition of the Sauter diameter. A solution to the problem of multiple light scattering in dense sprays has been proposed with the SLIPI (Structured Laser Illumination Planar Imaging) method. The spray is illuminated by a spatially intensity-modulated laser sheet. Photons that have undergone multiple scattering have a serpentine trajectory and do not retain the spatial coding of the laser sheet. There is thus a component of the scattered light signal that does not follow the spatial modulation of the laser sheet, and which corresponds to the contribution of multiple scattering. This phenomenon is illustrated in **Figure 2-4** in the case of a tank filled with a suspension of glass beads a few microns in size.

A demodulation algorithm makes it possible to eliminate the non-modulated component of the images, which corresponds to multiple scattering **(Figure 2-5)**. Sinusoidal modulation and 120° phase-shifted structures are sufficient to reconstruct a signal corrected for multiple scattering without loss of spatial resolution, but this requires the recording of a triplet of images[23][24]. In other applications[25], a system using a double-cavity pulsed laser is used to obtain pairs of images separated by a few hundred ns, with are 180° out of phase. Instantaneous images stripped of their non-modulated component are significantly improved over conventional LIF images.

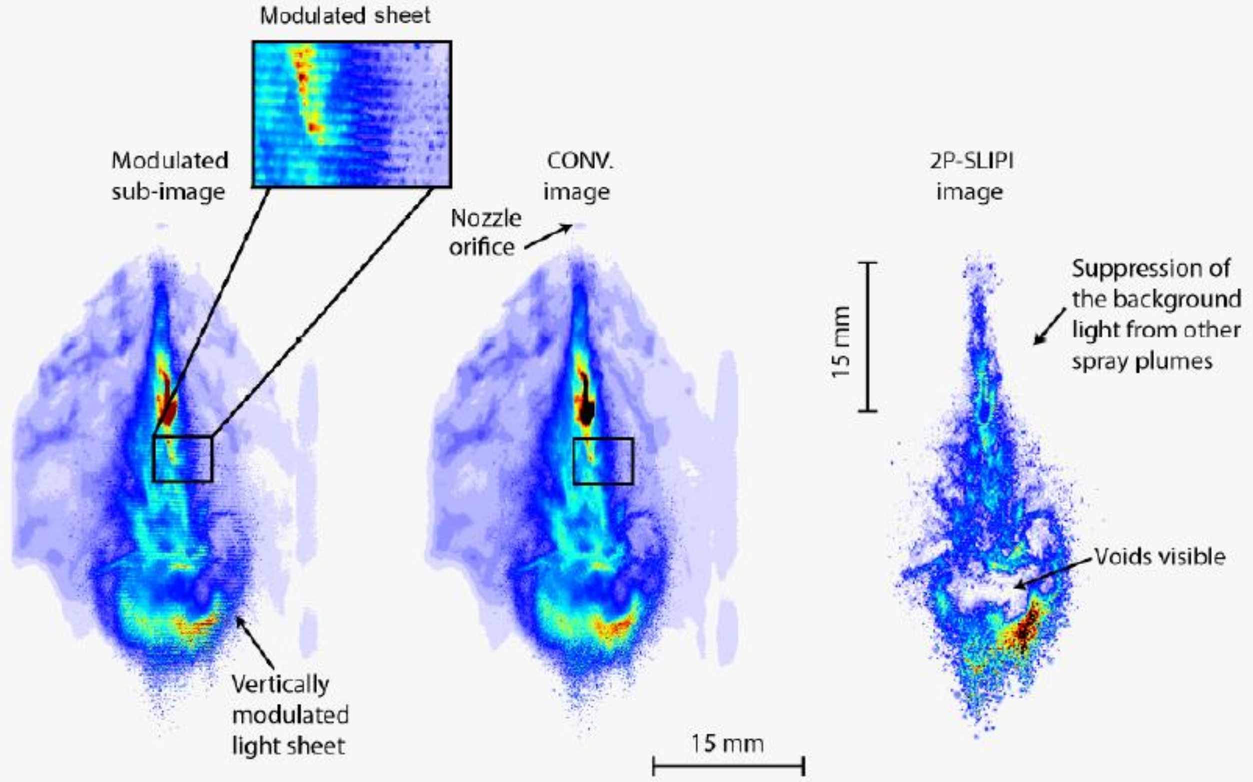

Figure 2-5 Instantaneous image of fluorescence in a spray. By recording two spatially modulated images in a very short time interval (typically a few hundred ns) and vertically shifting the modulations between the two images, it is possible to reconstruct an image in which the light background linked to multiple scattering is suppressed.

2.2.2 Droplet Temperature and Composition

Droplet temperature and composition can be inferred from the refractive index provided that the dependence of the refractive index on both temperature and composition is known[26]. The aim of Rainbow Refractometry (RR) is to measure the refractive index of droplets to deduce their temperature or their composition. Depending on the experimental setups and applications, RR can be categorized two types: Standard Rainbow Refractometry (SRR) and Global Rainbow Refractometry (GRR), the former one is applied to the measurement of single droplets and the latter one is used for a larger population of droplets[27].

2.2.2.1 Rainbow Refractometry (SRR)

A. Standard Rainbow Refractometry (SRR)

Standard Rainbow Refractometry (SRR) is based on the phenomenon of rainbow scattering, where light is reflected and refracted within a droplet, resulting in a distinctive pattern known as a rainbow in the backward scattering direction. **Figure 2-6** depicts the various orders observed for the light rays when a plane wave interacts with a transparent spherical particle. Some rays are reflected, and some are refracted when they meet the surface of the spherical particle. Order 0 rays are those that are immediately reflected from the surface, whereas order 1 rays are those that travel straight through the droplet. Following one internal reflection, the rays of order 2 appear, and it is these rays that give rise to the primary rainbow.

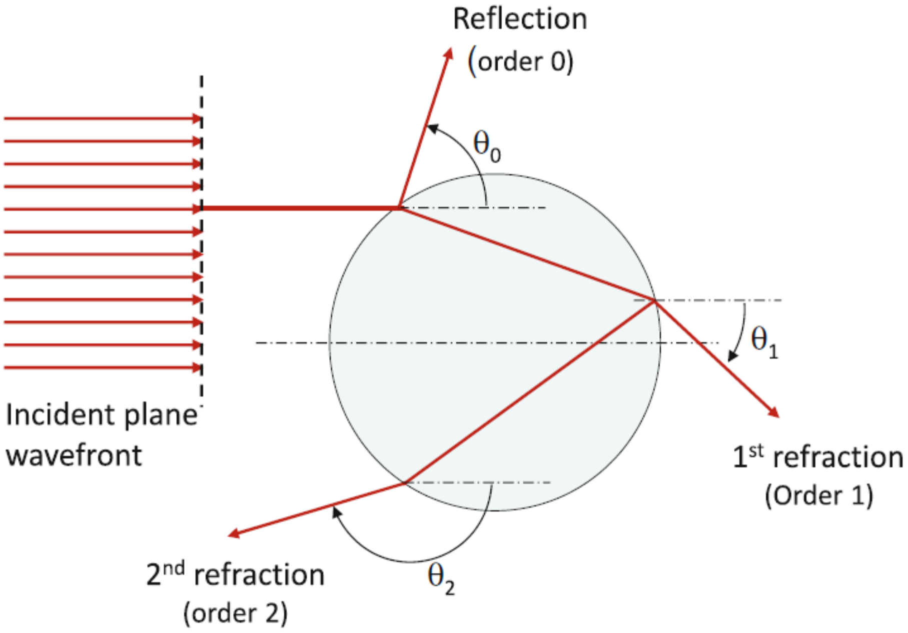

Figure 2-6 Interaction of light with a spherical droplet according to geometrical optics[26]

The superimposition of all order 2 rays reveals that these rays emanate from the particle with the greatest concentration in the region of a certain scattering angle known as the rainbow angle. The main rainbow correlates to an increase in the intensity of scattered light in this angular region. Higher-order rainbows (made up of rays of higher orders) can also be seen. According to van de Hulst[28] the principal rainbow angle θ_{rg} may be stated using geometrical optics assumptions as:

$$\theta_{rg} = 4arc\sin\left(\frac{1}{n}\sqrt{\frac{4-n^2}{3}}\right) - 2arc\sin\left(\frac{1}{n}\sqrt{\frac{n^2-1}{3}}\right) \qquad (2-1)$$

where n is the refractive index of the liquid of interest.

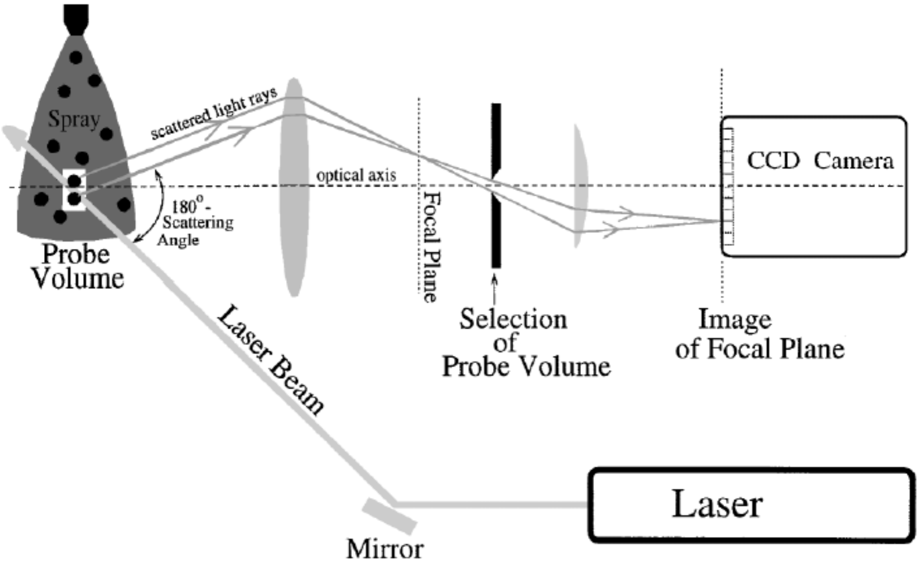

Figure 2-7 Optical layout for the setup used in standard rainbow thermometry. The scattering angle is defined as the angle between the incident and the scattered wave vectors[27]

SRR is essentially the detection of light scattered by a single transparent particle in order to calculate the angular position of the rainbow and consequently the refractive index from Eq $(2-1)$. However, geometrical optics does not take into consideration light diffraction and interference. Airy's rainbow theory tackles this issue by taking into account the wave nature of light[29], demonstrating that the rainbow angle, or more accurately the angular location of the principal rainbow pattern's initial maximum, is a decreasing function of droplet size:

$$\theta_{ra} = \theta_{rg} + \frac{1.0873}{\sqrt{(n^2-1)/3}} - \left(\lambda^2\frac{\sqrt{(4-n^2)/3}}{16D^2}\right) \qquad (2-2)$$

where λ is the light wavelength and D is the droplet diameter. Airy's theory is based on the notion that the intensity of light in a rainbow may be represented by a planar wave-front. Because of this approximation, there may be substantial inconsistencies, especially at small droplet sizes. The Lorenz-Mie theory (LMT) solves Maxwell's equation for the scattering of electromagnetic radiation by a sphere and hence applies to particles with tiny size parameters[26].

Standard Rainbow Refractometry, first introduced in[30][31][32], was used for the droplet size and temperature measurements, then applied later in spray flames by Sankar [33]. **Figure 2-7** shows the setup for the typical standard rainbow refractometry. In a SRR setup, a CW laser illuminates a single droplet or an ensemble of droplets to produce rainbows that are monochromatic. Spatial filtering may be required to simultaneously select single droplets when the method is applied to a spray. The CW laser can be replaced advantageously by a pulsed laser which allows the rainbow pattern to be frozen to eliminate perturbations from transient events such as oscillations of the droplet shape[34]. A CCD camera imaging the focal plane of a lens can be used to observe the angular distribution of the scattered light in the vicinity of the rainbow angle.

Figure 2-8 shows a typical image of the rainbow pattern which is composed of a low and a high frequency structure. The Airy fringes are perfectly visible in **Figure 2-8** and in the intensity-profile displayed in **Figure 2-9**. They correspond to the low frequency pattern. Airy fringes originate from interference between rays of order 2 which have experienced one internal reflection. These rays emerge from the droplet in the same angular direction but have different impact points on the droplet surface. Furthermore, interference between orders 0 and 2 rays give rise to the ripple structure—i.e., a high-frequency modulation of intensity—which Airy’s theory does not account for although the LMT does[26]. The droplet size can be calculated from the spacing between the Airy fringes without knowing the refractive index previously. The refractive index is then derived by using the equation $(2-2)$ from the angular location of initial maximum of the Airy fringes[35][36]. Another signal processing option is to infer the droplet diameter from the ripple frequency, which may significantly enhance measurement accuracy[37].

For a substance, the refraction index exhibits temperature dependence, allowing for the deduction of droplet temperature. In this respect, can be remarkably sensitive. It has been evidence that an alteration of the rainbow angle by 2.3° for a water droplet corresponds to a temperature increases from 0 ℃ to 100 ℃[26]. However, the drawbacks and limitations of SRR method are also evident.

First, if the temperature within the liquid is not uniform, this can lead to variations in the angular position of the standard rainbow pattern collected, and thus to errors in measurement errors [38][39][40]. Attempts have been done to consider the presence of internal gradients of refractive index. The rainbow pattern can be simulated using the LMT assuming a succession of concentric layers of different refractive index. An equivalent particle, defined as the homogeneous particle which scatters the light in forward and backward directions as does the particle with a radial gradient, can always be found. However, extra knowledge coming from an independent source (such as LIF) is required to assess the gradient level[41]. If nothing is done, i.e. neglecting the gradients and assuming a uniform refractive index, this can lead to a large error in temperature. This was reported by Massoli[42] who performed numerical simulations of evaporating droplets using Lorenz–Mie theory and a finely stratified sphere model with thousands of layers.

Second, an assumption of SRR method is that the droplet is spherical. In fact, droplets can have various shapes, and their shape can change with time. Non-spherical droplets can be subjected to errors in the size and refractive index calculations. According to[43][44], a sphericity default of only 1 % may lead to errors in temperature measurements as high as around 40℃. a sphericity default of only 1 % may lead to errors in temperature measurements as high as around 40℃. If the droplets are oversized and thus easily deformed, the rainbow pattern may become distorted or challenging to interpret accurately.

Finally, there is also a challenge to the alignment and calibration of the experiment. Proper alignment and calibration of the SRR system are essential for accurate measurements. Misalignment of the light source and the imaging system can introduce errors and affect the quality of the rainbow pattern.

Refractive index also changes with the chemical composition. This dependency can be exploited to determine the change of the composition of droplets. This idea has been implemented in several works. A recent example is the monitoring of CO_2 absorption in drops of water loaded with methylamine (30% by mass).[45]. The chemical reactions associated with CO_2 absorption create new species inside the droplet, changing its composition and refractive index.

However, when temperature and composition are changing simultaneously there might be some problem of ambiguity to separate the effects. The rainbow method has been used to measure the compositional history of droplets in an evaporating binary mixture. A method was presented that uses Airy theory and simultaneous size measurement by Mie scattering imaging. Experimental conditions were selected where there were no refractive index gradients inside the droplets, which could be due to either concentration or thermal gradients. The maximum droplet size was of the order of 50 µm to ensure a spherical shape of the droplet. Since the refractive index depended both on composition and on temperature, the droplet temperature had to be measured also. This was achieved in an indirect manner. Experimental conditions were chosen where the evaporation rates were sufficiently low so that the droplet temperature was approximately the same as the ambient temperature. Therefore, the temperature could be measured in the gas phase with a thermocouple. At the end, the composition of the droplet mixture could be determined from the measured refractive index and the known refractive indices of the individual components by a linear relationship since the study was restricted to ideal mixtures of linear alkanes.

In summary, SRR remains a valuable technique for measuring the temperature and size of droplets in many applications despite these drawbacks. To avoid limitations of SRR methods, on one hand, it is suggested to combine SSR with other measurement techniques to enhance the accuracy and applicability of the results, and on the other hand, Global Rainbow Refractometry (GRR) can be used to eliminate the errors of SRR.

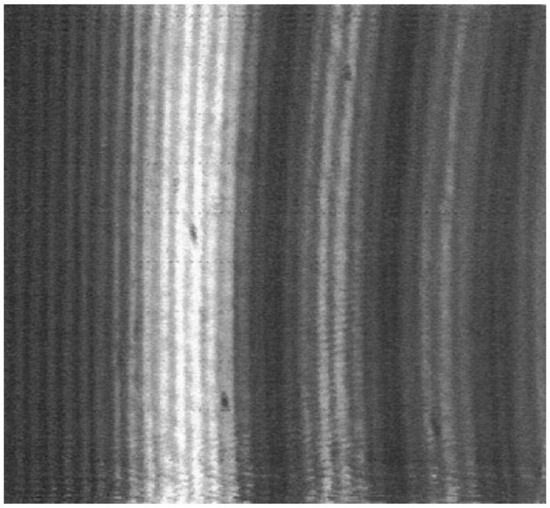

Figure 2-8 Standard rainbow pattern obtained from a single droplet in a water spray. Reprinted from [46]

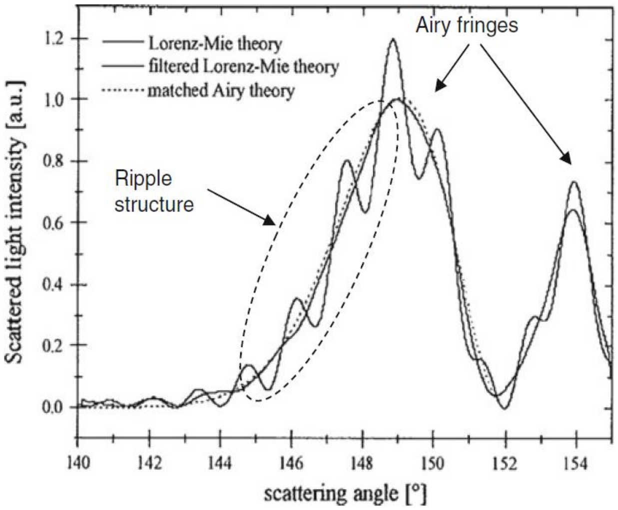

Figure 2-9 Scattering pattern by a spherical particle in the vicinity of the primary rainbow computed using LMT. Filtered LMT and Airy theory are also superimposed. Reprinted from [47]

B. Global Rainbow Refractometry (GRR)

Global Rainbow Refractometry (GRR), first initiated by van Beeck[43], is an extension of SRR that allows for the simultaneous measurement of droplet sizes and refractive indices within a large droplet population. As introduced earlier, one of the major biases of SRR are due to non-sphericity of the droplets.

The superposition of the rainbows created by multiple droplets results in a global rainbow. When perfectly spherical droplets have almost the same refractive index in the probing volume, the angular location of their rainbows is identical, therefore a global rainbow is formed by the constructive interferences of the spherical droplets. Conversely, non-spherical objects like spheroids or ligaments cause some destructive interferences. A uniform background will result from these destructive interferences provided that the non-spherical objects are randomly oriented[26][26].

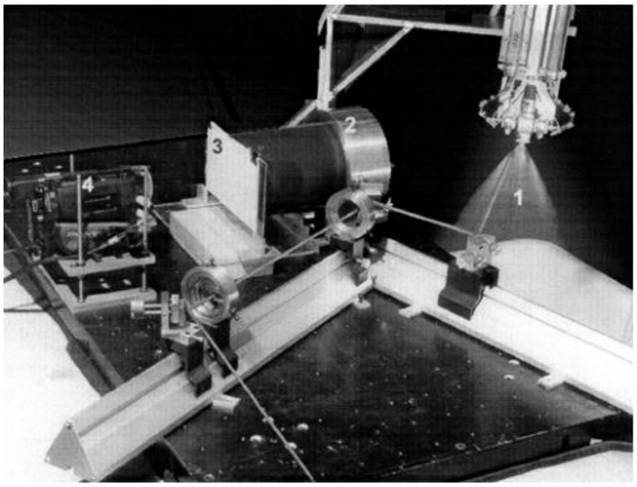

Figure 2-10 Photograph of the set-up for global rainbow thermometry showing the water spray (1), receiving lens (2), transparent screen (3) and video camera (4). The laser beam was added during poet-processing of the photograph and does not represent the real thickness. Retrieved from [48]

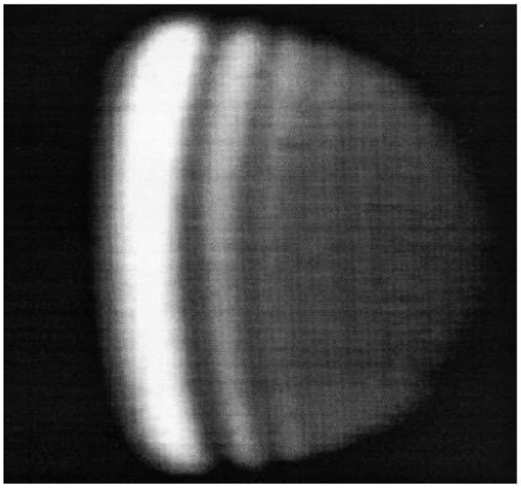

Figure 2-11 A typical global rainbow pattern in a water spray recorded by a video camera Retrieved from [46]

A typical setup for the global rainbow thermometry is shown in the **Figure 2-10**. A CW argon-ion laser beam illuminates a water spray. The laser beam is expanded to a thickness of 15mm. All the droplets crossing the laser beam contribute to the angular scattered light distribution visualized on a screen. This results in the so-called global rainbow pattern. To calibrate the magnification factor of the camera and the relationship between pixel number and the scattering angle, a specific calibration is required taking into account the focal length of the receiving lens[48].

Figure 2-11 shows a typical pattern of global rainbow. It can be noticed that the visibility of the pattern is reduced compared with the standard rainbow (**Figure 2-8)**. The ripple structure observed with SRR but contain no temperature information, is not visible in **Figure 2-11.**

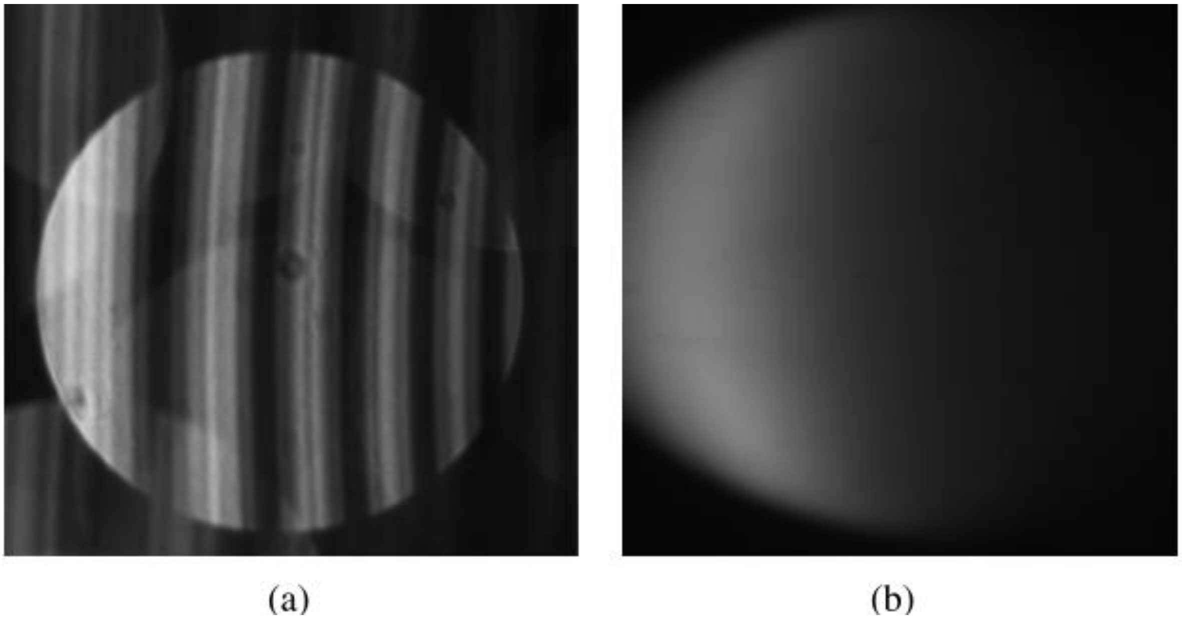

Figure 2-12 Experimentally recorded (a) standard and (b) global rainbow patterns.

Figure 2-12 respectively shows the rainbow patterns standard and global.

The mean droplet size and temperature are inferred from the recorded rainbow image. To that end, an inversion process is necessary. For fast, real-time inversion, van Beeck et al. [48] proposed empirical relations based on specific characteristic points of the Airy rainbow filtered in the spectral domain. The reliability of this method was assessed by simulations of the global rainbow based on LMT. If the accurate droplet size distribution is known, uncertainties can be mainly attributed to the difficulty in locating inflection points. Temperature uncertainties can be limited to only a few ° C. It was pointed out that the previous inversion method has some inherent weaknesses as it is based on characteristic points of rainbow-scattered light distribution. To address this issue, they [49] developed a more robust inversion algorithm based on the least square fit of the whole rainbow pattern. The method was demonstrated on silicon oil droplets suspended in a water bulk with a quite large distribution of droplet sizes. Concerning the development of the rainbow inversion method, more details can be found in [50][51][52][53][54][55].

Broadly speaking, Global Rainbow Refractometry (GRR) emerges as an advanced optical measurement methodology, concurrently assessing droplet size and refractive index across extensive droplet populations within the spray. It augments the functionalities of Standard Rainbow Refractometry (SRR) by capturing dynamic rainbow patterns through a high-speed image sequence, involving multiple droplets.

The data obtained through GRR allows a statistical representation of droplet size distribution and refractive index variations. However, the method of GRR requires sophisticated data analysis algorithms to extract droplet size and refractive index information from the rainbow patterns, which makes data processing more challenging and time-consuming, and as for the SRR, it needs careful alignment to ensure the accuracy of the measurements. In addition, GRR is most effective for droplets within a specific size range, and the technique is limited to capturing droplets with velocities within the camera's frame rate capabilities.

2.2.2.2 Raman Scattering (RS)

Raman scattering, also known as Raman spectroscopy, is a powerful analytical technique used to study the vibrational and rotational energy levels of molecules and materials and is widely used characterizing the composition and temperature of droplets. Enhanced Raman-scattering, a specialized variant of Raman spectroscopy that significantly amplifies the Raman signal of molecules absorbed on or near certain substrates, can be used to probe composition changes near the surface of droplets.

The phenomenon of Raman scattering is a form of light scattering. When the frequency of the scattered light is the same as the frequency of the incident light, we call it Rayleigh scattering for particles of size up to a few tenth of the light wavelength, When the frequency is different, we call it Raman scattering, as shown in **Figure 2-13**. Raman scattering, according to the frequency of the scattered light and the incident light, can be divided into Stokes Raman scattering and anti-Stokes Raman scattering, the former refers to the frequency of the scattered light being less than the frequency of the incident light, while the latter is the opposite. From the view of atomic and molecular, Raman scattering is the result of inelastic collisions of photons with atomic nuclei and molecular electron clouds. The transfer of energy between photons and molecules may result in an increase or a decrease in the molecules’ vibrational or rotational energies. As a result of this energy conversion process, scattered Raman photons are blue-shifted (anti-stokes shift) or red-shifted (stokes shift), as they contain more or less energy compared to the incident photons [56].

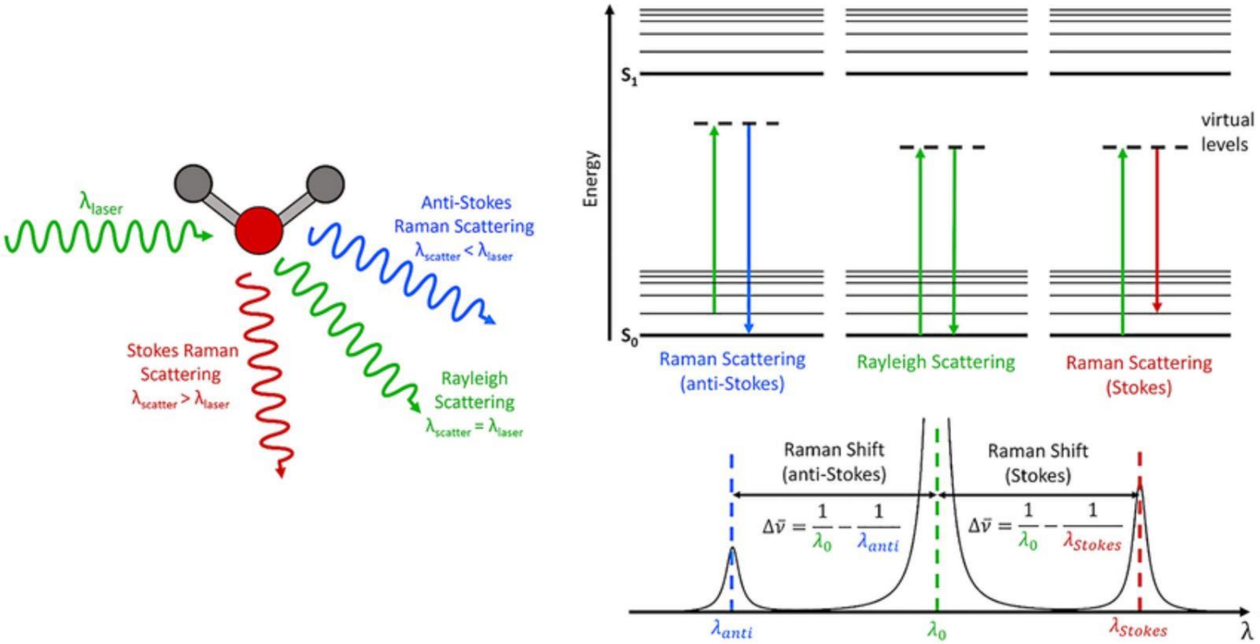

Figure 2-13 The principle of Raman Scattering [57]

Figure 2-14 illustrates the Stokes and anti-Stokes Raman Spectra of anatase (TiO2). It can be seen that the number of peaks produced by the Stokes Raman is the same as the number of peaks produced by the anti-Stokes Raman, but the peaks corresponding to the Stokes effect are higher than the peaks corresponding to the anti-Stokes effect, which implies that Raman scattering produces a much larger Stokes intensity than the anti-Stokes intensity. It is because the Stokes-Raman effect results from the transition from a lower energy level to a higher one while anti-stokes is a transition from a higher level to a lower one. Since the anti-Stokes scattering occurs from a thermally excited state which is, according to Boltzmann statistics, less populated than the ground state, the intensity is less for the anti-Stokes shift [58]. It is worth noting that at higher temperatures, that the thermal energy increases resulting a higher number of molecules in higher vibrational energy states. The ratio of molecules in lower vibrational energy states to molecules in higher vibrational energy states decreases, and the molecules are more likely to move from the higher vibrational energy states to the lower vibrational energy states, which corresponds to a greater likelihood of an anti-Stokes Raman. The strength of the anti-Stokes shift may be greater than that of Stokes at high temperatures.

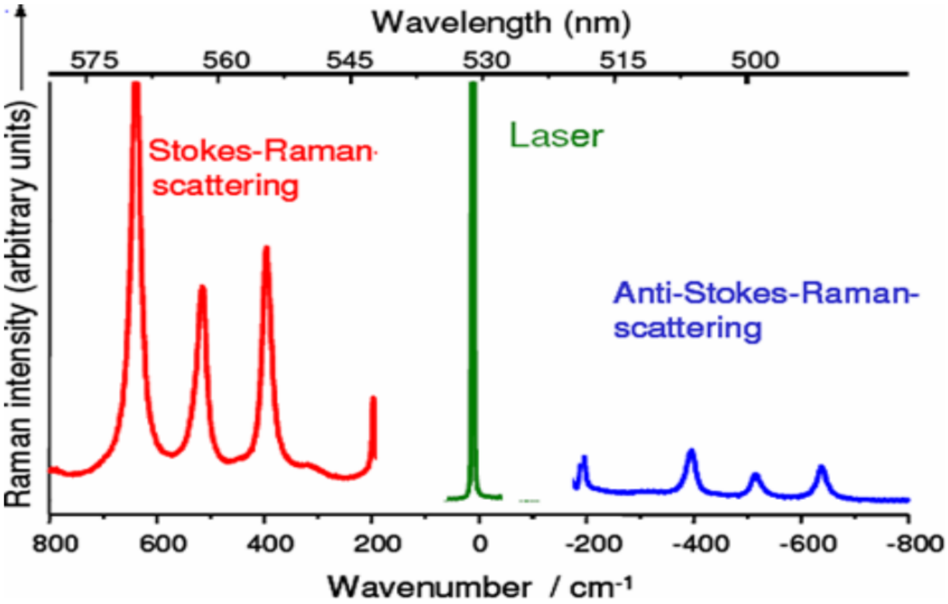

Figure 2-14 Stokes and anti-Stokes Raman Spectra of anatase (TiO_2) [58].

Typically, Raman spectra usually consist of a certain number of Raman peaks, each representing a corresponding Raman shift and intensity. Each peak corresponds to a specific molecular bonding vibration, which includes both single chemical bonds, such as C-C, C=C, N-O, C-H, etc., as well as group vibrations consisting of multiple chemical bonds, such as the breathing vibration of the benzene ring, the vibration of the long chains of polymers, and lattice vibrations. Raman spectroscopy can provide detailed information about the chemical structure, phases and morphology, crystallinity, and molecular interactions of a sample.

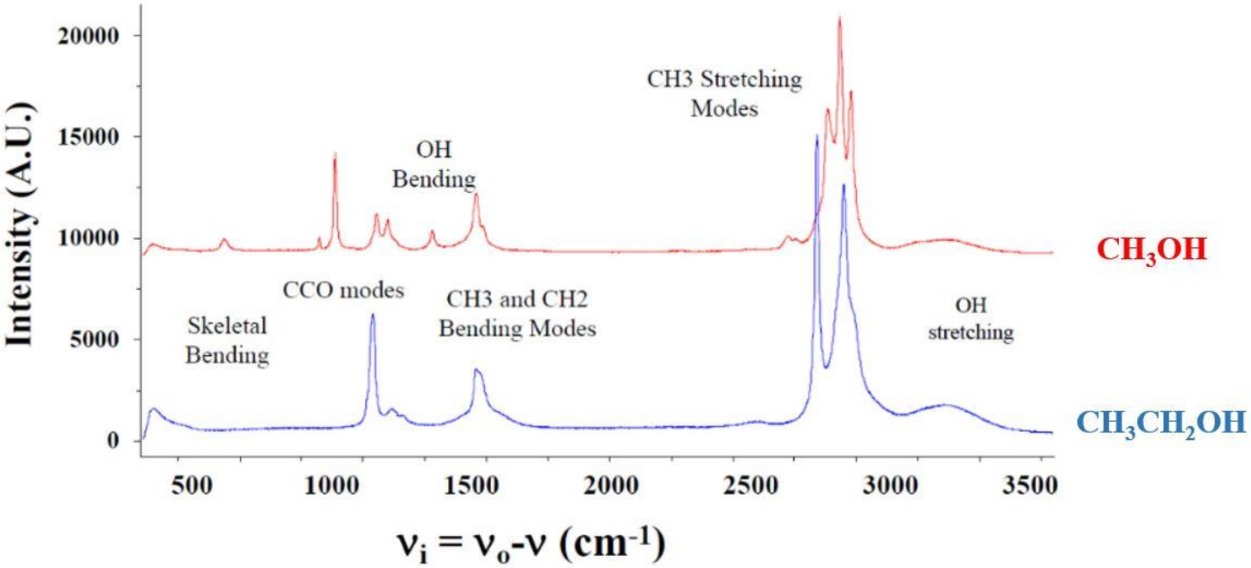

Figure 2-15 Raman spectra of methanol and ethanol

Figure 2-15 shows a section of Raman spectra of methanol (CH_3-OH) and ethanol (CH_3-CH_2-OH), which reveals the molecular structures, -OH, -CH_3, and -CH_2. A specific section of peaks in the Raman spectrum is shown in **Figure 2-16**. The position, width, height, and depolarization ratio of the peak can be seen and obtained from the graph. It is worth noting that in Raman spectroscopy, the transverse coordinate is usually the Raman shift, which is also a feature that distinguishes it from other spectra (e.g., fluorescence spectra whose coordinates are usually wavelengths). It is defined as the frequency difference (wavelength reciprocal) between the incident light and the Raman-scattered light. It provides information about the vibrational and rotational energies of the molecule and is valuable for identifying compounds and studying their structural properties. For example, a lot of information can be obtained from the analysis of Raman spectral lines, such as the Raman peak frequency to determine the composition of the substance, the change of the Raman peak position to determine the tension and stress of the substance, and the analysis of the polarization of the Raman peaks to determine the symmetry and orientation of the crystals, and so on.

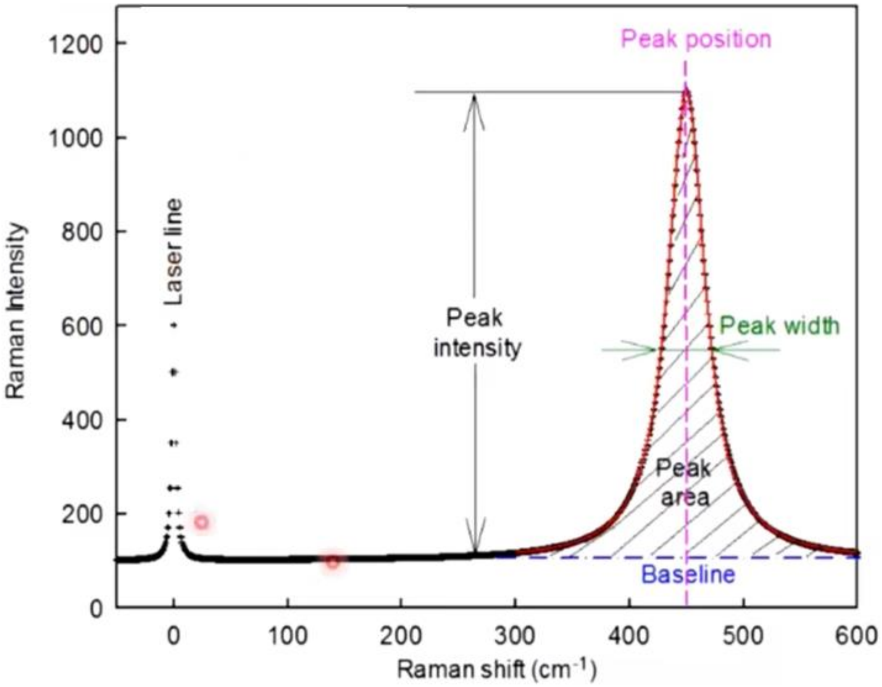

Figure 2-16 A typical Raman spectrum

Raman scattering intensity is a measure of the strength of the inelastic scattering process. It is directly related to the probability that a molecule undergoes a vibrational jump and emits or absorbs photons of different energies (frequencies) during the scattering process[59]. In other words, the intensity of the Raman effect depends on the number of molecules in which the Raman effect occurs.

In general, we can describe the Raman scattering efficiency of a particular molecule at a particular excitation wavelength by introducing a Raman scattering cross-section. The larger the Raman scattering cross-section, the more likely the molecule is to scatter light and produce a detectable Raman signal. The Raman scattering cross-section of a typical molecule is about $10^{-30}\sim10^{-24}cm^2$, which is ten orders of magnitude smaller than fluorescence[26] and three orders of magnitude smaller than the Rayleigh scattering cross-section.

The intensity of Raman scattering is affected by a number of factors and can be broadly classified into the following categories:

(1) Polarity of the molecule. The higher the polarizability of a molecule, the stronger its Raman scattering intensity. Polarizability reflects the ability of a molecule to deform under the action of an electric field, resulting in a larger Raman cross section.

(2) Polarization of the incident light. The polarization of the incident light affects the Raman scattering intensity. Raman scattering is more likely to occur when the polarization of the incident light matches the symmetry of the molecular vibrations.

(3) Sample concentration and thickness: The intensity of Raman scattering is proportional to the number of molecules in the sample. Higher concentrations usually result in stronger Raman signals. The thickness of the sample also affects the Raman scattering intensity. In thicker samples, the probability of multiple scattering events increases, which may result in a lower signal intensity.

(4) Temperature. Temperature can affect the intensity of Raman scattering in a different way. First, it can affect the population of vibrational states. At higher temperatures, molecules possess more thermal energy, resulting in a greater population of higher vibrational energy states. As a result, Raman-active vibrational modes are more likely to be thermally populated, leading to an increase in Raman scattering intensity. Second, higher temperatures can broaden the distribution of molecular energy levels. This thermal widening causes the Raman peaks in the spectrum to broaden, affecting the total Raman intensity. Last, it can affect the Boltzmann distribution. The Boltzmann distribution governs the intensity of Raman scattering for each vibrational mode and it is temperature-dependent. The Boltzmann distribution describes the relative population of different vibrational states based on their respective energies. As the temperature increases, the higher energy vibrational states are more populated, leading to changes in the Raman intensity distribution[60].

Figure 2-17 shows the schematic of a typical Raman microscope. Laser light is focused onto the sample surface by a microscope objective lens, which is also employed for the collection of the backscattered light. Notch or edge filters are used to eliminate photons at the laser wavelengths to transmit only Raman-shifted photons to the grating of a spectrometer. Raman mapping experiments can be realized by stepwise movement of the sample through the laser focus while acquiring a Raman spectrum. The typical parameters to be optimized in such Raman spectroscopic measurements are the laser wavelength, laser power, focusing element (objective lens), spectrometer grating, acquisition time, and pixel size and number[61].

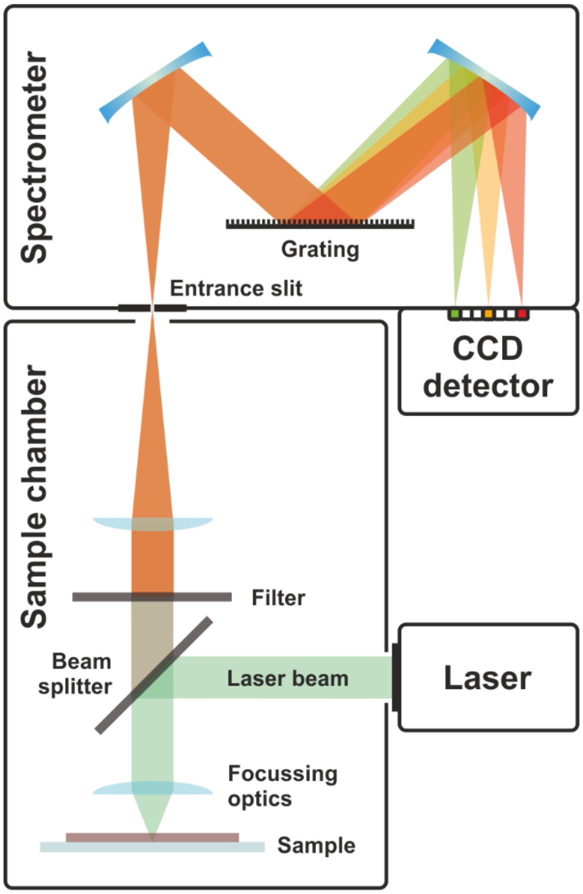

Figure 2-17 Schematic of Raman microscope[61]

Figure 2-18 shows the schematic of Raman microscope to test the droplets in a spray. The basic setup is the same as **Figure 2-17**, only adding a delay generator as well as a signal generator for measuring the droplets. When using pulsed excitation to study periodically flowing droplets, synchronization between the laser pulse and the droplet is required.

The principle of using Raman scattering to measure the temperature of droplets is based on the temperature dependence of molecular vibrations, because in Raman scattering, the incident photons exchange energy with the molecules, causing a shift in the energy levels of molecular vibrational modes. The positions (wavelengths) of the Raman peaks in the spectrum are determined by the molecular vibrations of the droplet. As the temperature changes, the molecular vibrations also change, resulting in shifts of the Raman peaks in the spectrum. Then, by analyzing the Raman spectrum and identifying the positions of the Raman peaks, it is possible to correlate these peak shifts to the temperature of the droplet using a calibration curve. The calibration curve is obtained by measuring the Raman spectra of droplets at known temperatures and establishing the relationship between the peak shifts and the corresponding temperatures.

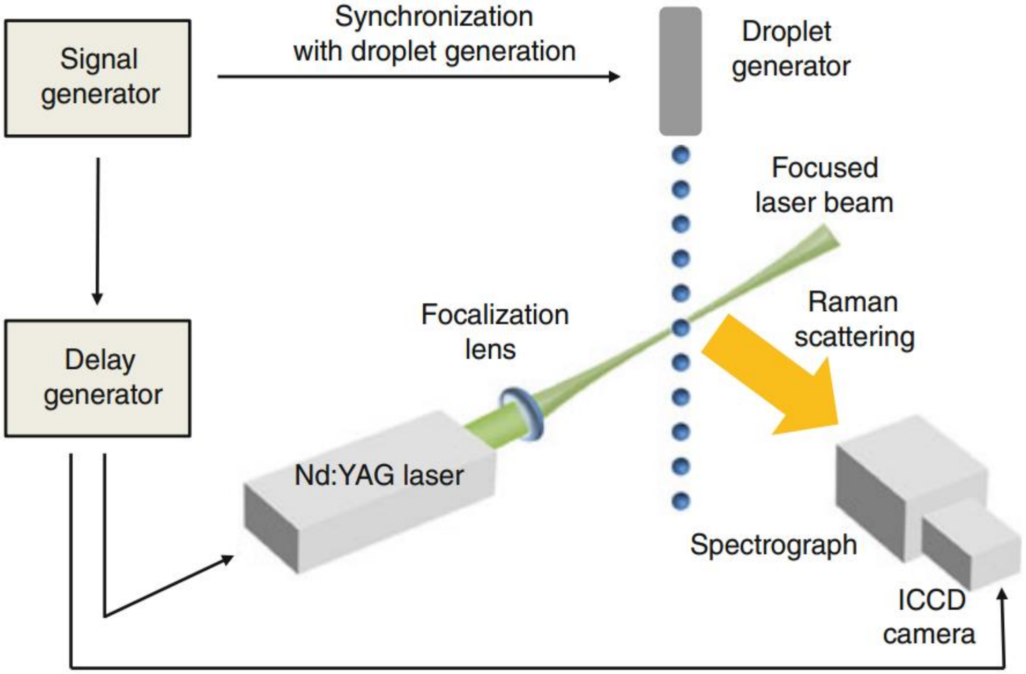

Figure 2-18 Schematic of Raman microscope for testing spray [58]

However, even though Raman scattering spectroscopy provides an excellent pathway to the temperature, the application of Raman scattering to the study of droplets faces many difficulties. Certain challenges in analyzing the molecular composition of droplets can be attributed to the effects of droplet size and shape. The lensing effect produced by the droplet interface results in an inhomogeneous distribution of the sources of Raman scattering within the droplet and a non-uniform angular distribution of the Raman signal scattered by the droplet because the Raman signal is proportional to the local excitation power density[26].

Carls[62] examined the chemical absorption of D_2O vapor by an acoustically levitated droplet of glycerol (diameter 25 μm). Buehler[63] used Raman scattering spectroscopy to study the evaporation of multicomponent droplets. They emphasized the challenges associated with droplets evaporating and going through a chemical transition. Because of the weak Raman signal, the approach requires an excessively long integration time.

In 1995, Vehring[64] explored CO_2 desorption from water droplets. The shift between the peaks belonging to gaseous CO_2 and dissolved CO_2 is employed in this work to distinguish the liquid and gaseous phases, while the area of the Raman peaks allows for concentration measurements in both phases. The scientists were able to assess concentration profiles in the gas phase in the vicinity of the droplet using this method. In 1998, Vehring [65] used a similar strategy but extended it to particles as tiny as 3 μm.

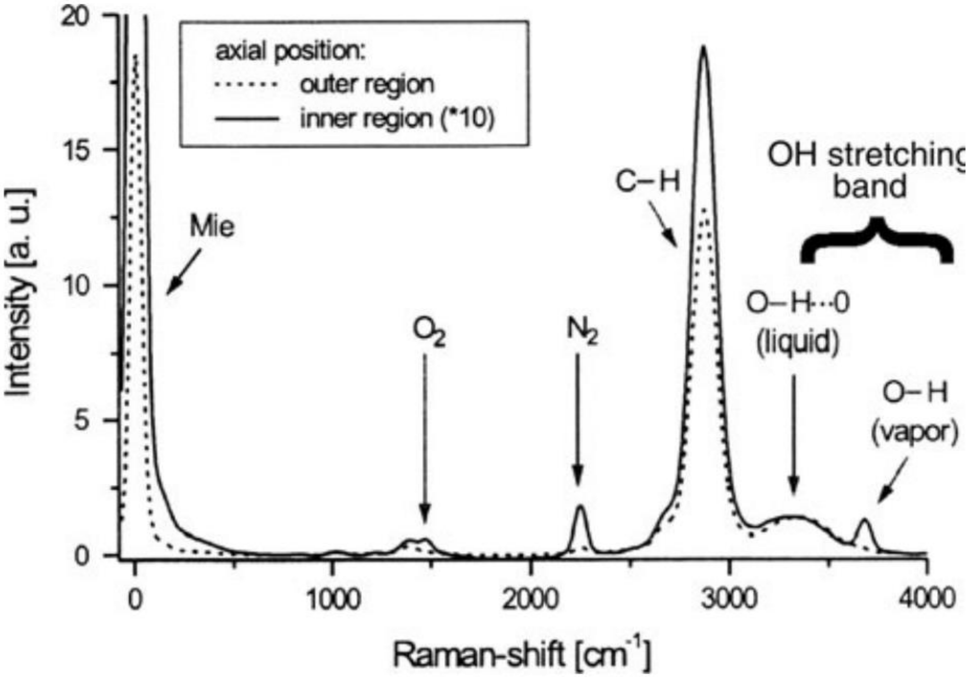

Figure 2-19 Typical Raman spectrum recorded in a spray inner region corresponds to the spray core. The outer region corresponds to the sprays edge[58]

In 2000, Muller [66] measured the temperature of ethanol and methanol droplets in a pre-heated direct injection petrol spray pumped into a 50-bar back-pressure chamber using the form of the OH stretching band. Calibration of the OH stretching in bulk liquid is essential to calculate the location of the Raman peak at a particular temperature, as shown in **Figure 2-19**, which also displays the OH emission of the vapor phase. When contrasted to the liquid phase, this emission is pushed towards shorter wavelengths.

In 2002, Stowers and Friedlander [67] used Raman spectroscopy to investigate the interaction of two aerosols flowing into nitrogen, one consisting of diethylsebacate (DES) particles and the other of dry ammonium sulfate particles. They measured the chemical composition of polydisperse droplets (diameters varying from 0.3 to 1.8 μm) in situ.

In 2009, Heinisch [68] explored the evaporation of water droplets levitated in an electrodynamic trap with varying velocities of nitrogen injection. Following calibration, the OH stretching band was utilized to monitor droplet temperature. The employment of a ratio between the signals recorded on two spectral windows, one near the maximum of the OH stretching band and the other at a higher frequency where the spectrum is most sensitive to temperature, makes it possible to achieve a temperature dependency of roughly 0.45 C/%, a temporal resolution of about 0.3 s, and an overall accuracy of 4°C.

Hankel [69] adopted Raman scattering to determine the temperature of the liquid phase in water sprays under normal and superheated conditions. The water inside the vessel was heated to various temperatures. Special emphasis was paid to measuring the temperature of the spray under superheated circumstances (starting water conditions within the vessel at 393K and 6 bar absolute). The temperatures inside the spray were measured immediately at the nozzle exit and downstream the nozzle in the z- and y-direction. Several methods were tested to determine the water droplet temperature while the amount of water vapor in the continuous gas phase contributes significantly to the Raman spectrum of the OH-stretching vibration band of water. Measurements can be made even in dense sprays with a wide interfacial area between the gas and liquid phases.

Previous examples were applications of spontaneous Raman scattering. The process of stimulated Raman scattering (SRS) occurs when the intensity of light in a Raman nonlinear medium reaches a certain level. The incident pump light induces strong molecular, which modulate the incident beam and produce frequency-shifted radiation. A third-order non-linear phenomenon involving a second photon stimulates a specific transition. This second photon result from resonant light. In droplets, light at certain frequencies can be trapped. Light waves called whispering gallery modes (WGMs) can be guided around a droplet almost perfectly by total optical internal reflection[26]. When the difference in frequency between both a pump photon and a Stokes photon resembles that of a specific vibrational transition, this transition can be enhanced. Stimulated Raman can be exploited to characterize the composition of multicomponent droplets, in particular, ethanol–water droplets [70][71][72][73][74]. The technique is called cavity-enhanced Raman scattering (CERS) and was initiated by Hopkins. It is also referred to as surface-enhanced Raman scattering (SERS). This approach was successfully applied in the investigation of ethanol-water droplets falling at ambient temperature and pressure in air, by activating both the CH and OH stretching bands for ethanol and water. Hopkins et al. [75] found out that the ratio of the integrated intensity of the CERS signal from water and ethanol reduced by half, while the ethanol volume fraction decreased by just 0.6%. This resulted in extremely precise composition measurements of the composition change **(Figure 2-20)**. It should be noted that the sensitivity of this ratio is also affected by the laser's excitation wavelength.

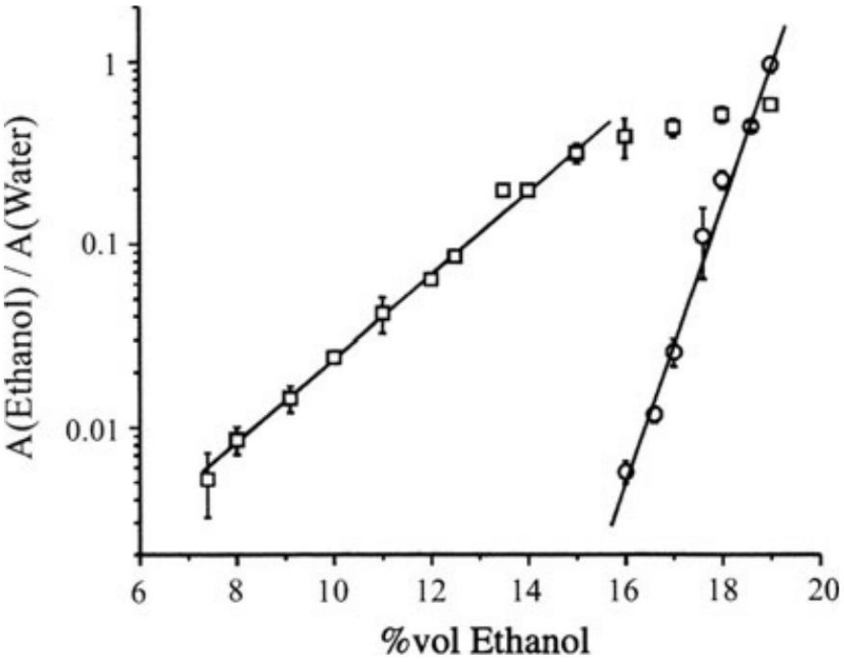

Figure 2-20 Example of calibration curve of the ethanol CERS signal as a function of composition. A is the integrated intensity on the spectral band (squares excitation at 532 nm, circles excitation at 355 nm). Reprinted from Hopkins et al[66]

All in all, Raman scattering is a powerful tool for characterizing droplets' temperature and composition despite some disadvantages and has been applied in a wide range of scientific and industrial applications, including combustion studies, environmental monitoring, and pharmaceutical research. Areas for future improvements in droplet measurement using Raman spectroscopy include:

(1) Improving the accuracy of Raman scattering temperature measurements, as variations in droplet composition, size, and refractive index can interfere with the scattering signal, resulting in biased temperature measurements.

(2) Improving the signal-to-noise ratio. Because Raman scattering produces a relatively weak signal, the accuracy of Raman measurements decreases when droplets are small or of low concentration.

(3) Avoid fluorescence interference. Fluorescence interferes with the Raman scattering signal, making it difficult to distinguish the Raman signal from background noise.

2.2.2.3 Laser-Induced Fluorescence (LIF)

In addition to the optical techniques that we discussed earlier for characterizing droplet temperature or composition (rainbow refraction and Raman scattering), another technique that has been recently developed and popularizing is laser-induced fluorescence (LIF), which has significantly contributed to various fields of modern science and technology by enabling precise and sensitive detection and analysis of fluorescent molecules. Laser-induced fluorescence can be used to measure both temperature and composition. Measurements applied to droplets mainly focused on the temperature and in most cases, they relies upon the temperature dependency of the intensity of the fluorescence signal[76][77][78][79][80].

A. Intensity-based LIF

We consider dye molecules uniformly dispersed in the liquid and that the attenuation of the laser beam and fluorescence light are negligible in the liquid system. As previously discussed in **Chapter 1**, the intensity of fluorescence signal I_f can be evaluated considering the fluorescence quantum yield ϕ, the measurement volume V_c, the concentration c of the fluorescent molecules (mol/m^3), the absorption coefficient ε_0 (m^2/mol) at the wavelength of the illuminating laser and the laser fluence I_0 (W/m^2). According to Lavieille[81], then the expression can be written as:

$$I_f(\lambda) = K_{opt}(\lambda)K_{spec}(\lambda)I_0\varepsilon_o C\phi V_c \qquad (2-3)$$

where $K_{opt}(\lambda)$ and $K_{spec}(\lambda)$ are two constants for the measurements related to the optical system arrangement[1] and fluorescence detection bands[2]. In the above formula, the fluorescence dependency on the temperature arises from the fluorescence quantum yield ϕ and the absorption coefficient ε_0. As explained before, ϕ decreases with temperature under the effect of collisional quenching. On the other hand, the absorption cross-section ε_0 is also function of the temperature. As a result, the fluorescence can increase or decrease with temperature depending on the laser wavelength. **Figure 2-21** compares the effect of temperature for several organic dyes which are soluble in water and can be easily excited at a wavelength of 532 nm. A lot of fluorescent dyes are commercially available, but not all are equally sensitive to temperature

---

[1] see the solid angle of detection $d\Omega$ introduced in **Chapter 1**

[2] the shape of the emission spectra $S(\lambda)$ through the parameter $P(\nu)$ introduced in **Chapter 1**

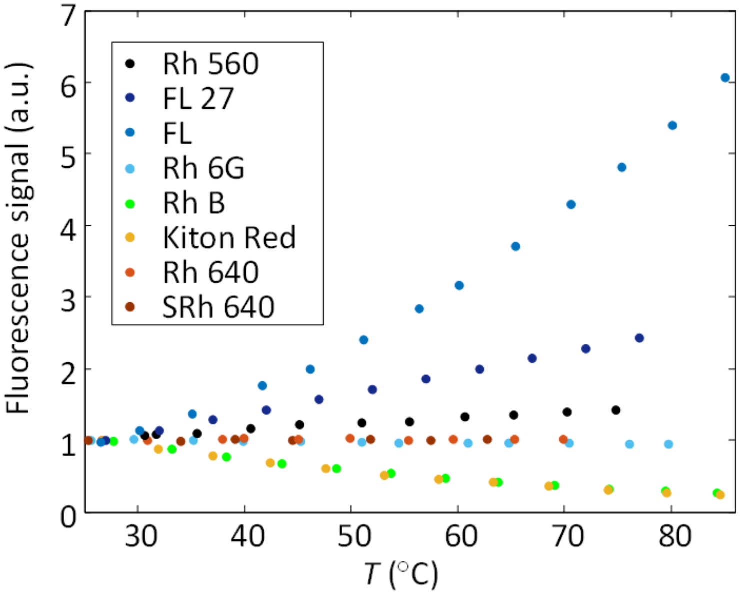

		Temperature sensitivity (%/°C)
Rh560	Rhodamine 560	+0,78
FL	Fluorescein	+3,22 (pH=5,6)
FL27	Fluorescein 27	+1,88
Rh6G	Rhodamine 6G	-0,07
RhB	Rhodamine B	−2,38 (pH=6,5)
KR	Kiton red	-2,43
Rh640	Rhodamine 640	+0,05
SRh-40	Sulforhodamine 640	−0,06

Figure 2-21 Water-soluble dyes at an excitation wavelength of 532 nm from Chaze et al. (2016)

By putting together temperature-dependent terms in equation $(2-3)$, a new expression of the intensity of the fluorescent signal can be introduced:

$$I_f(\lambda) = K_{opt}(\lambda)K_{spec}(\lambda)I_0CV_c\mathrm{e}^{\left(\frac{\beta(\lambda)}{\mathrm{T}}\right)} \qquad (2-4)$$

where $\beta(\lambda)$ is a coefficient featuring the sensitivity to temperature at a considered emission wavelength λ. From Equation $(2-4)$, measuring the fluorescence signal intensities can disclose the temperature based on a previously performed calibration. This method is called one-color LIF thermometry [82]. Despite being a non-invasive method, one-color laser-induced fluorescence is not commonly used especially in droplet flows. To work correctly, the detected fluorescence signal intensity must be solely a function of the temperature [83]. Large errors can be done if the power of the excitation laser fluctuates, if the concentration of the dye molecules is not homogeneously distributed throughout the system or constant during the measurement. The intensity of the fluorescence signal from a droplet depends on the droplet size and position relative to the laser beam and the receiving optics[3]. The use of the absolute intensity of the signal is not possible in sprays as droplets have random sizes and trajectories. More generally, in multiphase flows, light intensity is affected whenever light rays cross liquid/gas interfaces, due to optical effects such as reflection and refraction.

---

[3] Maximum intensity is achieved when the droplet is centered in the measurement volume formed by the intersection between the laser beam and the detector's field of view.

A solution usually adopted in droplet flows consist of detecting the fluorescence signal in two spectral bands. These two bands are affected in a similar way by optical effects. Even if the droplet position and its size are unknown, the effects of these parameters can be eliminated by doing the ratio of signal intensities detected on two spectral bands. The method of determining droplet temperature using intensity ratios is known as two-color LIF (2cLIF). To obtain an intensity ratio that varies strongly with temperature, it is critical to find two bands responding very differently to temperature. Methods can be categorized into one dye/2cLIF[81][84][85] and two dyes/2cLIF [86][87][88].

One-dye/2cLIF thermometry takes advantage of the fact that the emission spectrum varies with temperature. Based on Equation $(2-4)$, the ratio of fluorescence intensities detected in two spectral bands can be expressed as $(2-5)$:

$$R=\frac{I_f(\lambda_1)}{I_f(\lambda_2)}=\frac{K_{opt}(\lambda_1)K_{spec}(\lambda_1)I_0CV_c\mathrm{e}^{(\frac{\beta(\lambda_1)}{\mathrm{T}})}}{K_{opt}(\lambda_2)K_{spec}(\lambda_2)I_0CV_c\mathrm{e}^{(\frac{\beta(\lambda_2)}{\mathrm{T}})}}=\mathrm{Ke}^{\frac{\beta(\lambda_1)-\beta(\lambda_2)}{\mathrm{T}}} \qquad (2-5)$$

The constant K in $(2-5)$ can be further eliminated by taking a reference. The ratio R is measured with the same optical system in a position where the temperature is known and equal to T_0. Then, the ratios at different temperatures can be further simplified as:

$$In\frac{\mathrm{R}(T)}{\mathrm{R}(T_0)}=(\beta(\lambda_1)-\beta(\lambda_2))(\frac{1}{T}-\frac{1}{T_0})=\Delta\beta(\frac{1}{T}-\frac{1}{T_0}) \qquad (2-6)$$

Equation $(2-6)$ gives a linear relationship between the logarithm of the fluorescence ratio and the temperature function $(\frac{1}{T}-\frac{1}{T_0})$ at two temperatures. The constant of proportionality before the temperature function is the difference in coefficients between the detection bands. For higher temperature sensitivity, this constant should be maximized [89].

The 2 dyes/2cLIF relies on two fluorescent dyes A and B with emission spectra which are sufficiently shifted to permit the separation of their emissions by means bandpass filters. In the ideal case where the optical separation is perfect (i.e., no fraction of the light emitted by A is coming into the detection band for the light emitted by B and reciprocally), the ratio R of the fluorescence intensities detected from each dye can be written as followed[26]:

$$R_{AB}(T)=\frac{I_{f,A}}{I_{f,B}}=\frac{K_{opt,A}K_{spec,A}}{K_{opt,B}K_{spec,B}}\frac{C_A}{C_B}\mathrm{e}^{\frac{\beta_A-\beta_B}{\mathrm{T}}} \qquad (2-7)$$

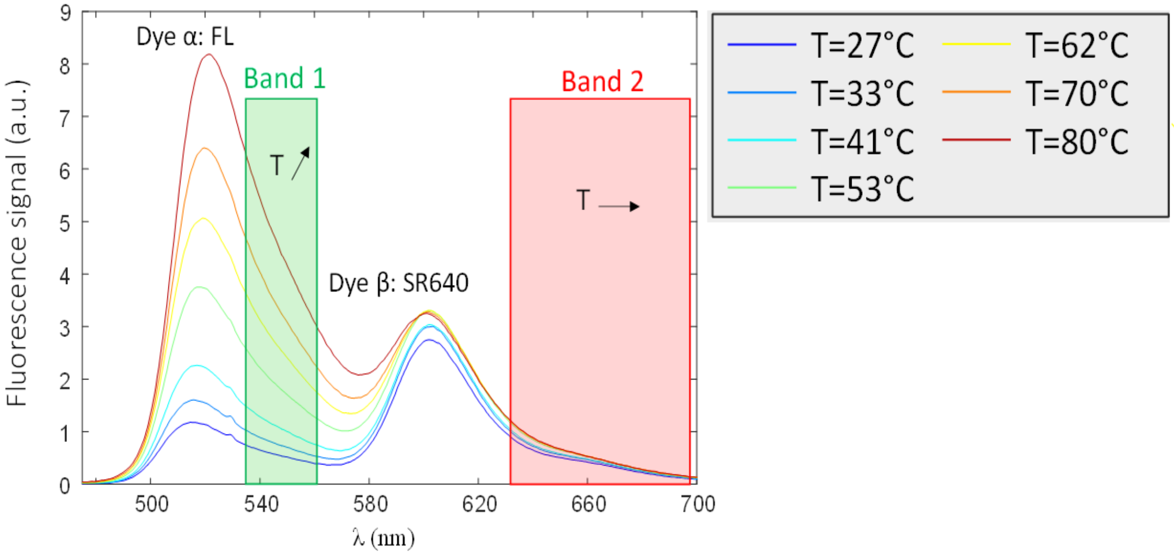

Figure 2-22 An example of a dye mixture Fluorescein/Sulforhodamine 640 used in the two-color/two-dyes method $[FL] = 5 \times 10^{-5}$mol/L, $[SR640] = 7.7 \times 10^{-7}$mol/L dissolved in water

Figure 2-22 shows an example of band selection in the case of a mixture of fluorescein/sulfo-rhodamine 640 dissolved into water. A very good temperature sensibility can be obtained as the peak on the left is due to the emission of fluorescein, whose signal increases with temperature. The peak on the right comes from sulfo-rhodamine 640, whose emission is little decreasing with temperature.

The 2color/1dye method was first used by Lavieille[81] in 2001 to study the evaporation of ethanol droplets. Using rhodamine B, Lavieille could obtain a variation of the order of 1.5% per K for the intensity ratio.

As show in **Figure 2-23** and **Figure 2-24**, Lavieille selected two bands to carry out the experiment: the first band was in [520-540 nm], which was insensitive to temperature changes, the second was in [>590 nm], which was very sensitive to temperature changes. In the experiment, two parts of the signals emitted by the two PMTs are processed through two synchronized fast acquisition boards in the computer. The final result found that the error caused by this technique was relatively small, about only ±0.3℃ from systematic error, and 0.5% error from the method of data processing, The absolute accuracy of this technique is probably of the order of 1℃ and it is already precise compared with former literature.

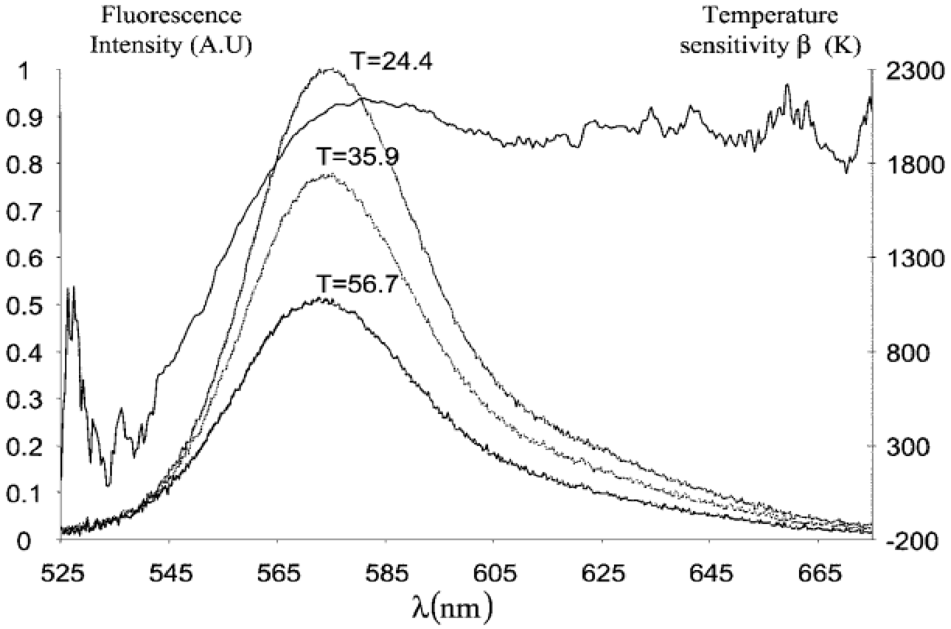

Figure 2-23 Distribution of the temperature sensitivity coefficient as a function of the wavelength

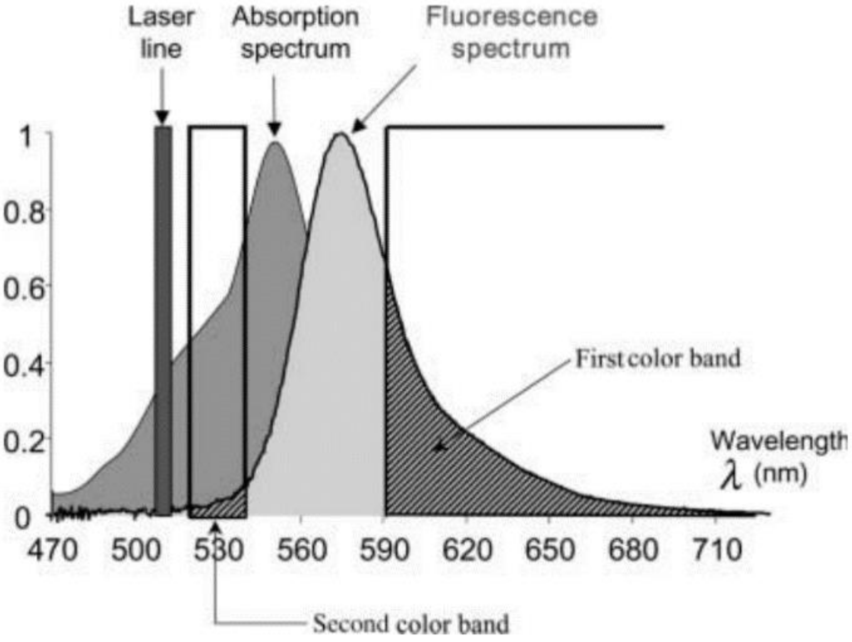

Figure 2-24 Sketch of two selected bands

Castanet[90] studied combusting ethanol droplets in a linear stream using two colors laser induced fluorescence in 2005. The results demonstrate that the droplet thermal evolution may be divided into two phases: a transient heating phase followed by a constant temperature phase at a temperature below the boiling point of the fuel (equilibrium temperature), which in the case of ethanol is around 60°C. A computation based on the heat diffusion equation resolution has been implemented, with a constant temperature maintained at the equilibrium temperature. The Peclet number obtained using the novel correlation based on the maximum droplet surface velocity is adequate to represent the droplet heating profiles. The distance parameter appears to have no major effect in the tested range (1:62 ≤ C ≤12:7).

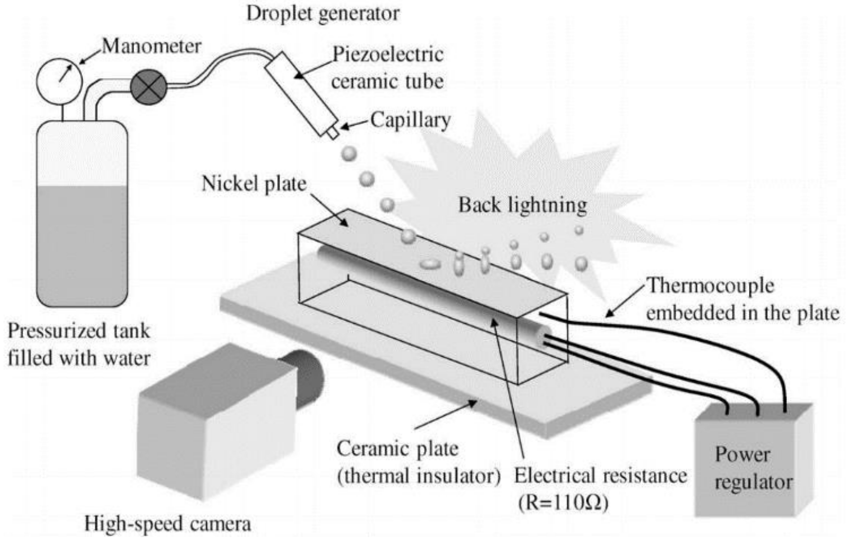

Figure 2-25 Schematic view of the experimental setup and the optical layout for shadow imagery

In 2009, Castanet[91] conducted an experimental study on the impact of water droplets on a smooth heated plate made of nickel. A high-speed camera was used to observe the impact processes such as rebound, splash and liquid film deposition. A two-color laser-induced fluorescence thermometer was used to measure the temperature of the droplets in different impact states.

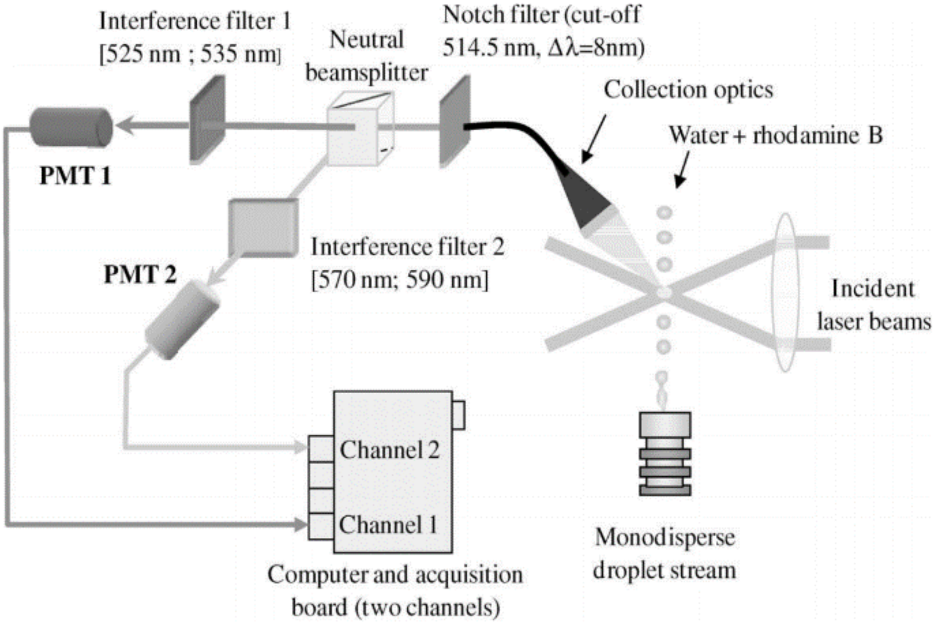

Figure 2-26 Two-color laser-induced fluorescence optical set-up

The experimental setups are shown in **Figure 2-25** and **Figure 2-26**. The measurements show that the increase in droplet temperature during impact can reach nearly 40 degrees Celsius in the case of splashing, while it is more limited in the case of bouncing. Droplet warming is more important when the normal component of the velocity is high, but if the impact is in the form of rebound, it can be seen that the wall temperature does not have a significant effect on the droplet warming.

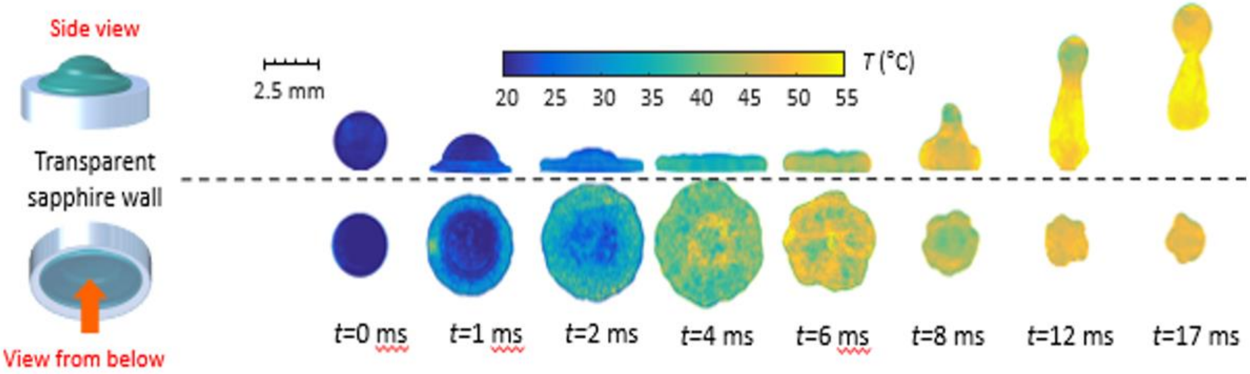

Figure 2-27 Side and bottom views of the temperature field within an impacting droplet

Later in 2017, Chaze studied the impact of drops on transparent sapphire heated around 600°C. They used the fluorescein/sulforhodamine 640 mixture presented in **Figure 2-27**. The 2cLIF method was improve to obtain instantaneous images of the temperature field inside the droplets. Photomultiplier tubes were replaced by cameras, and a pulsed laser was used to induce fluorescence.

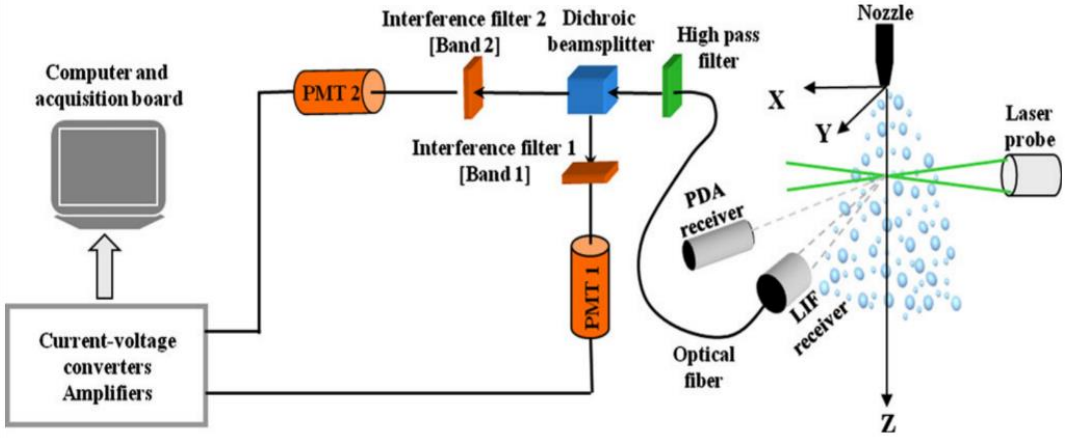

Figure 2-28 Spray facilities and optical devices for 2cLIF detection

In 2011, Labergue[92] combined measurements with laser-induced fluorescence and a phase Doppler analyzer **(Figure 2-28)** to determine the temperature of each droplet size class in a spray. They underlined several difficulties when using the 2c/1d method in polydisperse sprays.

Fluorescence intensity varies approximately as the droplet volume. With a conventional detector, measuring the signal intensity of all the droplets in a spray is challenging, because of the limited dynamic range of the detector[4]. Very small droplets are difficult to distinguish from the detector noise, while big droplets can saturate it. The situation becomes worse when multiple scattering is involved since a supplementary background noise is added to the measurements. As illustrated in **Figure 2-29(a)**, a larger number of droplets are generated by increasing the injection pressure, which leads to more light scattering. **Figure 2-29(b)** shows that the intensity ratio is subject to noticeable measurement biases. It varies with the injection pressure, while air was saturated in humidity to ensure that the droplet temperature does not change. Labergue[92] could mitigate the problem by using a long-distance microscope to collect the LIF signal, the latter having a very small depth of field. However, the intensity ratio is still not quite a constant.

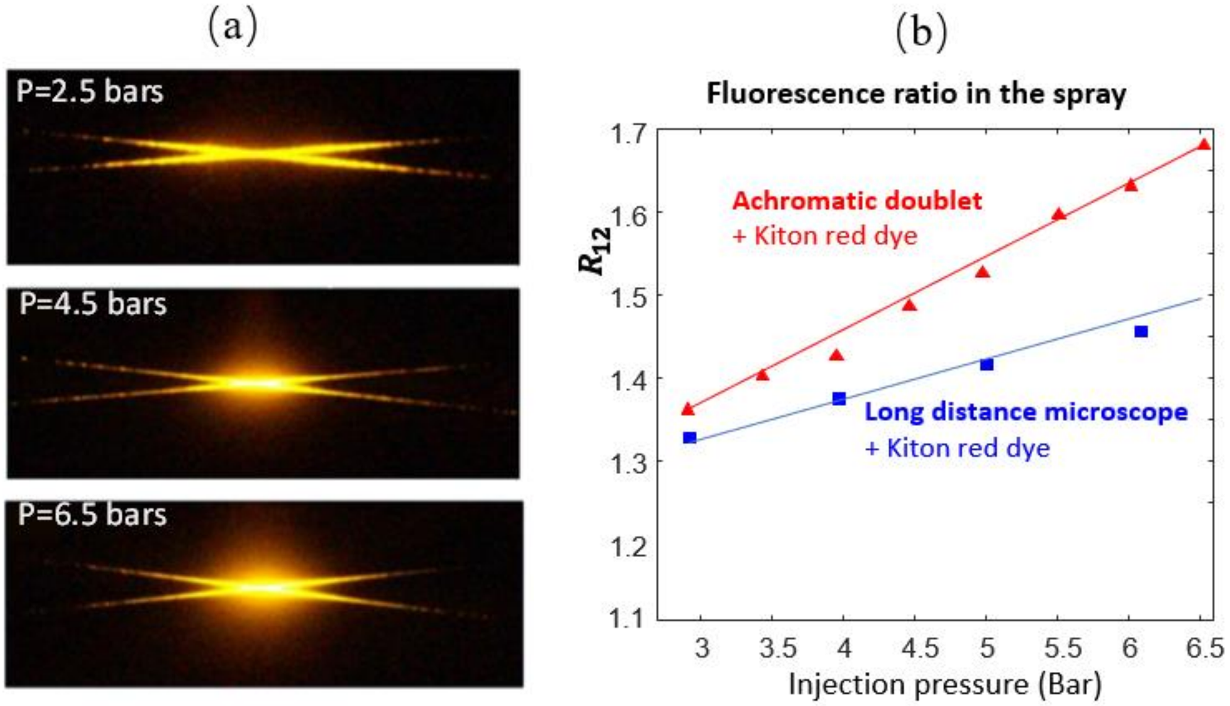

Figure 2-29 Relationship between incident pressure and fluorescence intensity ratio

In 2016, Similarly to address these issues (multiple scattering, indirect reflections, and surrounding background) in intensity-ratio based measurements, Mishra[93] used a combination of SLIPI (Structured Laser Illumination Planar Imaging) and two-color laser-induced fluorescence-specific pyrometry to measure the temperature of the water in both the cuvette and the hollow-cone aerosol dispenser. With this method, it was found that the sensitivity could be increased by a factor

---

[4] The dynamic range is defined as the difference between its noise floor and saturation intensity.

of 6 (at 85°C) when fluorescein was mixed with water. It was also found that the LIF ratio was independent of the change in laser power from 17.5 mw to 35 mw. The resulting ratios change considerably when the dye concentration is varied. This phenomenon is attributed to the overlap of the absorption and emission spectra of fluorescein, which produces a self-absorption effect in the spectral region from 500 nm to 520 nm. This suggests a promising approach for combining structured illumination and 2cLIF.

In 2020, Markus Michael Prenting et al.[94] investigated the potential of various dyes for temperature determination in ethanol by recording their fluorescence spectra as a function of temperature after excitation at the standard UV and visible wavelengths corresponding to the harmonics of the Nd:YAG laser. They compared their respective temperature sensitivity scores (i.e., the difference in "temperature sensitivity factor β") in a two-color intensity ratio approach, and in particular compared rhodamine B, a well-characterized dye in the literature, to coumarin 152, which exhibits a significantly larger Stokes shift, making it an ideal candidate for measurements where self-absorption is problematic. For a fixed spectral half-width, the temperature sensitivity of the ratio method was also evaluated as a function of the spectral spacing between the two detection windows in two-color LIF thermometry. The results indicate that the use of coumarin 152 as a tracer is particularly suitable for sprays or droplets exposed to evaporation, which leads to changes in concentration and thus signals self-absorption.

In 2023, Ulrich[95] applied the optimization of the 2c-LIF approach to the measurements in a monodisperse ethanol droplet, by selecting two contrarily temperature-dependent fluorescence dyes (FL and SRH). With this improved approach, a calibration curve with a promising temperature sensitivity of the signal ratio (2.02%/K for detection with the camera system) was attained in micrometric droplets of 100 μm without detection of MDR signals. Additionally, temperature measurement was implemented on the downstream of droplet chain. A cooling of around 20 K could be measured for a distance of 10 mm. Images detected close to the nozzle show the Rayleigh breakup of the liquid core. In this region of primary breakup, the results show strong deviations, probably resulting from optical effects inside the non-spherical structures and droplets. At distances between 2 mm and 9 mm, more spherical droplets are formed. There, a linear decay of the temperature is observed, which amounts to about 17.7 K. This is a realistic value for cooling by evaporation and heat transfer with the cold ambient air. An estimation of the cooling due to convective heat transfer is attained after the lumped capacitance model and accounts for a decrease of 7.3 K.

In conclusion, intensity-based laser-induced fluorescence (LIF) is an advanced and invasive spectroscopic technique that can be used to measure droplet temperature in sprays. By establishing the relationship between fluorescence intensity and temperature, droplet temperature can be obtained. The results show that 2cLIF yields more accurate and precise data due to the intensity ratio method compared to the intensity-based 1cLIF. Meanwhile, 2cLIF reduces the dependence on bulk calibration, improves the measurement accuracy, and allows simultaneous measurement of temperature and species concentration, eliminating ambiguities due to interdependence effects in 1cLIF. However, due to the complexity of measuring droplet temperature sprays (multiple scattering, indirect reflections, and ambient background interference), 2cLIF has evolved to incorporate with other methods to address these issues and further improve its accuracy.

B. Lifetime-based LIF

Lifetime-based laser-induced fluorescence provides us with another way to characterize droplet temperature and composition. It is worth noting that the fluorescence lifetime is an intrinsic property of the fluorescent molecule and is not affected by any external factors such as the sensitivity of the detector, the measurement time, the instrumentation, which greatly improves the accuracy of the measurements. Any disturbance in the measurement system or in the light transmission to the optics, modify the value for the intensity but not for the lifetime. Still, the fluorescence lifetime as for the intensity remains sensible to several factors such as the temperature, the chemical environment: pH, polarity, viscosity of the liquid solvent. Compared with the traditional intensity-based measurement methods, lifetime-based measurements are still little applied in the field of fluid mechanics and the study of heat and mass transfer phenomena. Currently, there are a limited number of articles that utilize fluorescence lifetime for measurements in fluid flows.

Time-correlated single photon counting (TCSPC) developed around the 1980s laid the foundation of the analysis of the fluorescence decay in the time domain. Prior to this, fluorescence lifetimes usually were measured in the frequency domain by a phase-modulation method. The method uses a light source that is pulsed or modulated at high frequency (up to 500 MHz) with acousto-optic modulators.

The development of ultrashort pulse laser (either femtosecond or picosecond laser), sensitive detectors such as photomultiplier tubes able to count individual photons, has considerably improved the capabilities of TCPSC.

In 2010, Casadevall I solvas[96] by using fluorescence lifetime imaging acquired the map of fluidic mixing in microdroplets with 1μs time resolution. The monosized water-in-oil droplets are generated at frequencies of about 1 kHz from two aqueous solutions flowing in parallel into a T-junction against an oil phase flow (**Figure 2-30**). Two different dyes, FITC (with a fluorescence lifetime of 4.1 ns) and Str-AF488 (with a fluorescence lifetime of 3.1 ns) were introduced into a solution for differentiation, and fluorescence data were recorded in conjunction with a confocal microscope and TCSPC, which incrementally scanned a droplet by using the objective lens of the microscope to focus laser and moving it over a micro-channel to obtain a cross-sectional image of the droplet.

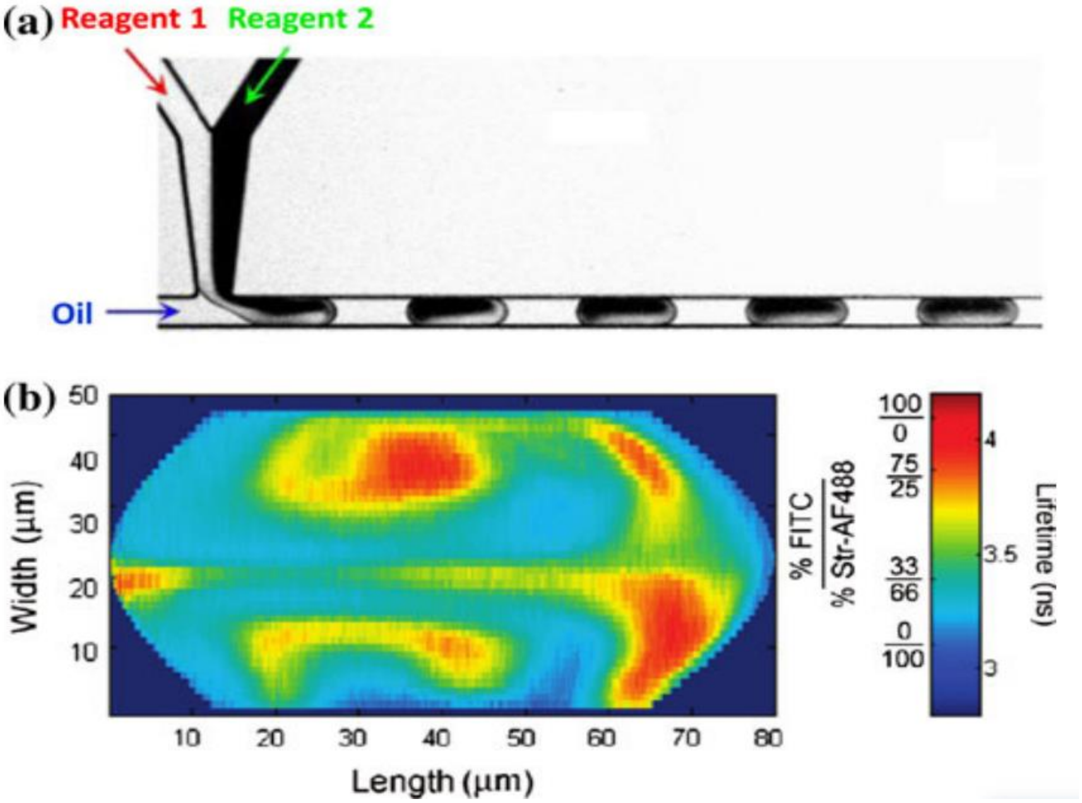

Figure 2-30 Lifetimes measurements in monosized water-in-oil droplets. a) On chip encapsulation in droplets of two originally separate aqueous reagents that fluoresce (FITC and Str-AF488). b) Two-dimensional maps of mixture fraction and average lifetimes within droplets with lμs time resolution (a ratio of 33 % FITC/66 % Str-AF488 represents a perfectly mixed solution)

Mendels [97] used fluorescence lifetime imaging microscopy (FLIM) to study a microfluidic T-mixer. Two complementary measurements were applied to study thermal and solute mixing. o flows of water and methanol are injected separately at the T-junction and FLIM is used to reconstruct the spatial distribution of the concentration in water in the mixture that forms downstream in a microchannel. 1,8-anilinonaphthalene sulphonate (ANS) is used as a fluorescence dye because its fluorescence lifetime changes considerably with the water concentration in the water/methanol mixture. In other experiments, Kiton red was used to measure the temperature in the mixture form when two water flows are injected at different temperature at the T-junction.

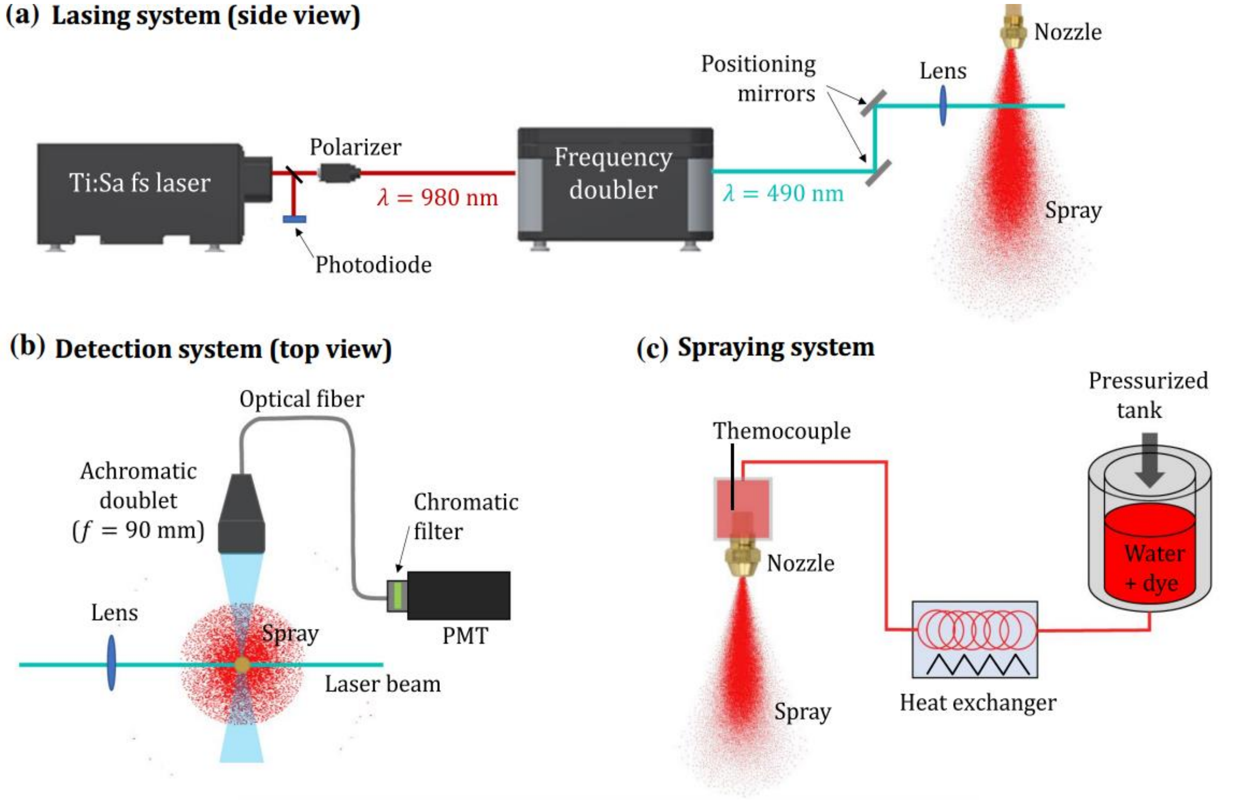

Figure 2-31 Experiment setup of spray measurement

In 2021, Mehdi et al[98] first used fluorescence lifetime to measure the local mean temperature of the droplets in sprays, which was based on the measurement of fluorescence lifetime such as Rhodamine B and Kiton red. **(Figure 2-31)** shows the optical system of the experiment. After passing through a polarizer and several mirrors, the laser is directed to the middle section of the spray, inside of which is the solution (water and fluorescent dye mixed) heated by the heat exchanged. The achromatic doublet collects the fluorescence signal and passes it to the PMT through the optical fiber, and PMT transfers the light signal collected to the electrical signal and then delivers it to the TCSPCS where the fluorescence lifetime can be obtained. The fluorescence lifetimes of different dyes in polydisperse sprays in two detection spectral bands [630 nm to 650 nm] and [540 nm to 560 nm] with different injection pressures were successfully derived. They then analyzed the liquid cooling in the spray at different injection temperatures (T=18.5℃,43.5℃, and 60℃) under the pressure of 5 bar and obtained the evolution of the droplet temperature measured in the centerline of the spray. Although the temperature measured using TCSPC is very close to the volume average temperature of the liquid phase, they still analyzed and discussed some potential errors that might influence the final results due to the multiple scattering.

In summary, laser-induced fluorescence based on fluorescence lifetimes is a promising method, but its research is relatively scarce, most of which lie in the study of fluorescence lifetimes of different substances and conditions affecting fluorescence lifetimes, only a few studies on the temperature and compositional characteristics of droplets in sprays.

2.3 Conclusion

Table 2-1 Summary of optical measurement discussed above

Techniques		Measurements	Advantages	Disadvantages
PDA		Size velocity	1. Non-intrusive. 2. High-precision. 3. Wide Velocity Range. 4. Simultaneous and Real-Time.	1. Complex Setup. 2. Spherical particles required. 3. Multiple Scattering problems. 4. Size Range Limitation.
RR	Standard	Size Refractive index Temperature	1. Non-Intrusive 2. Simultaneous measurement of droplet size and refractive index	1. Droplets are spherical 2. Difficulty in Dense Particle Fields 3. Limited Spatial Resolution
	Global		1. More precise than SRR 2. Well suited for complex flow.	1. Complex experiment set up and require careful alignment. 2. Spherical droplets required like SRR
RS		Temperature	1. Chemical structure detected 2. High Spatial resolution offered 3. Quantitative Analysis provided	1. Weak signal 2. Instrument Complexity 3. Fluorescence interference
LIF	Intensity	Temperature	1. Sensitive Detection 2. Quantitative measurement	1. Background interference 2. Photobleaching and Phototoxicity
	Lifetime		1. Less background interference 2. Quantitative analysis provided 3. Selective analysis of specific fluorescent molecules allowed	1. Complex Data Analysis 2. Building and maintaining a lifetime-based LIF setup can be costly

In conclusion, this chapter first introduces the applications of sprays in daily life and industrial production such as heat management systems, liquid fuel injectors, or spray drying, describes the importance and necessity of studying sprays, and points out that the study of sprays emphasizes on characterizing the properties and manifestations of their small droplets, such as size and velocity, temperature and composition.

Subsequently, several non-invasive optical measurements of spray droplets are highlighted, namely, phase Doppler anemometry for characterizing droplet size and velocity, as well as rainbow refraction (both standard and global), Raman scattering, and laser-induced fluorescence (both intensity and lifetime), which are mainly used to characterize the temperature or composition of droplets.

A detailed description of each of the above optical measurement methods is given from the basic concept to industrial application while the advantages and disadvantages of each method are pointed out (**Table 2-1**).

It can be concluded that Raman scattering requires complex instrumentation to cope with a lack of signal when small droplets are involved. Rainbow refraction requires accurate measurement of the angular position of the rainbow and assumptions must be made for the gradients of refractive index and the effect of droplet sphericity. Laser-induced fluorescence methods can be divided into two categories: intensity-based measurements and lifetime-based measurements. The use of intensity is somewhat problematic, as it depends on many parameters that cannot be controlled in a spray, such as droplet size and position relative to the optics. Ratio of intensities detected on two spectral bands can be a solution, but it requires a careful choice of dyes and detection bands to obtain reliable measurements. In dense sprays, multiple light scattering generates a high level of background noise, making it difficult to detect the smallest droplets, which can lead to measurement bias. For the lifetime-based fluorescence have great potential in solving some of the urgent problems in the spraying technology, like out-of-field fluorescence caused by light scattering, and in improving the accuracy and precision of the measurement results, although there is relatively scarce research related to lifetime-based laser-induced fluorescence methods.

Based on this, this paper focuses on the fluorescence lifetime-based laser-induced method to characterize the heat and mass transfer phenomena of droplets in sprays.

2.4 Reference

[1]. Liu, R., Zhang, L., & Zhang, X. (2019). Applications of spray cooling technology in aerospace field. In IOP Conference Series: Materials Science and Engineering (Vol. 470, No. 1, p. 012020). IOP Publishing.

[2]. Pais, M. R., Chow, L. C., & Mahefkey, E. T. (1992). Surface roughness and its effects on the heat transfer mechanism in spray cooling.

[3]. Yang, J., Chow, L. C., & Pais, M. R. (1996). Nucleate boiling heat transfer in spray cooling. Journal of Heat Transfer, 118(3), 668-671.

[4]. Rini, D. P., Chen, R. H., & Chow, L. C. (2002). Bubble behavior and nucleate boiling heat transfer in saturated FC-72 spray cooling. J. Heat Transfer, 124(1), 63-72.

[5]. Silk, E. A., Golliher, E. L., & Selvam, R. P. (2008). Spray cooling heat transfer: technology overview and assessment of future challenges for micro-gravity application. Energy Conversion and Management, 49(3), 453-468.

[6]. Mudawar, I., Bharathan, D., Kelly, K., & Narumanchi, S. (2009). Two-phase spray cooling of hybrid vehicle electronics. IEEE Transactions on Components and Packaging Technologies, 32(2), 501-512.

[7]. Cheng, W. L., Liu, Q. N., Zhao, R., & Fan, H. L. (2010). Experimental investigation of parameters effect on heat transfer of spray cooling. Heat and mass transfer, 46, 911-921.

[8]. Visaria, M., & Mudawar, I. (2009). Application of two-phase spray cooling for thermal management of electronic devices. IEEE Transactions on Components and Packaging Technologies, 32(4), 784-793.

[9]. Chaudhari, M., Puranik, B., & Agrawal, A. (2010). Heat transfer characteristics of synthetic jet impingement cooling. International Journal of Heat and Mass Transfer, 53(5-6), 1057-1069.

[10]. Esposito, E. I., Ekkad, S. V., Kim, Y., & Dutta, P. (2009). Novel jet impingement cooling geometry for combustor liner backside cooling.

[11]. Chambers, A. C., Gillespie, D. R., Ireland, P. T., & Kingston, R. (2010). Enhancement of impingement cooling in a high cross flow channel using shaped impingement cooling holes.

[12]. Choo, K. F., Chan, P. K., & Chua, Y. S. (2011). Zhibin Yan1, Rui Zhao1, Fei Duan1, Teck Neng Wong1, Kok Chuan Toh2. Two Phase Flow, Phase Change and Numerical Modeling, 285.

[13]. Williams, A. (2013). Combustion of liquid fuel sprays. Butterworth-Heinemann.

[14]. Zhang, J., Wang, Y., Muldoon, V. L., & Deng, S. (2022). Crude glycerol and glycerol as fuels and fuel additives in combustion applications. Renewable and Sustainable Energy Reviews, 159, 112206.

[15]. Sazhin, S. S., Kristyadi, T., Abdelghaffar, W. A., & Heikal, M. R. (2006). Models for fuel droplet heating and evaporation: comparative analysis. Fuel, 85(12-13), 1613-1630.

[16]. Abramzon, B., & Sirignano, W. A. (1989). Droplet vaporization model for spray combustion calculations. International journal of heat and mass transfer, 32(9), 1605-1618.

[17]. Maqua, C., Depredurand, V., Castanet, G., Wolff, M., & Lemoine, F. (2007). Composition measurement of bicomponent droplets using laser-induced fluorescence of acetone. Experiments in fluids, 43(6), 979-992.

[18]. Sazhin, S. S., Elwardany, A., Krutitskii, P. A., Castanet, G., Lemoine, F., Sazhina, E. M., & Heikal, M. R. (2010). A simplified model for bi-component droplet heating and evaporation. International Journal of heat and mass transfer, 53(21-22), 4495-4505.

[19]. Tong, A. Y., & Sirignano, W. A. (1986). Multicomponent droplet vaporization in a high temperature gas. Combustion and Flame, 66(3), 221-235.

[20]. Santos, D., Maurício, A. C., Sencadas, V., Santos, J. D., Fernandes, M. H., & Gomes, P. S. (2018). Spray drying: an overview. Biomaterials-physics and chemistry-new edition, 9-35.

[21]. Sollohub, K., & Cal, K. (2010). Spray drying technique: II. Current applications in pharmaceutical technology. Journal of pharmaceutical sciences, 99(2), 587-597.

[22]. Samantha, S. C., Bruna, A. S. M., Adriana, R. M., Fabio, B., Sandro, A. R., & Aline, R. C. A. (2015). Drying by spray drying in the food industry: Micro-encapsulation, process parameters and main carriers used. African Journal of Food Science, 9(9), 462-470.

[23]. Berrocal, E., Kristensson, E., Richter, M., Linne, M., & Aldén, M. (2008). Application of structured illumination for multiple scattering suppression in planar laser imaging of dense sprays. Optics express, 16(22), 17870-17881.

[24]. Kristensson, E., Berrocal, E., Richter, M., Pettersson, S. G., & Aldén, M. (2008). High-speed structured planar laser illumination for contrast improvement of two-phase flow images. Optics letters, 33(23), 2752-2754.

[25]. Kristensson, E., Berrocal, E., & Aldén, M. (2014). Two-pulse structured illumination imaging. Optics letters, 39(9), 2584-2587.

[26]. Lemoine, F., & Castanet, G. (2013). Temperature and chemical composition of droplets by optical measurement techniques: a state-of-the-art review. Experiments in fluids, 54, 1-34.

[27]. Van Beeck, J. P. A. J., Giannoulis, D., Zimmer, L., & Riethmuller, M. L. (1999). Global rainbow thermometry for droplet-temperature measurement. Optics letters, 24(23), 1696-1698.

[28]. Hu S, Richards RF, Richards CD (1994) Thermography of atomized droplets in flight using thermochromic liquid crystals. The seventh annual ILASS-Americas conference on liquid atomization and spray systems.

[29]. Airy G (1838) On the intensity of light in the neighborhood of a caustic. Trans Camb Phyl Soc 6:397–403

[30]. N. Roth, K. Anders, and A. Frohn, in Proceedings of the Seventh International Congress on Optical Methods in Flow and Particle Diagnostics (ICALEO 88) (Laser Institute of America, Orlando, Fla., 1998), pp. 294–304.

[31]. Massoli P, Beretta F, D'Alessio A, Lazzaro M (1993) Temperature and size of single transparent droplets by light scattering in the forward and rainbow regions. Appl Opt 32:3295–3301.

[32]. Sankar S, Ibrahim K, Buermann M, Fridrich M, Bachalo W (1993) An integrated phase doppler/rainbow refractometer system for simultaneous measurement of droplet size, velocity and refractive index. In: The third international congress on optical particle sizing, pp 275–284, Yokohama, Japan

[33]. S. V. Sankar, D. H. Buermann, and W. D. Bachalo, presented at the Seventh International Symposium on Applications of Laser Techniques to Fluid Mechanics,Lisbon, Portugal, July 11-14, 1994.

[34]. Van Beeck JP, Riethmuller ML (1998) Rainbow thermometry with a pulsed laser. In: 9th International Symposium on Applications of Laser Techniques to Fluid Mechanics, Lisbon, Portugal

[35]. Van Beeck JP, Riethmuller ML (1994) Simultaneous determination of temperature and size of droplets from the rainbow using airy theory. In: International symposium on applications of laser techniques to fluid mechanics. Springer, Lisbon, pp. 330–339

[36]. Van Beeck J, Riethmuller ML (1995) Nonintrusive measurements of temperature and size of single falling raindrops. Appl Opt34:1633–1639

[37]. Van Beeck JP, Riethmuller ML (1996) Rainbow phenomena applied to the measurement of droplet size and velocity and to the detection of non-sphericity. Appl Opt 35:2259–2266.

[38]. P. Massoli: Rainbow Refractometry Applied to Radially Inhomogeneous Spheres: The Critical Case of Evaporating Droplets. Appl.Opt. 37 (1998) 3227–3234.

[39]. K. Anders, N. Roth, F. Frohn: Theoretical and Experimental Studies of the Influence of Internal Temperature Gradients on Rainbow Refractometry. Proc. P ARTEC 4th Int. Congress on Optical Particle Sizing, Nuernberg, Germany 1995, 419–428

[40]. F. Corbin, A. Garo, G. Gouesbet, G. Grehan: Refractometrie d'arc-en-ciel: application au diagnostic des gouttes avec gradient d'indice, in Recueil des Actes du 5e Congres Francophone de Velocimetrie Laser, Rouen, France 1996, E1.1–E1.8. Universite´ et Institut des Sciences Appliquees de Rouen, URA CNRS 230/CORIA

[41]. Saengkaew, S., Charinpanitkul, T., Vanisri, H., Tanthapanichakoon, W., Biscos, Y., Garcia, N., & Grehan, G. (2007). Rainbow refractrometry on particles with radial refractive index gradients. Experiments in fluids, 43, 595-601.

[42]. Massoli, P. (1998). Rainbow refractometry applied to radially inhomogeneous spheres: the critical case of evaporating droplets. Applied optics, 37(15), 3227-3235.

[43]. Van Beeck JP, Giannoulis D, Zimmer L, Riethmuller M (1999) Global rainbow thermometry for droplet-temperature measurement. Opt Lett 24:1696–1698.

[44]. Moebius W (1910) Zur theorie des regenboges und ihren experimentellen prufung. Ann Phys 33:1493–1558

[45]. Chiewudomrat, S., Saengkaew, S., Grehan, G., Leveneur, S., & Estel, L. (2022). Evaluation of refractive index gradients in droplets by rainbow technique: application to CO 2 capture by monoethanolamine aqueous spray. Experiments in Fluids, 63(9), 153.

[46]. Van Beeck J, Grosges T, De Giorgi MG (2003) Global rainbow thermometry assessed by airy and lorenz-mie theories and compared with phase doppler anemometry. Appl Opt 42:4016–4022

[47]. Wilms J, Roth N, Weigand B, Arndt S (2004) Determination of the composition of multicomponent droplets by rainbow refractometry. In: International Symposium on Appl of Laser Techniques to Fluid Mechanics

[48]. Van Beeck, J. P., Zimmer, L., & Riethmuller, M. L. (2001). Global Rainbow thermometry for mean temperature and size measurement of spray droplets. Particle & Particle Systems Characterization: Measurement and Description of Particle Properties and Behavior in Powders and Other Disperse Systems, 18(4), 196-204.

[49]. Vetrano M, van Beeck J, Riethmuller M (2004) Global rainbow thermometry: Improvements in the data inversion algorithm and validation technique in liquid–liquid suspension. Appl Opt43:3600–3607

[50]. Han, Y. P., Méès, L., Ren, K. F., Gouesbet, G., Wu, S. Z., & Gréhan, G. (2002). Scattering of light by spheroids: the far field case. Optics communications, 210(1-2), 1-9.

[51]. Bonin, D., Saengkaew, S., Han, Y. P., & Gréhan, G. (2007). On non-sphericity detection in standard rainbow refractometry. In 8th International Congress on Optical Particle Characterization, Graz (Austria).

[52]. Wilms, J., Gréhan, G., & Lavergne, G. (2008). Global rainbow refractometry with a selective imaging method. Particle & Particle Systems Characterization, 25(1), 39-48.

[53]. Saengkaew, S., Godard, G., Blaisot, J. B., & Gréhan, G. (2009). Experimental analysis of global rainbow technique: sensitivity of temperature and size distribution measurements to non-spherical droplets. Experiments in fluids, 47(4-5), 839-848.

[54]. Saengkaew, S., Charinpanikul, T., Laurent, C., Biscos, Y., Lavergne, G., Gouesbet, G., & Gréhan, G. (2010). Processing of individual rainbow signals. Experiments in fluids, 48, 111-119.

[55]. Saengkaew, S., Ouboukhil, M., Estel, L., Gréhan, G., & LSPC, I. (2012). Combining Global rainbow refractometry and PDA to extract the refractive index value by class of size: Application to CO2 capture by MEA spray. ICLASS 12th (Heidelberg, Germany).

[56]. Schweiger, G. (1990). Raman scattering on single aerosol particles and on flowing aerosols: a review. Journal of aerosol science, 21(4), 483-509.

[57]. Dey, T. (2023). Microplastic pollutant detection by Surface Enhanced Raman Spectroscopy (SERS): a mini-review. Nanotechnology for Environmental Engineering, 8(1), 41-48.

[58]. Tarcea, N., Frosch, T., Rösch, P., Hilchenbach, M., Stuffler, T., Hofer, S., ... & Popp, J. (2008). Raman spectroscopy—A powerful tool for in situ planetary science. Strategies of life detection, 281-292.

[59]. Heller, E. J., Sundberg, R., & Tannor, D. (1982). Simple aspect of Raman scattering. The Journal of Physical Chemistry, 86(10), 1822-1833.

[60]. Tropea, C., Yarin, A. L., & Foss, J. F. (2007). Temperature measurement via absorption, light scattering and laser-induced fluorescence. Experimental fluid mechanics, Berlin, Heidelberg, 516-522.

[61]. Schmid, T., & Dariz, P. (2019). Raman microspectroscopic imaging of binder remnants in historical mortars reveals processing conditions. Heritage, 2(2), 1662-1683.

[62]. Carls, J. C., Moncivais, G., & Brock, J. R. (1990). Time-resolved Raman spectroscopy from reacting optically levitated microdroplets. Applied optics, 29(19), 2913-2918.

[63]. Buehler, M. F., Allen, T. M., & Davis, E. J. (1991). Microparticle Raman spectroscopy of multicomponent aerosols. Journal of colloid and interface science, 146(1), 79-89.

[64]. Vehring, R. D. H. P. G., Moritz, H., Niekamp, D., Schweiger, G., & Heinrich, P. (1995). Linear Raman spectroscopy on droplet chains: a new experimental method for the analysis of fast transport processes and reactions on microparticles. Applied spectroscopy, 49(9), 1215-1224.

[65]. Vehring, R. D. H. P. G., Moritz, H., Niekamp, D., Schweiger, G., & Heinrich, P. (1995). Linear Raman spectroscopy on droplet chains: a new experimental method for the analysis of fast transport processes and reactions on microparticles. Applied spectroscopy, 49(9), 1215-1224.

[66]. Muller, T. (2000). ID Spontaneous Raman Scattering for Comprehensive 2D Spray Characterization. In 8^< th> International Conference on Liquid Atomization & Spray Systems. ICLASS.

[67]. Stowers, M. A., & Friedlander, S. K. (2002). Chemical characterization of flowing polydisperse aerosols by Raman spectroscopy. Aerosol Science & Technology, 36(1), 48-61.

[68]. Heinisch, C., Wills, J. B., Reid, J. P., Tschudi, T., & Tropea, C. (2009). Temperature measurement of single evaporating water droplets in a nitrogen flow using spontaneous Raman scattering. Physical Chemistry Chemical Physics, 11(42), 9720-9728.

[69]. Hankel, R. F., Günther, A., Wirth, K. E., Leipertz, A., & Braeuer, A. (2014). Liquid phase temperature determination in dense water sprays using linear Raman scattering. Optics Express, 22(7), 7962-7971.

[70]. Homer, C. J., Jiang, X., Ward, T. L., Brinker, C. J., & Reid, J. P. (2009). Measurements and simulations of the near-surface composition of evaporating ethanol–water droplets. Physical Chemistry Chemical Physics, 11(36), 7780-7791.

[71]. Hopkins, R. J., & Reid, J. P. (2005). Evaporation of ethanol/water droplets: examining the temporal evolution of droplet size, composition and temperature. The Journal of Physical Chemistry A, 109(35), 7923-7931.

[72]. Hopkins, R. J., Symes, R., Sayer, R. M., & Reid, J. P. (2003). Determination of the size and composition of multicomponent ethanol/water droplets by cavity-enhanced Raman scattering. Chemical physics letters, 380(5-6), 665-672.

[73]. Howle, C. R., Homer, C. J., Hopkins, R. J., & Reid, J. P. (2007). Probing the evaporation of ternary ethanol–methanol–water droplets by cavity enhanced Raman scattering. Physical chemistry chemical physics, 9(39), 5344-5352.

[74]. Reid, J. P., Meresman, H., Mitchem, L., & Symes, R. (2007). Spectroscopic studies of the size and composition of single aerosol droplets. International Reviews in Physical Chemistry, 26(1), 139-192.

[75]. Hopkins, R. J., Symes, R., Sayer, R. M., & Reid, J. P. (2003). Determination of the size and composition of multicomponent ethanol/water droplets by cavity-enhanced Raman scattering. Chemical physics letters, 380(5-6), 665-672.

[76]. Sakakibara, J., Hishida, K., & Maeda, M. (1997). Vortex structure and heat transfer in the stagnation region of an impinging plane jet (simultaneous measurements of velocity and temperature fields by digital particle image velocimetry and laser-induced fluorescence). International Journal of Heat and Mass Transfer, 40(13), 3163-3176.

[77]. Pringsheim, P., & Schulman, J. H. (1950). Fluorescence and phosphorescence. Physics Today, 3(10), 35-35.

[78]. Coolen, M. C. J., Kieft, R. N., Rindt, C. C. M., & Van Steenhoven, A. A. (1999). Application of 2-D LIF temperature measurements in water using a Nd: YAG laser. Experiments in Fluids, 27, 420-426.

[79]. Seuntiëns, H. J., Kieft, R. N., Rindt, C. C. M., & Van Steenhoven, A. A. (2001). 2D temperature measurements in the wake of a heated cylinder using LIF. Experiments in Fluids, 31(5), 588-595.

[80]. Ross, D., Gaitan, M., & Locascio, L. E. (2001). Temperature measurement in microfluidic systems using a temperature-dependent fluorescent dye. Analytical chemistry, 73(17), 4117-4123.

[81]. Lavieille, P., Lemoine, F., Lavergne, G., & Lebouché, M. (2001). Evaporating and combusting droplet temperature measurements using two-color laser-induced fluorescence. Experiments in fluids, 31(1), 45-55.

[82]. Estrada-Pérez, C. E., Hassan, Y. A., & Tan, S. (2011). Experimental characterization of temperature sensitive dyes for laser induced fluorescence thermometry. Review of Scientific Instruments, 82(7).

[83]. Braeuer, A. (2015). Laser-induced fluorescence (lif) and phosphorescence (lip) techniques. In Supercritical Fluid Science and Technology (Vol. 7, pp. 313-345). Elsevier.

[84]. Bruchhausen, M., Guillard, F., & Lemoine, F. (2005). Instantaneous measurement of two-dimensional temperature distributions by means of two-color planar laser induced fluorescence (PLIF). Experiments in fluids, 38(1), 123-131.

[85]. Castanet, G., Lavieille, P., Lebouché, M., & Lemoine, F. (2003). Measurement of the temperature distribution within monodisperse combusting droplets in linear streams using two-color laser-induced fluorescence. Experiments in Fluids, 35(6), 563-571.

[86]. Kosseifi, N., Biwole, P. H., Mathis, C., Rousseaux, G., eliette Boyer, S. A., Yoshikawa, H. N., & Coupez, T. (2013). Application of two-color LIF thermometry to nucleate boiling. Journal of Materials Science and Engineering. B, 3(5B), 281.

[87]. Sakakibara, J., & Adrian, R. J. (2004). Measurement of temperature field of a Rayleigh-Bénard convection using two-color laser-induced fluorescence. Experiments in fluids, 37, 331-340.

[88]. Natrajan, V. K., & Christensen, K. T. (2008). Two-color laser-induced fluorescent thermometry for microfluidic systems. Measurement Science and Technology, 20(1), 015401.

[89]. Zhang, Y., Zhang, G., Xu, M., & Wang, J. (2013). Droplet temperature measurement based on 2-color laser-induced exciplex fluorescence. Experiments in fluids, 54, 1-10.

[90]. Castanet, G., Lavieille, P., Lebouché, M., & Lemoine, F. (2005). Experimental and theoretical investigation of the heating of combusting droplets in a linear stream. Combustion science and technology, 177(12), 2395-2422.

[91]. Castanet, G., Liénart, T., & Lemoine, F. (2009). Dynamics and temperature of droplets impacting onto a heated wall. International Journal of Heat and Mass Transfer, 52(3-4), 670-679.

[92]. Labergue, A., Delconte, A., Castanet, G., & Lemoine, F. (2012). Study of the droplet size effect coupled with the laser light scattering in sprays for two-color LIF thermometry measurements. Experiments in fluids, 52, 1121-1132.

[93]. Mishra, Y. N., Abou Nada, F., Polster, S., Kristensson, E., & Berrocal, E. (2016). Thermometry in aqueous solutions and sprays using two-color LIF and structured illumination. Optics express, 24(5), 4949-4963.

[94]. Prenting, M. M., Bin Dzulfida, M. I., Dreier, T., & Schulz, C. (2020). Characterization of tracers for two-color laser-induced fluorescence liquid-phase temperature imaging in sprays. Experiments in Fluids, 61, 1-15.

[95]. Ulrich, H., Sigl, S., Möhnle, M., Berrocal, E., & Zigan, L. (2023). Droplet Thermometry Based on an Optimized Two Dye Two-Color Laser-Induced Fluorescence Concept. Frontiers in Physics, 11, 1235847.

[96]. Casadevall i Solvas, X., Srisa-Art, M., deMello, A. J., & Edel, J. B. (2010). Mapping of fluidic mixing in microdroplets with 1 μs time resolution using fluorescence lifetime imaging. Analytical Chemistry, 82(9), 3950-3956.

[97]. Mendels, D. A., Graham, E. M., Magennis, S. W., Jones, A. C., & Mendels, F. (2008). Quantitative comparison of thermal and solutal transport in a T-mixer by FLIM and CFD. Microfluidics and nanofluidics, 5, 603-617.

[98]. Mehdi, S., Yangpeng, L., Hadrien, C., Fabrice, L., Xishi, W., & Guillaume, C. (2021). Fluorescence lifetime measurements applied to the characterization of the droplet temperature in sprays. Experiments in Fluids, 62, 1-19.

CONTENT 3

Chapter 3 Experimental Instrumentation

In this chapter, several commonly used experimental devices for fluorescence are introduced: femtosecond Ti:Sapphire laser, harmonic generator, photomultiplier tubes, and optical filters. These are the four main instruments described in detail. After that, the working principle of TCSPC is introduced in detail as well as the instrument response function (IRF) and pile-up effects. In addition, for simulating the fluorescence decay, mono-exponential and bi-exponential fitting are also presented. These constitute the main content of the chapter.

3.1 Introduction of Fluorescence Experimental Instrumentation

3.1.1 Femtosecond Ti:Sapphire Laser

Laser, as the light source that excites fluorescence generation, must first be presented. The working principle of a laser is that when a photon interacts with an excited molecule, it emits a second photon that is identical to the first photon, the emitted photons are all in phase with each other, producing a coherent beam of light. In simple terms, a laser is generated through light amplification by stimulated emission of radiation. Here are several reasons why a laser is used to induce fluorescence:

First, particular frequencies and wavelengths can be adjusted, allowing for the selective excitation of specific molecules or atoms. It improves the precision of the technique. For instance, the absorption intensity of the water-soluble rhodamine B dye is greater at excitation wavelengths between 500nm and 600nm, with a maximum value of around 550nm. By changing the laser generator, we can produce the 550nm green light needed to conduct the fluorescence experiment. Second, high-intensity light in short pulses can be offered in a laser generator, which is vital to the excitation and detection of fluorescence. For example, for low-concentration fluorescent dye solutions, high-intensity irradiation means that more molecules can absorb adequate energy to be excited, allowing changes in fluorescence intensity to be observed in a shorter period than with a low-intensity laser. Third, the laser can be concentrated to a tiny spot size, enabling local fluorescence excitation and measurement in a specific region of interest. Another essential feature of lasers is that they are non-invasive. For the study of fluid mechanics, it won’t affect the internal flow of fluid or the combustion and can be used to diagnose for flow field inside the combustion chamber and so on.

The laser used in our experiments is a Chameleon Ultra II made by Coherent Inc. It is a tunable Ti:Sapphire laser. On the one hand, the extremely short pulse duration enables fluorescence lifetime measurements with high temporal resolution, which can be accurately calculated to the order of picoseconds or even femtoseconds, thus allowing the study of fast dynamics and ultrafast processes in molecules and materials. On the other hand, it has a wide tuning range of excitation wavelength (usually from 680nm to 1080nm), hence for different fluorescence dyes, the excitation wavelength can be readily changed to be tuned on the absorption spectrum and its maximum of a considered fluorescent species. And, the high peak powers of femtosecond Ti:Sapphire laser offer the possibility for the multiphoton-excitation.

The laser delivers short light pulses with a duration of around 140 fs, measured at half width. This pulse duration is more than sufficiently short to enable high temporal resolution in fluorescence lifetime measurements, which can be accurately measured with pulse widths in the picosecond range. As the pulse width Δt decreases into the range of femtoseconds, the pulse spreads out in frequency. This can be described by performing the Fourier transform of a pulse. The spectral width Δλ in nm at half maximum can be expressed as [1]:

$$\Delta\lambda/2 = k \times \frac{\lambda_c^2}{\Delta t \cdot c} \qquad (3-1)$$

where λ_c is the central wavelength, c is the speed of light and k=0.441 for a Gaussian pulse shape. For a 140fs pulse at λ_c=800 nm, the spectral with $\Delta\lambda$ can be estimated at about 13 nm, while a 10fs pulse at the same central wavelength has a much broader spectral content with an estimated spectral width $\Delta\lambda$ of about 180 nm. Hence, the spectral width remains sufficiently small in the case of our femtosecond laser to maintain a good selectivity of fluorescent species by tuning the laser wavelength. This feature is essential for applications involving multiple fluorescent species.

Another important aspect to consider is the dispersion in the optical components (lenses, windows) used in the optical assemblies. In normal materials, low frequency components travel faster than high frequency components which means the velocities of large wavelength components are higher than that of shorter ones. These materials induce a positive group velocity dispersion on a propagating pulse. Because of dispersion, the laser pulse may lengthen or shorten over time as it travels through a material. This phenomenon can be described by the following equation:

$$\Delta\tau_{out} = \Delta\tau_{in}\sqrt{1 + \left(\frac{4\ln(2)\,GDD}{\Delta\tau_{in}^2}\right)^2} \qquad (3-2)$$

Where $\Delta\tau_{in}$ is the incident pulse duration (presently 140 fs) and $\Delta\tau_{out}$ is the output pulse duration. GDD is the group delay dispersion which increases with the travelled distance in the dispersive material. For example, the group velocity dispersion of fused silica is about +35 fs^2/mm at 800 nm. Based on this value, a 140fs long pulse, a 20-mm-thick fused-silica window yields a GDD of $+35 \times 20 = 700$ fs^2. Using the formula above, the temporal broadening of the pulse is approximately 0.7fs. This value remains quite small. In practice, no compensation is required in the optical assemblies.

Table 3-1 lists several relevant technical specifications of Chameleon Ultra II. A very important feature for measuring the fluorescence lifetime is the repetition rate of the laser pulses. In TSCPC (Time-correlated Single Photon Counting), only one photon is detected per laser pulse. Hence, the more laser pulses are received by the fluorescent medium, the more photons are detected, and the more statistically converged is the reconstructed curve of the fluorescence decay. The repetition rate of the laser pulses directly affects acquisition duration and measurement accuracy.

Table 3-1 Parameters of the femtosecond Ti: Sapphire laser

System specifications	
Noise (%)	< 0.15
Beam Ellipticity	0.9 to 1.1
Pulse Width (fs)	140 fs
Tuning Range (nm)	680 nm to 1080 nm
Average Power (W)	> 3.5 W
Beam Diameter (mm)	1.2±0.2 mm
Repetition Rate (MHz)	80 MHz
Output Power Stability (%)	< ± 0.5
Operating Temperature Range (℃)	15 ℃ to 35 ℃
Non-Operating Temperature Range (℃)	5 ℃ to 40 ℃

Figure 3-1 shows the average power (W) in different wavelengths, which is specified at the peak of the tuning range. For the Ti:Sapphire laser, the output power is around a few milliwatts to tens of watts, and it varies in different wavelengths. The average power of the laser is about 1.0W at 680nm, then starts to rise rapidly, reaching a maximum power of about 3.9W at 800nm, and then starts to fall slowly to about 0.25W at 1080nm.

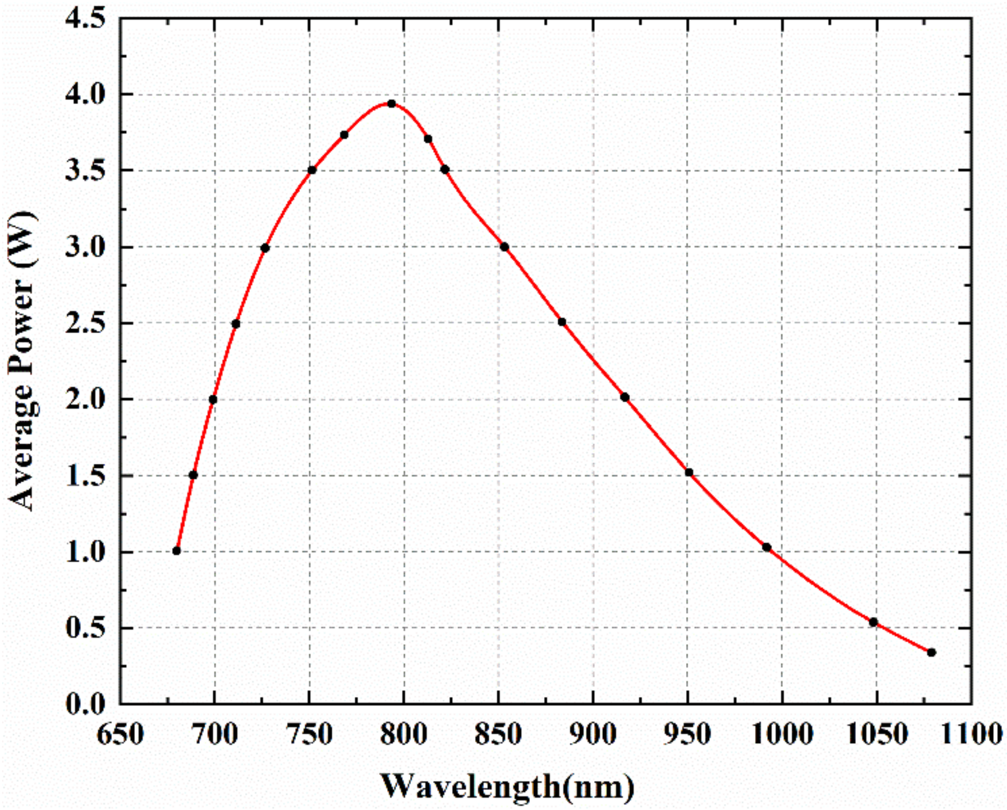

Figure 3-1 Average power in different wavelengths of Femtosecond Ti: Sapphire laser

Overall, the power of the laser allows for fluorescence experiments requiring high-energy excitation, in particular two-photon or multi-photon excitations.

3.1.2 Second and third harmonics generator

To extend the laser wavelength tuning range, a harmonic generation system "Harmonixx" made by APE, is used. The module is used for doubling or tripling the laser frequency by means of non-linear crystals. For instance, for a laser wavelength of 1080nm, the output wavelength is halved to 540nm after passing through the SHG module, and it is one-third of the original wavelength, around 360nm passing through the THG module.

Figure 3-2 Average power of the laser after SHG and power of the pump Ti:Sa Laser shows the average power of the laser after the SHG module. In the figure, the red line shows the power of the laser at different laser wavelengths for the Ti: Sapphire laser (the data is the same as figure 3-1), while the blue line shows, after the SHG module, the variation of the laser power with wavelength. For example, if the original excitation wavelength is 800nm, the power is about 3.9W, but when the wavelength is half, about 400nm, the power is about 1.6W.

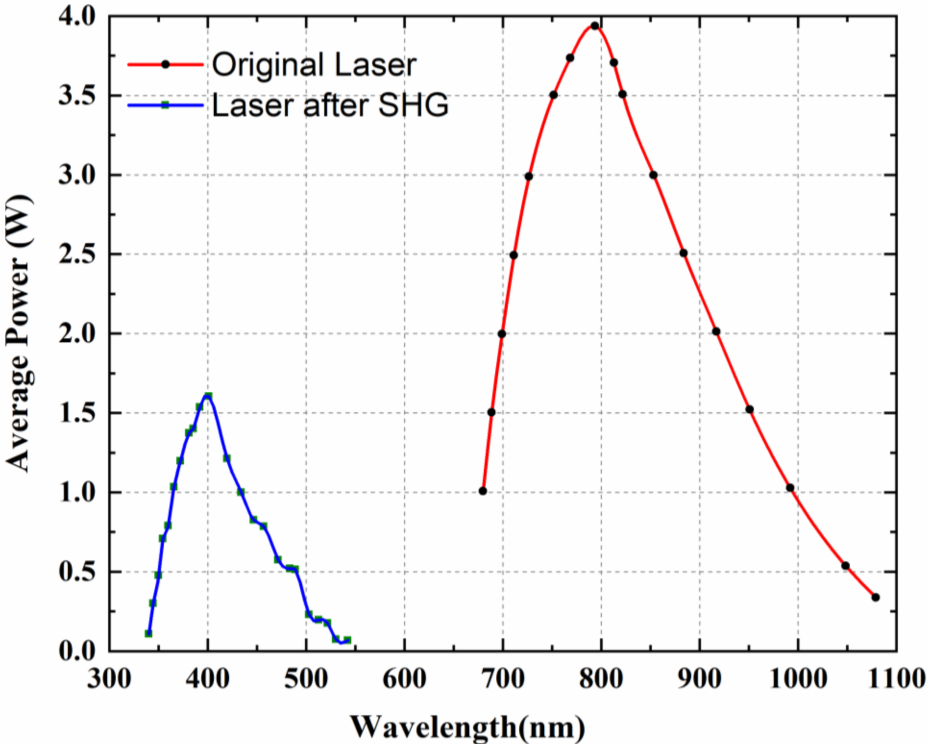

Figure 3-2 Average power of the laser after SHG and power of the pump Ti:Sa Laser

3.1.3 Photomultiplier Tubes (PMT) or Photomultiplier Assemblies (PMA)

Photomultiplier tubes (PMT) is widely used in fluorescence spectroscopy and particle detection imaging, and it is an instrument that converts optical signals into an electrical current. A photocathode, a sequence of dynodes, and an anode comprise the fundamental construction of a PMT. When a photon impacts the photocathode, a photoelectron is released and propelled towards the first dynode. Then electrons are accelerated by each dynode and "multiplied" when they hit the dynodes by a process known as secondary emission. This causes an electron cascade, with the number of electrons rising exponentially as they approach the anode. The anode gathers the final output current signal, which is proportional to the number of photons detected (light intensity)[1] as long as the maximum capacity is not exceeded.

An alternative to PMT are Single photon avalanche diodes (SPAD) which are solid-state photodetectors belonging to the same family as photodiodes and avalanche photodiodes. They use the photoelectric effect to generate charge carriers and the avalanche effect for internal amplification. A SPAD is able to detect single photons providing short duration trigger pulses that can be counted SPADs have a low dead time (less than 1 ns) and a high-count rate which is ideal for applications like fluorescence lifetime imaging microscopy (FLIM). Dark noise increases with the detector area, which is a limitation.

In the present case, the system used in our experiment is a "Hybrid" photomultiplier detector assembled by Picoquant Gmbh. It differs from traditional PMT in that it combines a photocathode and an avalanche diode. Incoming photons are detected by using a photocathode, which emits a photoelectron with the highest possible quantum yield. This photoelectron is strongly accelerated within a photomultiplier tube by means of high voltage in a vacuum, so that it finally hits an avalanche diode (electron bombardment). As a result, even more electrons are released, so that the original photoelectron is duplicated more than a thousand times. In this way, measurable signals are generated that can be used for data acquisition. For measurements in the time domain, this technology provides a narrow pulse height distribution which leads to a regular propagation time spread and thus to low timing jitter. In general, hybrid detectors have significantly lower dead times compared to PMTs or SPADs (Single photon avalanche diodes). PMTs can have dead times of tens of ns. Due to their high quantum efficiency, their large area (compared to SPADs), and fast time resolution these extremely light-sensitive detectors are commonly used in fluorescence lifetime microscopy and fluorescence correlation spectroscopy.

Figure 3-3 and **Table 3-2** show specifications of the detectors commonly used in the experiments, of which the cathode-40 model is used in this thesis.

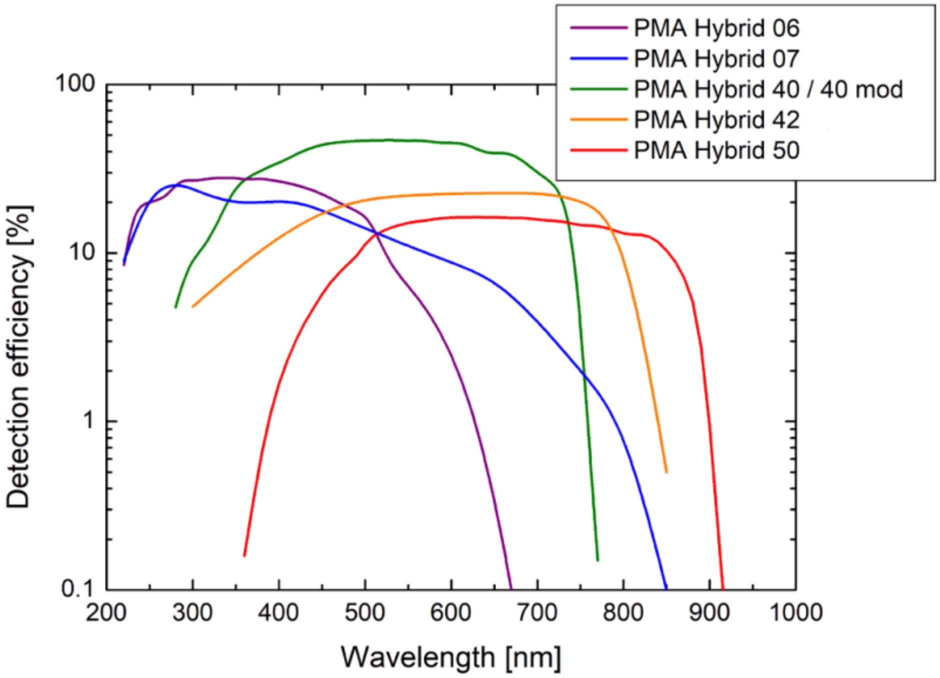

Figure 3-3 Spectral response of different type of PMA Hybrid

Table 3-2 Specifications of the detectors commonly used in the experiments

Type	06	07	40	40mod	42	50
Wavelength Range (nm)	220-650	220-850	300-720	300-720	300-870	380-890
Dark Counts (cps)	< 7	< 90	< 80	< 4000	< 110	< 250
Transit time Spread (ps)	< 50	< 50	< 120	< 120	< 130	< 160
Detector area diameter (mm)	6	6	3	5	3	3

For lifetime measurements, the time response of the detector is vital. The time response is characterized by the transit time, the rise time, and the transit time spread. The transit time is defined as the time delay between the arrival of a photon at the cathode and the arrival of the amplified pulse at the detector output. The rise time is the amount of time it takes for the output signal to increase from 10% to 90% of its highest value in response to a light pulse. The transit time spread (also called time jitter) is related to the distribution of the transit time [2]. The transit time of an electron bunch may vary statistically for each input photon. The transit time spread is usually defined as the standard deviation of 100 transit time values. The transit time spread is an important parameter as it gives the time resolution that can be achieved in the time reconstruction of the fluorescence decay with TCSPC.

Another important feature is the dark count, which is the spontaneous electrical pulses generated in the absence of any incoming light, caused by the thermionic emission of electrons from the photocathode and dynodes in PMT [3] or a thermal fluctuation in the avalanche diode. Dark counts will severely affect the accuracy and precision of fluorescence lifetime measurements if the fluorescence signal is relatively low. The dark count rate must be subtracted from the detection count rate when reconstructing the fluorescence decay.

3.1.4 Optical Filters

Various classifications of filters exist in fluorescence experiments, all serving the common purpose of blocking undesired wavelengths of light. They function by separating and selectively transmitting specific wavelengths of light, ultimately optimizing the signal ratio of fluorescence.

Here introduces the commonly used filters used in fluorescence experiments:

Firstly, there are excitation filters: Typically positioned at the forefront of a light source, these filters selectively transmit a specific excitation wavelength while blocking other wavelengths of light. Additionally, they minimize exposure to other wavelengths of light to prevent photobleaching of fluorophores. In our experiment, the excitation wavelength is controlled and selected when utilizing the Femtosecond Ti:Sapphire Laser. However, the incorporation of excitation filters ensures a consistent incident light wavelength.

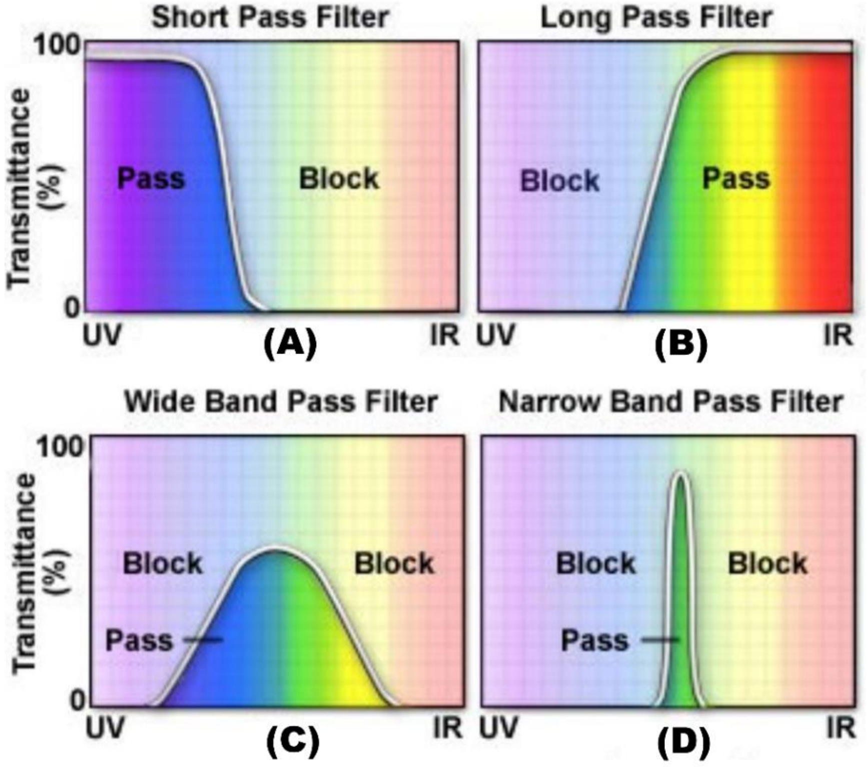

Figure 3-4 Working diagram of short-pass filters, long-pass filters and band pass filters[4]

Second, Emission filters: Emission filters are installed before the PMT, to isolate the fluorescence signal from any background or scatterer light, improving the signal-to-noise ratio of measurement. Neutral-density filters and bandpass filters are selected as the emission filters in our experiment. The former serves to attenuate light equally at all wavelengths （In the absence of neutral density filters, noise from ambient will be collected in large numbers）while the latter serves to selectively transmit fluorescence at a range of wavelengths centered on a specific wavelength or peak. Correspondingly, there are also the long-pass filters and short-pass filters. The former allows the long wavelengths of light to pass and block shorter wavelengths while the latter does the exact reverse. As shown in **Figure 3-4** **(A)** and **(B)** respectively elaborate the work of short-pass filters and long-pass filters. In the vicinity of UV light, the short-pass filter has a large transmittance while it is close to 0 near IR light. And the long-pass filter is in the reverse. **(C)** and **(D)** introduce separately wide band pass filter and short band pass filter. They have a relatively large transmittance in a specific wavelength range but almost zero near the UV and IR lights. Compared to the wide band pass filter, the narrow band pass filter has a higher transmittance in the narrow wavelength range allowed to pass. In addition, the neutral-density filters, are commonly defined by their Optical Density (OD) which describes the amount of energy blocked by the filter (as described in equations $(3-3)$ $(3-4)$). A high optical density value denotes the low transmission while a low optical density value indicates the higher transmission. The density filters OD=3.0 are used in our experiment to decrease the environmental noise.

$$OD = -\log\left(\frac{T}{100\%}\right) \qquad (3-3)$$

$$T(percent\ Transmission) = 10^{-OD} \times 100\% \qquad (3-4)$$

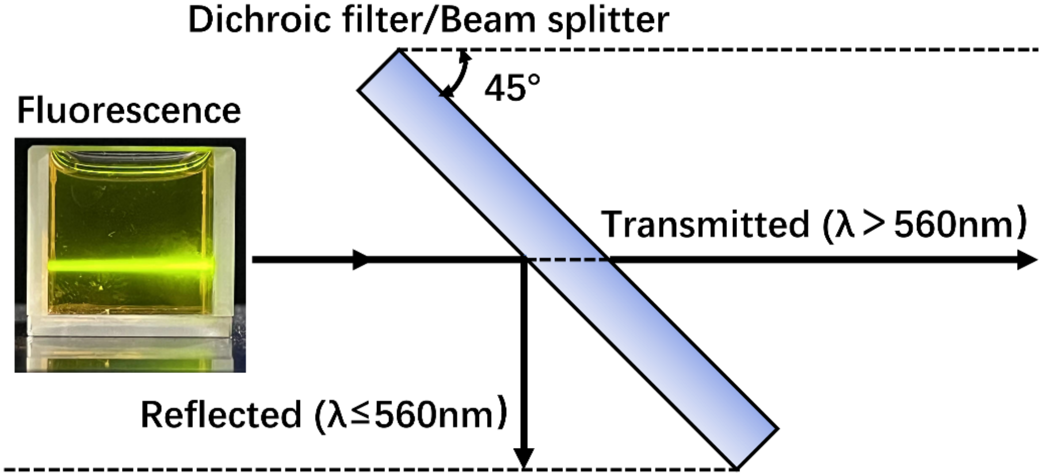

Figure 3-5 Working diagram of a dichroic filter/Beam splitter

Third, dichroic filters and beam splitter: Both of them are optical elements used in fluorescence microscopy to separate different wavelengths of light, the difference between them is that dichroic filters have a narrower spectral profile, reflecting and transmitting only a narrow range of wavelengths while the beam splitters typically have a broader spectral profile, reflecting and transmitting a wider range of wavelengths. Dichroic filters are thus more suitable for fluorescence microscopy to separate excitation and emission light paths where high selectivity and specificity are required. **Figure 3-5** shows the working diagram of the dichroic filter/beam splitter. A fluorescent signal is selectively passed (λ > 560nm) or reflected (λ < 560nm) by a beam splitter with an oblique angle of 45°.

3.2 Time-Correlated Single Photon Counting (TCSPC)

For signal processing and the acquisition of fluorescence decay, our choice is the Hydra-harp 400 system from Picoquant. Subsequently, the upcoming paragraph elucidates the principle of TCSPC measurement.

3.2.1 Principle of Time-Correlated Single Photon Counting (TCSPC)

Time-correlated single photon counting (TCSPC) [5] refers to a technique of measuring the fluorescence lifetime in the time domain. Basically, in TCSPC, a sample is excited with a short pulse of light, typically in the femtosecond or picosecond range. The generated fluorescence is received by the previously described photodetector. The aim of the detection is not to measure the intensity of the fluorescence emission but records the time between an excitation pulse and a single emitted photon.

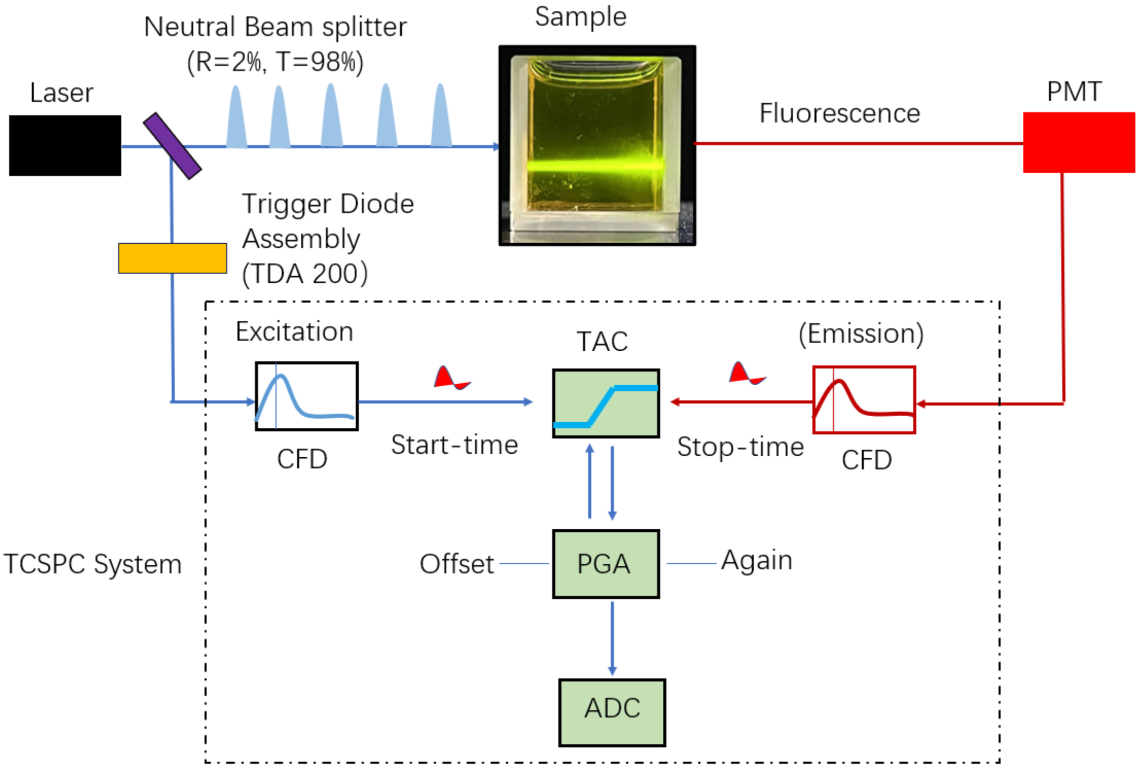

Figure 3-6 An electronic diagram of TCSPC

Figure 3-6 shows a schematic diagram of the TCSPC system used in the experiments. A small fraction of the laser pulse is diverted to a fast photodiode (TDA 200 assembled by Picoquant) by reflection on a neutral beam splitter. The TDA 200 unit responds to each excitation pulse with a fast negative output pulse (typ. 500ps) and a timing jitter of a few tens of ps. The output signal of the fast photodiode serves as a trigger to start the counting electronics. The time elapsed since the photodiode trigger is recorded in the TAC (Time-to-Amplitude Converter). The TAC starts accumulating charges until a photon is detected by the photodetector. When a fluorescent photon is detected, the amplitude which has accumulated in this time by the TAC is passed to the programmable gain amplifier (PGA) which amplifies the voltage. Then, an amplitude-to-digital converter (ADC) converts the voltage to a value which is a measurement of the photon's arrival time [6]. After that, the arrival time is recorded in the appropriate channel, building up a histogram of time against counts. To further improve the counting of photons, CFD (constant function discriminator) are introduced to eliminate low amplitude noise. Only pulses that surpass a threshold voltage, are considered as a real signal for starting and stopping the TAC. If no stop signal is received by the TAC (no photon has been detected) during the laser period, the charge accumulated is dispersed to reset the TAC for the next period.

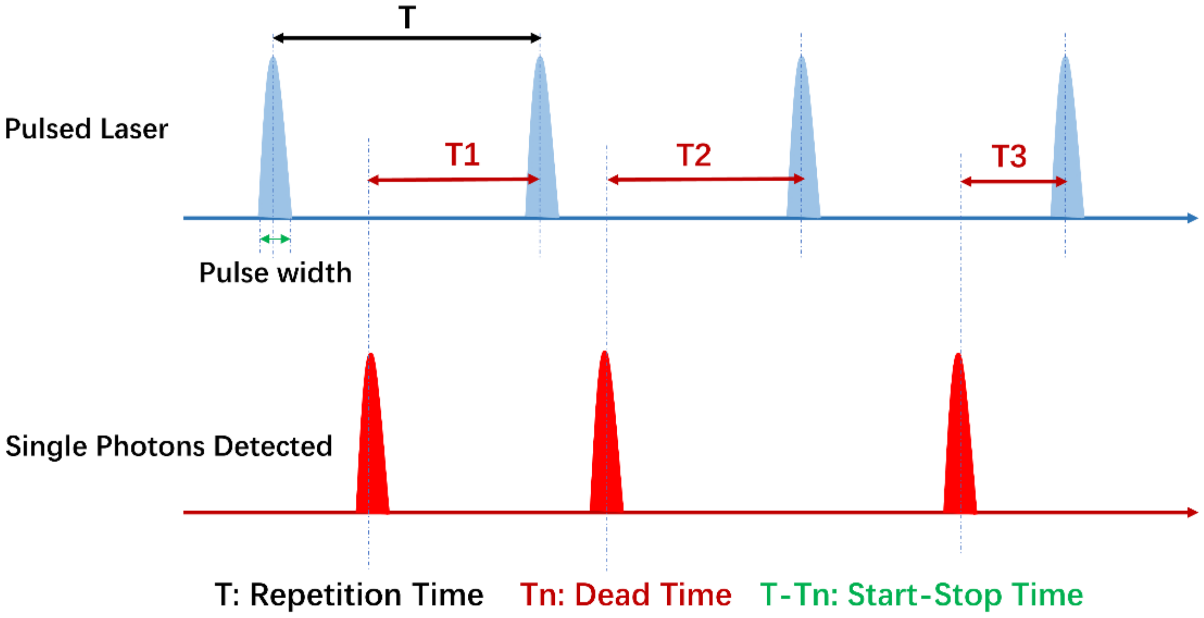

Figure 3-7 Repetition Time, dead time and start-stop times of photons

Figure 3-7 depicts dead time, start-stop time, and repetition time in the TCSPC system. When one pulsed laser is generated, a single photon is detected. The time between two successive pulses is called repetition time. The start-stop time can be defined as T-Tn in this figure, which, as explained before, represents the interval of the first pulse found and the single photon detected in PMT. The dead time is the time to process and rest after one cycle, during that time, the electronics cannot process any subsequent start or stop pulse. Notably, not each time a pulse is generated, can a photon be detected and collected in the PMT and also, the first photon detected in PMT doesn't mean the first photon emitted from the sample, because the fluorescence is a spontaneous and directionless emission, only in the certain direction, will they be detected in the PMT.

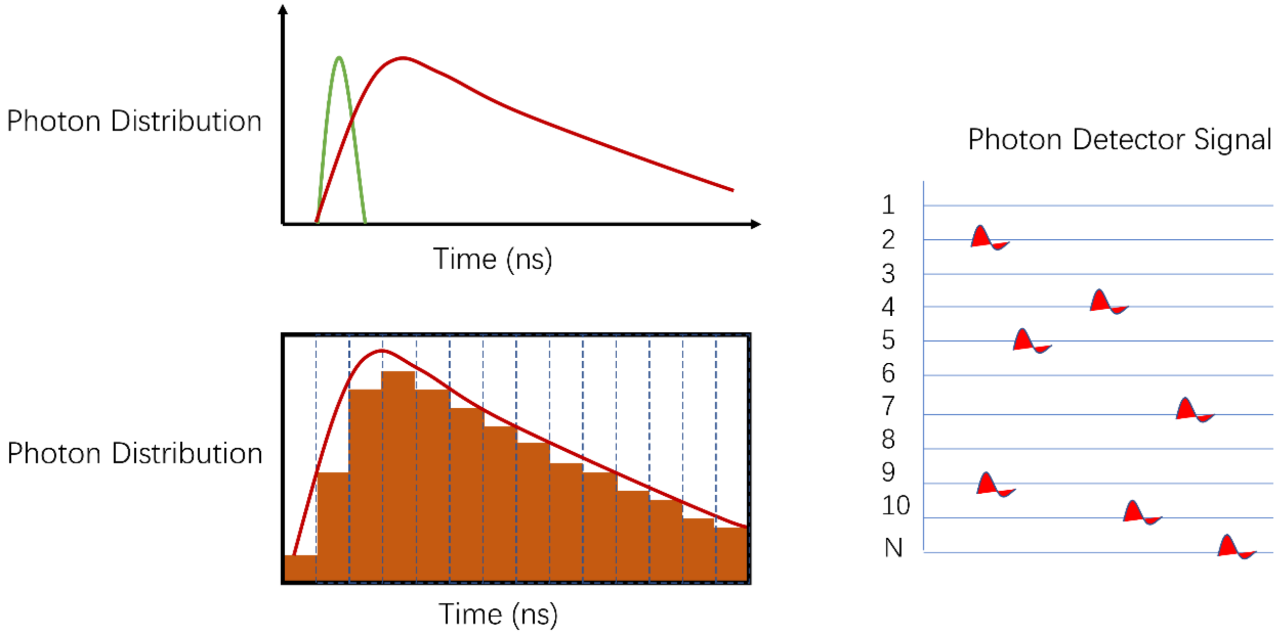

Figure 3-8 Photons Distribution

Figure 3-8 illustrates the photon distribution of the whole process of fluorescence. As shown in the photon detector signal, no photon is found in the 1st pulse and one photon is detected early in the 2nd pulse and no photon is captured in the 3rd pulse and so on. If we record the time spent on each photon with a pulsed light source repeated numerous times, we can measure a histogram of the photon distribution.

3.2.2 The Pile-up Effects

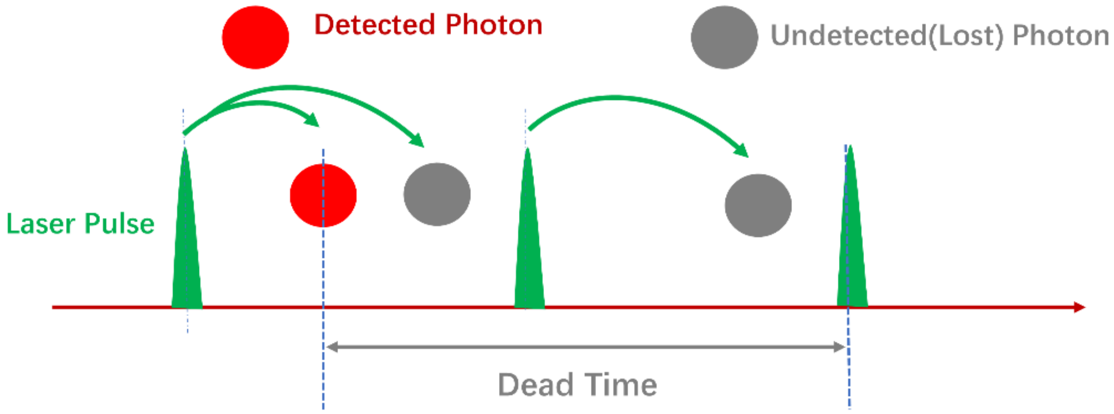

Figure 3-9 Pile-up effects (Lost Photons)

In the description before, a maximum of one photon can be detected after each laser pulse. In **Figure 3-9**, a second photon arrives within the period before the next laser pulse but after the first photon has been detected. This second photon is discarded (undetected or lost) because the photodetector and the electronics have a dead time during which they are blind. The electronics need time to reset and prepare for the next photon to be detected. The Hydraharp 400's dead time is around 40 ns-80 ns, depending on the number of photodetectors connected to the electronics (up to 2 photodetectors can be connected at the same time in our system). This is longer than the time between two laser pulses (12.5 ns) meaning that only one pulse over 4 or 5 can be really exploited for the measurements. Due to the deadtime, only the photons which arrive at the detector first are considered. The effect of missing “slower” photons in the count causes a distortion of the histogram which is called the pile-up effect. The histogram no longer faithfully reflects the Poissonian process of photon emission by fluorescent molecules.

The piles effect creates a bias toward a shorter fluorescence lifetime. **Figure 3-10** shows the decay curve (obtained by connecting the histogram bins) in a cuvette at different laser powers and thus at different count rates. It can be seen clearly that the slopes of the curves corresponding to various count rates are distinct, especially when the count rate is 9×10^6Cps. The decay is faster than for other count rates, thus a shorter lifetime would be found from the analysis of this decay curve. As the count rate decreases, the decay curves almost overlap, indicating that measurements are not affected by the pile-up effect anymore. Another visible consequence of the pile-up effect is that a mono-exponential decay would not appear as such, but rather takes on a somewhat bi-exponential shape.

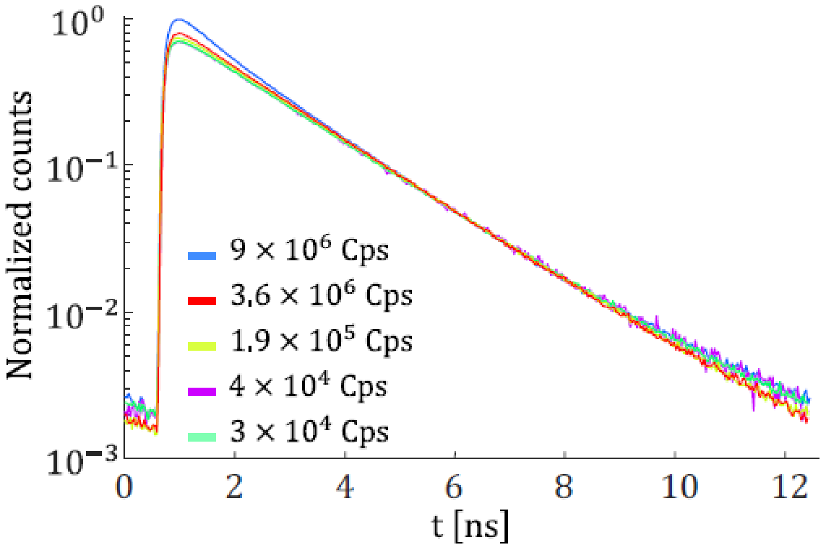

Figure 3-10 Illustration of the pile up effect. All the curves have been normalized to have the same value at $t = 6ns$.Due to the pile up effect, the lifetime value is underestimated for the highest count rates. The results of the fitting are: $\tau = 1.54ns$ at 9 MCps, $\tau = 1.71ns$ at 3.6 MCps, $\tau = 1.76ns$ at 0.19 MCps, $\tau = 1.77ns$ ns at 40 kCps and $\tau = 1.77ns$ ns at 30 kCps, Measurements in a cell containing rhodamine B at C = 10^{-5} M and T=20°C in the spectral band [630 nm-650 nm]

The pile-up effect is a serious limitation. An acquisition time of the order of a few seconds is required to guarantee the absence of pile-up problems as well as a good statistical convergence of the measurements. For our measurement system, we can conclude from **Figure 3-10** that the pile-up effect becomes noticeable at a count rate of around 9×10^6 Cps. In all our experiments, great care was taken not to exceed this value, as it would result in a systematic measurement error.

3.2.3 Reverse Mode

The presentation made before is that of system operating in the conventional Forward Mode. A drawback of this mode is observed as the period of the laser pulses (presently 12.5 ns) is less than the dead time of the electronics. All pulses that arrive during the dead time of the electronics will not trig a start. Increasing the repetition rate of the laser is not going to help obtaining a faster acquisition. A certain improvement is possible working in the reverse mode. An emitted photon from the sample is used to start counting and the next excitation laser pulse stops the counting. Starting the counting electronics from the receipt of an emitted photon means that the counting electronics will only be activated when there is a count to be recorded. The block diagram in **Figure 3-6** remains valid, except that start is now provided by the photodetector and the stop by the signal from the TDA 200 photodiode receiving the laser pulses. In the reverse mode, photons can be acquired as quickly as possible by the electronics. As a result, acquisitions can be performed with count rates of up to around 2×10^7 Cnt/s with our system. However, when comparing the effects of the count rate on the fluorescence decay, a distortion was still observed for count rates in the order of 4×10^6 Cnt/s. The pile-up effect remains thus a clear limitation in practice.

3.2.4 Instrument Response Function (IRF) and Tail Fit

The temporal response of all the components of the measurement chain must be considered as they are not responding infinitively fast. Especially, the photodetector has a relatively long time spread. The Instrument Response Function (IRF) denotes the time response of the measurement system to a hypothetical infinitively short lifetime. All components will contribute to both shape and width of the IRF and the full width half maximum (FWHM) will give an indication of the timing resolution of the instrument.

To evaluate the IRF, two different approaches were tested.

In a first measurement, a dispersion of glass spheres (approx. 100 µm in size) was used to scatter the laser light quite effectively. The laser power was attenuated very strongly so that the laser light could be captured directly (no bandpass filter was used to block the laser light). The laser wavelength was tuned in the visible at 490 nm using the SHG module to be in the detection range of the photodetector. This first measurement resulted in the IRF, shown in blue on the curve below.

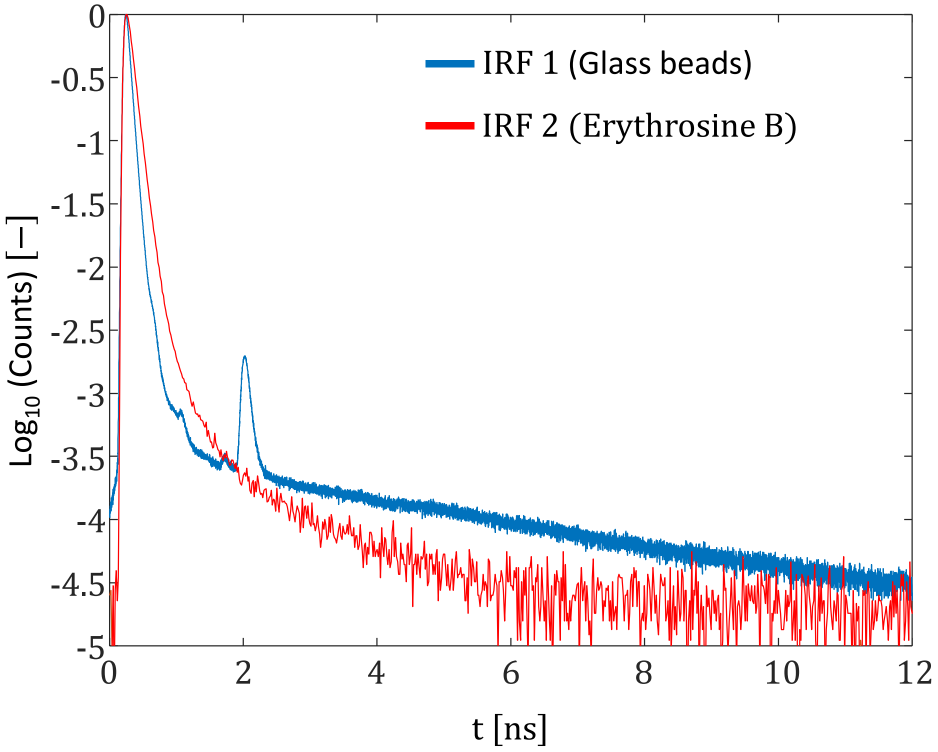

Figure 3-11 Measurements of the IRF by two approaches

In a second test, a fluorescent dye with a short lifetime in the range of a few tens of ps. According to Szabelski[7], the lifetime of erythrosine B decreases to 24 ps in 5.02 M of potassium iodide. Erythrosine B dissolved into an aqueous solution of KI (potassium iodide) is therefore a good option, but it needs to be saturated in KI. The specific preparation process of the solution can be seen in details[7][8][9]. The quantum yield of erythrosine B in the presence of 5.02 M KI is very small, about 0.0035, IRF was therefore recorded at a low count rate (of the order of a few thousands Cnt/s) compared to usual fluorescent dyes. To induce the excitation of erythrosine B, the SHG module described was used to generate a beam at the wavelength of 490 nm. The result of this measurement is also displayed in **Figure 3-11**.

The two IRFs obtained have a width half maximum (FWHM) that are very close, around 95 ps in the case of the scattering glass beads solution, and 120 ps in the case of the erythrosine B solution. A higher level of noise can be noted in the case of the solution of erythrosine B, due to the low emission of the dye which makes it more difficult to capture the fluorescence decay over more than 4 decades. In the case of glass spheres, the curve exhibits a second peak whose origin is a bit strange.

In addition to considering the instrument response function (IRF) when modeling the data collected by the TCSPC, the tail fitting setup is also important. The term "tail fitting" refers to the process of analyzing the decay tail of the fluorescence signal and fitting a mathematical model to the long decay tail. The decay of fluorophore emission is not an instantaneous process but occurs over a certain time interval. The tail fitting analysis involves fitting an appropriate decay model (usually an exponential decay function) to the long tail portion of the decay curve. This tail-fitting procedure helps to accurately determine the fluorescence lifetime of a sample.

Figure 3-12 shows the regions of measurement results analyzed by tail fitting. Tail fitting should only be performed in regions where there is no longer sample excitation, i.e., in regions where the excitation light pulse has disappeared. Therefore, the tail fitting procedure will be used to analyze samples with longer decay times. The image shows not only the decay data, but also the instrument response function. This is just to show the range of the fit. The tail fit does not require an instrument response function, and as long as the start of the fit range is known, it is usually not even necessary to measure the instrument response function (IRF).

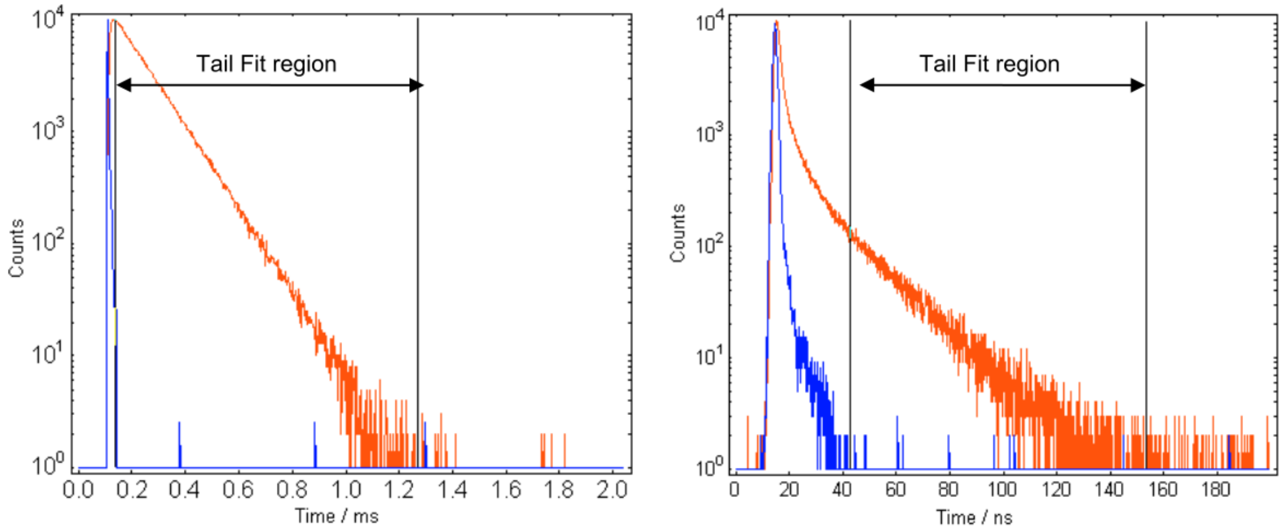

Figure 3-12 Tail fit region

3.2.5 Optical Arrangements for LIF

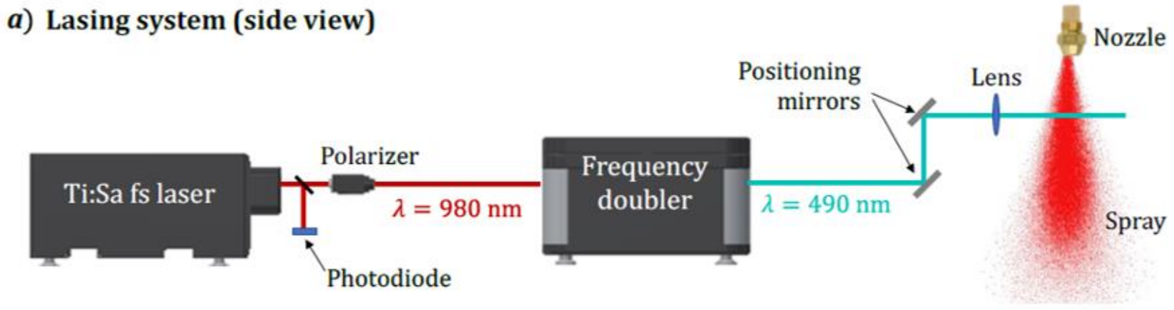
***a*) Lasing system (side view)**

***b*) Detection system (top view)**

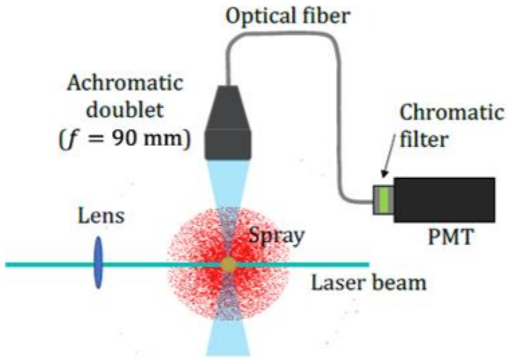

Figure 3-13 One-photon fluorescence experiment

Two types of optical set-up were considered in our experiments.

A. One-photon Fluorescence Experiment (Figure 3-13):

The SHG module is used to generate a laser beam in the visible and thus perform one photon excitation of the fluorescent molecule. A polarizer is used to modify the power of the laser beam by changing the polarizer angle. The laser beam is directed by several mirrors to a converging lens that is used to focalize the beam inside the liquid flow (cuvette, sprays…) seeded by the fluorescent molecules. The fluorescence signal is collected from the side at a scattering angle close to 90° by receiving optics. The front lens of the receiving probe can be modified to allow several working distances. The received light is then transmitted by an optical fiber to the photodetector. At the end of the optical fiber, a bandpass filter (or a combination of several filters) is used to remove the laser light and transmit to the detector only the fluorescence in a specific band of detection.

B. Two-photon fluorescence experiment (Figure 3-14):

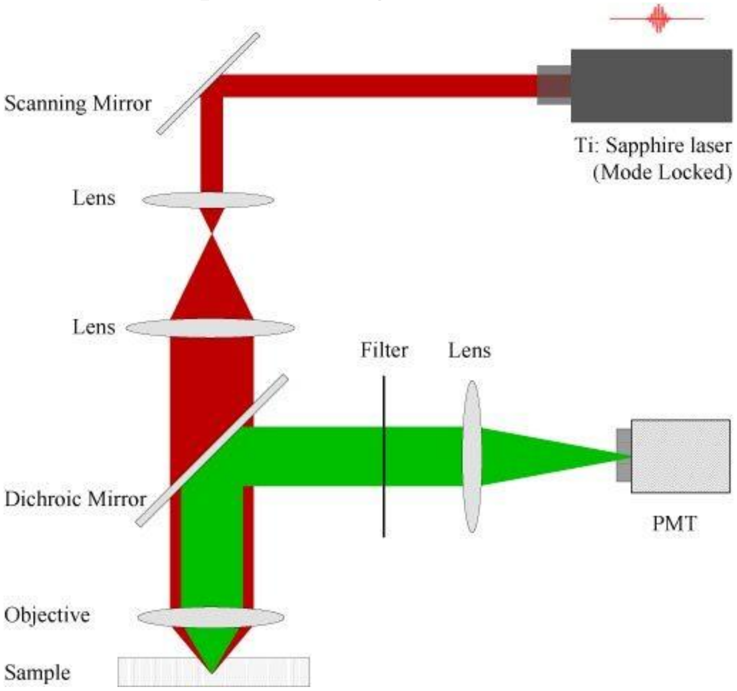

Figure 3-14 Two-photon fluorescence experiment

The layout is based on a conventional two-photon fluorescence microscope. The laser beam, with a wavelength in the infrared, is transmitted through a dichroic mirror towards an infinity-corrected microscope objective. The emission signal is collected by the same objective and reflected by the dichroic mirror to the direction of the photodetector. A filter is needed to attenuate the scattered light and transmits fluorescence in a specific band of detection. Although the microscope in LEMTA (Sutter Instruments, Movable Objective Microscope MOM) has scanning mirrors (galvanometer scanning systems). These elements will not be used in the studies presented in the following chapters.

3.2.6 Analysis of the Fluorescence Decay

In general, after an excitation by an ultrashort pulse of light, fluorescent molecules emit a signal that can be written as follows:

$$F(t) \propto \phi(t)\ k\ N_{abs} \qquad (3-5)$$

Here N_{abs} is the number of photons absorbed and k is related to the collection efficiency of the measurement system. Fluorescence typically follows a first-order kinetics. The term $\phi(t)$ expresses the fluorescence decay resulting from the progressive decrease of the number of molecules in the excited state. In general, it follows a mono-exponential evolution:

$$F(t)/F(t=0) = \mathrm{e}^{-t/\tau} \qquad (3-6)$$

The decay process is described by a single exponential function, called mono-exponential decay. Generally, it is used to fit the fluorescence decay data when only one main fluorophore is present in the sample while the bi-exponential or double-exponential is applied when two fluorophores are inside the one sample, for example, if you mix two different fluorescent dyes in one solution, then the decay fit should be fitted in bi-exponential. And also, bi-exponential is also used to describe the decay of some fluorophores like Rhodamine B, which is already illustrated in the literature[10][11][12]. The decay can be described as:

$$F(t)/F(t=0) = \alpha_1\, exp(-t\,/\,\tau_1) + \alpha_2\, exp(-t\,/\,\tau_2) \qquad (3-7)$$

In this expression, $\alpha_1\ and\ \alpha_2$ are called the pre-exponential factors, which respectively represent the fractional amount of fluorophore 1 and fluorophore 2 in the solution. And actually $\alpha_2 = 1 - \alpha_1$ because there are only two fluorophores inside. According to [13], an average fluorescence lifetime τ for this type of decay can be evaluated by:

$$\tau = \alpha_1\, \tau_1 + (1 - \alpha_2)\, \tau_2 \qquad (3-8)$$

Finally, if the sample contains a sophisticated mixture of fluorophores that decay through multiple pathways or different excited states, multi-exponential decay can be introduced. The intensity is expressed as:

$$\frac{F(t)}{F(0)} = \sum_{1}^{n} \alpha_i\, exp(-t\,/\,\tau_i) \qquad (3-9)$$

α_i represents the proportion of a given molecule in a mixture at t=0, $\tau_i$are the decay times and $\sum_1^n \alpha_i = 1$.

Remark: An alternative definition to the fluorescence lifetime can be proposed for the average lifetime $\bar{\tau}$. This latter can be viewed as the time that fluorophores remain in the excited state following excitation $(3-10)$. In that case, we should calculate it as:

$$\bar{\tau} = \frac{\int_0^\infty tI(t)\,\mathrm{d}t}{\int_0^\infty I(t)\,\mathrm{d}t} = \frac{\int_0^\infty t(\sum_1^n \alpha_i\, exp(-t\,/\,\tau_i))\,\mathrm{d}t}{\int_0^\infty \sum_1^n \alpha_i\, exp(-t\,/\,\tau_i)\,\mathrm{d}t} \qquad (3-10)$$

For the mono-exponential decay, $\bar{\tau} = \tau$, and for bi-exponential decay, it can be expressed as:

$$\bar{\tau} = \frac{\alpha_1 {\tau_1}^2 + \alpha_2 {\tau_2}^2}{\alpha_1\tau_1 + \alpha_1\tau_2} \qquad (3-11)$$

To compare theoretical decay with measurements, it is important to consider that the time response of the detector and the electronic components is not infinitely short. The measured photon count $N_c(t)$ is a convolution of the IRF and the fluorescence decay $F(t)$:

$$N_c(t) = \int_0^t F(t')\, IRF(t-t')\, dt' \qquad (3-12)$$

A non-linear least squares method is used to test if the model is consistent with the data and estimate the parameters of the fluorescence decay model (τ in the case of mono-exponential, α_1, τ_1 and τ_2 for the bi-exponential decay). Basically, parameters are adjusted until the goodness-of-fit parameter χ^2 is determined by:

$$\chi^2 = \frac{1}{n}\sum_{k=1}^{n} \frac{\left(N(t_k) - N_c(t_k)\right)^2}{N(t_k)} \qquad (3-13)$$

In the above expression, $N(t_k)$ is the measured counts at time t_k, $N_c(t_k)$ is the modeled number of counts at time t_k assuming a mono-exponential, a bi-exponential or a multi-exponential function for the fluorescence decay. The theoretical value of the photon count N_c is obtained after time convolution with the IRF. The noise coming from the photodetector and the environment is also considered by adding “noise” photons uniformly distributed in time to the count value N_c.

A good fit is characterized by a small value of χ^2 and the weighted residual between the measured and calculated decay curves randomly distributed around 0. A value of χ^2 close to 1, is considered a satisfactory fit in most cases. Finding the minimum of χ^2 is an optimization problem. The program used is based on matlab's function ‘lsqnonlin’ and the Levenberg-Marquardt method. It is necessary to provide initial guest values and a search range for the parameters to be estimated. These choices may sometimes affect the convergence to the solution.

Some fluorophores, like Rhodamine B as we said before, even when there are the only fluorescent species in solution, can exhibit quite complex behaviors. Their decay can be much better described by a bi-exponential decay than a mono-exponential one. This is illustrated in **Figure 3-15** for the case of kiton red. A large error is made if a mono-exponential model is chosen.

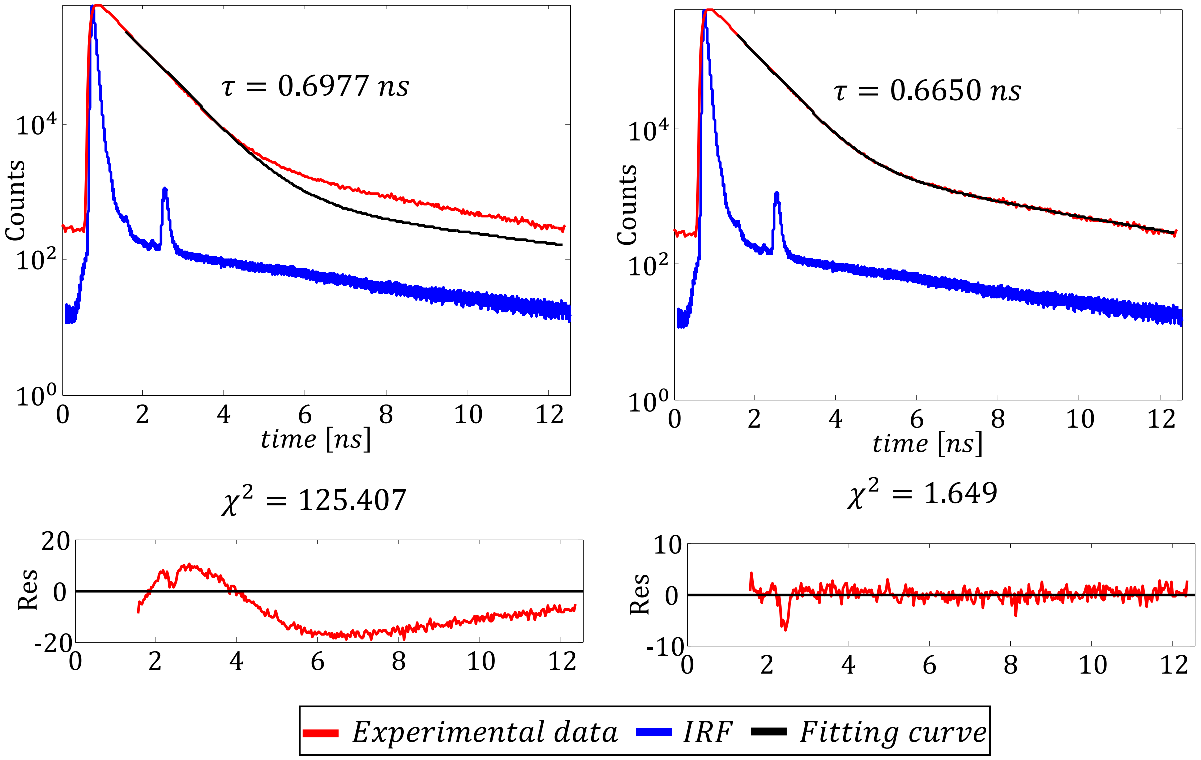

Figure 3-15 Fluorescence decay of kiton red in the band [630 nm - 650 nm], where the T=58°C and $C_{KR} = 10^{-5}\ M$. The decay of the fluorescence exhibits a clear biexponential trend.

In general, the time interval considered for fitting does not begin at time 0 (the rising section of the curve), but a few tenths of ns after the maximum. The term "tail fitting" refers to the process of analyzing the tail of the fluorescence decay. Tail fitting is less dependent on the IRF since the effects of IRF rapidly vanish in the convolution product. It may be not even necessary to measure the instrument response function (IRF) if the fitting interval starts1ns to 2ns after the rising edge. On the other hand, if the decay is bi or multiexponential, the starting point of the fit can significantly affect the estimation of the parameters.

Errors in parameter estimations:

Errors in the measurement will be more detailed in the conditions of applications of the technique in **Chapter 4** and **5**. A Monte Carlo error propagation method is used to evaluate the effect of the measurement conditions on the accuracy of the parameter estimates.

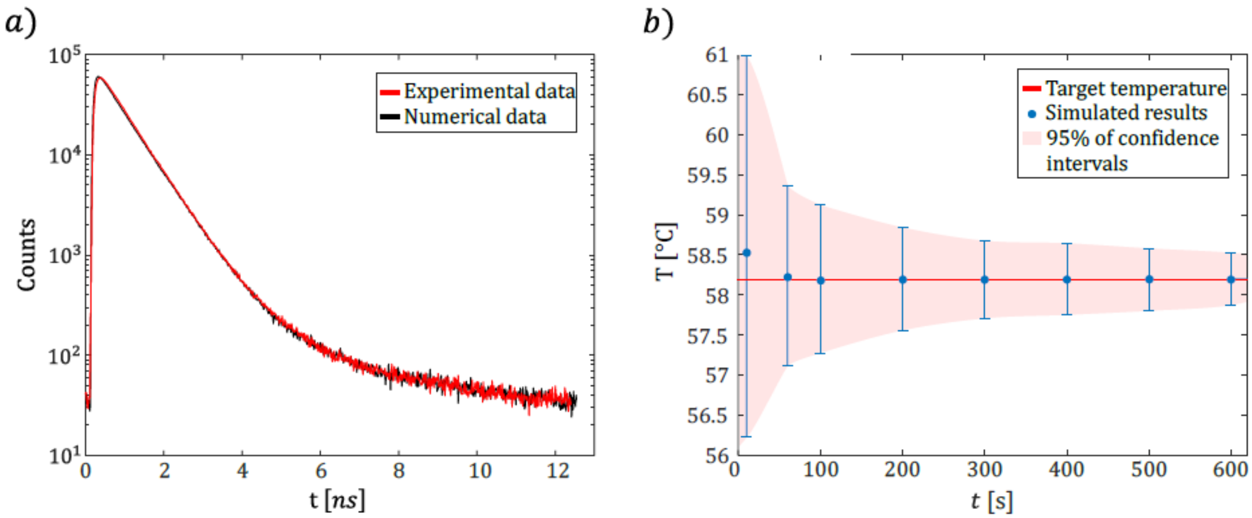

Figure 3-16 Example of the Monte Carlo approach to reconstruct a histogram of fluorescence decay (α_1=0.01311, τ_1=1.548 ns, τ_2=0.697 ns, acquisition time of 200 s, count rate of 2700 Cnt/s, and dark noise of 60 Cnt/s). Each point is the result of 1000 synthetic fluorescence decays equivalent to the ones displayed in a)

For given values of the parameters (τ if a monoexponential decay, $\alpha_1, \tau_1\tau_2$ if a biexponential decay), the idea is to generate synthetic histograms of the photon arrival times while taking into account the photon count rate, the acquisition time, the noise level, the IRF and the time-channel width (time width of the bins). An identical number of photons as those in the experimental decays are randomly distributed in time following a probability distribution that allows to mimic the fluorescence decay. Noise photons are also added randomly. They do have an equivalent probability to arrive at any time. **Figure 3-16** shows an example of fluorescence decay reconstructed with Monte Carlo. This synthetic histogram aims at reproducing a real measurement case for which it was obtained α_1=0.01311, τ_1=1.548 ns, τ_2=0.697 ns. The acquisition time was 200s and the count rate 2700 Cnt/s, with a noise of 60 cnt/s. These are conditions that may be encountered in a spray as the liquid fraction is small in the measurement volume. Comparison with experimental data leads a good agreement. A large number of histograms equivalent to **Figure 3-16 a)** are generated (typically a few thousands) and analyzed to estimate the parameters (α_1, τ_1 and τ_2) by minimizing χ^2. From these results, the standard deviation associated with the estimates of each parameter can be inferred. **Figure 3-16 b)** shows the standard deviation associated with the estimation of tau as a function of the acquisition time. Under these rather difficult conditions encountered in a spray, a few tens of seconds are required to measurement the average lifetime $\bar{\tau}$ with an accuracy of 0.05 ns.

3.3 Conclusion

This chapter is a short description of the experimental device commonly used for the study of laser-induced fluorescence in two parts.

The first part is the function of these experimental setups. Starting with the selection of a femtosecond Ti: Sapphire laser, the relevant parameters of the titanium sapphire laser are described. Then the harmonic generator is introduced, which extends the available range of laser wavelengths by halving the frequency or tuning it to one-third. The principle and function of photomultiplier tubes are then described. Finally, several filters commonly used in experiments are described, all of which serve roughly the same purpose of ultimately reducing the intensity of the received fluorescent signal by selecting the appropriate specific wavelength.

The second part is about the working principle of the TCSPC system, the fluorescence decay curves fitted by mono-exponential or multi-exponential approaches, the instrumental response function (IRF), and pile-up effects which have a significant impact on the experimentally fitted curves. Those mentioned above, are the basis for conducting the fluorescence experiment as well as analyzing the data.

3.4 Reference

[1]. Günter Toesko., Christian Dehnert. Ultrafast Laser Optics: Femtosecond laser optics combat pulse dispersion, color errors, and reflections. Retrieved October 15, 2023, from https://www.laserfocusworld.com/optics/article/16547107/ultrafast-laser-optics-femtosecond-laser-optics-combat-pulse-dispersion-color-errors-and-reflections

[2]. Akgun, U., Funk, G., Corso, J., Jia, Z., Southwick, D., Adams, L., ... & Onel, Y. (2014). Characterization of 1800 Hamamatsu r7600-m4 pmts for CMS HF calorimeter upgrade. Journal of instrumentation, 9(06), T06005.

[3]. Aiello, S., Classen, L., Giordano, V., Kalekin, O., Leonora, E., Peek, H., ... & KM3NeT collaboration. (2014, November). Characterization of the 80-mm diameter Hamamatsu PMTs for the KM3NeT project. In AIP Conference Proceedings (Vol. 1630, No. 1, pp. 118-121). American Institute of Physics.

[4]. Mortimer A., Michael W. Fluorescence Filters. Retrieved April 15, 2023, from https://www.olympus-lifescience.com/de/microscope-resource/primer/techniques/fluorescence/filters/

[5]. Lakowicz JR (2006) Principles of fluorescence spectroscopy

[6]. Becker, W., Hickl, H., Zander, C., Drexhage, K. H., Sauer, M., Siebert, S., & Wolfrum, J. (1999). Time-resolved detection and identification of single analyte molecules in microcapillaries by time-correlated single-photon counting (TCSPC). Review of scientific instruments, 70(3), 1835-1841.

[7]. Szabelski, M., Ilijev, D., Sarkar, P., Luchowski, R., Gryczynski, Z., Kapusta, P., ... & Gryczynski, I. (2009). Collisional quenching of erythrosine B as a potential reference dye for impulse response function evaluation. Applied spectroscopy, 63(3), 363-368.

[8]. Luchowski, R., Gryczynski, Z., Sarkar, P., Borejdo, J., Szabelski, M., Kapusta, P., & Gryczynski, I. (2009). Instrument response standard in time-resolved fluorescence. Review of Scientific Instruments, 80(3), 033109.

[9]. Ian (2023.Feberauray 23). How to measure the instrument response function. Time-Resolved Fluorescence. Retrieved April 20, 2023, from https://www.tcspc.com/doku.php/howto:how_to_measure_the_instrument_response_function_irf

[10]. Boens N, Qin W, Basarić N, et al (2007) Fluorescence lifetime standards for time and frequency domain fluorescence spectroscopy. Analytical Chemistry. https://doi.org/10.1021/ac062160k

[11]. Kristoffersen AS, Erga SR, Hamre B, Frette Ø (2014) Testing fluorescence lifetime standards using two-photon excitation and time-domain instrumentation: Rhodamine B, coumarin 6 and lucifer yellow. Journal of Fluorescence. https://doi.org/10.1007/s10895-014-1368-1

[12]. Stiti M, Yangpeng L, Hadrien C, et al (2021) Fluorescence lifetime measurements applied to the characterization of the droplet temperature in sprays. Experiments in Fluids 62: https://doi.org/10.1007/s00348-021-03264-x

[13]. Casadevall i Solvas X, Srisa-Art M, deMello AJ, Edel JB (2010) Mapping of Fluidic Mixing in Microdroplets with 1 μs Time Resolution Using Fluorescence Lifetime Imaging. Analytical Chemistry 82:3950–3956. https://doi.org/10.1021/ac100055g

CONTENT 4

Chapter 4 Characterization of Droplets in the Mixing Spray

The previous chapters have generally introduced some developments in spray measurements as well as some basic concepts and measurement devices for Laser-induced fluorescence (LIF). Details are as follows:

Chapter 1: It mainly describes the basic fundamental theory of laser-induced fluorescence. The phenomenon of fluorescence is first introduced, which is pointed out as an emitted light when electrons in the excited state return to the ground state. By introducing the Jablonski Diagram, the process of electron leap is presented in detail and states that energy dissipation in this leap causes the shift between the absorption spectra and emission spectra (Stokes shift). The notion of fluorescence lifetime is introduced after a short description of quantum yield and the fluorescence quenching that can lead to a change in fluorescence lifetime is explained and the fluorescence lifetimes of some commonly used fluorescent dyes are presented. The last section describes the difference between single-photon excitation and two-photon excitation in terms of absorption cross sections, as well as their respective advantages and disadvantages.

Chapter 2: It introduces the necessity and importance of studying sprays and points out how the heat and mass transfer in spray droplets are the key issues in the study of sprays. Meanwhile, it also presents some common techniques of spray measurement to detect the temperature and velocity of droplets, pointing out the corresponding advantages and disadvantages. The laser-induced fluorescence could be the distinguished way to characterize the temperature and composition of droplets.

Chapter 3: It provides a description of the experimental setup and apparatus used to perform the fluorescence measurements in this thesis. For instance, Femtosecond Ti:Sapphire generates the laser, the harmonics generator changes the wavelength, optical filters are used to select the wavelength needed, photomultiplier tubes (PMT) collect the photons and TCSPC calculates and analyzes the collected photons. In addition, problems that may be encountered when obtaining fluorescence decay curves, such as pile-up effects, are simultaneously analyzed and presented in this chapter, and the impact of instrument response function on fluorescence data analysis is also presented and considered.

This chapter (Chapter 4) serves as an introduction to the application of the laser-induced fluorescence technique in practical spray measurements. Mixing spray experiments aim to characterize the distribution of the entire spray area by measuring the lifetimes of multiple droplets.

The temperature and composition of the entire zone can be inferred by establishing the relationship between lifetime and temperature or composition. Fundamentally, the lifetimes of different fluorescent dyes vary considerably. For specific dyes like Rhodamine B, rhodamine WT, and pyrromethene 556, their fluorescence lifetimes change with temperature, whereas others such as oxazine4, eosin Y, or rhodamine 6G remain relatively constant or exhibit minimal changes in their lifetimes. Consequently, the composition can be determined by selecting various fluorescent dyes for mixed spraying, provided that the relationship between the mixing volume fraction and lifetimes of mixed dyes is known in advance. Additionally, mixing identical fluorescent dyes (with lifetimes sensitive to temperature) at different temperatures allows for the determination of temperature distribution in the mixing zone.

Prior to the mixing spray experiment, a comprehensive explanation of the selection process for fluorescent dyes is crucial and is provided herein. Additionally, we individually investigated the behavior of the selected fluorescent dyes in their respective single sprays, observing the variations in their lifetimes during these individual spray events. Simultaneously, to ensure the accuracy of the experiment, Monte Carlo methods are employed to analyze acquisition times, ambient noise, and various count rates (influenced by the laser power). This analysis facilitates a comprehensive understanding of their impact on the final results. The final step involves examining the relationship between the mixing volume fraction and the lifetimes of mixed dyes, as discussed earlier.

The chapter is organized as follows:

- Study the properties of fluorescent dyes and select the suitable fluorescent dyes.
- Investigate the lifetimes of fluorescent dyes as a function of temperature and concentration.
- Research the behavior of select dyes in the single spray and examine how other interference factors influence the lifetimes.
- Extend the measurement to the case of two mixing sprays to obtain the distribution of temperature and mixing fraction (volume fraction from each spray)

4.1 The Performance of Fluorescent Dyes

4.1.1 Selection of Fluorescent Dyes

Generally, the following factors need to be considered when selecting a fluorescent dye：

1. Excitation and emission wavelengths. It needs to be determined that the selected fluorescent dye can be excited at the appropriate wavelength of laser light. Consideration needs to be given if the band of emitted wavelengths is blocked and filtered by filters along with interfering light.

2. Photostability. For certain experiments that require the fluorescent dye to be exposed to excitation light for extended periods, it is important to ensure that the fluorescent dye is well stabilized while avoiding photobleaching (resulting in diminished fluorescence or the inability to emit light) due to excessive excitation intensity.

3. Quantum yield. A high quantum yield means that more absorbed excitation light can be converted to fluorescence emission, which means that more signals can be collected at the same time and are easier to converge when processed in TCSPC.

4. Other factors. The safety, suitability, economy, and storability of the fluorescent dye also need to be considered when selecting a suitable fluorescent dye.

These are some commonly used fluorescent dyes in the experiments of fluid, Rhodamine B, Rhodamine 6G, Rhodamine 101, Rhodamine 640, etc. of the Rhodamine family, and Eosin Y. All have high quantum yields and relative photostability, especially Rhodamine B and 6G that are commonly used for flow visualization, dye-based velocimetry techniques and laser-induced fluorescence measurements[1] [2]. Fluorescein is used for flow visualization and particle tracking velocimetry [3]. Oxazine family, such as Oxazine 1 and Oxazine 4, is typically applied to fluorescence imaging and chemistry. In addition, there are some other commonly used fluorescence dyes for imaging and flow research, we picked a few of them for the detailed analysis.

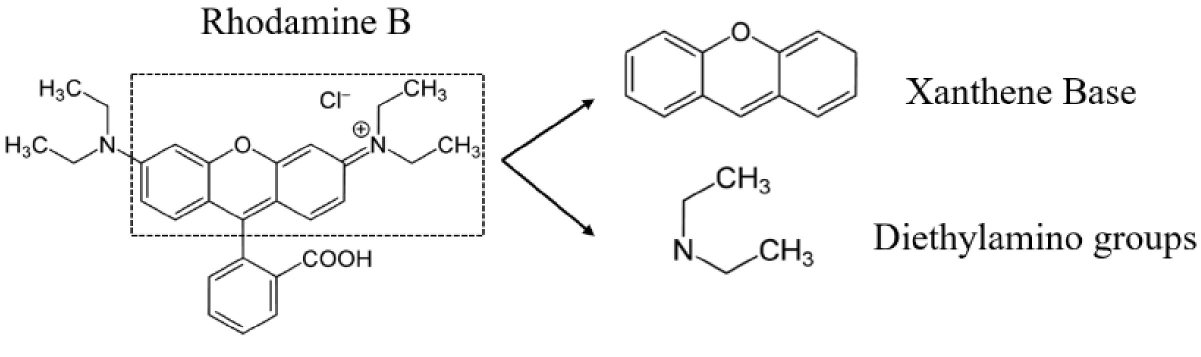

Figure 4-1 Structure of Rhodamine B

Rhodamine B is a widely used fluorescent dye, usually in the form of a reddish-purple powder or a concentrated solution dissolved in water or ethanol. Its chemical formula is $C_{28}H_{31}ClN_2O_3$ and its molar mass is 479.01 g/mol. As a xanthene dye, the specific structure of Rhodamine B is shown in (**Figure 4-1**).

One of the distinguished properties of Rhodamine B is its intense fluorescence signal, which is often used for high-sensitivity detection and imaging because of its high quantum yield that converts more absorbed photons into emitted photons. Typically, Rhodamine B can absorb the light in the green to orange region of the visible spectrum, from 510nm to 550 nm, and emits bright pink to red fluorescence in the range of approximately 570 to 610 nm. However, it is worth noting that the exact absorption and emission spectra of Rhodamine B can vary slightly depending on the specific experimental conditions, such as solvents.

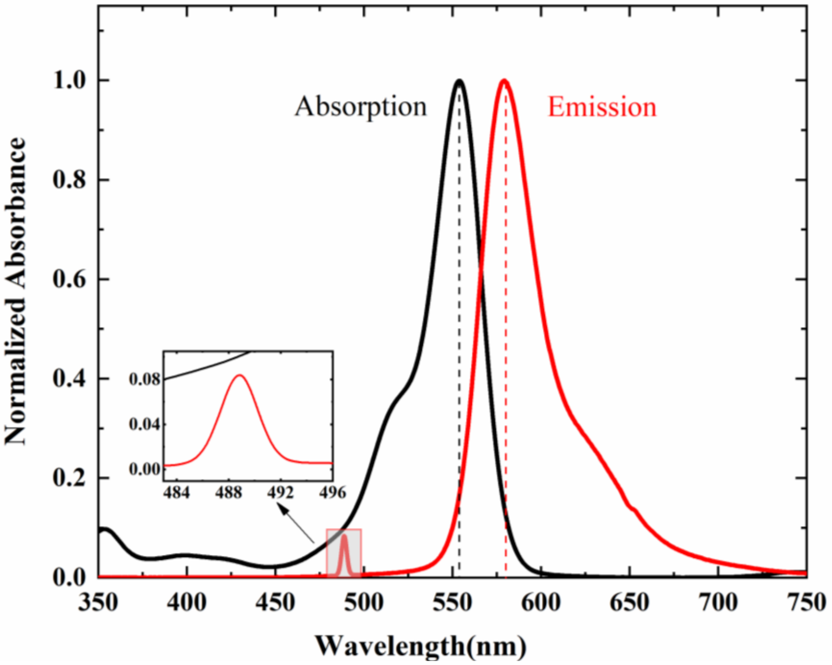

Figure 4-2 Absorption and emission spectrum of Rhodamine B in water

(**Figure 4-2**) shows the absorption spectrum and emission spectrum of Rhodamine B in water. Generally, in spectroscopy, there are two types of spectra. One is the fluorescence absorption spectrum, which represents the process by which a substance absorbs photon energy of a specific wavelength and it leads to electrons leaping to higher energy states when exposed to the excitation light; the other is the emission spectrum, which refers to the range of wavelengths of electromagnetic radiation emitted by a substance when it undergoes a transition from an excited state to a lower energy state. It is the opposite of absorption, where the substance emits photons rather than absorb them.

Both of these two spectra are usually expressed in terms of wavelength on the x-coordinate, and absorption intensity or absorbance on the y-coordinate. The position and intensity of the absorption or emission peak can be shown in the spectrum. The shape and characteristics of the fluorescence spectrum can provide information about molecular structure, energy levels, and electronic excited states.

As shown in the (**Figure 4-2**), y-coordinate is the normalized absorbance, which shows the ability of the amount of light absorbed by the Rhodamine B solution, it is also called optical density, which is defined as the logarithm of the ratio of incident to transmitted radiant power through a sample. The x-coordinate is the wavelength of the light. In the aqueous solution, the absorption spectrum of Rhodamine B rises sharply from 500nm where the absorbance is close to 0.2, at 554nm, it gets to the peak value of absorbance. This means that the maximum fluorescence signal can be collected if the Rhodamine B is excited at 554nm. After reaching the peak, the absorbance starts to decline steeply, and at 600nm, it is close to 0. Even if the wavelength is increased further, the Rhodamine B still fails to absorb the excited light energy. For the emission spectrum of Rhodamine B, the main region is concentrated between 550nm and 700nm, with a peak at 579nm. A minor peak appears between 484nm and 492nm may be caused by the excitation light. It is worth noting that the exact absorption and emission spectra of Rhodamine B can vary slightly if it is dissolved in other solvents, or the pH of solutions alters.

In different solvents, the polarity, viscosity, or other properties of the medium surrounding the fluorescent dye may be different [4][5]. Taking Rhodamine B as an example, the polarity influences the transition energy and solubility of Rhodamine B. Viscosity affects the relaxation kinetics of the excited state of Rhodamine B (high-viscosity solvents promote the non-radiative relaxation process, which can broaden or change the emission spectra); in addition, the electronic structure and the energy levels can be affected by the different solvents (since all the fluorochromes in this chapter were dissolved in water, the effect of solvents on the fluorescence lifetimes will be discussed in the next chapter). Even in the same solvent, the pH value can lead to changes in the absorption and emission spectra due to changes in the protonation state of the dye molecule (which can lead to changes in its electronic structure). In general, the higher the pH, the more red-shifted the absorption and emission spectra are, the more Eosin Y tends to absorb at longer wavelengths and fluoresce at longer wavelengths; correspondingly, the lower the pH, the more blue-shifted the absorption and emission spectra are.

One remarkably significant property of Rhodamine B is that, unlike some other dyes in the rhodamine family, the fluorescence lifetime of Rhodamine B varies with temperature. The lifetimes of Rhodamine B have a sharp drop as temperature increases. This dependence is attributed to the flexible rotating bonds of the chemical structure attached to the xanthene base[6], as shown in

(**Figure 4-1**). This is possibly due to the increase in rotation of the diethylamino groups, which causes the formation of an alternative charge-shift quenching channel and a drop in the quantum yield[7]. Therefore, if we need to perform experiments that require obtaining temperatures, Rhodamine B offers us a possibility.

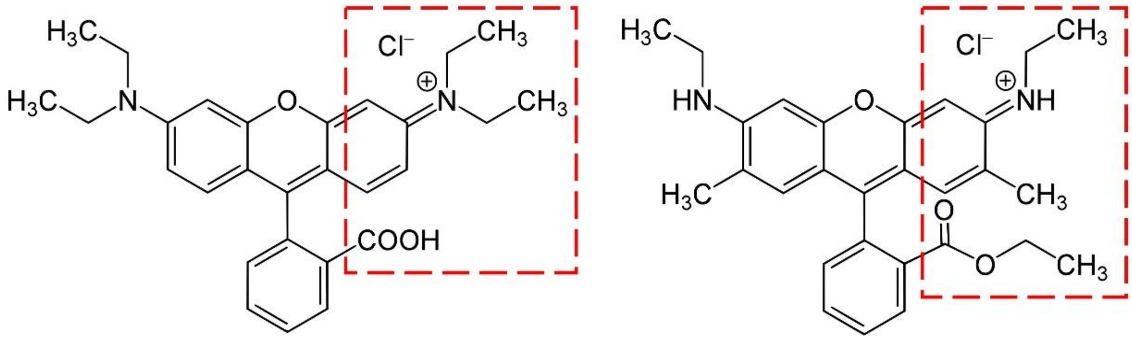

(a) Rhodamine B (b) Rhodamine 6G

Figure 4-3 Comparison of Rhodamine B and rhodamine 6G

Another notable fluorescence dye is Rhodamine 6G, which typically appears as a dark reddish purple or brown crystalline solid. Its chemical formula is $C_{28}H_{31}N_2O_3CI$ and the molar mass is 479.01 g/mol. Although the chemical formulas of rhodamine 6G and Rhodamine B are almost identical, they are distinct compounds with different molecular structures and properties. (**Figure 4-3**) is the comparison of the structure of Rhodamine B and Rhodamine 6G. They have the same xanthene base group, but Rhodamine 6G has two methyl groups (CH_3) attached to it whereas Rhodamine B has only diethylamino. Rhodamine 6G is compatible with a wide range of solvents, like butanol, ethanol, methanol, isopropanol, and so on.

Rhodamine 6G is well known for its high quantum yield (around 0.95) and photostability[8], and is therefore commonly used as a laser dye. Another feature of Rhodamine 6G is its broad absorption spectrum. It can be excited by a variety of light sources. (**Figure 4-4**) shows the absorption and emission spectrum of rhodamine 6G in water. As shown, Rhodamine 6G can be excited between 450nm and 575nm, with a peak at around 525nm. The wavelength of fluorescence that it emits ranges from 510nm to 675nm, and more fluorescence signal exists at around 555nm. Rhodamine 6G absorbs light at wavelengths from 450nm to 525nm more readily than Rhodamine B. This means that If they are exposed to the same laser light, Rhodamine 6G emits much more fluorescent signal than Rhodamine B, but the emission spectra of the two dyes are very similar.

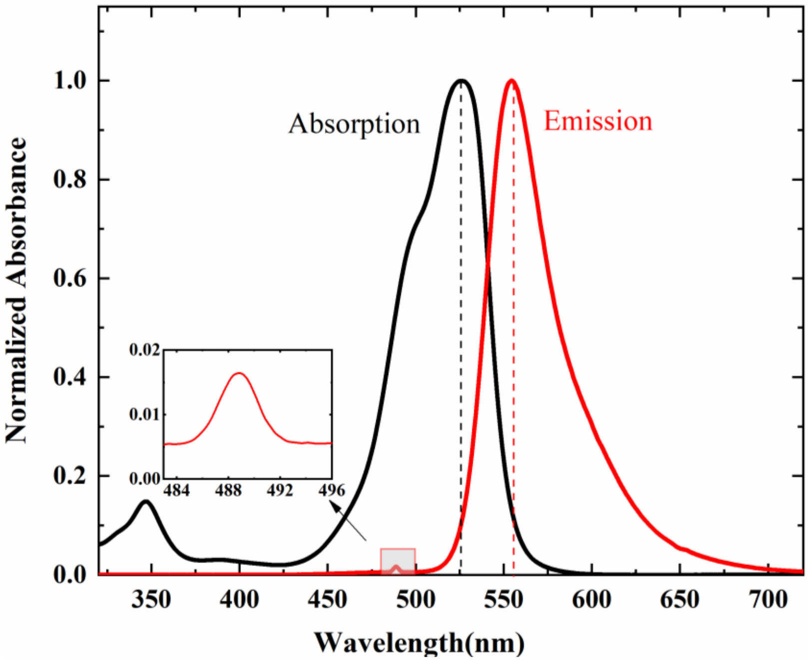

Figure 4-4 Absorption and emission spectrum of Rhodamine 6G in water

Eosin Y is another interesting dye, which belongs to the Eosin family. It is a tetrabromo derivate of fluorescein with a slight yellow color [9]. The powder of Eosin Y is red, and its density is around 1.018 g/cm^3. It is soluble in most solvents like ethanol, methanol, iso-propanol, and so on. The chemical formula is $C_{20}H_6Br_4Na_2O_5$ and the molar mass is 647.8905 g/mol and structure of Eosin Y is shown in (**Figure 4-5**).

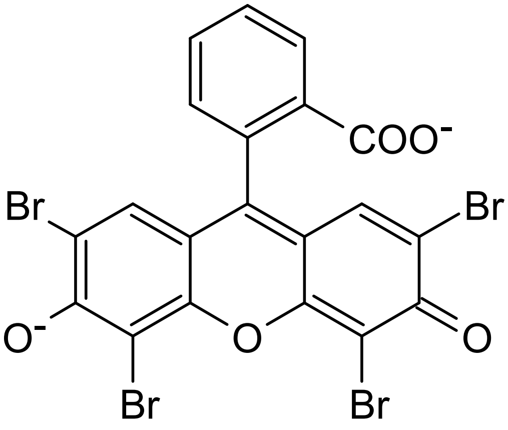

Figure 4-5 Structure of Eosin Y

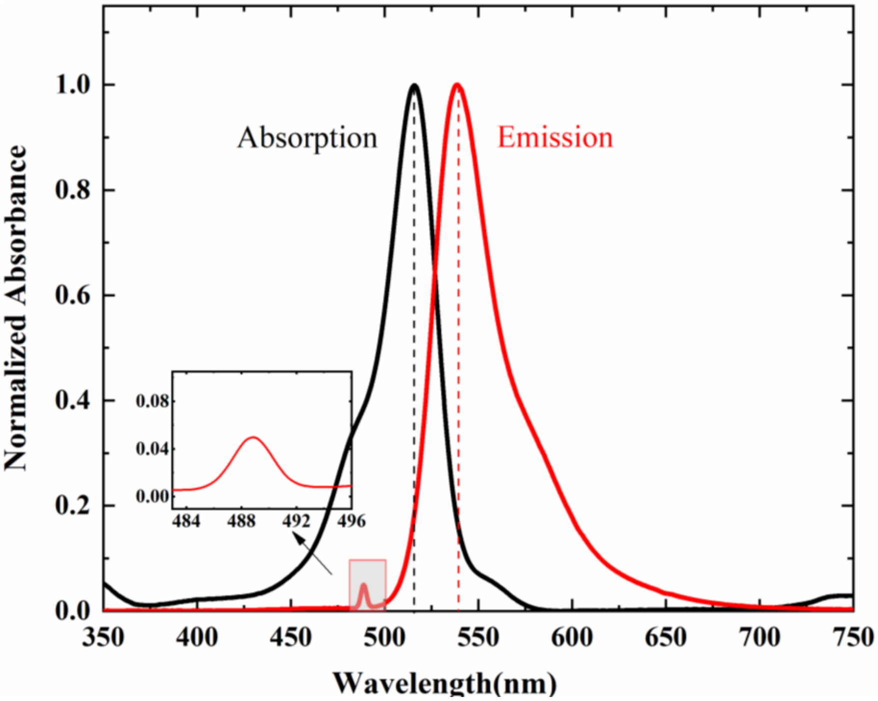

Figure 4-6 Absorption and emission spectrum of Eosin Y in water

The quantum of Eosin Y is around 0.67 [10].The absorption spectrum of Eosin Y in water is shown in (**Figure 4-6**), the wavelength of main excitation zone is 450nm to 570nm, the max value of absorbance is around 520nm, and for the excitation spectrum, it ranges from 500nm to 675nm, the peak is around 540nm.

Except for the fluorescence dyes that we discussed above, we also test the absorption and emission spectra of several fluorescent dyes, such as Rhodamine 640(also called Rhodamine 101), which are shown in (**Figure 4-7 and Figure 4-8**). From the experimental results, the fluorescence absorption spectra of Pyrromethene 556, Oxazine 4 and Rhodamine 640 are in the range of 400 nm to 525 nm, 500 nm to 650 nm and 475 nm to 620 nm, respectively. The corresponding emission spectra are categorized into 480 to 700 nm, 600 to 850 nm and 560 nm to 775 nm.

It is necessary to state here that the concentration of the solution has a strong influence on the measured absorption and emission spectra.

For the absorption spectrum, a high concentration solution leads to [11][12]:

1. Broadening of the absorption peak. Intermolecular interactions, molecular aggregation, the existence of many species in distinct settings, or other factors can all contribute to this widening. Certain elements may alter energy levels and lead to a wider absorption profile.

2. Saturation effects. After a certain threshold, raising the concentration can have saturation consequences. When a substance's absorptive capacity is reached and its concentration continues

to rise without producing more absorption, this is known as saturation. In larger doses, saturation might result in a plateau or a reduction in the strength of absorption.

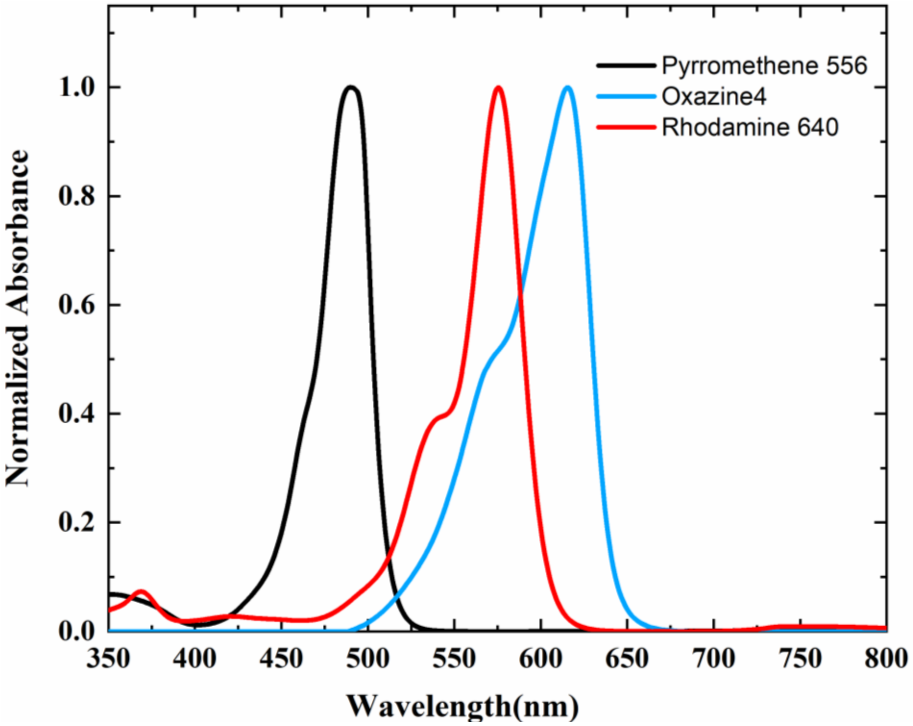

Figure 4-7 Absorption spectrum of (Pyrromethene 556, Oxazine4 and Rhodamine 640) in water

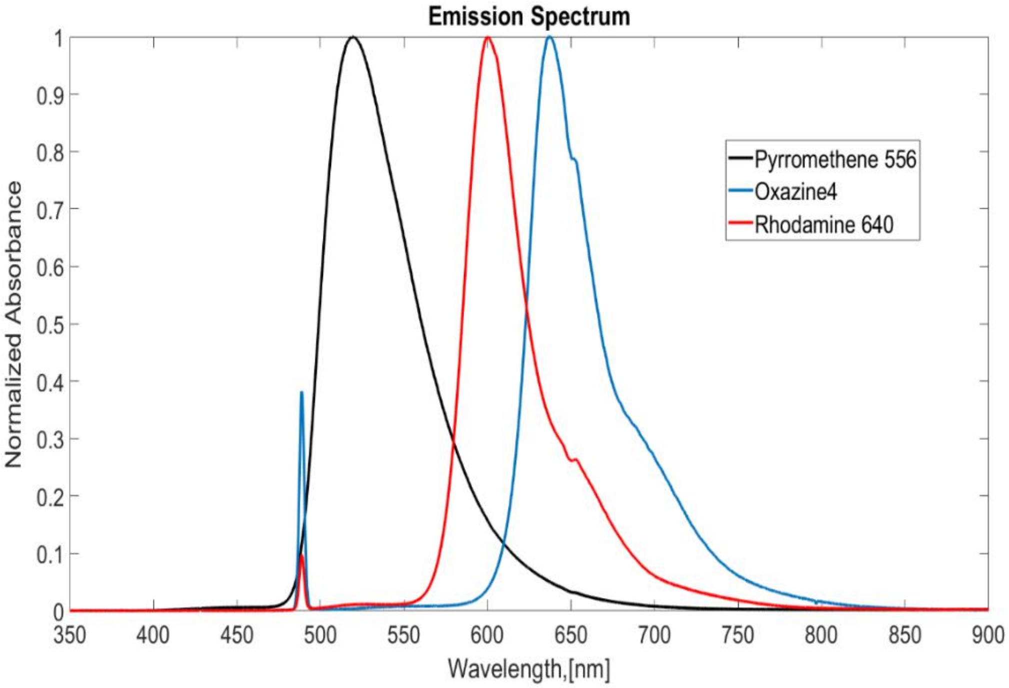

Figure 4-8 Emission spectrum of (Pyrromethene 556, Oxazine4 and Rhodamine 640) in water

For the emission spectrum, too high a solution concentration leads to:

1. Quenching. At higher concentrations, the possibility of interactions between emitting substances also increases, which can lead to quenching, where the emission intensity decreases due to non-energy transfer processes, such as collisional deactivation or energy transfer to other molecules in the solution. Correspondingly, the fluorescence signal will undergo a reduction.

2. Aggregation Effects. The material in solution may occasionally undergo self-aggregation or form aggregates with other molecules at greater concentrations. The emission spectrum may shift as a result of these aggregates' differing electronic characteristics from those of the individual molecules. This may cause the form of emission peaks to move, widen, or otherwise alter.

In all the spectroscopic experiments that we mentioned before, the concentration of the solution used for the absorption spectrum is essentially 1×10^{-5}mol/L while it is 5×10^{-6}mol/L for the emission spectrum. In the experiment, we notice that 1×10^{-5}mol/L is good enough for absorption, which ensures sufficient absorbance and meanwhile no saturation. For the emission spectrum, the spectrometer received an excessive signal (high intensities observed) at this concentration, so it has been reduced to 5×10^{-6}mol/L.

(Figure 4-9) shows the absorption spectrum of Rhodamine 640 at different concentrations. For these three different concentrations of Rhodamine 640, the higher concentration correspond to a larger absorption peak, 5×10^{-5}mol/l, 3×10^{-5}mol/l, and 1×10^{-5}mol/l corresponds to the peaks of approximately 3.0, 2.85, and 1.0, respectively. However, despite the different concentrations, the peak absorption wavelengths correspond to approximately 575nm. The shape of the peak changes at high concentrations——it becomes much flatter rather than having a clear protrusion, probably because of the divergence at high concentrations. With no obvious notch, the shape of absorption spectrum smooths a bit at 550nm then rises sharply to a peak. Therefore, it is of importance to make sure that there are sufficient absorbance and no divergence meanwhile, avoiding the effect on the shape of the spectrum due to a high concentration.

Several fluorescence dyes commonly used in the laboratory and their respective absorption and emission spectra have been described above. And one purpose of our experiment is to characterize the composition of the mixing spray by fluorescence lifetime. So, it is needed to be determined that the signal of these two dyes that excited by the same wavelength laser can be collected sufficiently and at the same time, that temperature has no effect on the lifetimes. The second is to obtain the temperature field distribution of mixing spray by mixing the same fluorescent dyes at different temperatures. By analyzing the relationship between the temperature and fluorescence lifetime, we can derive the temperature of droplets in the mixing spray.

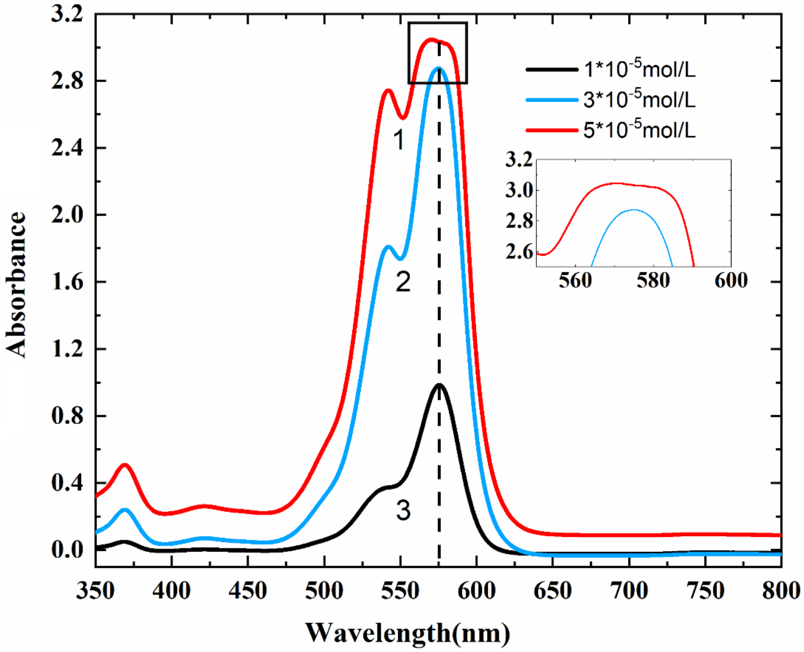

Figure 4-9 Absorption spectrum of Rhodamine 640 in different concentrations

As displayed in **Table 4-1**, we conducted measurements of the lifetimes of the fluorescent dyes mentioned earlier at room temperature (approximately 20°C) and around 50°C. It is evident that Eosin Y, Rhodamine 6G, and Rhodamine 640 exhibit temperature-independent lifetimes, whereas Pyrromethene 556 and Rhodamine B display temperature-dependent behavior. The lifetimes of Rhodamine B decline from 1.70ns to 0.70ns while the Pyrromethene 556 has a reduction of 0.83ns when temperature rises from 20°C to 50°C. In contrast to Pyrromethene 556, Rhodamine B displays greater sensitivity to temperature variations, rendering it a common choice as a temperature indicator in fluorescence studies.

Table 4-1 Lifetimes of several common fluorescent dyes (in water)

Fluorescent Dyes	Two-Photon λ_{ex}(nm)*	Lifetimes (20°C)	Lifetimes (50°C)
Eosin Y	700nm	1.11ns	1.19ns
Oxazine 4	700nm	2.49ns	2.50ns
Rhodamine B	800nm	1.70ns	0.70ns
Rhodamine 6G	700nm	3.80ns	3.82ns
Rhodamine 640	980nm	4.22ns	4.26ns
Pyrromethene 556	980nm	4.53ns	3.70ns

* The wavelength of two-photon excitation is theoretically about twice the wavelength of single-photon excitation, but in practice it will fluctuate around twice the wavelength.

Consequently, Rhodamine B is selected as the dye for investigating the temperature of mixing spray. Eosin Y and Rhodamine 6G are chosen for studying the composition of the mixing spray due to their robust fluorescence signals at the identical excitation wavelength and their distinctive, temperature-independent lifetimes.

4.1.2 Temperature and Concentration Calibration in Cuvettes

Before studying the mixing of two spray, the temperature response of a few dyes was examined in detail. In this section, we report the results obtained for Rhodamine B (RhB), Rhodamine 6G (Rh6G) and Eosin Y (EY). A series of fluorescence lifetimes are recorded by heating the cuvette at the corresponding temperatures.

All the fluorescent dyes are dissolved in water and concentration are set as 1×10^{-5}mol/l. The cuvettes are also stirred to ensure that the temperatures of solutions are uniform when heated through a thermal resistance. A thermocouple is positioned in the cuvette to measure the temperature.

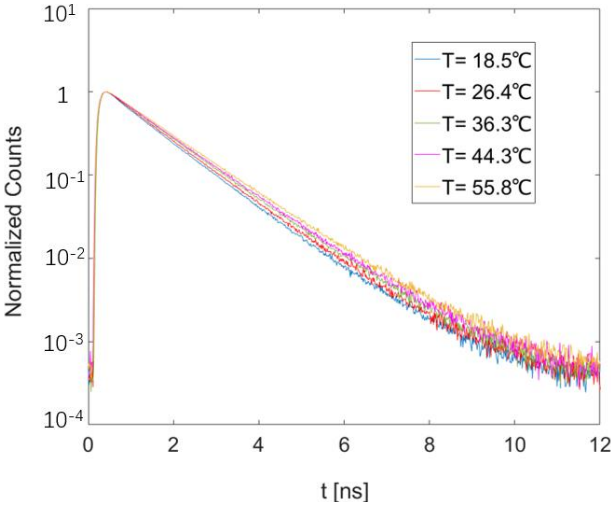

Figure 4-10 Fluorescence decay of Eosin Y at different temperatures

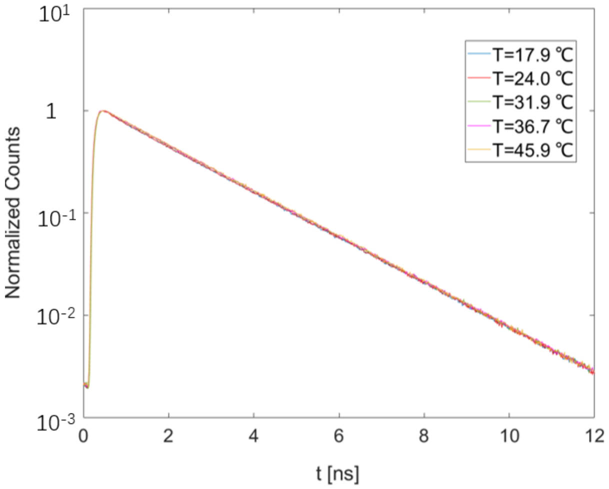

Figure 4-11 Fluorescence decay of Rhodamine 6G at different temperatures

Figure 4-10 and **Figure 4-11** shows the fluorescence decay of EY and Rh6G for different temperatures. It can be observed that the slope of the decay curve for EY exhibits a very slight decrease with rising temperature, but overall, it remains relatively constant. In contrast, the decay curve for Rh 6G remains unchanged when varying the temperature in the cuvette.

Figure 4-12 depicts the fluorescence decay of Rhodamine B at different temperatures within the detection band of 570 nm to 580 nm. It is evident that the rate of decay accelerates as temperature increases. As explained in **Chapter 1**, the reciprocal of the slope of the decay curve corresponds to the fluorescence lifetime. The lifetime at 51.2°C is about half that observed at 20.2°C. This behavior is in good agreement with the literature.

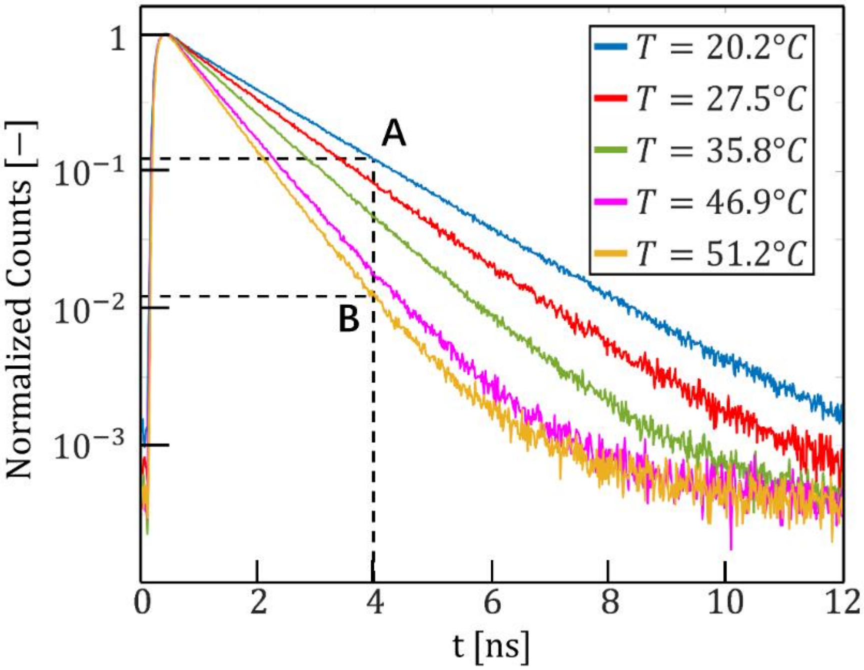

Figure 4-12 Fluorescence decay of Rhodamine B at different temperatures

Figure 4-13 depicts the results of simulations using mono-exponential and bi-exponential equations for the decay curves of these three fluorescent dyes. Time convolution with the instrument response function (IRF) of the TCSPC measurement system was considered when fitting with mono-exponential or bi-exponential functions.

As can be seen from A) and B), for rhodamine B, the biexponential decay agrees with the experimental decay, whereas the mono-exponential always has some deviation, especially when the temperature is increased. The goodness-of-fit parameter χ^2 for the mono-exponential is about 13.9 at 60 °C, whereas for the bi-exponential simulation of the decay curve it is only 1.9. Therefore, for rhodamine B, the goodness-of-fit parameter χ^2 for the bi-exponential simulation is smaller than that for the mono-exponential at both high and low temperatures, around 1 (A smaller χ^2 implies that the model's predicted values are closer to the actual decay), so we chose the biexponential to simulate the decay curve of Rhodamine B to obtain the lifetime.

By compiling the data obtained at different temperatures, a correlation was established for the coefficients involved in the biexponential model of RhB. Knowing the average lifetime τ, the fluorescence decay of RhB can be evaluated using the following formula [13]:

$$\phi(a,\tau) = a\, exp(-t/t_1) + (1-a)\, exp(-t/t_2) \qquad (4-1)$$

where $a = 0.9901 \cdot 10^{-1} \cdot \tau(ns) + 0.04371$, $t_2(ns) = -0.411765 \cdot \tau(ns) + 1.4594$ and $t_1(\mathrm{ns}) = a^{-1} \cdot \tau(\mathrm{ns}) + (1 - a^{-1}) \cdot t_2(ns)$. In this expression, τ is the mean fluorescence lifetime**.** The above correlation is valid in the range 0.6 ns $\leq \tau \leq$ 2 ns). For Rhodamine 6G, the decay curves of mono-exponential or bi-exponential simulations almost overlap, making both acceptable, while bi-exponential simulations are more suitable for eosin Y.

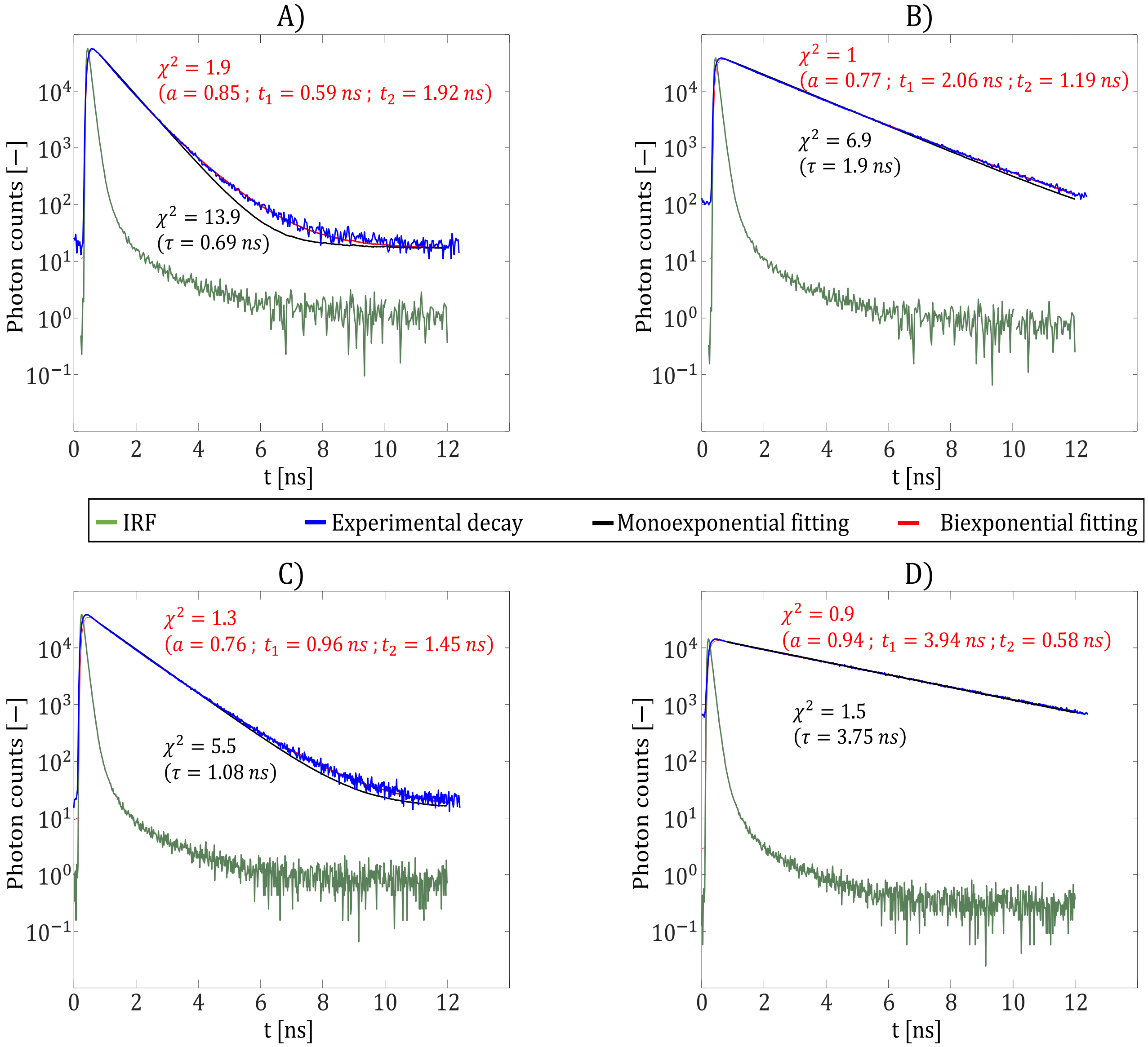

Figure 4-13 Fluorescence decays of Rhodamine B A) at 60°C and B) at 19°C; Eosin Y C) at 20°C and Rhodamine 6G D) at 20°C. The decays are fitting by a mono-exponential and a biexponential functions.

Figure 4-14 shows the evolution of the fluorescence lifetime with temperature for the three fluorescent dyes. For Rh6G and EY, lifetimes are weakly sensitive to temperature. Lifetime of

Rh6G fluctuates slightly around 3.80ns, while that of EY increases a little but about 0.10 ns when temperatures increase from 20℃ to 60℃. These two dyes, Rh6G and EY, can be considered as temperature independent. Meanwhile, because of their lifetimes are very different, Rh6G and EY are good candidate to evidence the mixing of two sprays, one seeded with Rh6G and the other with EY, with no interference with a possible change in temperature of the droplets.

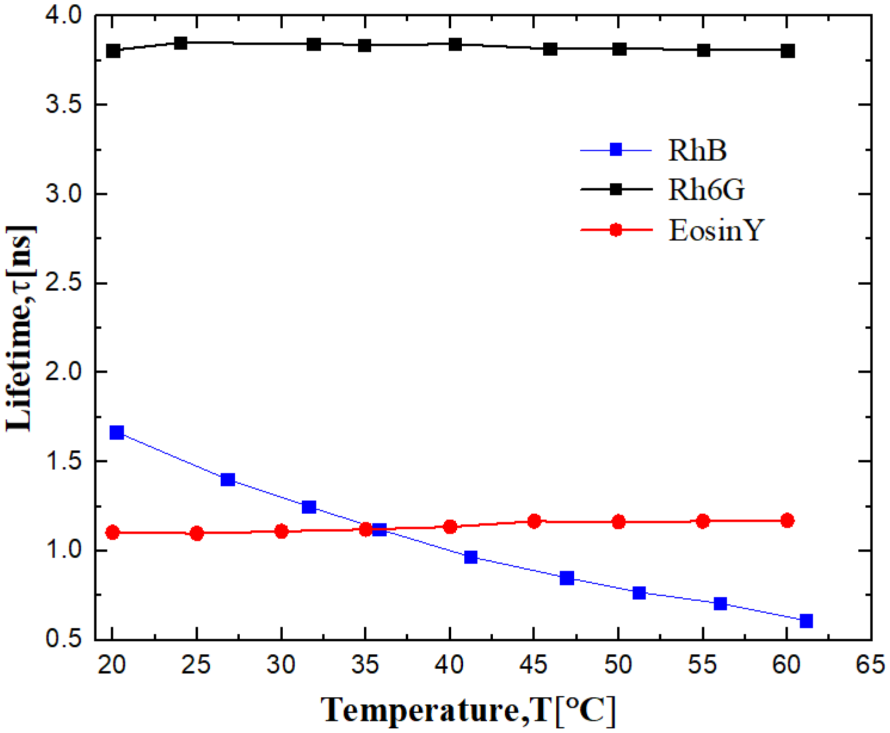

Figure 4-14 Fluorescence lifetimes variation with temperature (Rhodamine B, Rhodamine 6G and Eosin Y in water)

For Rhodamine B, the lifetimes have sharply dropped from 1.70ns at 20℃ to 0.6 ns at 61℃, which undergoes a significant change with temperature compared with others. The temperature dependence of fluorescence lifetime is congruent to Arrhenius law equation $(4-2)$, given by [14]:

$$\frac{1}{\tau_{au}(T)} = exp\ (\frac{-E_a}{RT}) \qquad (4-2)$$

where E_a means the activation energy for the reaction, τ_{au} is fluorescence lifetime and R is the universal gas constant (8.314 J / mol).

Referring to our experiment result, the relation between $In(\tau_{au})$ and $1/\,RT$ can be described as (**Figure 4-15**) and the equation $(4-3)$:

$$In(\tau_{au}) = \frac{19890}{RT} - 7.631 \qquad (4-3)$$

Thus, in the case where the independent variable is only temperature, if the lifetime of rhodamine B is obtained, the temperature can be inferred.

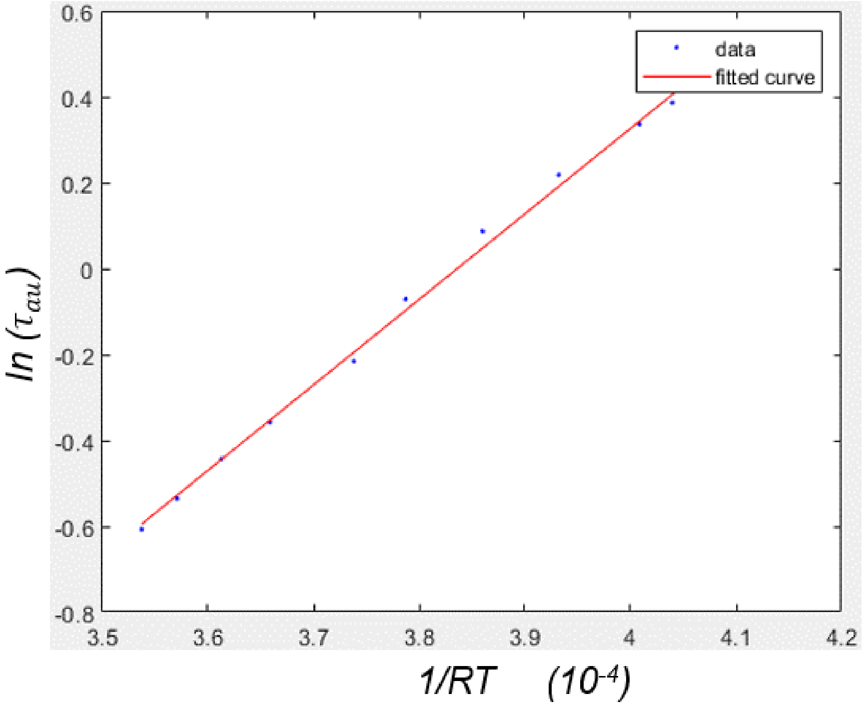

Figure 4-15 Relation between $In(\tau_{au})$ and 1/ RT of Rhodamine B in water

Since the concentrations for the temperature calibration experiments were all 1 × 10^{-5}mol/l, the effect of solution concentration on fluorescence lifetime can be excluded.

Figure 4-16, Figure 4-17 and **Figure 4-18** respectively present the evolution of the fluorescence lifetime of Rhodamine 6G, Eosin Y, Rhodamine B as a function of concentrations, respectively. The lifetimes are normalized by their maximum value observed for the lowest concentrations. When the concentration is below around 10^{-3} mol/L, the lifetime almost remains constant at its maximum value, but it decreases sharply when the concentration rises from 10^{-3} mol/L to 10^{-1} mol/L.

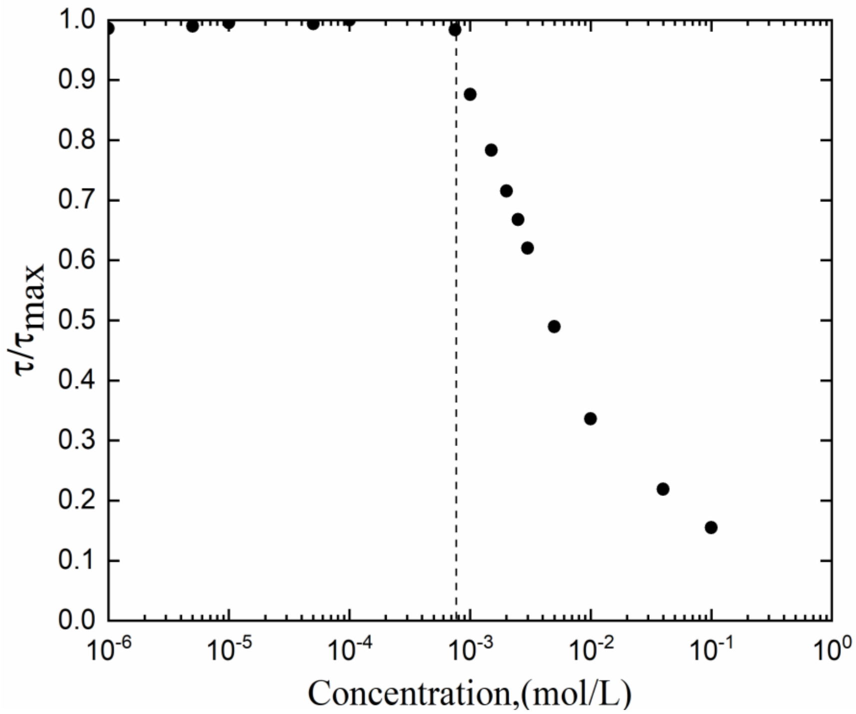

Figure 4-16 Effect of concentration on the lifetime of Rhodamine 6G in water (20℃)

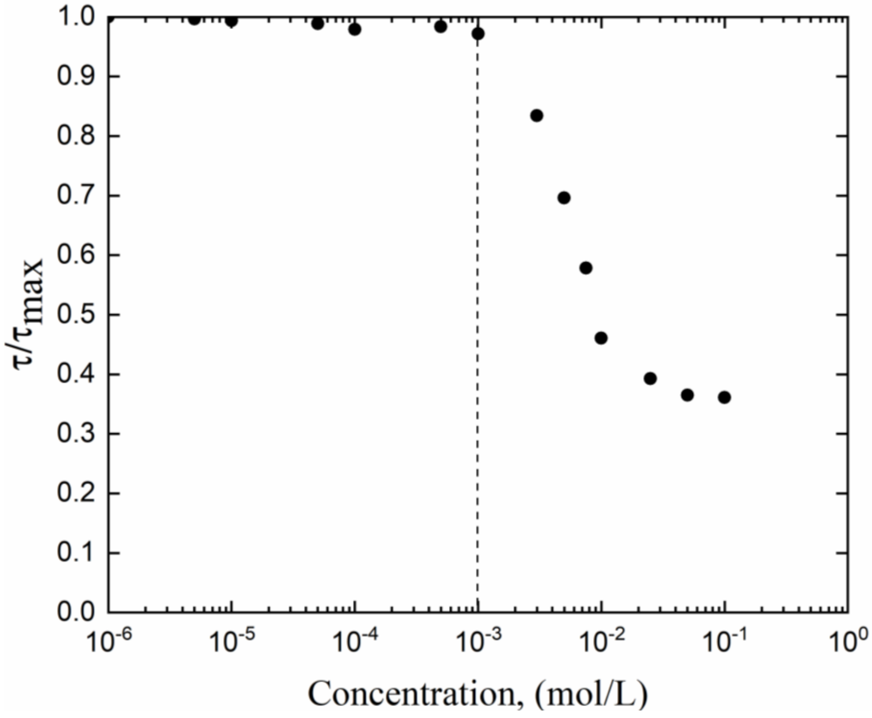

Figure 4-17 Effect of concentration on the lifetime of Eosin Y in water (20℃)

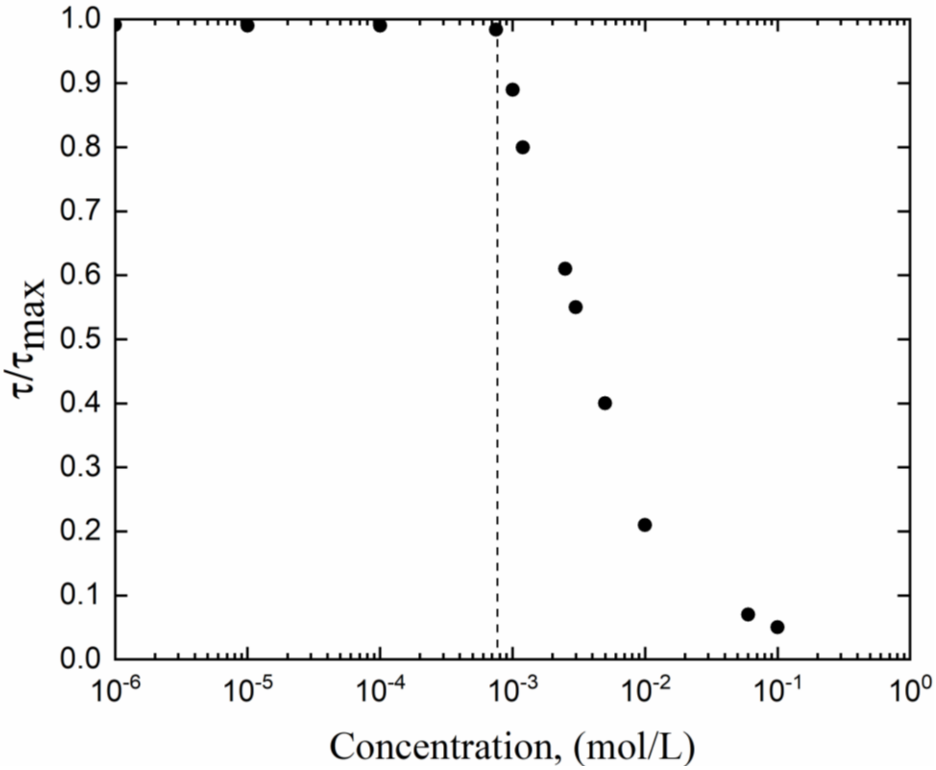

Figure 4-18 Effect of concentration on the lifetime of Rhodamine B in water (20°C)

As discussed before, dye molecules in high concentrations lead to a shortening of the fluorescence emission, which is known as concentration quenching or self-quenching and is mainly attributed to the resonance energy transfer process between the fluorophores (homo-transfer) [15]. The underlying mechanism of concentration quenching involves the formation of excited-state dimers or aggregates, where the energy from the excited state of one molecule is transferred to a neighboring molecule without emitting a photon. As a result, the fluorescence emission is decreased, and the fluorescence lifetime is shortened. Also, the high concentration can deform the emission spectrum significantly in energy positions as well as relative intensities of different peaks, which also can be a problem.

Therefore, to minimize concentration quenching and maintain the desired fluorescence properties, it is necessary to do the concentration calibration experiment, which typically involves selecting an appropriate concentration range that avoids these detrimental effects of quenching. And all the solution concentrations of our experiment are below the 10^{-3}mol/L to avoid quenching.

Table 4-2 Lifetime of Rhodamine B as a function of temperature at different concentrations

A: C_{RhB}=1×10^{-4}mol/l		B: C_{RhB}=1×10^{-5}mol/l		C: C_{RhB}=5×10^{-5}mol/l	
Temperature	Lifetime	Temperature	Lifetime	Temperature	Lifetime
18.8℃	1.73 ns	18.8℃	1.72 ns	19.0℃	1.70 ns
28.3℃	1.34 ns	27.5℃	1.34 ns	30.8℃	1.27 ns
37.1℃	1.08 ns	35.5℃	1.14 ns	40.7℃	0.95 ns
47.4℃	0.81 ns	45.5℃	0.91 ns	49.3℃	0.77 ns
55.4℃	0.68 ns	53.1℃	0.72 ns	59.3℃	0.59 ns
61.5℃	0.56 ns	62.4℃	0.57 ns	65.1℃	0.52 ns

Table 4-2 and **Figure 4-19** illustrate the trend of fluorescent lifetimes of Rhodamine B with temperatures at three different concentrations, where the simulated curves are in exponential form. The lifetimes nearly keep constant at the corresponding temperature even the concentration varies. Hence, for these three concentrations, they have no impact on the lifetime, corresponding to the plot (**Figure 4-18**) that we obtain.

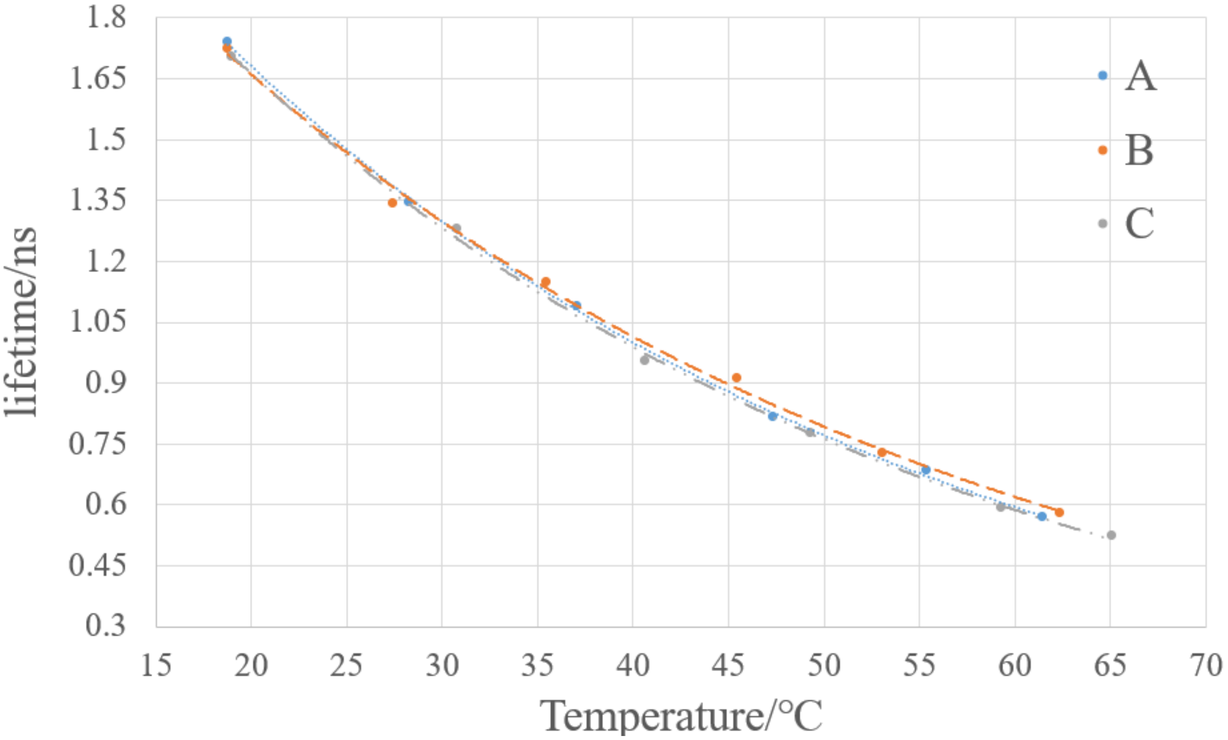

Figure 4-19 Lifetime variation of rhodamine B with temperatures at different concentrations

4.1.3 Peformance of Rhodamine B in a Single Spray.

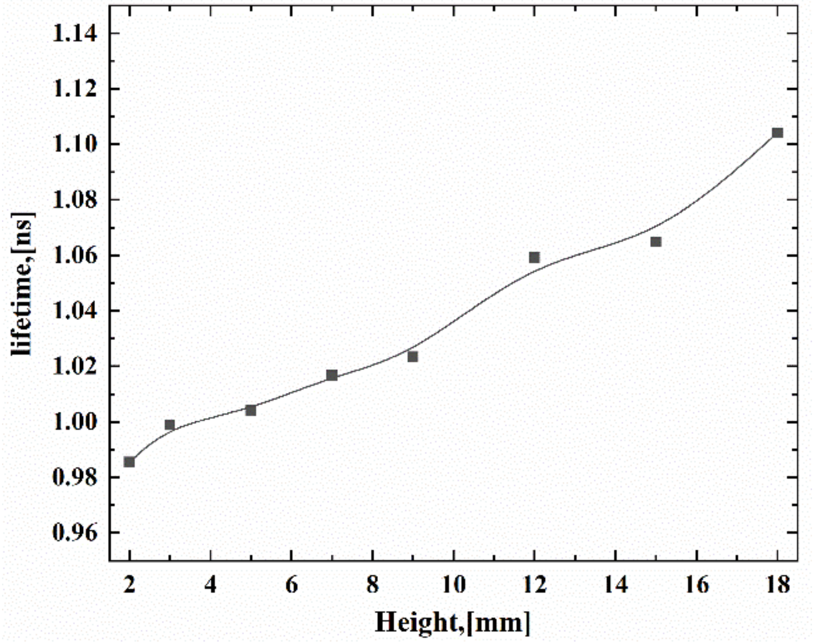

Figure 4-20 Lifetimes of Rhodamine B at the different heights

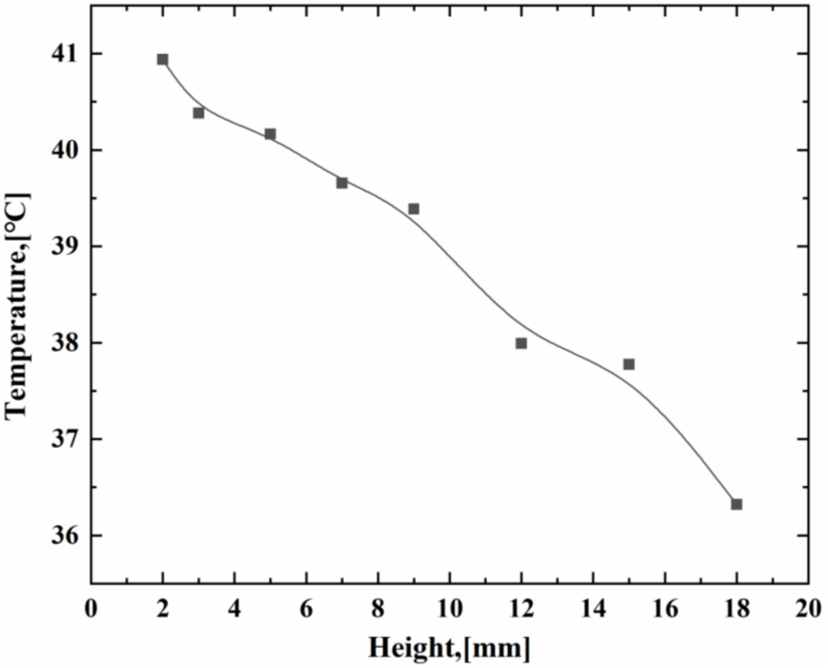

Figure 4-21 Lifetimes of Rhodamine B at the different heights

All of the experiments that we discussed above are done in the cuvettes. It is necessary to see the performance of those fluorescence dyes in a single spray. Due to its temperature-dependent property, an experiment with Rhodamine B is done to assess the reliability of the measurement technique in a single spray. The whole experiment is performed under two-photon excitation to avoid light scattering and obtain a better fluorescence signal.

A full cone spray is generated by a pressure-swirled atomizer (Danfoss oil nozzle, angle 30° type S, 0.50 US gal/h, 1.87kg/h). Before entering the nozzle, the liquid flows across a heat exchanger, which allows to control the injected liquid temperature. A K-type thermocouple inserted in the inlet pipe of the spray nozzle is used to determine the liquid injection temperature. The entire spraying system is mounted on translation stages to move the spray relatively to the optics and perform measurements at different positions.

Figure 4-20 and **Figure 4-21** show the lifetimes and temperatures of droplets at different heights along the middle of the spray axis. The acquisition time of every point is around 30s to be sure that measurements are fully converged. Through the relation between the temperature and lifetime of Rhodamine B, we can estimate the temperatures of droplets at the corresponding positions. The hot droplets are progressively cooled due to the heat transfer with the air at lower temperatures. It can be seen that the lifetime increases from 0.98 ns to 1.10ns which corresponds to a temperature reduction from 40.9 °C to 36.3°C when the height increases from 2mm to 18mm. These values are in line with the results obtained in the previous study [16].

4.2 Model of Mixing Spray and Calibration of Mixing in a Cuvette

After doing some calibration experiments of temperature and concentration, and testing the performance of a single spray of Rhodamine B, the following content is about the simulations and experiment of mixing spray. All experiments of mixing spray are also performed under two-photon excitation.

4.2.1 Mixing Models

In general, for two-photon excitation, the fluorescence signal follows the equation $(4-4)$:

$$F(t) = C\ \delta\ V_m\ \phi(t)\ k\ I_0^2 \qquad (4-4)$$

where F means fluorescence signal, δ is the molar absorptivity of the two-photon absorption process, ϕ is fluorescence quantum yields, V_m is the volume of measurement, k represents the efficiency of transmission that the detector receives from the fluorescence (It is a parameter that can be increased by solid angle (Ω) of detector and decreased by the filters) and I_0 represents the intensity of incident laser (the fluorescence signal is proportion to the square of intensity in two-photon absorption).

For the mono-exponential behavior, the fluorescence quantum yields can be expressed as below $(4-5)$:

$$\phi = exp\left(-{}^{t}/_{\tau}\right) \qquad (4-5)$$

where τ is the actual lifetime and τ_{n0} represents the natural lifetime.

The total fluorescence emitted by the sample $(\overline{F}_1)$ can be calculated by integrating the equation of the fluorescence signal over a time domain $(4-6)$:

$$\overline{F} = \int_0^{+\infty} F(t)\, dt \qquad (4-6)$$

Then, the total signal over a time domain can be written as $(4-7)$:

$$\overline{F} = \int_0^{+\infty} C\delta\, exp\left(-{}^{t}/_{\mathrm{\tau}}\right) V_m k I_0^2\, dt = C\,\delta\,\tau V_m k I_0^2 \qquad (4-7)$$

For the two signals respective from fluorescent dye 1 and dye 2, excited by the same laser and instruments (which means the intensity of light I_0, k the efficiency of transmission and the volume of excitation V_m keep the same), the equations can be rewritten $(4-8)$:

$$\begin{cases} F_1 = C_1\delta_1\tau_1 V_m k I_0^2 \\ F_2 = C_2\delta_2\tau_2 V_m k I_0^2 \end{cases} \qquad (4-8)$$

Introducing $F(t) = F_1(t) + F_2(t)$, which represents the sum of the signals of two different dyes, the equation can be $(4-9)$:

$$F(t) = [C_1\delta_1\, exp\left(-{}^{t}/_{\tau_1}\right) + C_2\delta_2\, exp\left(-{}^{t}/_{\tau_2}\right)]\, V_m k I_0^2 \qquad (4-9)$$

By introducing $\alpha_1$and α_2 :

$$\alpha_1 = C_1\delta_1\,, \alpha_2 = C_2\delta_2 \qquad (4-10)$$

The equation $(4-9)$ can be $(4-11)$:

$$F(t) = [\tfrac{\alpha_1}{\alpha_1+\alpha_2} exp\left(-{}^{t}/_{\tau_1}\right) + \tfrac{\alpha_2}{\alpha_1+\alpha_2} exp\left(-{}^{t}/_{\tau_2}\right)]\, V_m k I_0^2(\alpha_1 + \alpha_2) \qquad (4-11)$$

By introducing the average coefficient α:

$$\alpha = \frac{\alpha_1}{\alpha_1 + \alpha_2} = \frac{C_1\delta_1}{C_1\delta_1 + C_2\delta_2} \qquad (4-12)$$

The equation $(4-11)$ can be $(4-13)$:

$$\begin{cases} F(t) = [\alpha\, exp\left(-{}^{t}/_{\tau_1}\right) + (1-\alpha)\, exp\left(-{}^{t}/_{\tau_2}\right)]\, V_m k I_0^2(\alpha_1 + \alpha_2) \\ \dfrac{F(t)}{F(t=0)} = [\alpha\, exp\left(-{}^{t}/_{\tau_1}\right) + (1-\alpha)\, exp\left(-{}^{t}/_{\tau_2}\right)] \;\; Normalizedby\ F(t=0) \end{cases} \qquad (4-13)$$

Introducing the volume fraction ψ to represent the change in the volume of dye 1 $(4-14)$:

$$\psi = \frac{V_1}{V_1 + V_2} \qquad (4-14)$$

Then,

$$C_1 = \frac{C_{10}V_1}{V_1 + V_2} = C_{10}\psi \qquad (4-15)$$

$$C_2 = \frac{C_{20}V_2}{V_1 + V_2} = C_{20}(1-\psi) \qquad (4-16)$$

where C_{10}, C_{20} represent the original concentration of dye 1 and dye 2 before the mixing of volume V_1 and V_2 of the two dyes 'solutions, the equation $(4-12)$ can be expressed as $(4-17)$:

$$\alpha = \frac{\alpha_1}{\alpha_1 + \alpha_2} = \frac{C_1\delta_1}{C_1\delta_1 + C_2\delta_2} = \frac{\psi C_{10}\delta_1}{\psi\, C_{10}\delta_1 + (1-\psi)C_{20}\,\delta_2} \qquad (4-17)$$

Suppose$(4-18)$:

$$\beta = \frac{C_{20}\delta_2}{C_{10}\delta_1} = (C_{20}/C_{10})\,\delta, \left(\delta = \frac{\delta_2}{\delta_1}\right) \qquad (4-18)$$

Then, $(4-19)$:

$$\alpha = \frac{\psi}{\psi + (1-\psi)\beta} \qquad (4-19)$$

The expression $(4-19)$ establishes a relationship between the mixing fraction ψ and the average coefficient α. The molar absorptivity δ_1, δ_2 ,thus δ, β are assumed to be unsensitive to temperature if the fluorescent dyes are temperature-independent, such as Rhodamine 6G and Eosin Y.

Equation $(4-9)$ is based on the assumption that the fluorescence decay can be expressed as the sum of two independent decays (one for each spray). For that, there must be no interaction of the two sprays in the measurement volume. If two droplets (one from each spray) are present at the same time in the measurement volume, the photons coming from the droplet with the short-lived fluorescence could reach the PMT systematically before the photons from the droplets with the long- lived fluorescence. Because of the dead time of the detector, this could bias the histogram of the photon arrival times in favour of the spray with the short-lived fluorescence. However, the problem is very limited here because of the densities of the two sprays, the small size of the 2P excitation volume and the optical configuration. When two droplets are present in the excitation volume and the optical configuration. When two droplets are present in the excitation volume at the same time, the droplet in front of the objective deflects most of the photons coming from the backside droplet. Thus, we expect the results to remain about the same as with a single droplet.

The analysis of the fluorescence decay measured in the sprays makes it possible to evaluate parameters α, τ_1 and τ_2. Then, using Equation $(4-19)$, the volume fraction ψ can be derived provided that the value of β is known. The individual temperature of the two sprays (namely T_1 and T_2) can be also retrieved from the lifetimes τ_1 and τ_2 if they are temperature dependent. The fluorometric temperature T_{LIF} of the mixing can be defined by:

$$T_{LIF} = \frac{R}{E_a} \cdot ln(\tau_{LIF}/A) \qquad (4-20)$$

where the average lifetime τ_{LIF} is defined as:

$$\tau_{LIF} = \alpha\, \tau_1 + (1-\alpha)\, \tau_2 \qquad (4-21)$$

It is interesting to note that T_{LIF} is also the temperature that would be obtained from an intensity-based measurement which is not affected by any perturbation of the excitation and the transmission of the fluorescence signal in the sprays. Indeed, the time-integrated intensity $\overline{F}$ can be evaluated by:

$$\overline{F} = \int_0^{+\infty} F(t)\, dt = F(t=0) \cdot \{\alpha\, \tau_1 + (1-\alpha)\, \tau_2\} = F(t=0) \cdot \tau_{LIF} \qquad (4-22)$$

$\overline{F}$ varies the same manner as τ_{LIF} with the temperature. Therefore, Equation $(4-22)$ relates $\overline{F}$ to the temperature T_{LIF} provided a linear response of the dyes to the laser excitation (no saturation of the fluorescence signal).

T_{LIF} differs from the mixing temperature T_m given by the conservation of energy and the volume fraction ψ:

$$T_m = \psi\, T_1 + (1 - \psi)\, T_2 \qquad (4-23)$$

Even in the case of a single dye ($\beta = 1$), the analysis shows that T_{LIF} deviates from T_m. In fact, T_{LIF} is closer to the temperature within the spray with the lowest values of fluorescence lifetime. This deviation between T_{LIF} and T_m is further quantified in **Figure 4-32** for the case of the measurements described in **Chapter 4.3.4**

In the general case, the fluorescence decay in each of the two sprays differ from a mono-exponential decay but can be modelled by a biexponential decay. The methodology described above remains mostly valid, but it must be replaced by a combination of two bi-exponential:

$$F(t) = k\, \delta_1\, C_1\, I^2\, \phi_1(a_1, t_{11}, t_{12}, t)\, V_1 + k\, \delta_2\, C_2\, I^2\, \phi_2(a_2, t_{21}, t_{22}, t) V_2 \qquad (4-24)$$

where $\phi_i(a_i, t_{1i}, t_{2i}, t) = a_i \exp(-t/t_{1i}) + (1 - a_i) \exp(-t/t_{2i})$, $0 \le a_i \le 1$ and the indice $i = 1$ or 2 refers to the dye used to seed the i^{th} spray. Normalizing the fluorescence signal by $F(t = 0)$,

$$\frac{F(t)}{F(t = 0)} = \alpha\, \phi_1(a_1, t_{11}, t_{12}, t) + (1 - \alpha)\, \phi_2(a_2, t_{21}, t_{22}, t) \qquad (4-25)$$

Here, the expression for the average coefficient α is exactly the same as Equation $(4-19)$ Parameters (a_1, t_{11}, t_{12}) for spray 1, and (a_2, t_{21}, t_{22}) for spray 2, must be determined prior to the measurements to determine the volume fraction and the temperature of the two sprays if the dyes are temperature dependent.

4.2.2 Performance of Mixing Dyes in a Cuvette

Mixtures of Rhodamine 6G and Eosin Y in different proportions are prepared in a cuvette to validate the mixing model in **4.2.1.** The initial concentrations of the solution before the mixing are $C_{\textbf{Rhodamine 6G}} = 3\times10^{-6}$mol/L and $C_{\textbf{Eosin Y}} = 10^{-5}$mol/L. When the mixing(volume) fraction ψ=0, it means it is pure Eosin Y aqueous solution while it is pure Rhodamine 6G aqueous solution when ψ=1. By mixing the different volumes of Eosin Y and Rhodamine 6G, the fluorescence decay can be obtained as shown in **Figure 4-22**. Photon counts have been normalized, and it can be seen that it falls faster as the value of ψ decreases.

For each case, the bi-exponential law is adopted for the fitting, and the mean lifetime $\bar{\tau}$ can be determined by the corresponding curve. Because the lifetimes of pure aqueous solutions of Eosin Y and Rhodamine 6G are respectively, $\tau_1 = 1.1$ ns and $\tau_2 = 3.7$ ns, thus the average coefficient α is evaluated as follows:

$$\alpha = \frac{\bar{\tau} - \tau_2}{\tau_1 - \tau_2} \qquad (4-26)$$

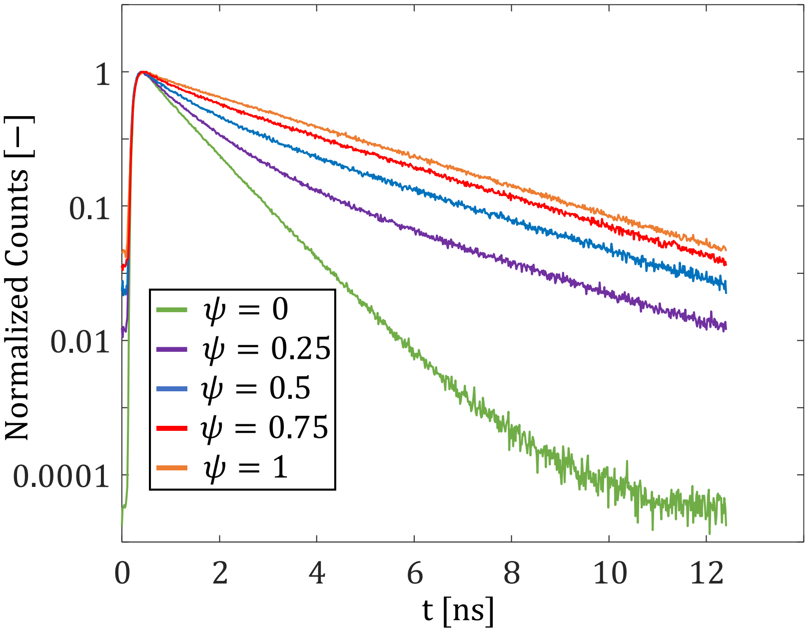

Figure 4-22 Fluorescence decay of the couple Rh6G/EY when mixed in different proportions. These results were obtained in a cuvette at room temperature of 20 °C (ψ = 0 when there is no Rh6G in solution). The initial concentrations of the solutions before the mixing were C_{Rh6G} = 3×10^{-6} mol/L and $C_{EY} = 10^{-5}$ mol/L. Different volume fractions ψ were obtained by changing the volume of liquid from the two solutions added in the cuvette

Figure 4-23 shows the evolution of the average coefficient α as a function of the volume fraction ψ. Calibrations are carried out for three concentration ratios C_{Rh6G}/C_{EY}=0.1, 0.3 and 1.05 between the two solutions mixed in the cuvette. An acceptable agreement with the prediction of the model $(4-19)$ is obtained by adjusting the value of β to 0.33, 1.0 and 3.5. From these observations, it can be deduced that the ratio of the two-photon molar absorptivity $\varepsilon_{Rh6G}/\ \varepsilon_{EY}$ is approximately equal to 3.3 at an excitation wavelength of 700 nm.

The mixing experiment involving Rhodamine 6G and Eosin Y in the cuvette serves as the foundation for the spray study. C_{Rh6G} is set at 3×10^{-6}mol/L, while C_{EY} is maintained at 10-5mol/L (with β=1) as the chosen dye concentrations for the mixing spray, wherein the average coefficient α equates to the volume fraction ψ.

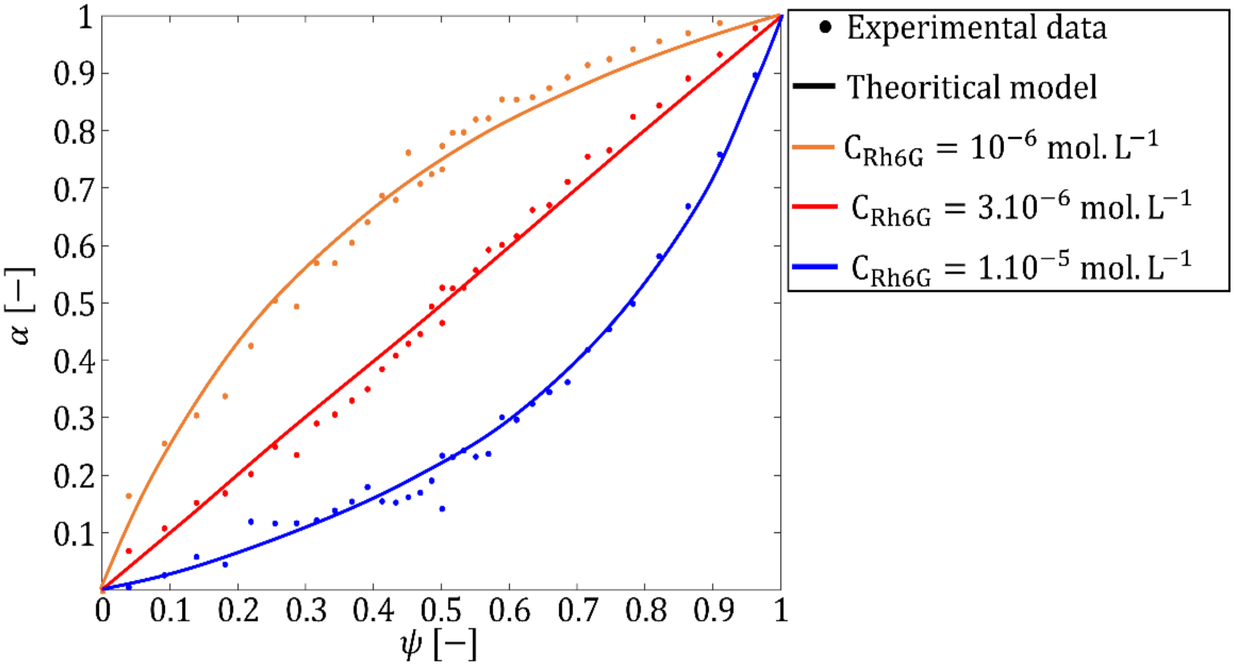

Figure 4-23 Evolution of the average coefficient a as a function of the volume fraction ψ for different concentrations of Rh6G and EY. The experimental data (in dot) are compared to the prediction of Eq. $(4-19)$ (in red) adjusting β to 0.33, 1 and 3.5. Measurements correspond to a concentration of Rh6G equal to 10^{-6} mol/L, 3×10^{-6} mol/L and 1×10^{-5} mol/L, while the concentration of EY is fixed at 10^{-5} mol/L

4.3 Mixing Spray Experiment

4.3.1 Two-Photon Measurement Volume

As we mentioned before, the two-photon excitation technique is superior in spray experiments because it avoids scattering and provides information about the excitation of the droplet at a specific point. Therefore, the elaboration of the two-photon measurement volume is essential before we perform measurements of the mixed spray.

Since the fluorescence excitation depends on the simultaneous absorption of two photons, its probability is proportional to the square of the laser light intensity $I_{laser}(r,z)$. Considering a Gaussian laser beam **(Figure 4-24)**, the intensity profile of the laser beam is given by:

$$I_{laser}(r,z) = I_0 \cdot \left(\frac{w_0}{w(z)}\right)^2 \cdot exp\left(-\frac{2r^2}{w^2(z)}\right) \qquad (4-27)$$

where I_0 is the incident intensity, r is the transverse radius, z is the path length. At the beam waist ($r = w_0$ and $z = 0$), the intensity I_{laser} drops to $1/e^2$ of the incident intensity I_0. The evolution of the beam radius $w(z)$ along the z direction is determined by:

$$w^2(z) = w_0^2 \cdot \left[1 + \left(\frac{z}{z_0}\right)^2\right] \qquad (4-28)$$

where the Rayleigh length ($z_0 = \pi\, w_0^2/\lambda$) is a critical distance for the intensity distribution in the z direction. Parameters z_0 and w_0 depend on the magnification of the microscope objective lens used to focus the laser beam.

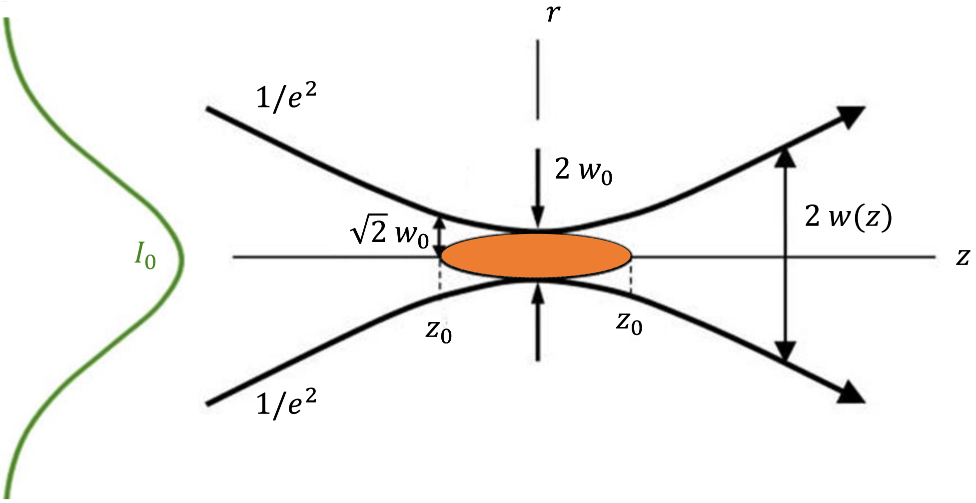

Figure 4-24 Illustration of the key parameters used to describe the Gaussian beam propagation and to model the size of the fluorescence spot

Considering a small liquid volume dV containing the fluorescent dye, the number of photons absorbed dN_{abs} can be written as:

$$dN_{abs} = \delta\, C\, I_{laser}^2\, dV \qquad (4-29)$$

In this expression, δ denotes the molecular two-photon absorption cross-section of the fluorophores in the liquid solution. It is usually quoted in (GM), where 1 GM equals to 10^{-50} cm^4 s photon^{-1}. Equation $(4-29)$ implies a sufficiently moderate laser fluence (well below the saturation threshold of the two-photon fluorescence) to be a linear regime of fluorescence excitation.

A high magnification objective comes with a very small fluorescence spot size and thus a reduced fluorescence signal due to the low probability of intercepting droplets. Additionally, a reasonable working distance is recommended to limit the deposition of droplets onto the lens surface. Due to these requirements, a microscope objective with a long working distance of 25 mm (50X Mitutoyo Corrected Infinite Plane Apo NIR B) is chosen. **Figure 4-25** shows images of the fluorescence spot recorded in a cuvette filled with an aqueous solution of Eosin Y. The images are obtained using a camera (XIQ SuperSpeed) which has a 2/3" sensor size. The zoom lens OPTEM 125C mounted on this camera, allows to obtain a field of view of 1.02 × 1.35 mm when the magnification is maximum. A chromatic bandpass filter [570 nm- 620 nm] is placed in front of the zoom lens to eliminate the parasitic light which is not fluorescence. Due to the smallness of the beam waist w_0, the fluorescence profile along the transverse direction r cannot be extracted accurately from these images. However, it is possible to determine z_0 and thus w_0. Based on Equation $(4-29)$, the fluorescence signal can be written as:

$$dF \propto \phi\, \eta\, \delta\, N_{abs} \qquad (4-30)$$

Here η is related to the collection efficiency and ϕ is the fluorescence quantum yield. In a section of the fluorescence spot located at z:

$$F(z) \propto 2\pi\, \delta\, C\, \phi\, \eta \int_{r=0}^{+\infty} r\, I_{laser}^2(r,z)\, dr \qquad (4-31)$$

Using Equations $(4-27)$ and $(4-28)$, the profile of F normalized by its maximum value at $z = 0$, can be expressed as:

$$\frac{F(z)}{F(z=0)} = \frac{z_0^2}{z^2+z_0^2} \qquad (4-32)$$

The same integration has been performed with the experimental images. The corresponding curves are shown in the right-hand side of **Figure 4-25**. A good agreement with Equation $(4-32)$ is obtained when the laser power P is low. For the high values of P, a saturation of the fluorescence can be evidenced near the center of the fluorescence spot ($z = 0$). Among the three dyes tested, Eosin Y proved to be the most sensitive to this phenomenon. For an excitation wavelength $\lambda =$ 700 nm and $P = 2.2$ W, the decrease in the florescence intensity F around $z = 0$ indicates that photobleaching is occurring (**Figure 4-25 D**). While the ratio F/F_0 is not expected to vary with the laser fluence, the estimated value of z_0 has to be increased with P to maintain an acceptable match between the experimental data and the theoretical model based on Equation $(4-32)$ due to the effects of fluorescence saturation. In the followings, the experiments with Rhodamine B are performed tuning the fs laser on the wavelength of 800 nm at which the output power is 3.5 W. For Eosin Y, a wavelength of 700 nm was preferred as it is more efficiently absorbed, and the laser power was fixed at P =1.5 W. Saturation and photobleaching are encountered for these high values of the laser powers, however the fluorescence lifetime is not affected contrary to the signal intensity. The Rayleigh length z_0 can be estimated to be about 60 μm from (**Figure 4-25 A)**. Considering

A) P=1. 6 W, λ= 800 nm

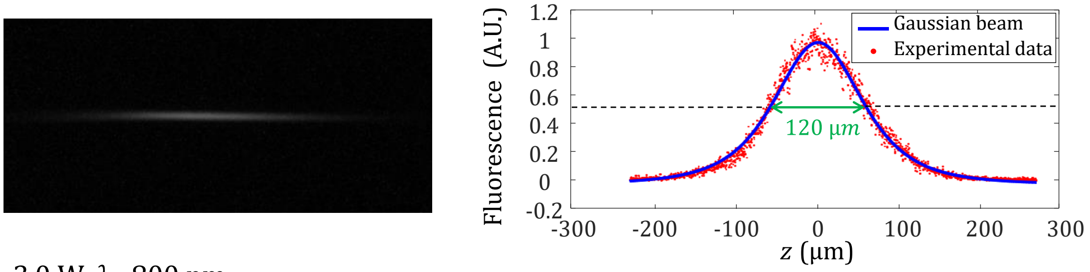

B) P=3.0 W, λ= 800 nm

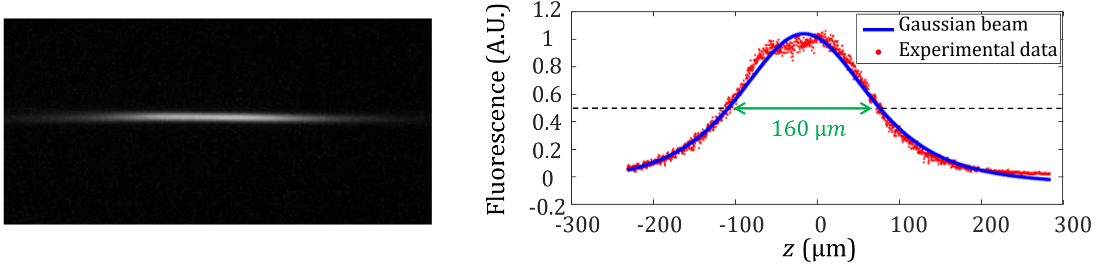

C) P=0.8 W, λ= 700 nm

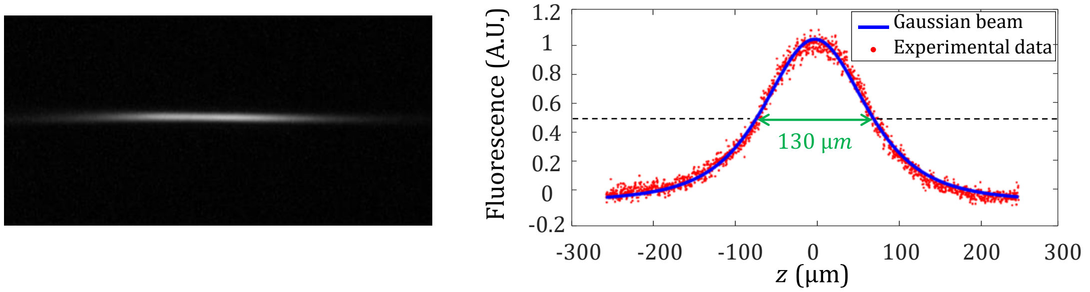

D) P=2.2 W, λ= 700 nm

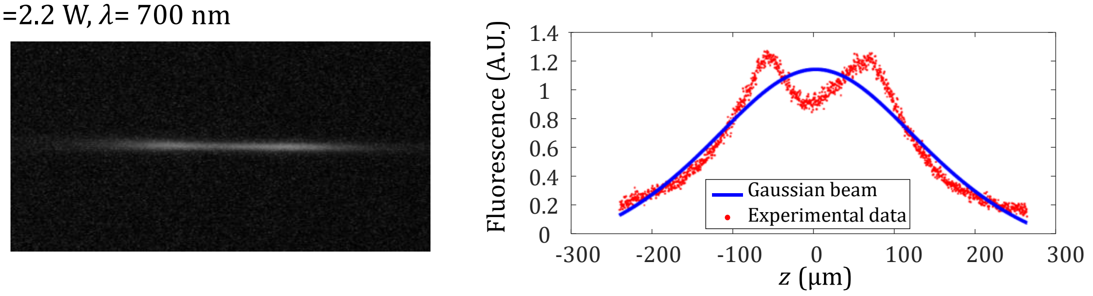

Figure 4-25 Fluorescence distribution observed in a cuvette filled with Eosin Y dissolved into water ($C_{\mathrm{Eosin\ Y}}$ =10^{-5} mol/L) for a laser excitation at A) and B) 800 nm and C) and D) at 700 nm for two different laser power for each excitation wavelength. The fluorescence signal is integrated along the transverse direction r, then the Rayleigh length $z_0$is estimated using the least mean square method and comparison to the theoretical model (Equation 4-32). Saturation of the fluorescence and photobleaching can be evidenced in b) and d) when the laser power P is high.

that $z_0 = \pi\, w_0^2/\lambda$, this yields to a beam waist w_0 of about 3.9 µm. This clearly small value is a bit of a limitation for the measurement as it limits the interception of the excitation volume with the droplets and thus the count rate. At the same time, this allows to have a reduced probability of having two droplets illuminated at the same time.

4.3.2 Experimental Setup for Mixing spray

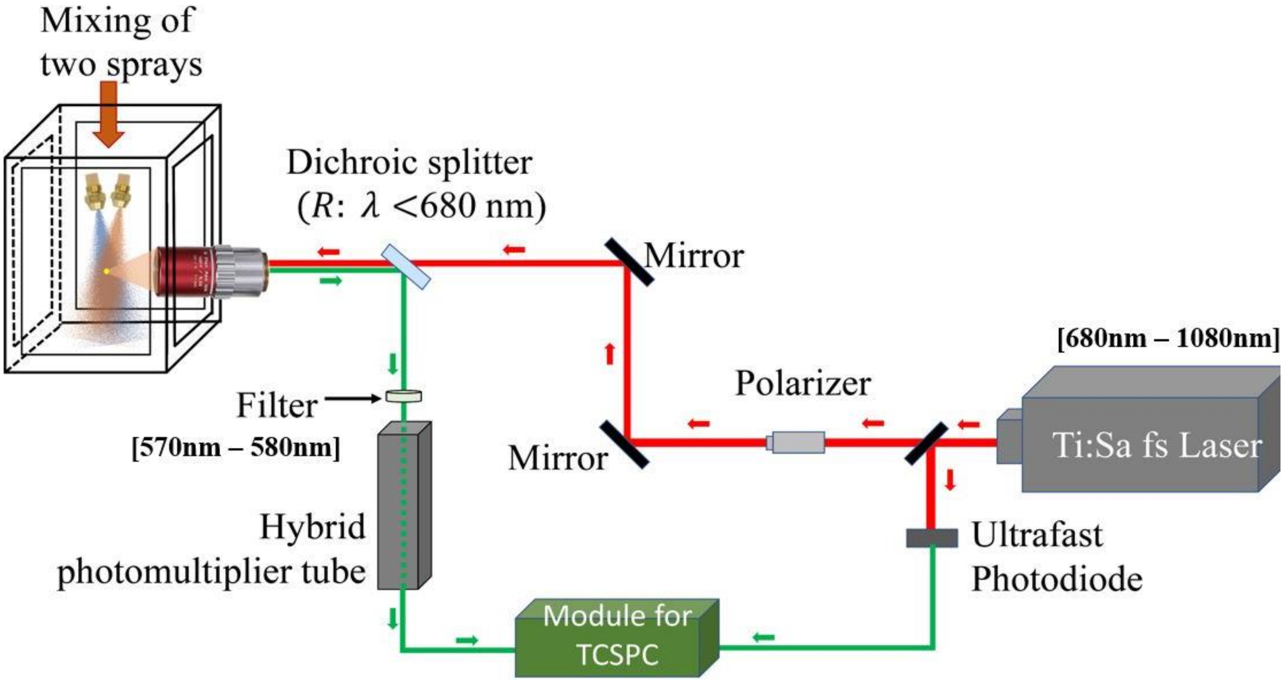

Figure 4-26 Experimental setup

Figure 4-26 shows the experimental equipment used to perform the mixing spray experiment.

The laser beam is generated by a femtosecond Ti:Sa laser (Coherent Chameleon Ultra II) with an emission wavelength tunable from 680nm to 1080nm. A fast hybrid photomultiplier tube (R10467, Hamamatsu) with a Peltier cooler to reduce the dark count rate, is used for photon counting. The output of the detector is sent to a time-correlating counter (HydraHarp 400 controller, PicoQuant GmbH) which operates in forward start stop mode to measure the arrival times of individual photons.

The whole process is as follows:

A laser pulse generated by femtosecond Ti:Sa causes a photon event at the detector and the electronics measure the delay between the laser pulse and the subsequent photon event. This measurement implies a sharp timing of the laser pulse, which is obtained from a fast photodiode (TDA 200 from Pico Quant GmbH) connected to the timing electronics. As shown in **Figure 4-26**, this photodiode receives the reflected light from a beam splitter (99% T, 1% R) placed at the laser output and allows detecting the laser pulses with a small-time jitter due to a very sharp falling edge (Fall time typ. 250 picosecond). After its collection by the microscope lens, the fluorescence signal is diverted by a dichroic plate towards to a fast hybrid photomultiplier tube (R10467 from Hamamatsu) sensitive to a single photon. A bandpass filter [570nm-580nm] is placed in front of the photomultiplier tube to limit the detection of unwanted photons. The three dyes considered in the present study (Rhodamine B, Eosin Y and Rhodamine 6G) emit with a good efficiency in this spectral band.

4.3.3 Mixing Spray 1: Rhodamine 6G and Eosin Y

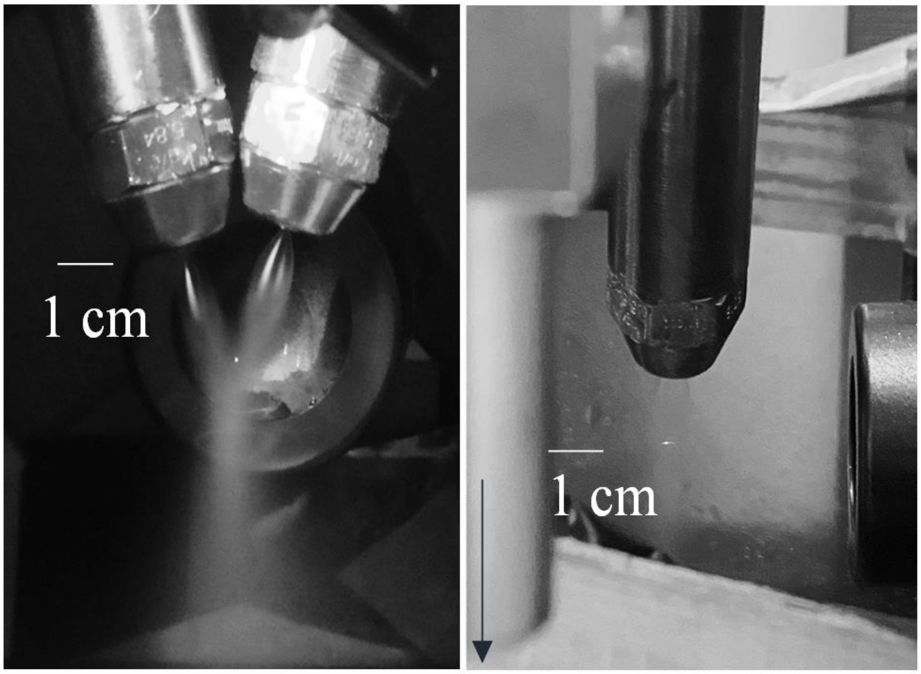

Figure 4-27 Side view of the mixing sprays. The bright spot observed in the middle of the sprays corresponds to the region of biphotonic fluorescence

As shown in **Figure 4-27**, a hot spray filled with water and Rhodamine 6G at 60°C and a cold spray seeded with water and Eosin Y at room temperature (19°C) are injected with a short distance and a tilt angle between them. Since Eosin Y and Rhodamine 6G are not temperature-dependent, these measurements are intended to provide only the average coefficient α and subsequently the volume fraction ψ.

The two nozzles are identical, and the same inlet pressure is set. The spraying system (the nozzles and the mixing chamber) is shifted by two motorized moving stages relatively to the microscope objective by steps of 0.5mm in the x and z directions. An acquisition time of 30s is applied at each measurement location, which proved more than sufficient to ensure a converged histogram of the fluorescence decay and assess the value of the volume fraction ψ. Several methods can be used to evaluate the average coefficient α and thus the mixing fraction ψ:

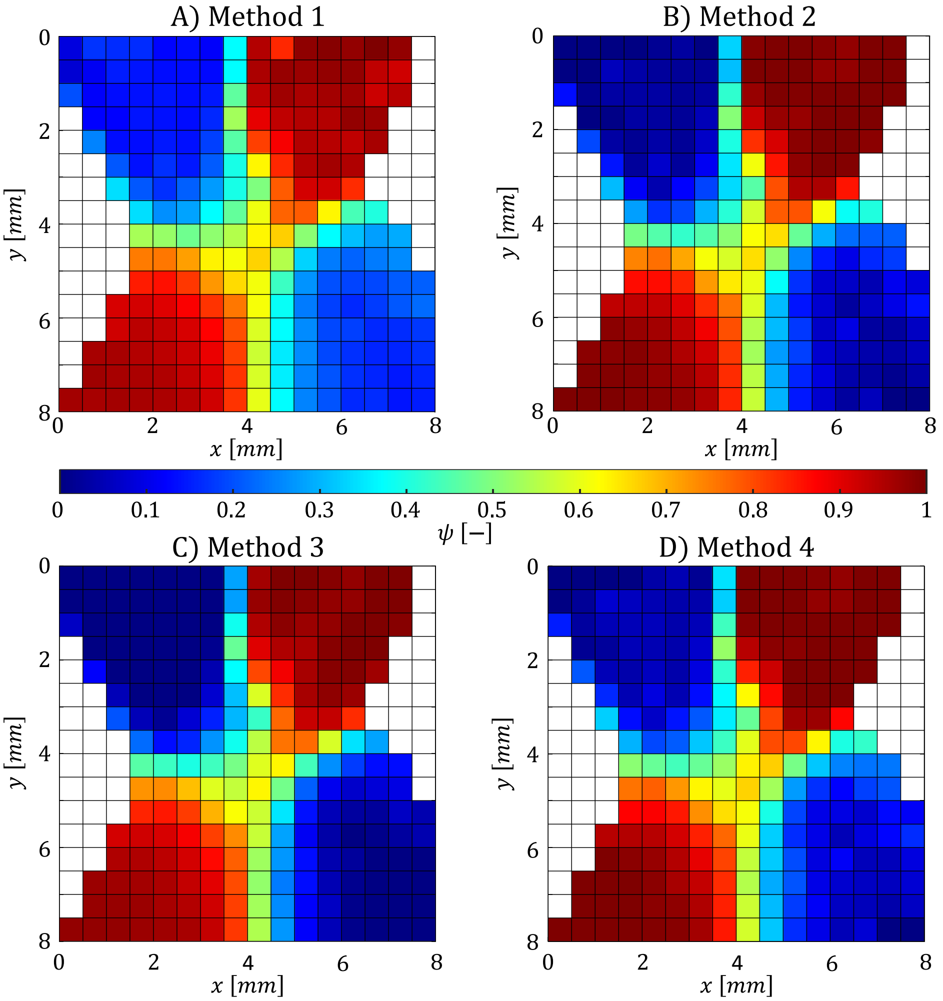

Figure 4-28 Distribution of the volume fraction ψ in the mixing region of the two sprays. The liquid flow rate of the two sprays is about 0.6 L/min. A map of the distribution of ψ is constructed to obtain a 2D image of the mixing fraction in the mixing region of the two sprays using several methods (ψ=0 means there is no Rhodamine 6G in the mixture)

Method 1: The fluorescence decay is fitted by a biexponential without any constraint imposed on the estimation of parameters α, τ_1 and τ_2. The value of α obtained from this, is converted into the volume fraction ψ using the calibration curve in **Figure 4-23**.

Method 2: The fluorescence decay is fitted, as for method 1, by a biexponential without any constraint. Then, the mean lifetime τ is evaluated. Finally, Equation $(4-26)$ is used to obtain a value of α assuming $\tau_1 = 1.1$ ns and $\tau_2 = 3.7$ ns. This value is converted into the volume fraction ψ using **Figure 4-23**.

Method 3: The fluorescence decay is fitted by a biexponential with the constraint to have $\tau_1 = 1.1$ ns and $\tau_2 = 3.7$ ns. Only the parameter α is estimated using the least squares minimizing χ^2 in Equation $(3-13)$.

Method 4: The approach described in **Section 4.2.1** is applied to account for the biexponential nature of the decays of both fluorescent dyes. The decay parameters (a_1, t_{11}, t_{12}) and (a_2, t_{21}, t_{22}) for the two dyes are fixed and only the average coefficient α is adjusted as in method 3. For this method, the values of the fitting parameters chosen are $a_1 = 0.03$, $t_{11} = 1.04$, $t_{12} = 4, a_2 = 0.91$, $t_{12} = 0.75$ and $t_{22} = 3.87$.

The results of the above methods are compared in **Figure 4-28**. Since the two sprays are identical and arranged symmetrically from a vertical plane, it seems rather consistent to obtain a left/right symmetric distribution of the volume fraction when the two sprays cross each other and emerge diagonally on the opposite side. Method 1 clearly suffers from measurement biases. It is apparent that the volume fraction does not decrease down to 0 as expected. The advantage of methods 2 and 3 is mainly that they are based on the estimation of a single parameter ($\bar{\tau}$ in method 2 and α in method 3), which limits the propagation of errors. These two methods give roughly equivalent results. Deviations are marginal with method 4, which accounts for the true bi-exponential nature of the dyes' fluorescence decay.

4.3.4 Mixing Spray 2: Hot and Cold Rhodamine B

An even more valuable type of measurement is the combined determination of the temperatures of both sprays and the mixing fraction. This can be achieved by using Rhodamine B as a fluorescent dye. As the absorption cross-section of Rhodamine B is not dependent on the temperature[17][18], the value of β in Equation $(4-19)$ is equal to 1 which means $\alpha = \psi$. An accurate assessment of both the temperature and the mixing fraction requires a sufficiently high-temperature difference between two sprays. In the present work, the injection temperatures of the two sprays are set to 20°C and 56°C respectively. To ensure good data convergence, the acquisition time is fixed at 100 s, and measurement points are discarded from the acquisition when the photon count rate is below 2000 cps since the measurements require more time of acquisition for a good statistical convergence.

As previously mentioned, the fluorescence decay of Rhodamine B deviates significantly from a mono-exponential but can be well described by a bi-exponential. The result is illustrated in **(Figure 4-29 A)** by using the same approach as method 1 as we explained before. It is apparent that α never falls to 0 nor reaches 1, in the regions where only one spray is present in the measurement volume. The estimation of the average coefficient α is affected by a large error.

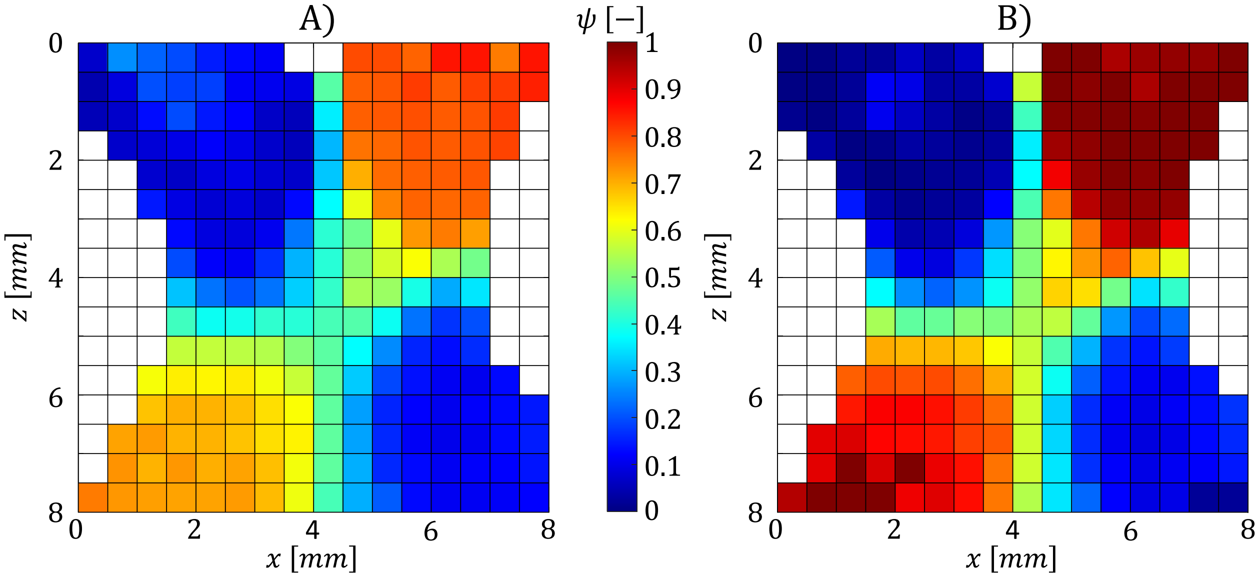

Figure 4-29 Spatial distribution of the volume fraction $\psi = \alpha$. The values are obtained by assuming either a biexponential decay (A) based on Equation $(4-13)$, or the combination of two biexponential decays (B) using Equation $(4-33)$

To avoid this problem, it is necessary to consider the combination of two biexponential and adopt the method in Equation $(4-24)$ $(4-25)$. Denoting τ_1 and τ_2 the mean fluorescence lifetimes in the two sprays, the fluorescence signal in the mixing region can be rewritten as:

$$\frac{F(t)}{F(t=0)} = \alpha\, \phi(\tau_1, t) + (1-\alpha)\, \phi(\tau_2, t) \qquad (4-33)$$

Here, the function ϕ is determined from the temperature calibration of the Rhodamine B temporal responses. For each measurement in the sprays, the triplet $(\alpha = \psi, \tau_1, \tau_2))$ is evaluated using the least squares method, i.e., minimizing the value of χ^2. The obtained distribution of the volume fraction is shown in **Figure 4-29 B**. It does not appear to be affected by the same biases as in **Figure 4-29 A**, since values of ψ are getting close to 0 and 1 in the regions where the two sprays are separated.

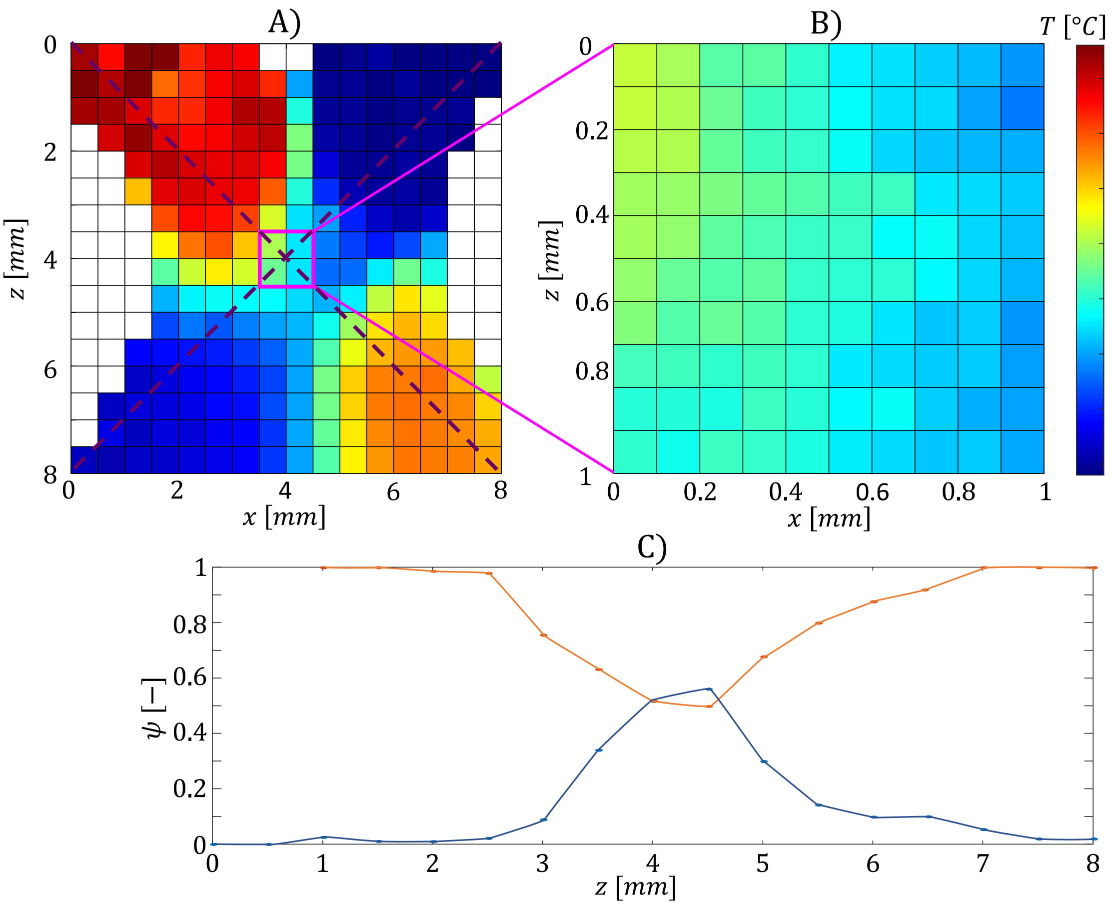

Figure 4-30 Evolution of the mixing temperature T_m and the mixing fraction ψ. A) 2D map of the spatial distribution of the mixing temperature T_m and B) data in the mixing zoom with a spatial step of 0.1 mm. C) Evolution of the volume fraction ψ along the two dotted violet lines plotted in A)

Parameters τ_1 and τ_2 are related to the temperature of both sprays following Equation $(4-2)$. Hence, the temperatures T_1 and T_2 can be determined as well. Using the values of ψ, T_1 and T_2, it is also possible to calculate the mixing temperature T_m based on equation $(4-23)$. As observed in **Figure 4-30 A,** the temperature distribution follows a rather similar evolution compared to that of the volume fraction. However, the temperature does not fully recover its initial value after the mixing region. The hot spray ($T_{inj} = 56°\mathrm{C}$) appears to get slightly cooler after the mixing, while the cold spray ($T_{inj} = 20°\mathrm{C}$) appears to be heated up by a few °C. **Figure 4-30 B,** shows experimental measurement in the mixing zone obtained by using a more refined step of 0.1 mm for the scanning. Data are in good agreement with **Figure 4-30 A,** and allow to observe more precisely the evolution of the mean temperature near the center of the mixing region. **Figure 4-30 C,** shows the evolution of the volume fraction ψ along the diagonal lines which are drawn as violet dots in **Figure 4-30 A.** As expected, the value of ψ approaches 1 in the hot spray region and 0 in the cold spray region but a deviation (about 5%) is sometimes observed. Between z=3 mm and z=5 mm, ψ is varying due to the mixing of the sprays. It is decreasing for the hot spray diagonal down to about 0.5, and it increases for the cold spray diagonal up to about 0.5. Downstream to the mixing zone (z>5 mm), the mixing fraction ψ returns progressively to a value close to its initial value.

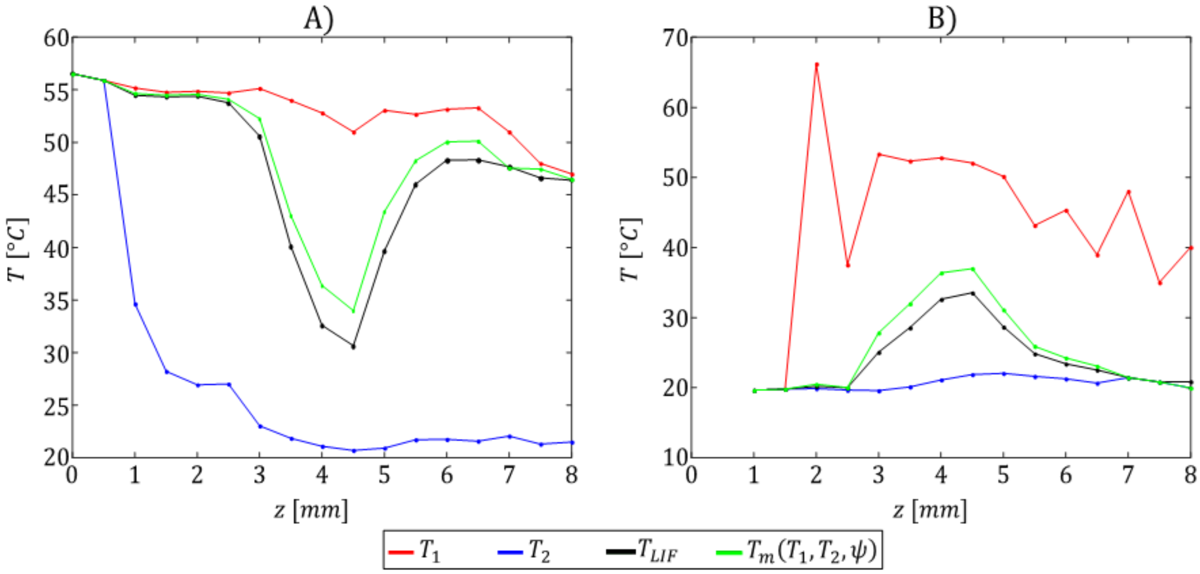

Figure 4-31 Evolution of the fluorometric temperature T_{LIF}, the mixing temperature T_m and the temperatures T_1 and T_2 of the two sprays along the diagonals of the hot and cold sprays plotted in **Figure 4-30 A**. A) represent the result along the hot spray and B) along the cold spray.

Figure 4-31 A, shows the evolution of the temperature in the hot and cold sprays (respectively T_1 and T_2), the temperature T_{LIF} derived from the average fluorescence lifetime and the mixing temperature T_m as a function of the vertical position z on the hot and cold spray diagonals drawn in **Figure 4-30 A.** It can be observed that T_m is systematically a few degrees lower than T_{LIF}, and the largest differences can be pointed out in the center of the mixing zone. Considering a temperature T_1=20°C for spray 1 and T_2=56°C for spray 2, the evolution of T_{LIF} and T_m as a function of the volume fraction ψ are shown in **Figure 4-32**. The difference between T_{LIF} and T_m reaches about 5°C when ψ is close to 0.4. To obtain **Figure 4-32**, Equation $(4-1)$ was first used to evaluate the fluorescence lifetimes T_1 and T_2, then Equation $(4-21)$ was as an approximation to estimate T_{LIF} as ψ ranging from 0 to 1.

In **Figure 4-31 A**, T_1 and T_2 are found identical and close to 56°C at the beginning (z <0.5 mm) because there is only one spray. When spray 2 (cold spray) starts to be present in sufficient quantity (in the mixing zone), the temperature T_2 decreases to take a value close to 20°C, which is comparable to the injection temperature of the cold spray. At the center of the mixing zone (approximately for z between 2.5 mm and 5.5 mm), T_1 and T_2 are consistent with the expected values. After the mixing zone (z> 5.5 mm), most of the liquid remaining in the measurement volume is from the hot spray, and it is observed that the temperature T_1 of the hot spray has slightly decreased from the injection temperature. The temperature T_2 continues to be evaluated with good accuracy despite the small amount of liquid from spray 2. Similar conclusions can be drawn in **Figure 4-31 B** for the results obtained along the axis of the cold spray. The hot spray has a low volume fraction except in the central region (2.5 mm <z< 5.5 mm). Fluctuations affecting the temperature T_1 of the hot spray can be observed everywhere else.

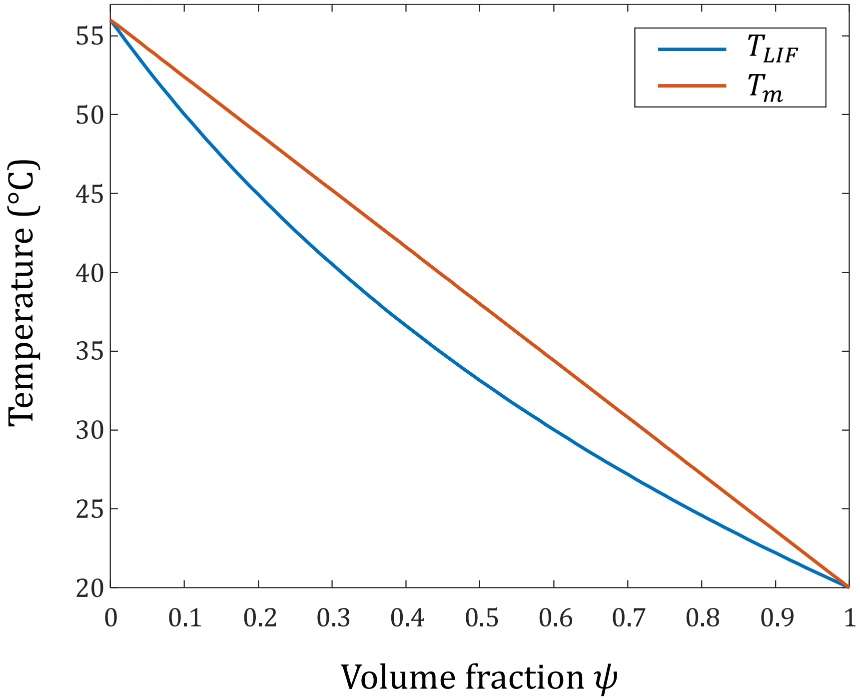

Figure 4-32 Evolution of the temperatures T_m and T_{LIF} as a function of the mixing fraction ψ. Results obtained from the fluorescence model assuming T_1=56°C and T_2=20°C

Even if the temperatures T_1 and T_2 are reasonably well recovered in **Figure 4-31**, the measurement method suffers from limitations when one of the sprays is weakly present in the measurement volume. In this case, the temperature of the weakly present spray cannot be reliably determined. Based on the results presented in **Figure 4-30** and **Figure 4-31**, it seems that the volume fraction of a given spray must exceed a certain level in order to determine its temperature with an accuracy. To further investigate this issue, additional tests were conducted. **Figure 4-33** provides further insights into the accuracy of the temperature measurements of the sprays. In **Figure 4-33 A**, the measurement position is situated in a region of the cold spray is dominant (x=1.5 mm and z=7 mm). It is evidenced that the temperature T_1 of the hot spray can be changed in a large range while the fitting of the experimental fluorescence decay remains quite acceptable. The confidence interval for the hot spray temperature T_1 extends from about 44°C to 72°C, which is very large. In contrast, the temperature T_2 of the cold spray ranges between 21°C and 22.5°C, which is rather good for a measurement accuracy. Further investigations demonstrate that T_m and T_{LIF} are measured with an accuracy better than 1°C even when T_1 is measured with the largest error in **Figure 4-31**. Both T_m and T_{LIF} can still be measured correctly while the mixing fraction, T_1 or T_2 are significantly wrong as errors compensate.

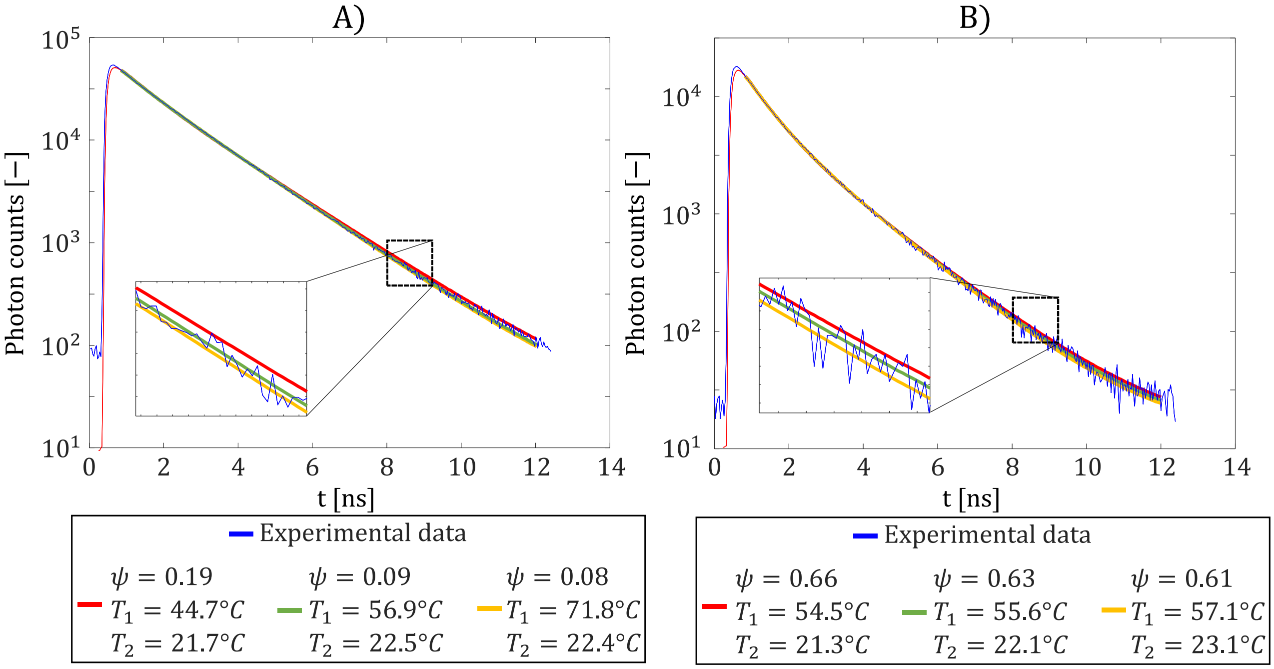

Figure 4-33 Estimations of the temperatures T_1 and T_2 of the hot and cold sprays in a region where the cold spray is predominant (a) ($x = 1.5\ mm;\ z = 7\ mm$) and in a region situated near the center of the mixing zone (b) ($x = 4.5\ mm;\ z = 4\ mm$)

Figure 4-33 B corresponds to a position in the center of the mixing zone, where the volume fraction of the two sprays is comparable (x=4.5 mm and z=4 mm). It can be clearly observed that both temperatures T_1 and T_2, as well as the mixing fraction ψ, are estimated with a good accuracy in that case. Further investigations, presented in **Section 4.4**, were carried out using the Monte Carlo method to evaluate the measurement uncertainties of the different parameters. They reveal that the measurement errors on the average temperatures T_m and T_{LIF} are always acceptable (less than 1°C) under the measurement conditions of the experiments (a minimum count rate of 2000 Cps and an acquisition time of 100s).

4.4 Result Validation (Monte Carlo)

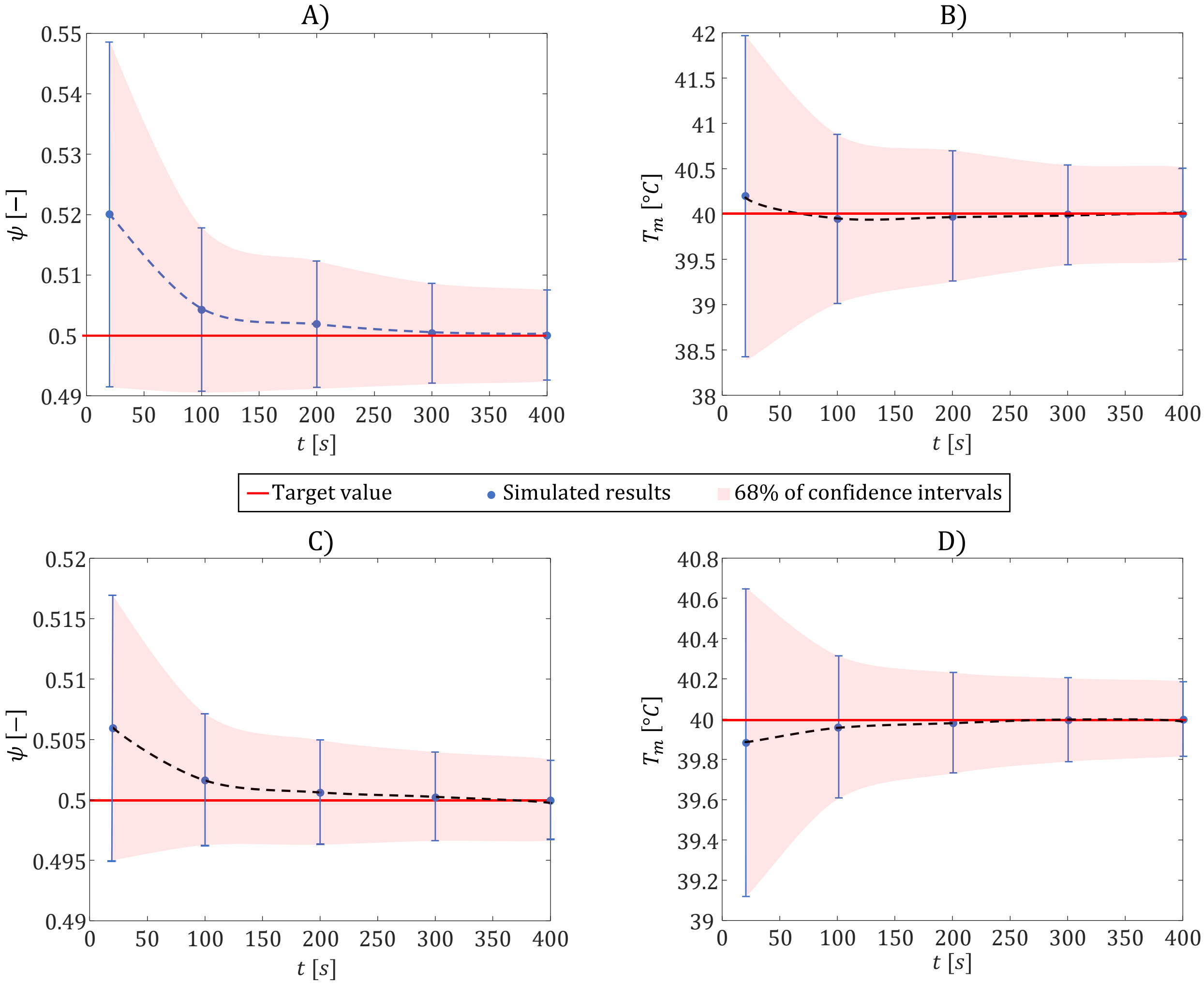

Figure 4-34 Confidence intervals of the estimations of the volume fraction ψ and the mixing temperature T_m when the acquisition time is modified. Each data point is the result of the computation of 2000 synthetic fluorescence decays with the Monte Carlo method. A noise of 28 Cps is considered. The count rate of A) and B) is 2 000 Cps and 15 000 Cps for C) and D)

A Monte Carlo method was implemented to estimate the measurement uncertainties. It consists in generating synthetic histograms of the photon arrival times, while taking into account the photon count rate, the acquisition time, the noise level, the IRF, and the time-channel width. Such method has been already employed by [19] for assessing the precision of temperature measurements in a single spray. In this study, a mono exponential function was used to describe the fluorescence decay. Results obtained with the method are presented hereafter for T_1=56°C and T_2=20°C. Two counts rate, 2000 Cps and 15000 Cps, are also considered. The count rate of 2000 cps corresponds to the worst-case scenario (no measurements were performed with a lower count rate in the experiments). The count rate of 15000 cps is a median value among the measurements. For some given values of the volume fraction ψ and the count rate, more than 2000 synthetic histograms are generated using the Monte Carlo method. These histograms are analyzed the same manner as their experimental counterparts in order to estimate the temperatures T_1 and T_2, the volume fraction ψ, the mixing temperature T_m and the LIF temperature T_{LIF}. Based on the thousands of generated data, the average and the standard deviation can be calculated for those quantities, which allows to evaluate the uncertainties of their measurements.

Figure 4-34 shows the influence of the acquisition time on the estimates of the volume fraction ψ and the mixing temperature T_m. The coloured areas on the graphs correspond to the confidence intervals of half-width equal to the standard deviations σ_ψ or σ_{T_m}. It can be observed that an acquisition time of 100s is a good compromise. It allows having a limited estimation error while maintaining an acceptable acquisition time. This value of the acquisition time was thus retained in the experiments and in the tests performed in the following for evaluating the uncertainties with the Monte Carlo method.

Using the same approach, uncertainties were also quantified for different values of the volume fraction ψ at a fixed acquisition time of 100s in **Figure 4-35**. Significant differences can be observed between σ_{T_1} and σ_{T_2}. These can be explained by the fact that the hot spray has a much shorter fluorescence lifetime than the cold spray. When ψ approaches 1, there is very little of the hot spray passing in the measurement volume in comparison to the cold spray. Therefore, the presence of the hot spray is difficult to detect based on the fluorescence decay. Not only it is hardly visible at the long times but also at the short times. So σ_{T_1} is large while σ_{T_2} is small. When ψ gets close to 0, the hot spray has a stronger influence on the fluorescence decay especially at the short times, but the cold spray keeps a significant influence at the long times. The uncertainty on the temperature T_2 of the cold spray does not increase that much. The value of σ_{T_2}remains smaller than 1°C for values of ψ as low as 0.1. Finally, it is interesting to note that the uncertainties on the parameters T_m and T_{LIF} remains always lower than 1°C while the uncertainty on the temperature of the hot spray $\left(\sigma_{T_1}\right)$ reaches several °C. This is due to the fact that the different parameters are correlated, and errors can compensate each other. The error on the volume fraction ψ remains lower than 1% when the hot spray is predominant in the measurement volume (more precisely for ψ<0.4).

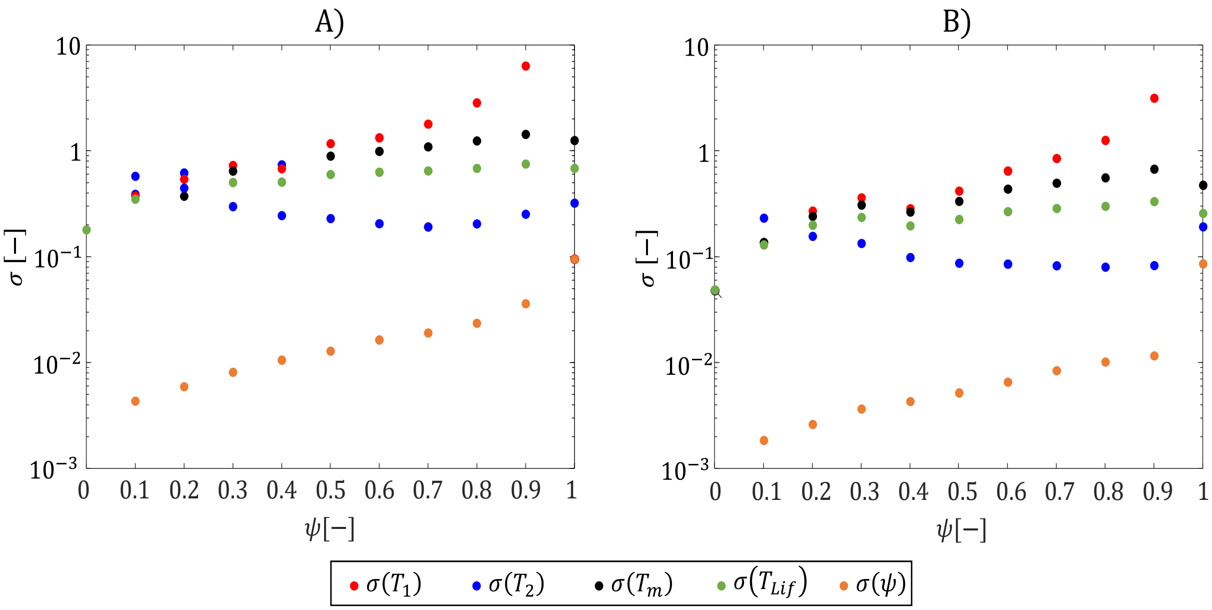

Figure 4-35 Evolution of the standard deviation of the estimated temperature of the hot (T_1) and cols (T_2), the mixing fraction (ψ), the mixing temperature (T_m) and the LIF temperature (T_{Lif}) as a function of the mixing fraction. Each point is the result of 2000 synthetic fluorescence decays using an acquisition time of 100 s, a noise count rate of 28 Cps and in A) 2 000 Cps and B) 15000 Cps count rate.

4.5 Conclusion

In this chapter, we introduce and validate a novel method for measuring the local temperature of sprays through two-photon absorption.

Initially, we carefully selected and examined various fluorescent dyes, considering factors such as their fluorescence lifetimes, excitation spectra, and emission spectra and opted for Rhodamine B, Eosin Y, and Rhodamine 6G as the fluorescent dyes for the mixing sprays. We conducted tests to determine their fluorescence lifetimes under varying temperatures and concentrations. The outcomes revealed that, for solutions with concentrations below 10^{-3} mol/L, the fluorescence lifetimes of all these three dyes remained constant. Additionally, the fluorescence lifetimes of Rhodamine B exhibited a reduction as the temperature increased, whereas those of Eosin Y and Rhodamine 6G remained unaffected. Subsequently, we assessed the performance of Rhodamine B in individual sprays to validate the viability of the two-photon excitation experimental method. During the measurement period, we employed the TCSPC system to process the lifetime variation of Rhodamine B within individual spray.

Finally, we tested the performance in mixed sprays. The possibility of measuring the mixing fraction alone was first tested in the case of a mixture of two sprays seeded separately with Eosin Y and Rhodamine 6G, which have very different fluorescence lifetimes but both insensitive to temperature. The combined measurement of temperature and mixing fraction using Rhodamine B alone, was carried out for a thermal contrast of approximately 40°C between the two sprays. The biexponential behavior of the fluorescence decay of Rhodamine B must be considered to obtain acceptable values of the mixing fraction. It was found that the volume fraction of a spray must exceed about 10% to make it possible to derive its temperature with an acceptable accuracy of about 2°C-3°C. Measuring the volume fraction ψ and the mixing temperature weighted by the liquid volume of the sprays (T_m), is a clear advantage of the proposed multi-exponential analysis over conventional approach based either on the signal intensity or on the average fluorescence lifetime (τ_{LIF}). The latter only permit to determine the temperature τ_{LIF}, which can deviate from T_m by several °C. The temperatures $\tau_{LIF}$and T_m can be accurately measured using TCSPC, even when the estimates of the hot spray temperature can reach a few °C in the mixing zone.

4.6 Reference

[1]. Arcoumanis, C., McGuirk, J. J., & Palma, J. M. L. M. (1990). On the use of fluorescent dyes for concentration measurements in water flows. Experiments in Fluids, 10(2-3), 177-180.

[2]. Yamaoka, Y., Nambu, M., & Takamatsu, T. (2011). Fine depth resolution of two-photon absorption-induced photoacoustic microscopy using low-frequency bandpass filtering. Optics express, 19(14), 13365-13377.

[3]. Hayashi, T., Farahani, H. F., Rangwala, A. S., & Sakaue, H. (2021, August). Dual-Luminescence Imaging and Particle Tracking Velocimetry for Simultaneous Temperature and Velocity Field Measurements in Hydrocarbons Liquid. In Fluids Engineering Division Summer Meeting (Vol. 85291, p. V002T04A010). American Society of Mechanical Engineers.

[4]. Mercadé-Prieto, R., Rodriguez-Rivera, L., & Chen, X. D. (2017). Fluorescence lifetime of Rhodamine B in aqueous solutions of polysaccharides and proteins as a function of viscosity and temperature. Photochemical & Photobiological Sciences, 16, 1727-1734.

[5]. Magde, D., Rojas, G. E., & SEosin Ybold, P. G. (1999). Solvent dependence of the fluorescence lifetimes of xanthene dyes. Photochemistry and photobiology, 70(5), 737-744.

[6]. Berezin, M. Y., & Achilefu, S. (2010). Fluorescence lifetime measurements and biological imaging. Chemical reviews, 110(5), 2641-2684.

[7]. Paviolo, C., Clayton, A. H. A., Mcarthur, S. L., & Stoddart, P. R. (2013). Temperature measurement in the microscopic regime: a comparison between fluorescence lifetime-and intensity-based methods. Journal of microscopy, 250(3), 179-188.

[8]. Kubin, R. F., & Fletcher, A. N. (1982). Fluorescence quantum yields of some rhodamine dyes. Journal of Luminescence, 27(4), 455-462.

[9]. Lai, M., & Lü, B. (2012). Tissue preparation for microscopy and histology.

[10]. SEOSIN YBOLD, P. G., GOUTERMAN, M., & CALLIS, J. (1969). Calorimetric, photometric and lifetime determinations of fluorescence yields of fluorescein dyes. Photochemistry and photobiology, 9(3), 229-242.

[11]. Lavorel, J. (1957). Influence of concentration on the absorption spectrum and the action spectrum of fluorescence of dye solutions. The Journal of Physical Chemistry, 61(12), 1600-1605.

[12]. Mookherji, A., & P. Tandon, S. (1966). Influence of concentration on the ultraviolet absorption spectrum of bicarbonate ion in state of aqueous solution. Journal of the Physical Society of Japan, 21(6), 1176-1178.

[13]. Wang, M., Stiti, M., Chaynes, H., Becker, S., Berrocal, E., Lemoine, F., & Castanet, G. (2022). Two-photon fluorescence lifetime imaging applied to the mixing of two non-isothermal sprays: temperature and mixing fraction measurements. Experiments in Fluids, 63(11), 172.

[14]. Mendels D A, Graham E M, Magennis S W, et al. Quantitative comparison of thermal and solutal transport in a T-mixer by FLIM and CFD[J]. Microfluidics & Nanofluidics, 2008, 5(5):603-617.

[15]. Ghosh M, Nath S, Hajra A, et al. Fluorescence self-quenching of tetraphenylporphyrin in liquid medium[J]. Journal of Luminescence, 2013, 141(17) :87-92.

[16]. Mehdi, S., Yangpeng, L., Hadrien, C. et al. Fluorescence lifetime measurements applied to the characterization of the droplet temperature in sprays. Exp Fluids 62, 174 (2021).

[17]. Coppeta, J., & Rogers, C. (1998). Dual emission laser induced fluorescence for direct planar scalar behavior measurements. Experiments in Fluids, 25(1), 1-15.

[18]. Chaze, W., Caballina, O., Castanet, G., & Lemoine, F. (2016). The saturation of the fluorescence and its consequences for laser-induced fluorescence thermometry in liquid flows. Experiments in Fluids, 57, 1-18.

[19]. Stiti, M., Labergue, A., Hervy, F., Castanet, G., Becker, S., & Lemoine, F. (2021). Characterization of supercooled droplets in an icing wind tunnel using laser-induced fluorescence. Experiments in Fluids, 62, 1-18

CONTENT 5

Chapter 5 Composition of Evaporating of Two-Component Droplets

In the preceding chapters, we explored the efficacy of laser-induced fluorescence in characterizing droplets within mixing sprays. This technique facilitated the prediction of temperature distribution, affirming the viability of laser-induced fluorescence for spray temperature and composition measurements.

The primary focus of this chapter is the examination of multi-component droplets and their composition during evaporation, utilizing induced fluorescence lifetime measurement. The chapter unfolds with discussions on: (1) Introduction to the importance and necessity of studying two-component droplets (2) Absorption and fluorescence spectra of common fluorescent dye droplets in different solvents (3) Exploration of the effects of different factors (solvent, concentration, temperature, and dimerization) on fluorescence lifetimes (4) Selection of multi-component droplets (5) Modeling of heat and mass transfer for evaporation from a two-component droplet (6) Experiments on the evaporation from a two-component droplet.

5.1 Introduction

As previously mentioned, sprays hold a significant role in various engineering applications. In evaporators and combustion chambers, the process of liquid atomization enhances the surface area between the liquid and gas phases, leading to accelerated rates of droplet evaporation.

An essential concern in these scenarios involves predicting droplet evaporation, particularly when the liquid comprises multiple components. The utilization of multicomponent droplets is more practical and prevalent than mono-component droplets in such applications. Essentially, the majority of practical liquid fuels burned in combustion-powered devices, stationary power plants, and incinerators are multicomponent [1]. Because the differing properties of fuels effects the combustion behavior of the mixture and the combination of different components in multicomponent droplets can lead to improved performance compared to mono-component droplets, such as increasing burning rates and reducing extinction diameter and soot formation and in industries such as pharmaceuticals, using multicomponent droplets can enhance drug delivery.

The evaporation of multicomponent droplets involves more complicated mechanisms. In the evaporation of multicomponent droplets, the composition and thus the physical properties of the liquid and gas phases are constantly changing with time due to the difference in volatility of the vaporizing components. The slow rate of mass diffusion inside the liquid results in strong concentration gradients near the droplet surface when compared to heat diffusion. In the gaseous phase, the Stefan flow generated by the vapor released at the droplet surface results in a strongly coupled transport of the species [2]. Another issue is also the increases in the evaporation of the components due the non-ideal behavior of the liquid mixture. Obtaining detailed droplet composition information from a measurement technique would be particularly valuable in applications such as spray condensers, gas scrubbers, and spray dryers, where conditions are often too complex to be addressed through numerical simulations.

A small number of physical phenomena have been exploited for measuring non-intrusively the composition of droplets in sprays [3]. Some of those phenomena can be used to measure the droplet temperature because they are both temperature and composition dependent.

Raman spectroscopy is one of the preferred methods for detecting chemical species in mixtures. The frequency shift associated with Raman scattering depends on the nature of the scattering molecules. By analysing the positions and relative strengths of the peaks in the Raman spectrum, quantitative information about the chemical composition can be obtained. However, the weakness of the Raman signal can be problematic when dealing with small scattering particles. Morphology-dependent resonances (MDR) can interfere with the Raman spectrum, leading to changes in the relative intensity of the peaks [4].

Rainbow refractometry has been extensively used for measuring the temperature and composition of droplets. This technique involves measuring the angular position of the rainbow produced in backscattering by individual droplets or a group of droplets. The angular position of the rainbow is shifted as the refractive index varies with composition. Composition measurements have been achieved in n-alkanes based on the variation of the refractive index with the number of carbon atoms. Recently, Promvongsa et al. [5] used rainbow refractometry to characterize the composition of ethanol/water droplets. However, for water-ethanol mixtures, the relationship between refractive index and volume fraction of ethanol is not strictly monotonic, resulting in a loss of accuracy in certain composition ranges. Assumptions about the spatial distribution of the refractive index inside the droplet are usually necessary to interpret the results [6]. The angular position of the rainbow is particularly sensitive to refractive index gradients near the droplet surface, which can be significant due to low mass diffusion coefficients.

Laser-Induced Fluorescence (LIF) is also a useful method for characterizing the chemical composition of liquid mixtures. In some cases, fluorescent molecules naturally present in the mixture can be used for this purpose. Maqua et al. [7] employed LIF to study the vaporization of ethanol/acetone droplets. Acetone molecules fluoresce in the UV range, unlike ethanol molecules. As the droplets vaporize, the fluorescence intensity gradually decreases due to the higher volatility of acetone compared to ethanol. Interpreting these measurements required developing an optical model that accounted for the droplet size, position relative to the optics, and light absorption, which plays a significant role at high molar fractions of acetone.

Another approach to characterizing composition is by adding a specific dye to the liquid mixture, typically at a concentration of a few μg/L. The polarity, viscosity, and chemical interactions of the liquid solvent can affect the emission and absorption of fluorescent dyes. In multiphase flows where moving liquid interfaces can perturb the fluorescence signal, a ratio-metric method is necessary. These measurements are conceptually similar to temperature measurements using fluorescence ratios. Copetta and Rogers [8] pioneered pH measurements in aqueous solutions using a two-colour approach. They used a pair of dyes (fluorescein and Rhodamine B) with emission spectra shifted in wavelength to obtain detection bands with distinct responses to pH. However, they reported potential issues in their measurements, such as bias due to reabsorption, especially in the case of pH-dependent fluorescein. Recently, Koegl et al. [9][10]suggested using two-colour LIF to characterize the composition of n-decane/butanol blends. They observed significant changes in the absorption and emission spectra of the Nile Red dye with varying volume fractions of butanol. However, the emission spectrum of Nile Red is also strongly sensitive to temperature, making it challenging to separate the effects of temperature and composition. Consequently, the fluorescence ratio can be used to determine the butanol concentration when the temperature is held constant. In a similar vein, Maqua et al. [11] developed a method based on three spectral detection bands in a study of ethanol/acetone droplet evaporation. These bands were used to calculate two intensity ratios with different sensitivities to temperature and composition. By analysing the variations in these two ratios, Maqua et al. [11] were able to infer both temperature and composition. However, the accuracy of composition measurements was limited due to the detection bands were more sensitive to temperature than composition. Identifying suitable detection bands in ratiometric methods can be a complex and time-consuming task.

As an alternative, fluorescence lifetime measurements can be employed. Unlike intensity, fluorescence lifetime is an absolute quantity. It is possible to measure the composition of binary mixtures using a single detection band and a single fluorescent dye. Reabsorption is expected to have minimal impact on lifetime measurements as long as secondary emissions of photons induced by reabsorption remain negligible. The main objective of the present study is to develop a new measurement technique based on fluorescence lifetime. While a few studies, such as Mendels et al. [12], have used fluorescence lifetime to measure composition in the field of fluid mechanics, they did not extensively investigate the effects of temperature on their measurements or the consequences of dye enrichment. However, in the case of droplet evaporation, both temperature and dye concentration are likely to vary significantly.

Therefore, measuring the evaporation of droplets may be a challenge. This chapter focuses on the lifetime based on laser-induced fluorescence to figure out the evaporation of binary droplets in the acoustic suspension state.

First, the effect of the solvents on the lifetimes are explored in terms of the fluorescence lifetimes of different dyes. Then, the focus will be shifted to describe the composition of the binary mixture. Finally, the method will then be used to study the evaporation of binary droplets under acoustic suspension.

5.2 Fluorescence Lifetime Measurement of Different Fluorescent Dyes

The fluorescence lifetimes of some fluorescent dyes have been investigated in **Chapter 4**, but it is worth noting that the solvents mentioned in **Chapter 4** are essentially aqueous solutions. In this section, we explore the fluorescence lifetimes of many different fluorescent dyes in different solvents, with the main purpose of laying the groundwork for future studies on bicomponent droplet evaporation. The effect of the solvent on the absorption and emission spectra as well as the lifetime of different fluorophores are investigated in order to select a suitable mixture of fluorescent dyes.

5.2.1 Fluorescenct Dyes Absorption and Emission Spectrum

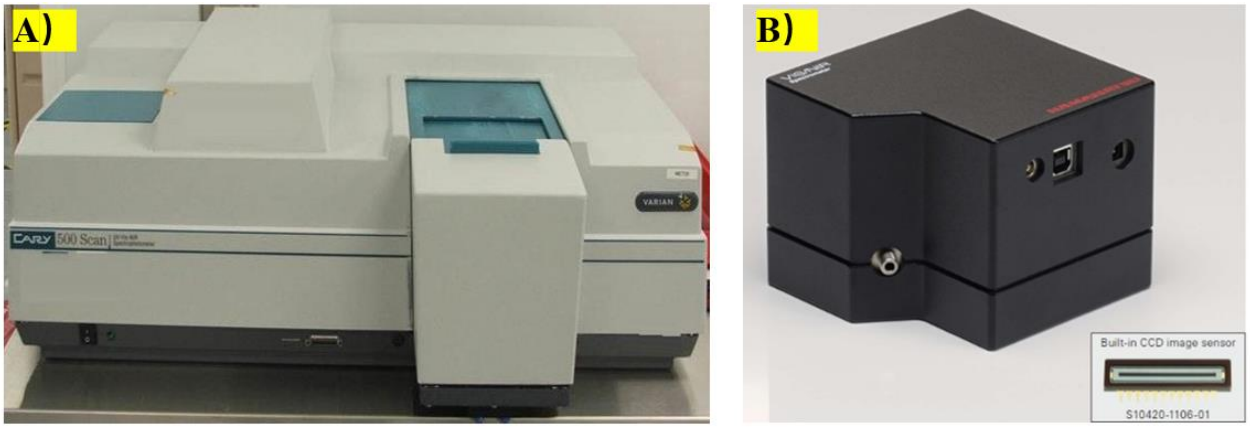

Figure 5-1 Absorption and Emission spectrometer

A) Cary 500 Scan UV-VIS NIR Spectrophotometer B) HAMAMATSU VIS/NIR Spectrometer

Below is a brief description of the dyes and solvents that are considered in this work. Present investigations are conducted with six fluorescent dyes: Eosin Y (EY), Oxazine 4 (OX4), Pyrromethene 556 (PM556), Rhodamine 640 (Rh640), Rhodamine 6G (Rh6G), and Rhodamine B (RhB).

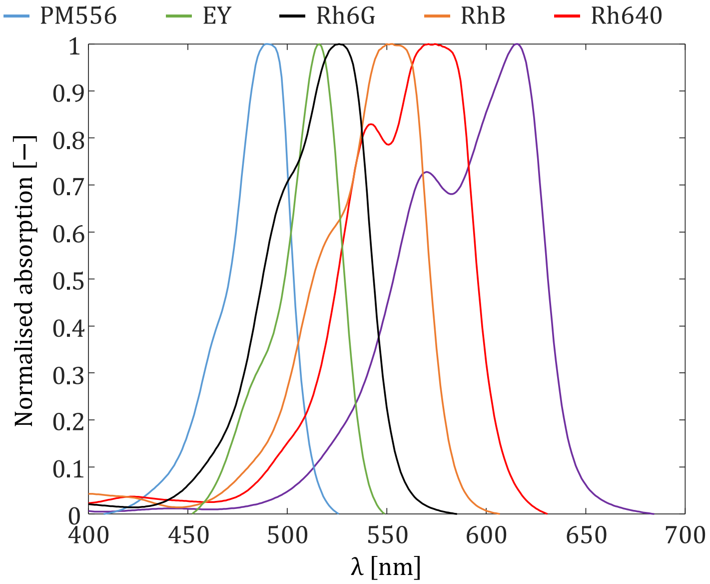

Figure 5-2 Absorption spectrum of EY,OX4,PM556,Rh640,Rh6G and RhB in the aqueous solution

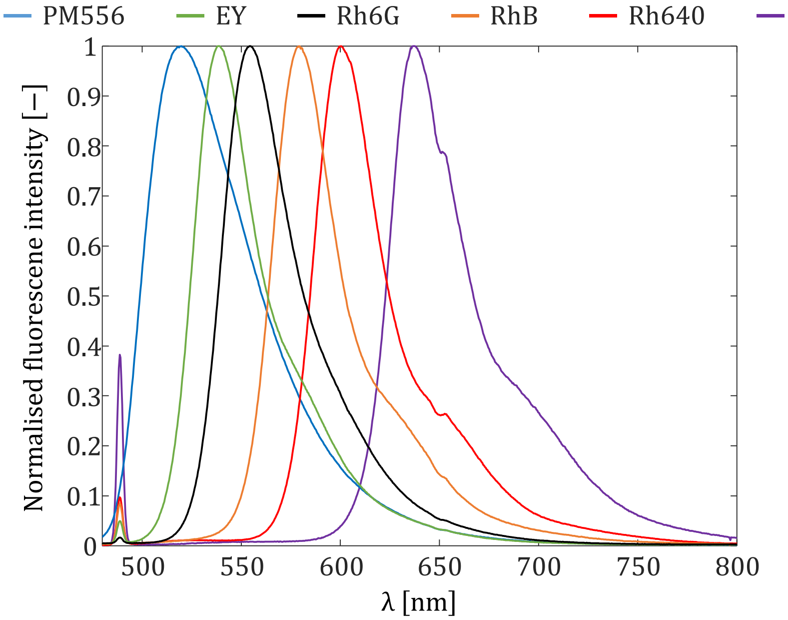

Figure 5-3 Emission spectrum of EY, OX4, PM556, Rh640, Rh6G and RhB in the aqueous solution

Figure 5-2 and **Figure 5-3** show the emission and absorption spectra of these dyes in water at temperature of 20°C and an initial pH of 6.7. These absorption and emission spectra are acquired by spectrometer as shown in **Figure 5-1**. It can be seen that the absorption peaks of these fluorescence dyes (PY556, EY, Rh6G, RhB, Rh640, OX4) corresponds to wavelength of about 485nm, 520nm. 525nm, 560nm, 575nm, 620nm while the emission peaks are around at 525nm, 540nm, 555nm, 580nm, 610nm, 650nm.

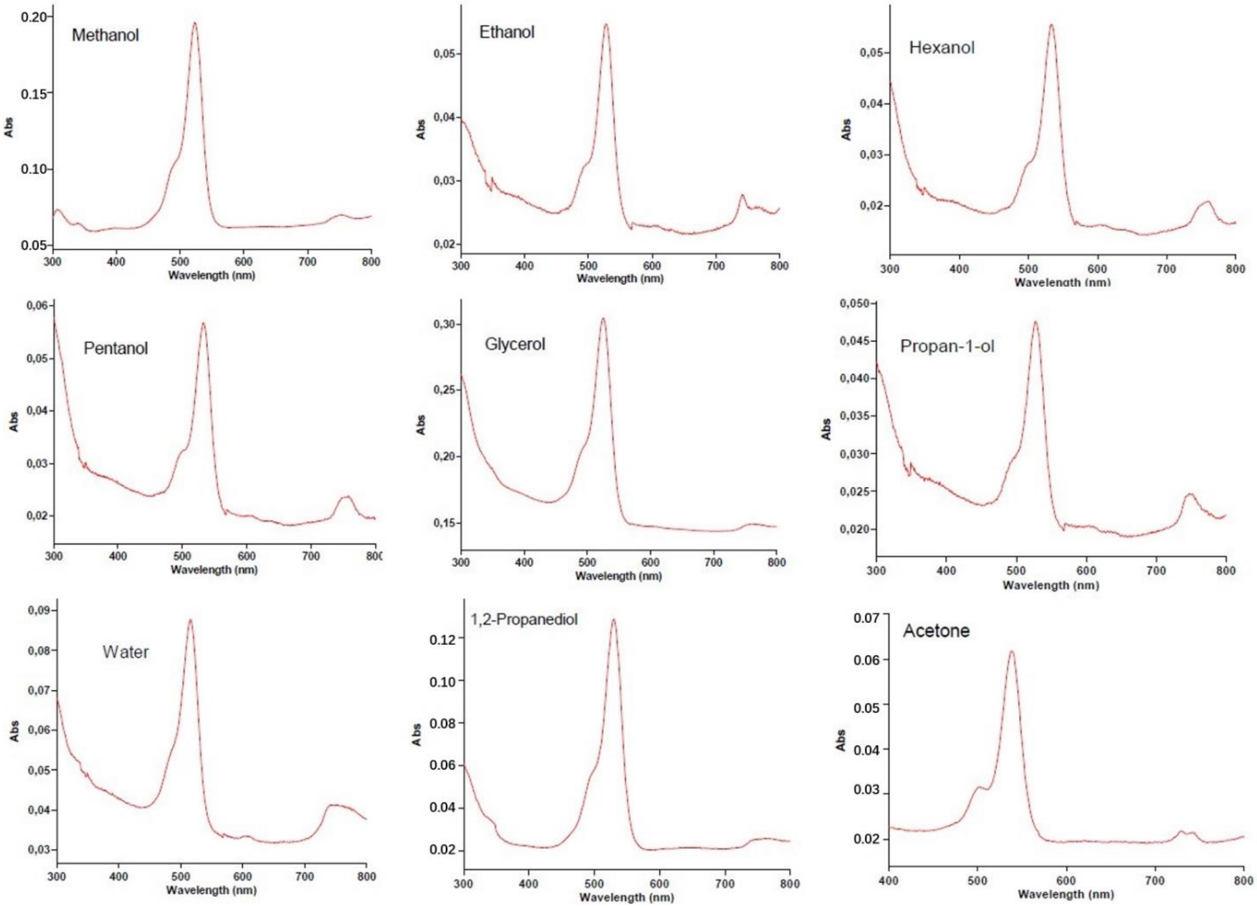

Figure 5-4 Absorption spectrum of EY in different solvents (these are original cases which haven't been normalized, the solvents are respective: methanol, ethanol, hexanol, pentanol, glycerol, propan-1-ol, water, 1-2-Propanediol and acetone)

Figure 5-4 shows absorption spectra of Eosin Y in different solvents and highlights the effect of the solvent on the absorption spectrum of fluorescence dyes. It has been clarified in **Chapter 4.1.1** that the polarity and the viscosity vary with the solvents, which may lead to difference in transition or relaxation process of molecule, thus leads to the distinction of the performance of spectra. From the **Figure 5-4**, it can be seen that the wavelength of the Eosin Y absorption peak is around 520 nm although it is dissolved in different solvents.

Correspondingly, **Figure 5-5** illustrates the emission spectra of Eosin Y in different solvents. The Eosin Y maximum emission in glycerol, acetone and 3-pentanone are about 540 nm, 555 nm and 563 nm, while it is around 545 nm in the other studied solvents.

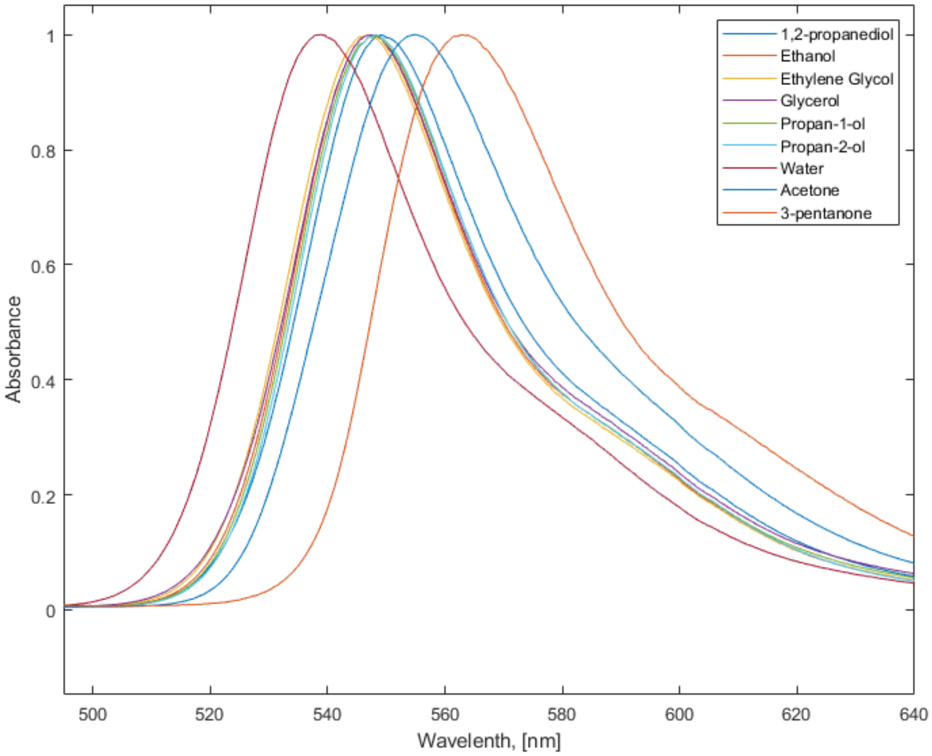

Figure 5-5 Emission spectrum of EY in different solvents (1,2 propanediol, ethanol, ethylene glycol, glycerol, propan-1-ol, propan-2-ol, water, acetone and 3-Pentanone)

The choice of an appropriate fluorescent dye is a major concern for the development of a measurement technique. Beside a high sensitivity to the chemical composition, the dye must be easily soluble in the liquid solvent. Its absorption cross section and quantum efficiency must be high enough to facilitate measurements. If a large volume of liquid needs to be seeded, a low price is also considered.

Due to their ionic nature, most of the dyes mentioned above are insoluble in non-polar solvents, such as Hexane, Toluene, Diethyl ether or Carbon Tetrachloride. Our investigations were therefore limited to polar solvents. The dielectric constant of the solvent provides a rough measure of a solvent's polarity (non-polar solvents have a low dielectric constant and do not have a significant separation of positive and negative charges within their molecules. And non-polar solvents are typically organic substances, hydrocarbons or halogenated hydrocarbons). Solvents with a dielectric constant ε_r less than 15 are generally considered nonpolar.

All the dyes considered in the present study are miscible within the solvents in a large proportion. Among the solvents, some are protic (water, methanol, ethanol, n-propanol, isopropanol, n-pentanol, ethylene-glycol, glycerol) or some are aprotic (acetone and 3-pentanone). Aprotic mainly means that these solvents are not capable of forming hydrogen bonds.

Table 5-1 gives an overview of physical properties related to the tested solvents. A more comprehensive overview of the solvent effects can be found in specialized books such as Lakowicz [13]. Solvent polarity plays a significant role on the spectral behaviour of fluorescent dyes. Following the excitation, fluorescent molecules tend to gain a larger dipole moment. In polar solvents, dipole solvents tend to reorient their position around the excited state of the fluorophore. As the solvent polarity increases, this effect becomes larger, resulting in a lower energy of the excited state and thus an emission at longer wavelengths. Based on theoretical models for the dipolar interactions in a continuous dielectric medium, the energy difference between absorption and emission was postulated to be a function of the orientation polarizability $\Delta v(\Delta v = \frac{\varepsilon_r - 1}{2\varepsilon_r + 1} - \frac{n^2 - 1}{2\,n^2 + 1})$ where n is the refractive index and ε_r is the relative permittivity. This theoretical parameter Δv is not able to cover the various effects of the solvent polarity. More specific effects related to the chemical interactions between the molecules may occur.

In Intramolecular charge transfer (ICT), charge transfer and geometrical modifications occur within the fluorescent molecules after their photoexcitation. Molecules in the ICT state may become the emitting species in polar solvent, while in a nonpolar solvent, the species without charge separation may have a lower energy. Hence, the polarity of the solvent can affect which states of the excited molecules becomes the emitting species. Given the complexity of the solvent effects at the molecular level, empirical scales based on solvatochromic effects are commonly used. One of the most widely used scale is the $ET(30)$ scale [14], which corresponds to the transition energy in kcal/mol between the ground state and the lowest excited state of a reference dye, namely betanine. As can be seen in **Table 5-1**, $ET(30)$ values are roughly correlated with the relative permittivity ε_r[15]. Finally, viscosity can have a significant effect on fluorescence. For some class of fluorescent molecules, named molecular rotors [16] the fluorescence quantum yield is known to increase in viscous solvents. This effect is due to a decrease in the rate of intramolecular rotational motions. Those provide a non-radiative return path to the ground state by dissipating the energy.

Table 5-1 Some relevant parameters of common solvents

	Relative Permittivity ε_r	Refractive Index n	Dipole moment	Orientation Polarizability Δv	ET (30)	Viscosity
Water	80.10	1.333	2.95 D	0.696	63.1	1×10^{-3}
Glycerol	46.50	1.473	4,21 D	0.589	57	1.412
Ethylene glycol	37.00	1.431	2.27 D	0.604	56.3	16.06×10^{-3}
Methanol	33.00	1.331	1.69 D	0.663	55.4	0.545×10^{-3}
1,2-Propanediol	32.00	1.431	2.27 D	0.596	54.1	54.00×10^{-3}
Ethanol	24.50	1.361	1.66 D	0.623	51.9	1.10×10^{-3}
1-Propanol	20.33	1.387	1.65 D	0.590	50.7	1.959×10^{-3}
2-Propanol	19.92	1.378	1.66 D	0.595	49.2	2.40×10^{-3}
Pentanol	15.30	1.408	1,70 D	0.548	49.1	4.00×10^{-3}
Acetone	20.70	1.359	2.88 D	0.610	42.2	0.306×10^{-3}
3-pentanone	17.30	1.391	2.70 D	0.572	39.3	0.47×10^{-3}

5.2.2 Lifetime Measurements of Fluorescent Dyes in Various Solvents

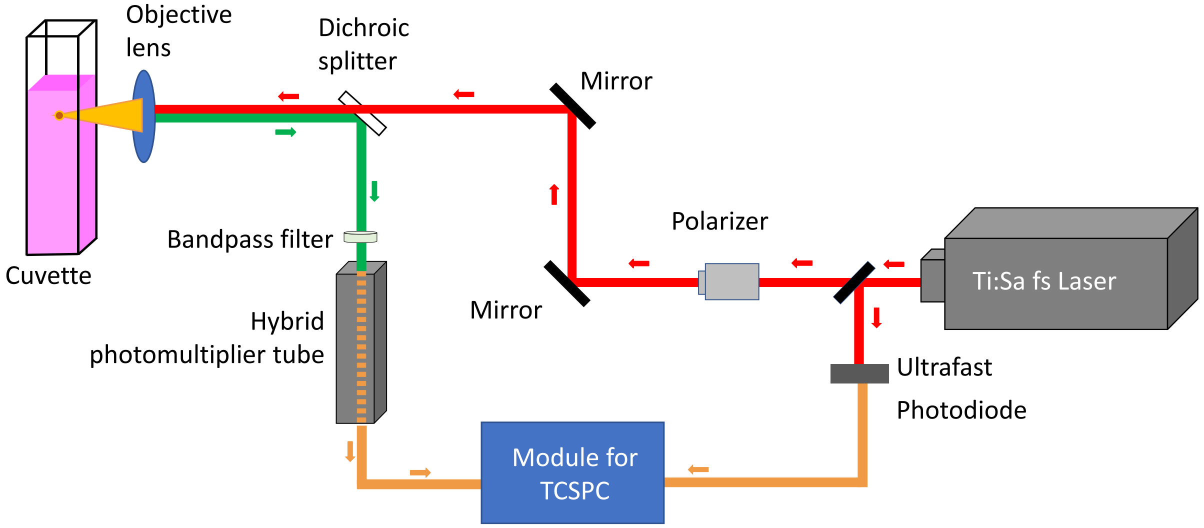

Figure 5-6 Experimental setup used to measure the fluorescence lifetime of the dyes

In section **5.2.1**, the measurements of absorption and emission spectra have been done, which provides a basis for the selection of excitation light and filters in fluorescence lifetime experiment. In this section, several fluorescence lifetime measurements will be carried out with the aim to choose the appropriate fluorescence dyes and solvents for studying evaporation of bicomponent droplet.

Time Correlated Single-Photon Counting method (TCSPC) is used to measure the fluorescence lifetime in the time domain. The experimental setup presented in **Figure 5-6** is quite similar to a previous study by [17], where the fluorescence lifetime was used for measuring the temperature of water droplets injected into a polydisperse spray. he photoexcitation of the fluorescent dye is performed by means of a femtosecond Ti:Sa laser (Coherent Chameleon Ultra II). The laser has a pulse width of about 140 fs and its emission wavelength can be tuned from 690 to 1080 nm. For an excitation in the visible range, the frequency of the laser beam is doubled using a second harmonic generator. A hybrid photomultiplier tube (R10467, Hamamatsu) cooled by a Peltier cell is used to detect the fluorescence photons. The output current of the photomultiplier is transmitted to a time-correlating counter (HydraHarp 400 controller, PicoQuant GmbH) which is operating in forward start stop mode to determine the arrival times of the photons. These measurements require a sharp timing of the laser pulse emission, which is achieved using a fast photodiode (TDA 200 from PicoQuant GmbH), which is also connected to the timing electronics. This photodiode receives the laser light reflected by a beam splitter (99% T, 1% R) positioned at the laser output. The time difference between the event and the detection of a photon by the photomultiplier tube (PMT) is recorded in a histogram that displays the number of the photons as function of time. A bandpass filter is mounted in front of the photomultiplier tube to limit perturbations due to the ambient light. When necessary, this filter is changed to match the emission of the fluorescent dye.

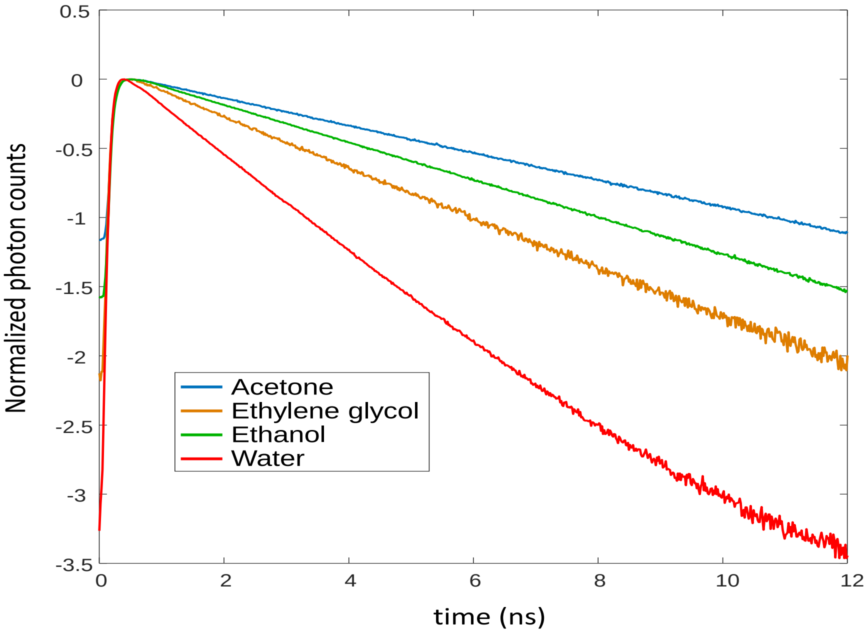

Figure 5-7 Fluorescence decay of Eosin Y in various solvents. These measurements were obtained in a cuvette at room temperature ($C_{EY}=10^{-6}$mol/L, T=20°C, the detection band is [570 nm-590 nm]).

As an example, **Figure 5-7** shows the fluorescence decay of EY dissolved in various solvents (acetone, ethylene glycol, ethanol, and water). The fluorescence decay is much faster in water. which is the solvent with the highest polarity. The fluorescence lifetime of EY gets shorter as the solvent polarity increases.

The fluorescence lifetime τ is defined as the time that fluorescent molecules remain in the excited state before returning to the ground state. It is commonly assumed that the fluorescence decay follows a mono-exponential decay. However, to obtain a better fit, we noticed that the fluorescence decay is usually better described by a bi-exponential function. The fluorescence decay can be then described as follows:

$$F(t)/F(t=0) = \alpha_1\, exp(-t\,/\,\tau_1) + \alpha_2\, exp(-t\,/\,\tau_2) \qquad (5-1)$$

where a is an average parameter between 0 and 1. From Eq. (2), the fluorescence lifetime τ is computed as:

$$\tau = a\,\tau_1 + (1-a)\,\tau_2 \qquad (5-2)$$

This value of the lifetime can be viewed as the lifetime a fluorophore with a mono-exponential decay which would have the same steady-state fluorescence intensity $\left(F_\infty = \int_0^\infty F(t)\,dt\right)$. When the solvent is a mixture of two chemical species, considering a two-exponential decay is essential. In practise, parameters, a, τ_1 and $\tau_2$are obtained by a non-linear least squares method, consisting to minimize the difference between the theoretical decay given by Eq$(5-1)$ and the experimental decay[18]. Since the fluorophore interacts with both solvent species and its lifetime differs in each of them, the decay must be at least a combination of two exponentials. However, despite a two-exponential fitting greatly improves the quality of the fit compared to a one-exponential decay, adjusted values of parameters τ_1 and τ_2 cannot be easily related to the lifetimes of the fluorophore in the two-solvent species, nor does the parameter a can be identified to the mole fraction of the binary mixture.

The accuracy of the valuation of τ depends on several factors. Firstly, the timing jitter of the different elements that constitutes the TCSPC system may induce a bias in the measurement. The instrument response function (IRF), i.e., the time spread introduced by all the components in the measurement system, was evaluated at 90 picoseconds width at half maximum (FWHM). This is small in comparison to the fluorescence lifetime. Nevertheless, the theoretical model in Eq$(5-1)$ is convoluted to the IRF, before the parameters a, τ_1 and τ_2 are estimated. The noise coming from the PMT and the environment is considered by adding a “noise” uniformly distributed in time to the fluorescence model. The TSCPC technique is remarkable for its high signal to noise ratio. The noise (count rate in the dark) is about 70 Cps while the count rate is usually about 10^5-10^6 Cps in the measurements. This enables to capture without difficulty variations over more than 3 decades in the recorded histograms, provided that enough photons are collected.

In the present study, special care has been taken to ensure that enough photons are registered in the histograms (at least 2 million). Under these conditions, repeated measurements indicate that the measurement accuracy of the fluorescence lifetime is approximately 0.02 - 0.03 ns. This value is given as an indication, since the uncertainty may vary from case to case. This value of the uncertainty was obtained by repeating the measurements several times and by using a Monte Carlo method (as illustrated in **chapter 4**). In the Monte Carlo method, artificial fluorescence decays are built up by randomly choosing the arrival times of the photons while considering an adequate model for the fluorescence emission (Eq$(5-1)$). Characteristics of the measurement system (instrument response function (IRF), noise level, number of collected photons) can be also accounted for. For instance, the IRF induces a time convolution in the timing response of the measurement system.

Due to the multiexponential nature of the fluorescence decay, slightly different values may be obtained for the coefficients a, τ_1 and τ_2, if one changes the time interval over which the fitting of those parameters is performed. It is usually observed a slight increase of the average lifetime τ (Eq$(5-1)$) when the initial time of the fit is increased. Unfortunately, it is difficult to obtain a good fit from the time when the laser pulse is released (i.e., a fit which includes the rising phase of the curves in **Figure 5-7**). In practice, the start of the fit is set a little time after the apex (around 0.3 ns). In the following, the results will be given for a time interval of the fit from 0.8 ns to 12 ns.

Finally, TCSPC is well-known to suffer from measurement errors when the incoming flux of photons is too high since the detection capability of the PMT is restricted by a dead time. The detector cannot detect a second photon for several ns when it arrives after a first one. To preserve the Poissonian nature of the fluorescence emission, no more than a single photon must be detected per laser pulse. To meet this important requirement, the laser power and the dye concentration are adjusted to have a count rate of less than 3 MCps in all our measurements.

The fluorescence lifetime of the dyes was measured in various solvents and are presented in **Table 5-2**.

Table 5-2 Fluorescence lifetimes (unit **ns**) of EY, OX4, Rh640, RhB, Rh6G and PM556 in various solvents*

	EY	**OX4**	**Rh640**	**RhB**	**Rh6G**	**PM556**
Water	**1.12**	**2.50**	**4.22**	**1.66**	**3.80**	**4.71**
Glycerol	**2.11**	**2.74**	**3.94**	**3.33**	**3.78**	**3.96**
Ethylene glycol	**2.24**	**2.91**	**3.92**	**2.51**	**3.41**	**4.34**
Methanol	**2.77**	**3.65**	**4.61**	**2.08**	**4.11**	**4.85**
1,2-Propanediol	**2.41**	**2.91**	**4.03**	**2.99**	**3.57**	**4.04**
Ethanol	**2.92**	**3.45**	**4.67**	**2.33**	**3.94**	**4.61**
1-Propanol	**2.74**	**3.35**	**4.55**	**2.88**	**3.73**	**4.37**
2-Propanol	**2.90**	**3.42**	**4.22**	**2.72**	**3.67**	**4.34**
Pentanol	**2.99**	**3.18**	**4.05**	**2.74**	**3.56**	**4.33**
Acetone	**4.03**	**5.02**	**6.13**	**1.90**	**4.89**	**5.08**
3-pentanone	**3.80**	**3.86**	**4.46**	**2.43**	**4.38**	**5.06**
Hexanol	**2.94**	**3.21**	**3.99**	**2.63**	**3.26**	**3.51**

*(The excitation wavelength was 490 nm for all the dyes except in the case of OX4, for which it was 535 nm. For EY, RhB, Rh6G and PM556, the detection band was [570 nm- 580 nm]. For Rh640 and OX4, the detection was shifted to the spectral band [610 nm - 630 nm] more suitable for obtaining signal. Measurements were performed at room temperature (around 20°C). In the case of water, care was taken to use always the same deionized water (pH=6.5))

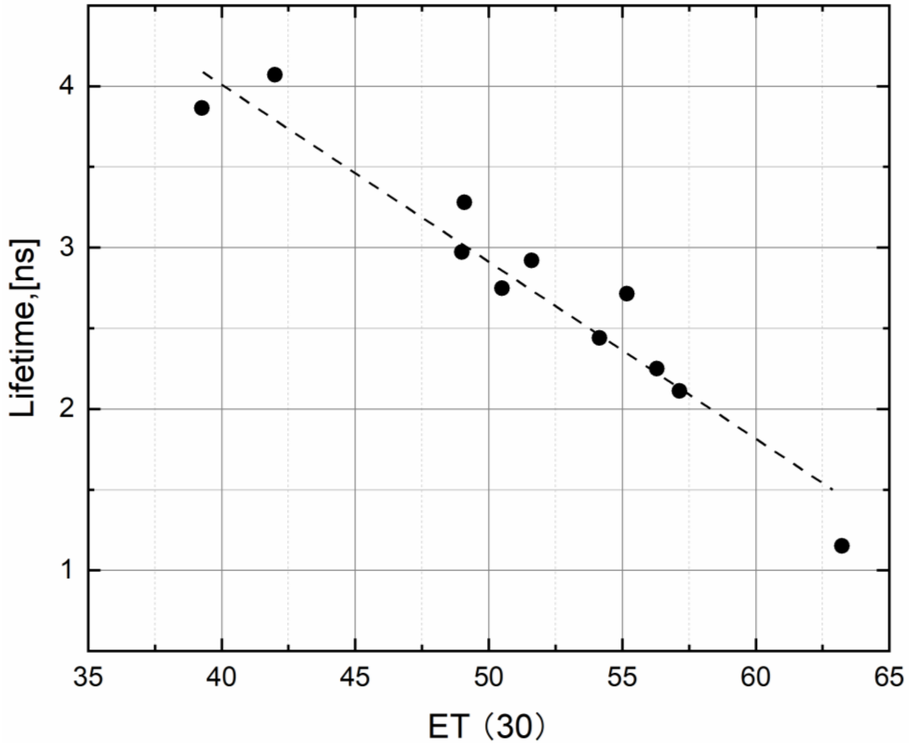

Figure 5-8 Effect of the polarity coefficient ET (30) on the fluorescence lifetime of Eosin Y

As previously discussed, there is no definitive explanation for the effects of solvents on fluorescence. In certain situations, the dominant effect of parameters such as the polarity or the viscosity can be identified. Nevertheless, a few general comments can be made. First, it can be noted that the fluorescence lifetime is often longer in acetone and in 3-pentanone which are aprotic solvents. In most cases, the fluorescence lifetime is lower in protic solvents especially in water, followed by bi and tri alcohols. The fluorescence lifetime of EY and Ox4 seems to decrease essentially with the polarity of the solvent. This behaviour is illustrated in the case of EY in **Figure 5-8** Effect of the polarity coefficient ET (30) on the fluorescence lifetime of Eosin Y. It can be observed that the fluorescence lifetime of EY decreases approximately linearly with the polarity scale ET (30).

In the case of RhB, the polarity of the solvent does not have the same effect. It has been reported that viscosity greatly influences the fluorescence lifetime of RhB in mono and poly alcohols[19]. This is consistent with the high values of the lifetime observed in glycerol and 1,2-propandiaol.

As far as the fluorescence lifetime is envisaged for measuring the composition in binary mixtures, it is important to keep in mind the measurement accuracy of the fluorescence lifetime is of the order of 0.03 ns. Many fluorescent dyes are appropriate for measuring the composition when the solvent species have very different polarity (for example water/acetone). In contrast, when the polarity of the mixture compounds is quite the same (for example ethanol/isopropanol or ethylene glycol/glycerol), the fluorescence lifetime can hardly be used to evidence a change in composition.

5.2.3 Effect of the Temperature on the Lifetime

The effect of the temperature on the fluorescence lifetime is a critical problem in evaporative systems where heat and mass transfers occur in conjunction. To determine the effect of temperature, lifetime measurements were carried out in a 50 ml glass cuvette in which a heating resistor was immersed. A PID controller connected to a thermocouple allows to vary the power supplied to the resistor to reach the required temperature in the cuvette. For the sake of conciseness, the results presented hereafter refers to a limited number of cases.

Figure 5-9 show the effect of the temperature for various fluorescent dyes in water. Among the dyes tested, RhB, Rh WT and PM556 are by far the most sensitive to temperature in water. The temperature-dependency of the fluorescence quantum yield of RhB is commonly attributed to the flexibility of the diethylamino groups positioned on its xanthene core, which accelerates the rate of non-radiative internal conversion.

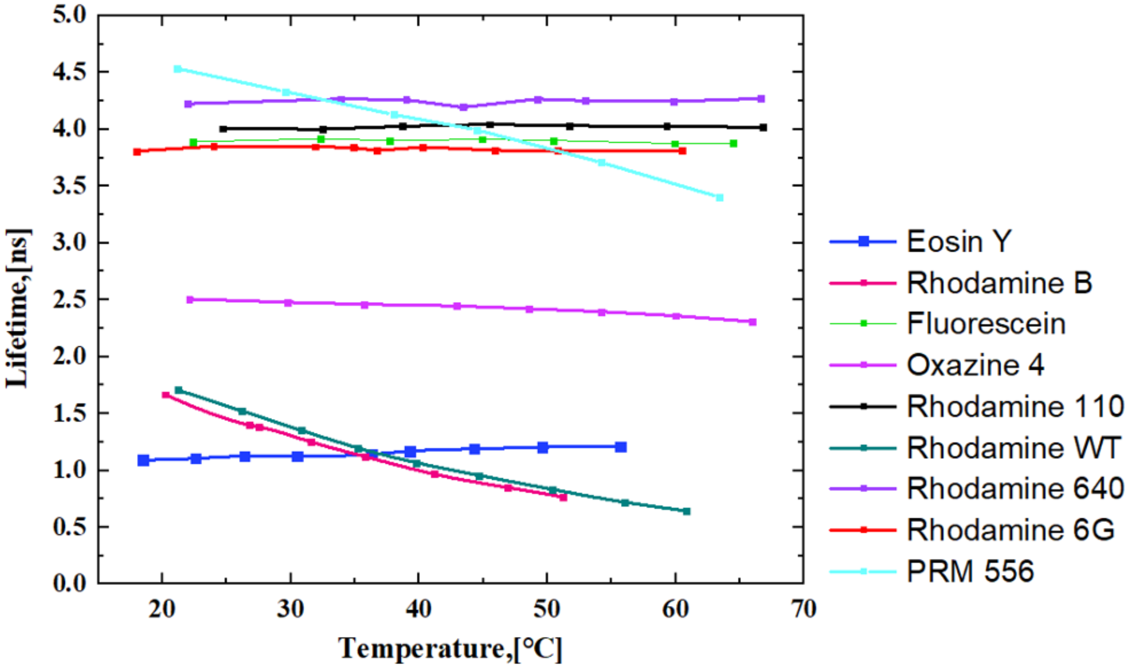

Figure 5-9 Influence of temperature on the fluorescence lifetime of the dyes in water. The dye concentration was set at 10^{-5}mol/L. Measurements were performed using deionized water at initial pH=6.5 at 20°C.

To our knowledge, an effect of temperature for PM556 and Rh WT have never been reported. For the other dyes, the temperature effect is much more limited. A small decrease in the fluorescence lifetime of OX4 and a limited increase in the fluorescence lifetime of EY can be noticed when the temperature variation exceeds several tens of °C. In the other solvents, the fluorescence lifetimes are observed to keep the constant nearly. RhB and Eosin Y are selected for the further study.

Table 5-3 Estimated values for parameters EA and A in the Arrhenus law for Rhodamine B

	Water	Acetone	Ethanol	1-Propanol	2-Propanol	3-Pentanone	Ethylene Glycol
E_a	19830	16190	10150	7483	8890	14200	12130
A	(-)7.612	(-)4.885	(-)3.202	(-)1.951	(-)2.581	(-)4.885	(-)3.964

Figure 5-10 shows that the fluorescence lifetime of RhB decreases with the temperature in all the solvents. An Arrhenius law can be employed to model the effect of temperature on the fluorescence decay of RhB:

$$\tau = A\, e^{E_a/RT}. \qquad (5-3)$$

The pre-exponential coefficient A and the activation energy E_a in the above formula are provided in **Table 5-3** for the different solvents.

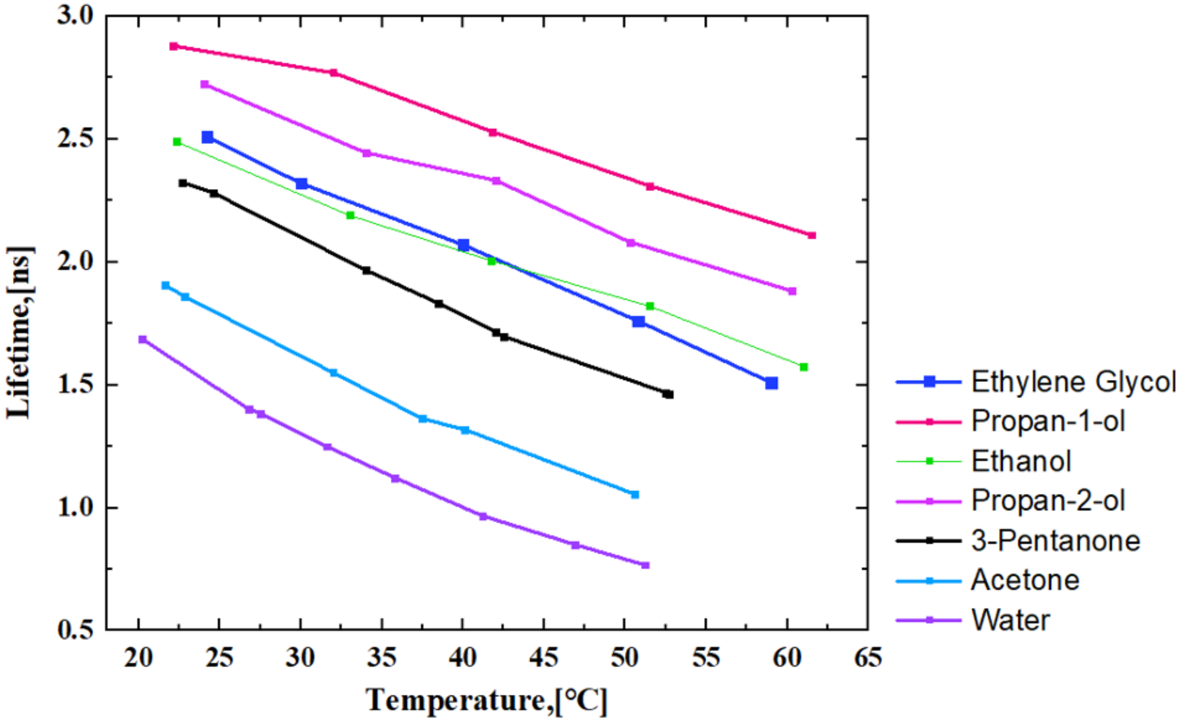

Figure 5-10 Evolution of the fluorescence lifetime of RhB as a function of the temperature in various solvent. Concentration of RhB is fixed at 10^{-6} mol/L.

Values for E_a are close to those already reported in previous studies performed for RhB dissolved in water [20]. It can be seen that the nature of the solvent has effect both on the pre-exponential factor A and the activation energy E_a.

Measuring the fluorescence lifetime could serve as an unambiguous temperature measurement when there is almost the same lifetime in the mixture compounds and the effect of component can be neglected. For example, when RhB is dissolved in a mixture of ethanol and ethylene glycol, the fluorescence lifetime can be used as a judgment of temperature, because at any temperature, the fluorescence lifetime of RhB alone in ethanol or ethylene glycol is very close.

Figure 5-11 show that the fluorescence lifetime of EY exhibits little temperature variation in the various solvents. To confirm this point, additional measurements were carried out in several mixtures. The cuvette was covered with an airtight lid to limit the evaporation and the liquid mixture was continuously stirred. As shown in **Figure 5-11**, measurements in water, ethanol, propan-2-ol, 3-pentanone, ethylene glycol, acetone and propan-1-ol reveal no temperature dependency. The results obtained in the case of EY deserve a few comments. Several studies have evidenced that EY can be used as a temperature probe[21][22][23]. However, in these studies, measurements are based on the intensity of the fluorescence signal. The temperature dependence of the intensity is not related to the quenching rate in the case of EY. Neglecting reabsorption, the fluorescence intensity F can be determined by:

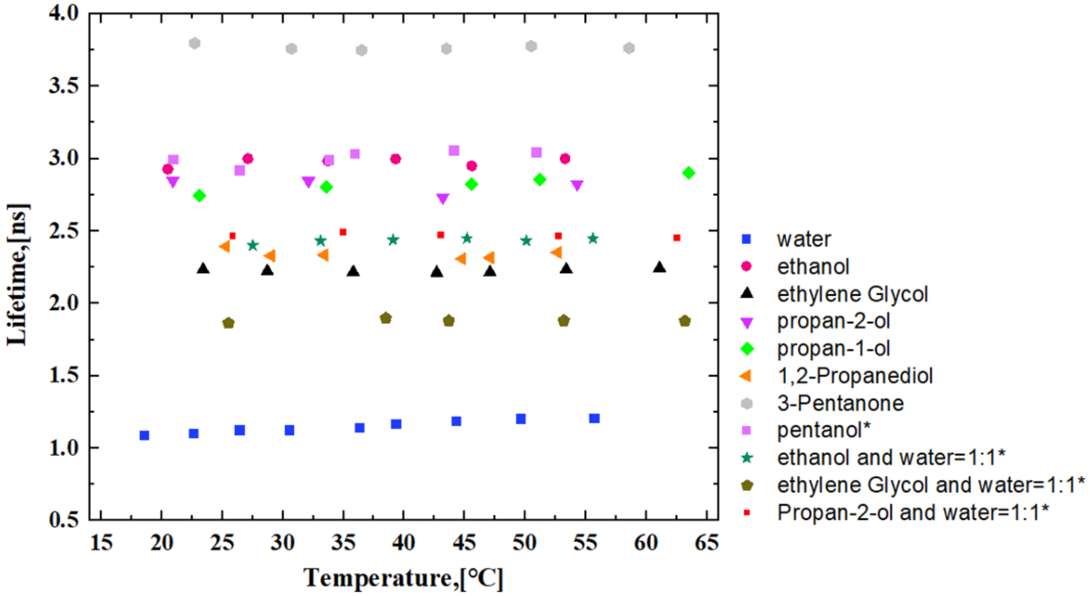

Figure 5-11 Influence of temperature on the fluorescence lifetime of EY in different solvents, and in two binary mixtures (volume fractions: 50% water:50% ethanol; 50% water: 50% propan-2-ol, and 50% water: 50% ethylene glycol).

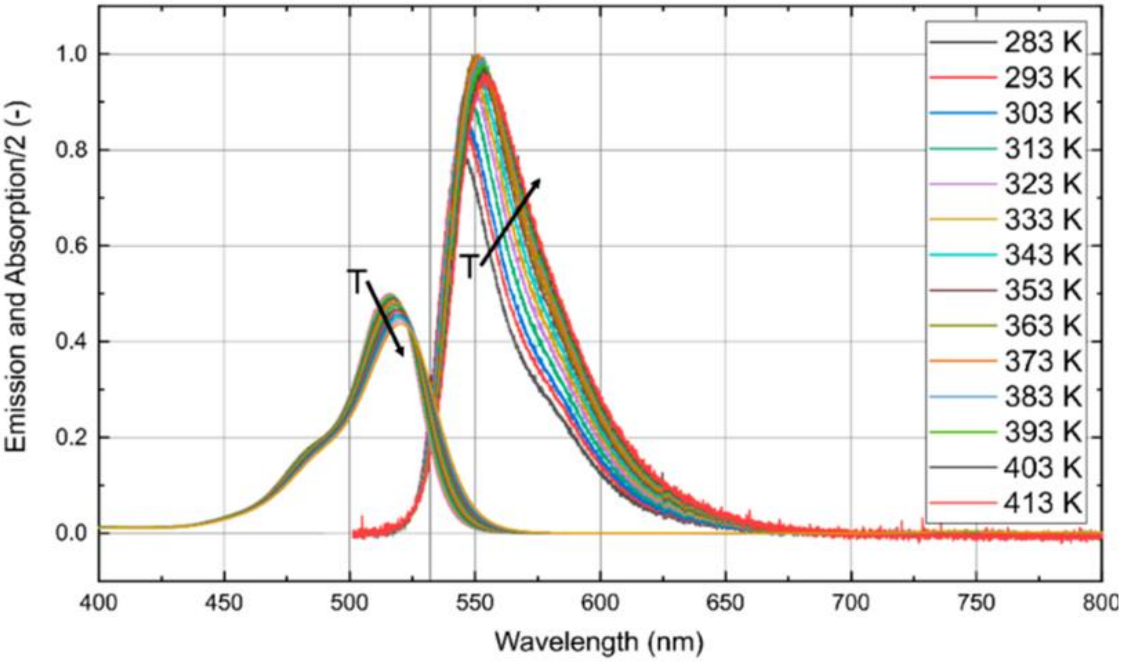

Figure 5-12 Absorption and emission spectra of EY dissolved into water at different temperatures. For the emission spectrum, a Nd:YAG laser at 532 nm was used. Figure is extracted from [23].

$$F \propto \varepsilon(\lambda_0) I_0 \, \phi \tag{5-4}$$

where ε is the absorption coefficient at the laser wavelength λ_0. I_0 is the laser intensity and ϕ denotes the fluorescence quantum yield which can be expressed as:

$$\phi = \tau/\tau_n \tag{5-5}$$

where τ_n is a constant corresponding to the natural lifetime of the dye. Since the fluorescence lifetime τ is not sensitive to temperature in the case of EY, Equation $(5-4)$ implies that the temperature dependence of the intensity comes from the absorption coefficient $\varepsilon(\lambda_0)$. This conclusion is supported by the data from [24].

5.2.4 Effect of the Dye Concentration on the Lifetime

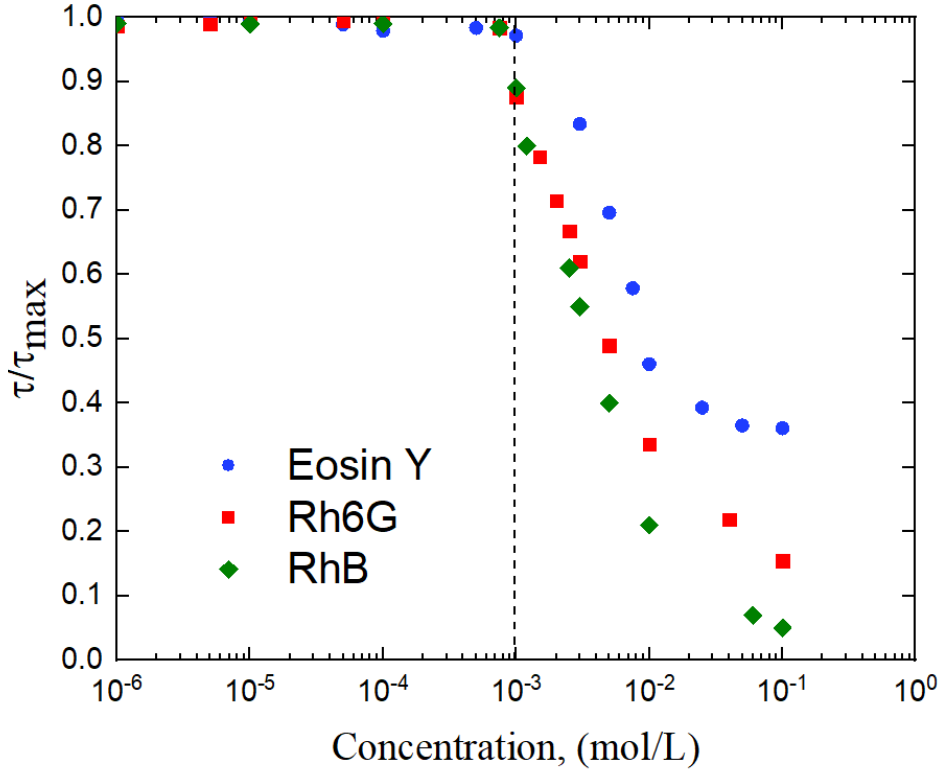

Figure 5-13 Evolution of the fluorescence lifetime of RhB, Rh6G and EY as a function of the concentration of the fluorescent molecule in water. Values are normalized by the fluorescence lifetime $\boldsymbol{\tau_0}$ at low concentration.

Another effect of the high concentration are energy transfers between adjacent fluorescent molecules. To evidence this effect, a microscope objective was used, and a two-photon excitation of the fluorescence was performed. The two-photon fluorescent spot was positioned very close to the edge of the glass cell. To further limit the contribution of secondary fluorescence, photons were detected in a spectral band, which is not reabsorbed. Measurements are reported in **Figure 5-13** in the case of EY, Rh6G and RhB.

A sharp decrease in the fluorescence lifetime is observed as the concentration approaches 10^{-3} mol/L due to self-quenching. This phenomenon corresponds to an energy transfer to another fluorescent molecule. It does not involve any emission and reabsorption of photons. The efficiency of the energy transfer E can be evaluated as:

$$E = 1 - \tau/\tau_0 \qquad (5-6)$$

where τ_0 is the lifetime at low concentration with no self-quenching.

In the Forster theory for resonance energy transfer, the fluorophore is viewed as an oscillating dipole, whose energy can be transferred to another dipole with a similar resonance frequency. The transfer efficiency is strongly dependent on the doner/acceptor distance r. Presently, the donor and acceptor are two molecules of the same fluorescent dye. According to Lakowicz [13], the rate of energy transfer from a donor to an acceptor $k_T(r)$ is given by:

$$k_T(r) = \frac{1}{\tau_0}\left(\frac{R_0}{r}\right)^6 \qquad (5-7)$$

where the Förster distance R_0 is typically of the order of a few nm. Based on Equations $(5-6)$ and $(5-7)$, the efficiency E is expected to evolve as:

$$E = \frac{R_0^6}{R_0^6 + r^6} \qquad (5-8)$$

It shows the variation of E calculated by Equation $(5-6)$ as a function of the distance r between the fluorescent molecules. The distance r is evaluated from the dye concentration C using the following expression:

$$r = 0.1 \cdot (C\ N_{Av})^{-1/3} \qquad (5-9)$$

where N_{Av} is the Avogadro number.

Experimental results are compared to the theory (Equation $(5-8)$). For that, the value of R_0 is adjusted manually. It corresponds to the distance r for which the efficiency E is equal to 0.5. Experimental results are in rather good agreement with the Forster theory assuming a Forster distance R_0 between 5 and 8 nm. It is expected that the intervening solvent does not have a significant effect on the efficiency of the energy transfer, which depends primarily on the distance between donor and acceptor molecules.

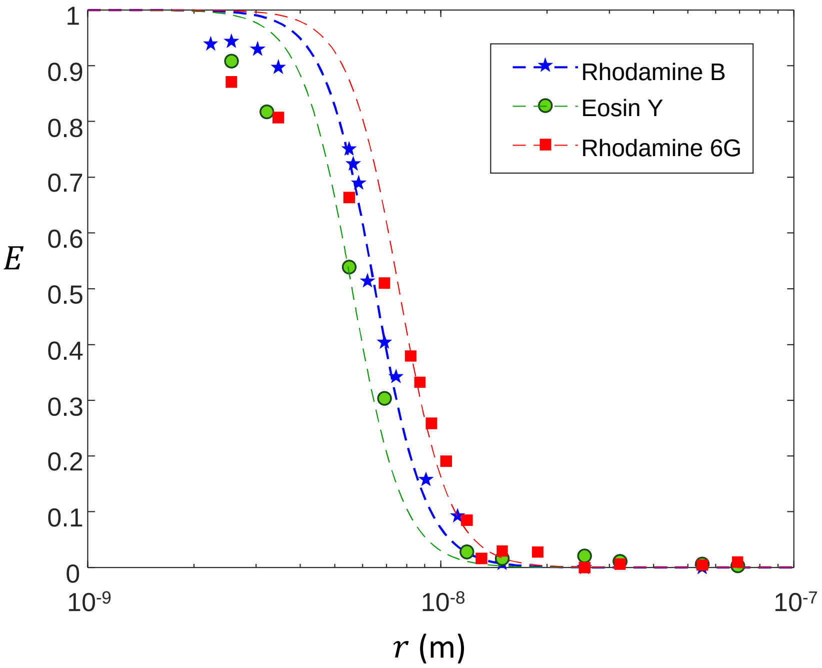

Figure 5-14 Evolution of the transfer efficiency calculated from Equation $(5-6)$ as a function of the distance between the dye molecules in water. The dotted lines correspond to the theoretical value of the efficiency. According to Equation$(5-8)$ assuming $R_0 = 6.5$ nm for RhB, $R_0 = 7.7$ nm for Rh6G and $R_0 = 5.6$ nm for EY.

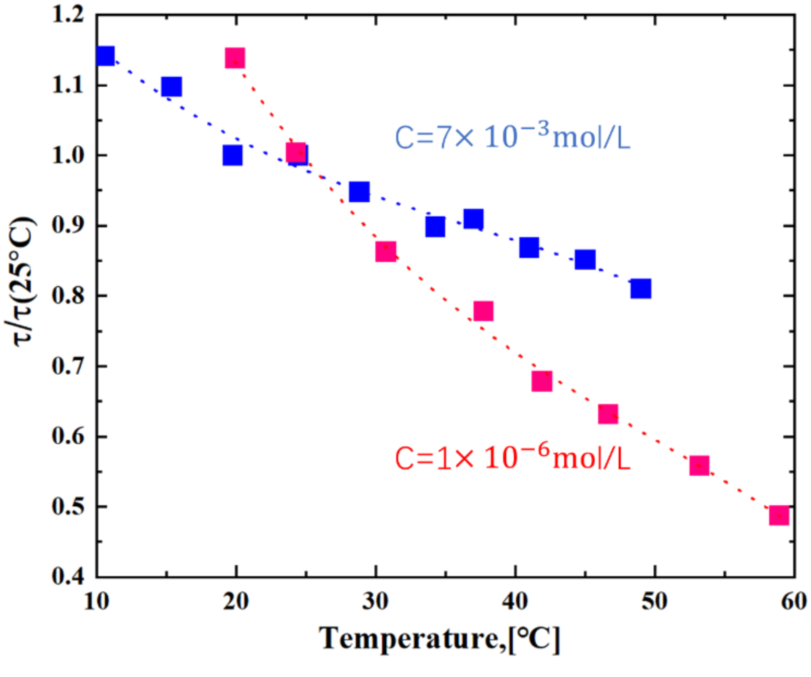

Figure 5-15 Evolution of the fluorescence lifetime of RhB dissolved into water at two concentrations $c = 10^{-6}$ mol/L and $c = 7 \times 10^{-3}$ mol/L.

As the distance between fluorescent molecules reaches the Forster distance R_0, it is observed that the temperature dependency of the fluorescence lifetime decreases substantially in the case of

RhB. The temperature sensitivity of RhB is mainly caused by collisional de-excitation with solvent molecules and the dissipation of energy due the local viscosity. At high concentrations, these non-radiative deactivation pathways are replaced by energy transfer to other fluorescent molecules (self-quenching). The sensitivity to the temperature of the fluorescence lifetime is therefore modified. This reducing value of the temperature sensitivity with high concentration experiments were previously observed by Markides et al[25].

5.2.5 Effect of Dimerization

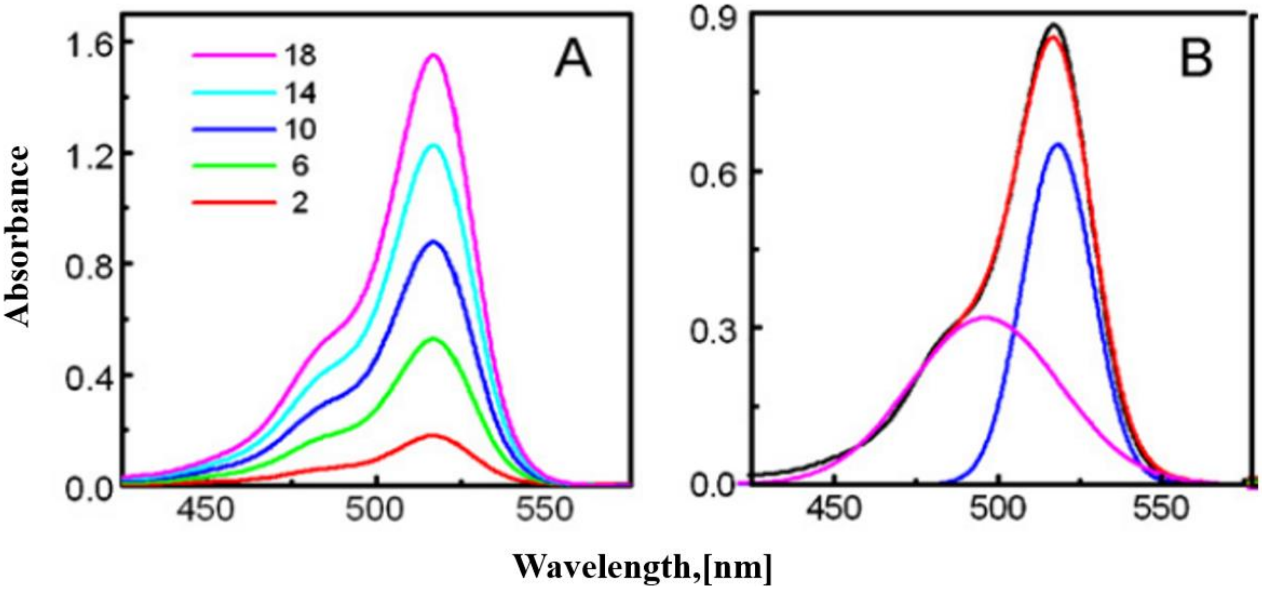

Figure 5-16 (A) Absorption spectra of EY dissolved into water at different concentrations (in µM, mentioned inside the figure). (B) Resolved absorption spectra of 10 µM EY in H_2O (purple for the dimer and blue for the monomer). The red and black lines represent the reconstituted and original spectra of EY respectively. Figure extracted from Chakraborty et al. (2011) [26].

Xanthene dyes like EY are prone to form dimers. The self-association of dye molecules is a frequently encountered phenomenon owing to the strong intermolecular (van der Waals-like force) attractive forces between the molecules. As an example, EY dissolved into water exhibits an intense band of absorption near 517 nm with a shoulder at 496 nm. According to Chakraborty et al [26], the band at 517 nm corresponds to the monomeric form of EY, while the shoulder observed near 496 nm corresponds to the dimeric form of EY. **Figure 5-16** shows the absorption spectrum of EY resolved into monomer and dimer contributions.

There exists an equilibrium between the monomer (M) and the dimer (D):

$$M + M \leftrightarrow D \qquad (5-10)$$

The equilibrium constant of this reaction is calculated by:

$$K_D = C_D/C_M^2 \qquad (5-11)$$

EY dimerizes through the stacking of two monomers in parallel, which arranges in a card-pack manner. Chakraborty et al. [27] evaluated the value of K_D in several solvents. K_D was found to be higher in water and alcohols. The –OH group present in these protic solvents promote aggregation. K_D value of aqueous EY was evaluated to 9.7×10^4 M^{-1} by Chakraborty et al., 3.0×10^4 M^{-1}by Da et al. For low EY concentrations (typically less than 10^{-6} mol/L), the dimer is present to a minor extent. However, for relatively high dye concentrations (typically above 10^{-5} -10^{-4} mol/L), the concentration of the dimer exceeds that of the monomer. The dimeric species exhibit distinct changes as compared to the monomeric species. In a recent study, Masami Enoki [28] investigated the spectroscopic properties of the monomer and dimer forms of EY in water. They were able to determine their respective absorption coefficient, fluorescence quantum yield and fluorescence lifetimes. For the monomer, the quantum yield in water is equal to 0.23 and its fluorescence lifetime is valued at 1.1 ns. In contrast, for the dimer, the fluorescence yield is about 0.005 and the lifetime is about 20 picoseconds. The monomeric and dimeric forms of EY have molar absorption coefficients $\varepsilon_M(\lambda)$ and $\varepsilon_D(\lambda)$ that are comparable in value. The total absorbance A(λ) is the contribution of both the monomeric and dimeric forms.

$$A(\lambda) = \varepsilon_M(\lambda)\, C_M + \varepsilon_D(\lambda)\, C_D \qquad (5-12)$$

The presence of the dimer has therefore an important impact on the absorption. It also affects the intensity of the fluorescence by changing the quenching rate. A modified Stern–Volmer equation was proposed by De et al.

$$\left(\frac{F_0}{F}\right) - 1 = \tau^0\, k_{q_M}\, C_M + \tau^0\, k_{q_D}\, C_D \qquad (5-13)$$

Here, F_0 and τ^0 are the fluorescence intensity and fluorescence lifetime at low concentration and in the absence of dimer. $k_{q_M}$and k_{q_D} are two quenching constants for the monomer and the dimer. In contrast, no effect of the dimer on the measured fluorescence lifetime is expected since the fluorescence lifetime of the dimer is too short to be resolved. Our analysis of the fluorescence decay starts a few nanoseconds after the release of the laser pulse.

5.2.6 Selection of the Dyes

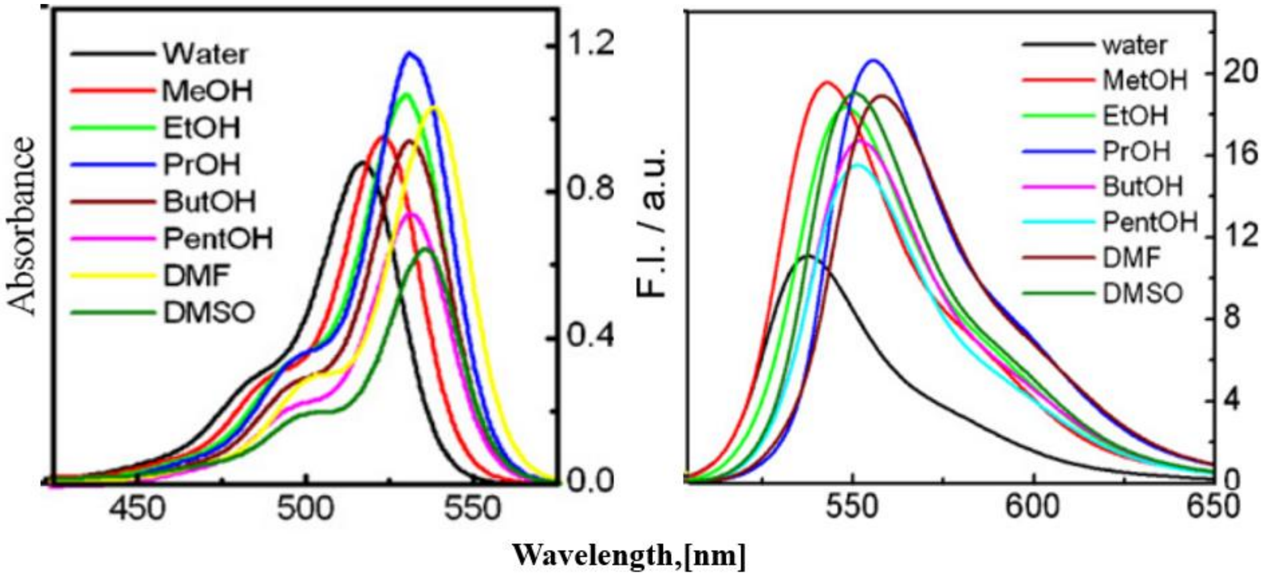

Figure 5-17 Absorption and emission spectra of EY dissolved in the different solvents. Figure extracted from Chakraborty et al. (2011) [26].

Following this preliminary study, EY was chosen to characterize the composition of evaporating droplets. There is no ambiguity related to temperature variation. Provided that the concentration does not reach a critical value of about 10^{-3} mol/L, dye enrichment caused by the solvent evaporation is not a critical problem. The solvent effect seems to correlate well with the ET (30) scale. This allows to have an idea of the mixtures in which the measurement of the chemical composition is the most appropriate.

Measuring the fluorescence lifetime of EY offers an efficient and simple way to determine the composition, but intensity-based measurements are certainly also feasible. **Figure 5-17** shows the evolution of the absorption and emission spectra of EY in different solvents. The wavelength of the emission peak correlates with the polarity coefficient ET (30). The emission spectrum is shifted to the longer wavelengths in water compared to the poly and mono alcohols and the aprotic solvents. Intensity based measurement would be difficult to implement due to the ambiguity in the measurements when the temperature varies since the absorption and emission spectra of EY are both temperature-dependent. In addition, a high concentration of the dye is likely to cause problems (reabsorption, dimerization effect on the intensity and absorption) to a larger extent than in the case of lifetime-based measurements.

5.3 Evaporation of Bicomponent Droplets

5.3.1 Introduction of Acoustic Levitator

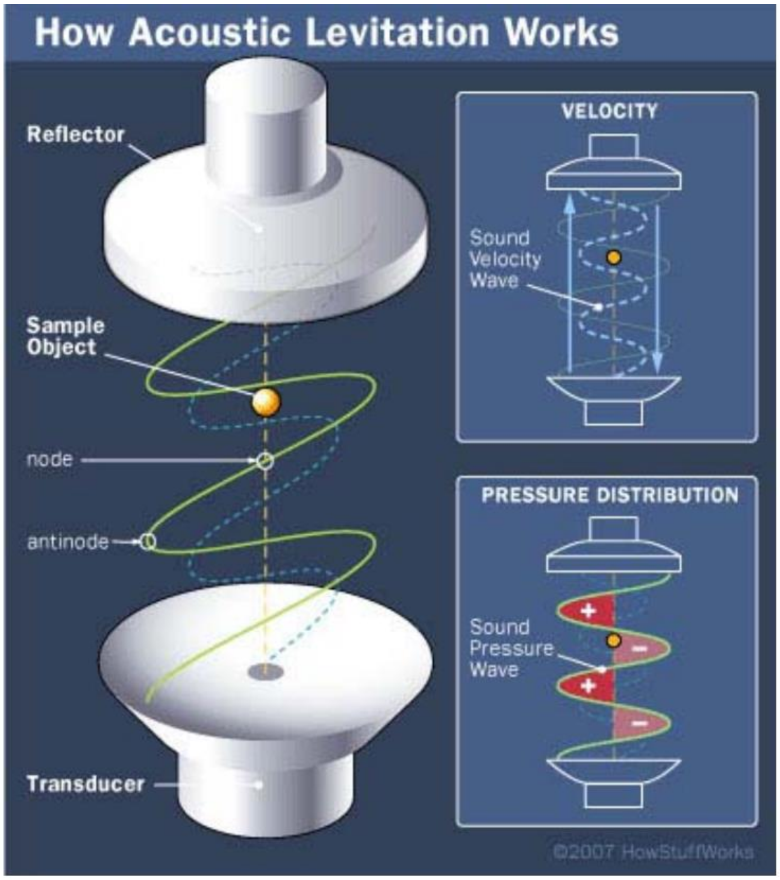

Figure 5-18 Scheme of the principle of acoustic levitation. Extracted from Jason Yang and Michael Redlich

Acoustic levitation is a useful experimental technique for analyzing the evaporation kinetics of single droplets. The experimental value of a levitator is that it suspends droplets without any mechanical contact by making use of a quasi-steady sound-pressure distribution in a confined space. This also helps in maintaining the thermodynamic properties of the levitated droplet and ensures that the heat transfer to an evaporating droplet is only due to the presence of an ambient gaseous medium. Due to these advantages, an acoustic levitator is useful for tracking the life history of an evaporating droplet. In the present study, an acoustic levitator supplied by Tec5 GmbH was used to carry out the experiments. The experimental setup with the levitator is depicted in **Figure 5-18**. The essential component of the levitator is an acoustic resonator consisting of a transducer and a reflector to produce standing ultrasound waves. The transducer is a stainless-steel horn, which is excited to vibrate by a piezo crystal driven by an electrical signal. Due to the vibration, the horn emits sound waves at the vibration frequency, which in the present case is 58 kHz. For acoustic levitation the distance between transmitter and reflector is adjusted to create a system of standing waves with nodes and antinodes. The distance between the transducer and the reflector is adjusted with the help of a micrometer in order to maintain a standing wave, typically containing 4–6 pressure nodes. The reflected wave interferes with the primary wave. The intensity of the acoustic field can be adjusted by modifying the distance between the transducer and the reflector by means of a micrometric screw (i.e., by modifying the resonance tuning). It can be also controlled by changing the voltage applied to the transducer. An enhancement of the levitation force is achieved by curving the surfaces of the reflector. This curvature creates a restoring force in the radial direction and thus keeps the droplet on the central axis of the levitator.

A particle in the field of a sound wave is subjected to hydrodynamic forces. The acoustic radiation force acting on a body in a standing wave has been discussed by different authors. A particle stabilizes in the acoustic field at a position slightly below a pressure node. The pressure difference between the top and the bottom of the droplet generates a force that overcomes gravity. According to Yarin et al., the overall acoustic force acting on an axisymmetric particle is equal to:

$$F_L = F_z = -2\pi \oint_{Top}^{Bottom} P_a \frac{\partial r}{\partial s} r \, dS \qquad (5-14)$$

where P_a is the acoustic radiation pressure. dS is a surface element of the particle. The term $\partial r/\partial s$ is the derivative of the distance r with respect to the arc length s for a point $M(r,z)$ on the surface of the particle. The expression of the acoustic radiation pressure is given by:

$$P_a = \frac{\langle p'^2 \rangle}{2\rho_0 c_0^2} - \frac{\rho_0}{2} \langle v_k' \cdot v_k' \rangle \qquad (5-15)$$

p' is the pressure perturbation in the acoustic field. c_0 and ρ_0 are respectively the sound velocity and the density in the unperturbated air. $\langle \; \rangle$ denotes the time average over a long period of time compared to the wave cycle. The acoustic gas velocity is:

$$\overrightarrow{v'} = \vec{\nabla}\left(-\frac{1}{\rho_0}\int_0^t p' dt\right) \qquad (5-16)$$

When a particle is located in the levitator, a scattered acoustic field appears in addition to the incident one. The total pressure perturbation is given by the sum of the incident wave $(p_i{}')$ and the scattered wave $(p_s{}')$:

$$p' = p_i' + p_s' \qquad (5-17)$$

The scattered wave has the same frequency as the incident wave $\left(p_i' = A_{0e}e^{-i\omega t}\right)$ but an amplitude function of the position relative to the particle:

$$p_s' = p_s(r,z)e^{-i\omega t} \qquad (5-18)$$

The scattered acoustic field can be found by solving the Helmholtz equation:

$$\Delta p_s + \left(\frac{\omega}{c_0}\right)^2 p_s = 0 \qquad (5-19)$$

where ω is the angular frequency. Equation $(5-19)$ is solved with the boundary condition expressing that the particle is practically impenetrable by sound,

$$\vec{n} \cdot \vec{\nabla}(p_i' + p_s') = 0 \qquad (5-20)$$

where the vector $\vec{n}$ is outer normal to the surface. Far from the particle, the scattered field is vanishing:

$$p_s \rightarrow 0, \text{ as } r \rightarrow +\infty \qquad (5-21)$$

Solutions of equation $(5-19)$ with the above boundary conditions have been explored by several authors for different conditions and shape of the particle[29][30]. According to [31], it is determined that the acoustic levitation force F_L acting on a rigid immovable sphere located in the incident wave. A simplified expression for the case of a relatively long ultrasonic wave $(\Omega \ll 1)$ can be written as followed [32][33][34]:

$$\frac{F_L}{\rho_0 c_0^2 a_0^2} = \pi \left(\frac{A_{0e}}{\rho_0 c_0^2}\right)^2 \, sin(2\Omega L)\, f(\Omega) \qquad (5-22)$$

where the size parameter $\Omega = k\, a_0$, with k the wavenumber and a_0 the diameter of the spherical particle. The function $f(\Omega)$ is given by:

$$f(\Omega) = \frac{5}{6}\Omega \frac{3}{(2\Omega)^2}\left[\frac{sin(2\Omega)}{2\Omega} - cos(2\Omega)\right] \qquad (5-23)$$

In Equation $(5-22)$, L is the displacement of the centre of the spherical particle relative to the pressure antinode.

A global mechanical equilibrium is achieved when the gravitational force acting on the levitated particle is balanced by the acoustical radiation force:

$$F_L = m\,g \qquad (5-24)$$

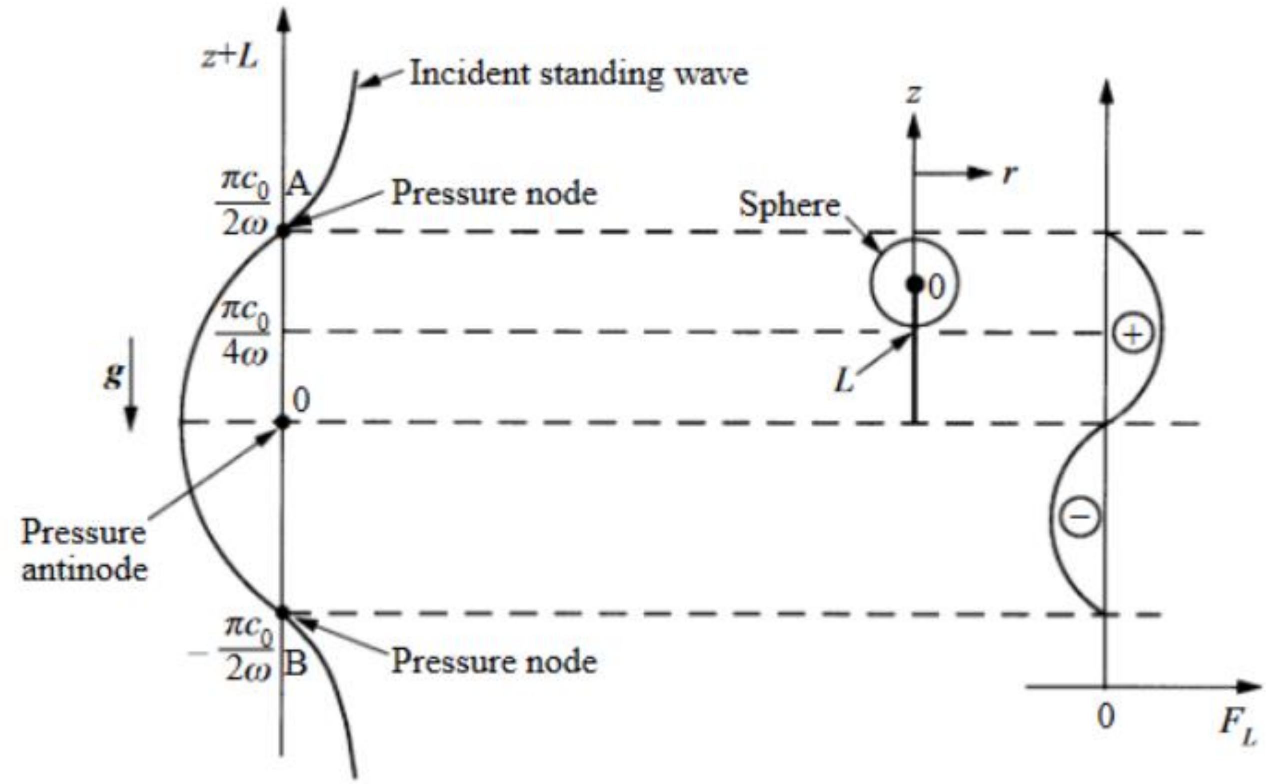

Figure 5-19 Sketch of the incident acoustic wave and the acoustic levitation force acting on a spherical particle. In the reference frame, z=0 corresponds to a pressure antinode. Extracted from Yarin et al.

A particle will experience a difference of force oriented upward against the gravity, when it is positioned in the vicinity of a pressure node. In contrast, the acoustic force is directed downward when the particle is close to a pressure antinode. An overview of the evolution of F_L along the z-axis is given in **Figure 5-19**. To avoid that the particle overlaps successive nodes and antinodes, which would be detrimental for the levitation force, the droplet diameter a_0 should be less than $\lambda/2$ (which gives us in the present case about 3 mm). When placed in an acoustic levitation chamber, the shape of a levitated droplet is not spherical. The droplet is deformed by the acoustic radiation pressure. To predict the shape of a levitated droplet, a pointwise equilibrium of the acoustic, capillary, and hydrostatic pressures must be considered. The fluid pressure at the droplet surface is given by:

$$p = p_0 + p_a - \gamma K \qquad (5-25)$$

where p_0 is the unperturbed ambient air pressure. p_a is the acoustic radiation pressure which is not uniform over the droplet surface. K is the surface curvature and γ is the surface tension coefficient. From the Bernoulli equation, it is expected that:

$$p_a - \gamma K + \rho_l\, g\, z = Cte \qquad (5-26)$$

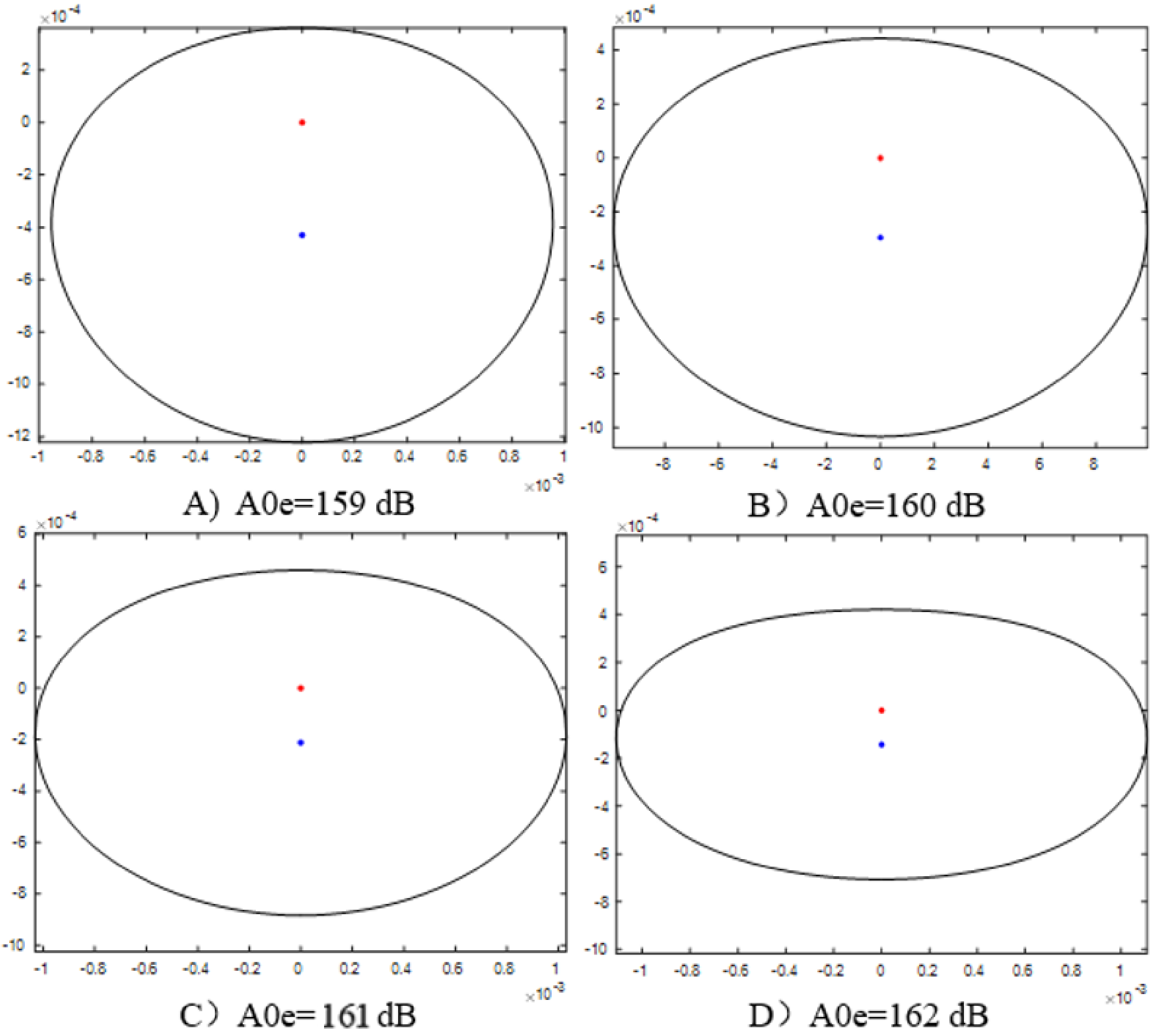

A) A0e=159 dB

B）A0e=160 dB

C）A0e=161 dB

D）A0e=162 dB

Figure 5-20 Evolution of the shape and position of an ethanol droplet (**ρ_l** =789 kg/m3 and **γ**=22 mN/m) as a function of the acoustic pressure. The center of the droplet corresponds to the blue point and the nearest pressure node is represented by a red point. Calculations are made using the model developed by Yarin et al

A significant contribution from Yarin et al [29] has been the determination of the acoustic radiation pressure distribution at the surface of a particle which retains an axisymmetric shape with respect to the z-axis. This allows them to develop an iterative numerical method to find both droplet shape and displacement from the pressure node. Both the local mechanical equilibrium and the global equilibrium must be satisfied at the end of the calculations. The implementation of the method developed by Yarin et al. is beyond the scope of this study. G. Castanet has adapted it based on the information given by the authors. As an illustration, **Figure 5-20** shows the shape and position adopted by a droplet of ethanol whose volume is fixed (here 3 μL). The decibel level (dB) indicated in the caption of the figure is related to the amplitude of the pressure wave using the following relationship:

$$dB = 20\log_{10}(A_{0e}) + 74 \qquad (5-27)$$

where A_{0e} is the sound pressure amplitude expressed in dyne/cm^2. As the acoustic pressure of the incident wave is increased, the droplet is more and more flatten. For small perturbations by the ultrasonic wave, the shape of the droplet is close to an oblate spheroid. Acoustic levitation of a droplet is possible over a limited range of sound pressure level. If the acoustic pressure is too low, the levitation force is too weak to compensate the weight. On the other end, when the acoustic pressure is increased, the deformation of the droplet becomes too larger for the droplet to maintain its integrity owing to the capillary forces. A critical Bond number should be introduced to account for this effect.

To carry out the experiments, the droplet is introduced into the levitator using a syringe with a volume of a few μL. To help the detachment of the droplet from the syringe needle, the sound pressure can be temporarily increased. The levitator is located in an air-conditioned room. The temperature and humidity in the room are measured with a thermometer and a humidity sensor. The ambient temperature is measured with an accuracy of 0.1°C and the relative humidity is given by the sensor with an accuracy of 1%.

5.3.2 Fluorescence Lifetime Measurement Applied to a Levitating Droplet

The system used to measure the fluorescence lifetime is about the same as the one described in **Section 5.2.2** for the preliminary study of the effect of the solvent. Few technical modifications have been made to carry out measurements on suspended levitating droplets. Optics have been selected to illuminate the droplet in volume. A beam expander composed of an afocal doublet of convergent lenses (f_{e1} =30 mm and f_{e2} =150 mm). This optical arrangement allows to obtain a collimated laser beam with a diameter of about 6 mm, which is much larger than the diameter of the acoustically levitating droplet.

Regarding the collection of the fluorescence signal, an optical probe is placed at 90° to the incident laser beam. The collection probe is used to transmit the fluorescence signal to the photomultiplier through a single-mode optical fiber and the fiber core has a diameter of 50 µm (**Figure 5-21**).

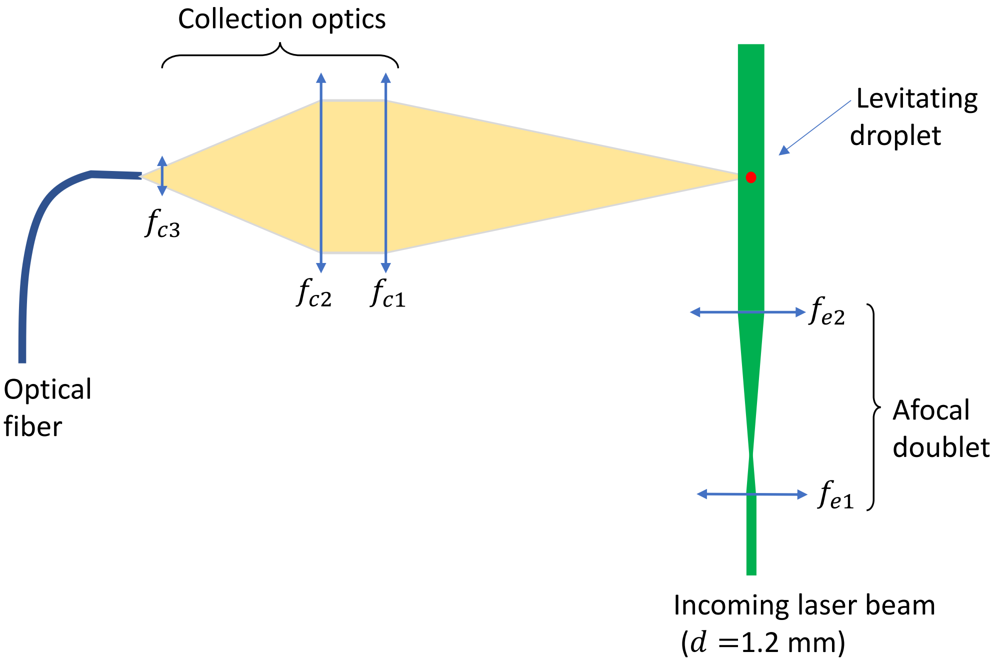

Figure 5-21 Arrangement of the optics in the experiments to measure the fluorescence lifetime in an acoustically levitated droplet

The collection optics is composed of a front lens with a focal length f_{c1}= 200 mm (which can be replaced) and an aperture diameter of 38 mm. A second lens (f_{c2}=100 mm) focuses the light into a third lens of very short focal length whose position can be finely tuned to allow the transmission of the signal to the core of the fiber. Ray tracing can be used to evaluate the collection volume near the focal point of the lens f_{c1}. In the absence of a droplet, the rays coming into the collection probe forms a light beam with a diameter of about 500 µm at the beam waist. The Rayleigh length[5] is estimated to about 1 cm.

The fluorescence signal originates from the regions inside the droplet which are in the field of view of the receiving optics (collection volume) and at the same time illuminated by the laser beam (excitation volume). To define properly the collection and excitation, it is necessary to solve an optical problem considering the refraction and reflection of light rays at the surface of the droplet. Whatever the method chosen (resolution of the Maxwell equations, geometrical optics),

---

[5] the distance along the propagation direction from the waist to the place where the area of the cross section is doubled.

calculations are made complicated, because the droplet is neither a sphere nor a perfect ellipsoid. Moreover, the droplet shape continuously evolves over time with the evaporation and its position also changes. As the droplet mass decreases, its center moves closer to the pressure node. Gradients of refractive index can be significant close to the droplet surface where the composition is changing. For all the reasons above, it is difficult to rigorously define the measurement volume. As a rough estimate, the case of a spherical droplet perfectly centered with respect to the optics has been considered. **Figure 5-22** is intended to provide an illustration in this simplified case. It deals with a spherical water droplet of diameter 2 mm. Ray tracing is limited to light rays that are one-time refracted on the droplet surface. Light focusing inside the droplet limits the collection volume and excitation of the fluorescence. The fluorescence signal in this case originates from a region of the droplet at the center of the droplet, whose size is approximately 1/3 of the droplet diameter.

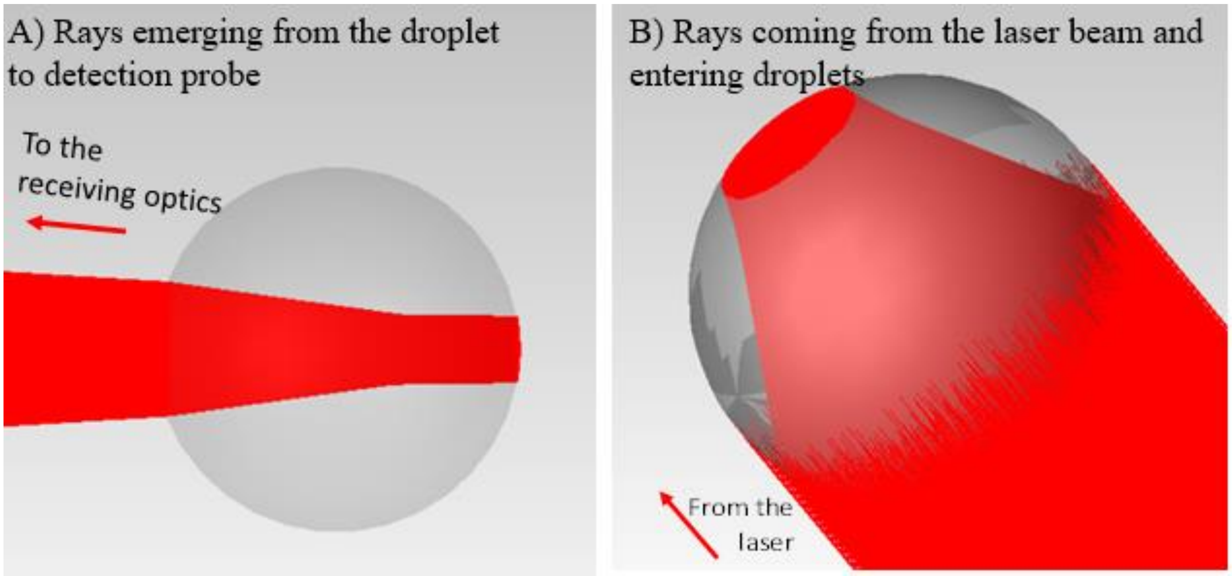

Figure 5-22 Example of ray tracing to determine the regions within the droplet that contributes the most to the fluorescence signal. These results are only light rays that have undergone a single refraction at the surface of the droplet. The droplet is a sphere of radius 1 mm and the refractive index is equal to $n = 1.33$. It is also assumed to be perfectly centered optically.

At the beginning of the experiments, special care is taken to ensure that the droplet is positioned near the centre of the laser beam and on the axis of the receiving optics. To help us with this optical alignment, the entire levitator is moved vertically along the vertical axis until a maximum of signal (count rate) is measured. The position of the levitator and the optics are not changed any more during the experiment even though the droplet is moving vertically towards the pressure node due to its vaporization.

Excitation wavelength:

Among the solvents tested, EY has a maximum of absorption at wavelengths which range from 517 nm (water) to 540 nm (acetone). These wavelengths are available using the second harmonic generator (APE Harmoni SHG), when the ultrashort laser is tuned at wavelength between 1040 nm and 1080 nm. Nevertheless, the laser power is extremely low at these wavelengths (no more than a few mW). For this reason, an excitation at a shorter wavelength was preferred. The laser was tuned at a wavelength of 980 nm, for which the output power is about 1.1 W. The laser beam was then converted to a 490 nm beam in the frequency doubling module. A much stronger fluorescence signal is obtained, even if the excitation wavelength significantly differs from the maximum of absorption of EY. The frequency-doubled laser beam has a maximum power of 230 mW at 490 nm.

Photodegradation of the fluorescent dye

Preliminary tests in a cell have evidenced a loss of fluorescent signal when the liquid solution is illuminated quite for a long time. However, the effect was very limited especially if the solution was stirred. In the case of droplets with a small volume of only a few μL, photodegradation may be a more critical problem. For this reason, several experiments were performed to evaluate the impact of photodegradation on lifetime measurements. Experiments were conducted using droplets of ethylene glycol that had been suspended for an extended period. Owing to the hygroscopic nature of ethylene glycol, these droplets consisted of a mixing comprising around 20% water and 80% ethylene glycol. The water concentration remained consistently stable and is influenced by relative humidity. For a comprehensive discussion of the hygroscopic effect, a variation of the fluorescence intensity due to a change in the droplet volume can be safely ruled out. **Figure 5-23** shows the time evolution of the photon count rate when the droplet is continuously illuminated by the laser beam at the maximum power ($\mathrm{P} = 230$ mW). For this test, it should be noted that the laser beam has not been expanded (its diameter is equal to 1.2 mm). A neutral optical density of 3 was placed in front of the photomultiplier to avoid the saturation of the photodetector, while the dye concentration was increased to 10^{-5} mol/L. It is obvious that the fluorescence signal intensity (expressed in cps) rapidly decreases inside the droplet. Over a period of about 15 minutes, the fluorescence intensity is divided by 10. The degradation continues thereafter without interruption but at a slower pace. The logarithmic scale shows that the signal degradation follows an exponential trend which can be approximately fitted by exp $(-\mathrm{t}/\mathrm{t}_1)$, where $\mathrm{t}_1 = 500$ s. It should be mentioned that the phenomenon is non-reversible. The intensity of the signal does not recover its initial level when the illumination of the droplet by the laser beam is stopped for a while.

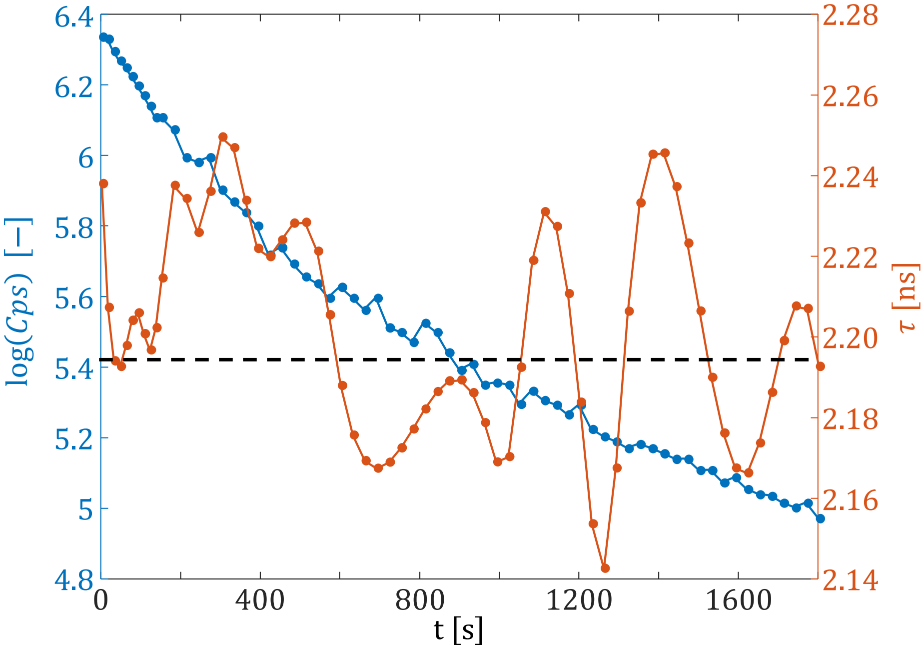

Figure 5-23 Degradation of the fluorescence signal from an acoustically levitated droplet of ethylene glycol. The droplet is illuminated by a laser beam at 490 nm and the laser power is $P = 230$ mW.

Fluorescence lifetime measurements were performed on the same droplet. **Figure 5-24 s**hows that photodegradation does not affect the fluorescence lifetime which remains constant. The fluctuations observed in this figure correspond to a standard deviation of 0.026 ns. Therefore, their value is consistent with the uncertainty already established for the fluorescence lifetime measurements.

The conditions of this first test are far from those in which the measurements will be performed later. Without the addition of a neutral density of 3, the power of the laser excitation and the concentration of the dye can be drastically reduced, so the effect of photodegradation is negligible. A count rate close to the pile-up limit could be obtained for a laser power around 10mW and a dye concentration of 5×10^{-7} mol/L. Here again, it is verified that the lifetime is constant with a very low standard deviation. No explanation was found for the difference observed between the lifetime values at $P = 5$ mW and $P = 10$ mW in **Figure 5-25**.

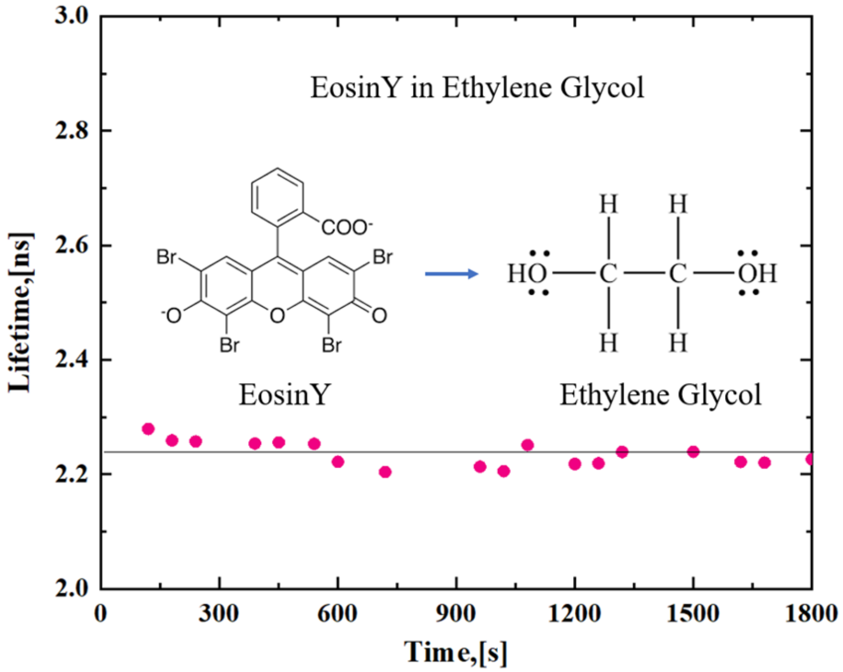

Figure 5-24 Droplet of EosinY in the Ethylene glycol

However, the differences are very small and not very significant. Finally, it should be noted that the above results were obtained by illuminating the droplet continuously, whereas in the experiments of evaporation, the droplet is illuminated only once every 10s for a period of about 2 to 3 s.

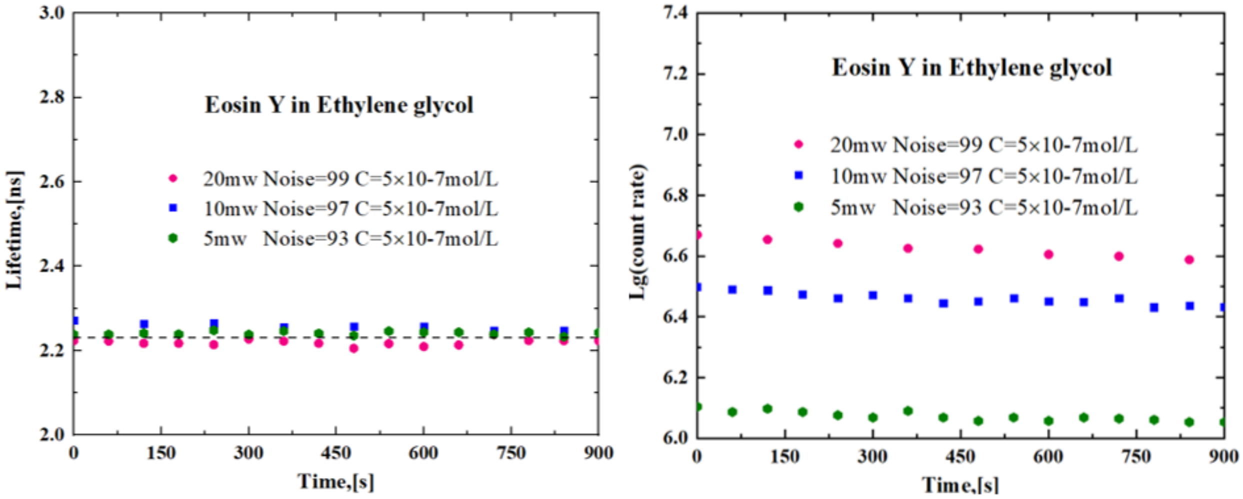

Figure 5-25 Evolution of the photon counting rate and the fluorescence lifetime under the same laser power illumination as the evaporation measurements

Fluorescent dye concentration

Measurements in the drops were performed with an initial dye concentration of 5×10^{-7} mol/L, as there is enough signal for a count rate close to 10^6 cps. Having established that:

- Self-quenching become significant only for concentrations above $C_{crit} = 10^{-3}$ mol/L;
- The dye concentration remains uniform inside the droplet;
- Photodegradation is negligible for the level of laser power, measurements should be valid until the diameter of the droplet reaches the critical value:

$$d_c = \left(\frac{C_0}{C_{crit}}\right)^{\frac{1}{3}} \cdot d_0 \qquad (5-28)$$

This represents a size decrease in a ratio of 20, which is comfortable enough to study the change in composition within evaporating droplets.

Calibration of the mixing fraction

To measure the droplet composition, it is necessary to have calibration curve that relates the volume or mass fraction of the mixture to the value of the fluorescence lifetime. These calibrations are conducted separately in a cell while taking care to ensure the accuracy of the measurements as they will be used later to analyse all the experimental results. The chosen mixtures are binary mixtures with water as one of the components. The reason is quite simple. When mixtures of volatile species evaporate, the temperature of the droplet can decrease considerably, resulting in the condensation of the water present in the air on the surface of the droplet. Since all our experiences take place in the open air, the air is never dry. In practice, the calibration experiment starts with a volume of component A. A determined quantity of component B is added step by step. After each addition of B, the solution is stirred, and the fluorescence lifetime is measured. A precision weighing scale (balance) is used to determine the mass of liquid B introduced after each addition. The mass and volume fractions are then calculated. **Figure 5-26** shows the evolution of the fluorescence lifetime as a function of the volume fraction of water in three types of mixtures: water/ethanol, water/isopropanol, and water/ethylene glycol.

In all these mixtures, there is no linear relationship between the fluorescence lifetime and the volume fraction. For low water mixtures, the variation of the fluorescence lifetime with the volume fraction is generally less important. In practice, this means a lower accuracy in the measurement of the mixture fraction. To depict the above calibration curves, the following polynomial interpolations were derived using the least squares method:

- Water / ethanol mixture:

$$f_v = -3493\,\tau^6 + 4.604\,\tau^5 - 24.48\,\tau^4 + 67.04\,\tau^3 - 99.67\,\tau^2 + 75.94\,\tau - 22.11 \qquad (5-29)$$

- Water/ ethylene glycol mixture:

$$f_v = 6.694\,\tau^6 - 71.78\,\tau^5 + 317.5\,\tau^4 - 741.4\,\tau^3 + 963.1\,\tau^2 - 660\,\tau + 187.6 \qquad (5-30)$$

- Water / propan-2-ol mixture:

$$f_v = 0.6503\,\tau^6 - 7.423\,\tau^5 + 34.61\,\tau^4 - 84.65\,\tau^3 + 114.8\,\tau^2 - 82.28\,\tau + 25.46 \qquad (5-31)$$

- Water / propan-1-ol mixture:

$$f_v = 7.5733\,\tau^4 - 16.8\,\tau^3 + 10.887\,\tau^2 - 3.39\,\tau + 2.87 \qquad (5-32)$$

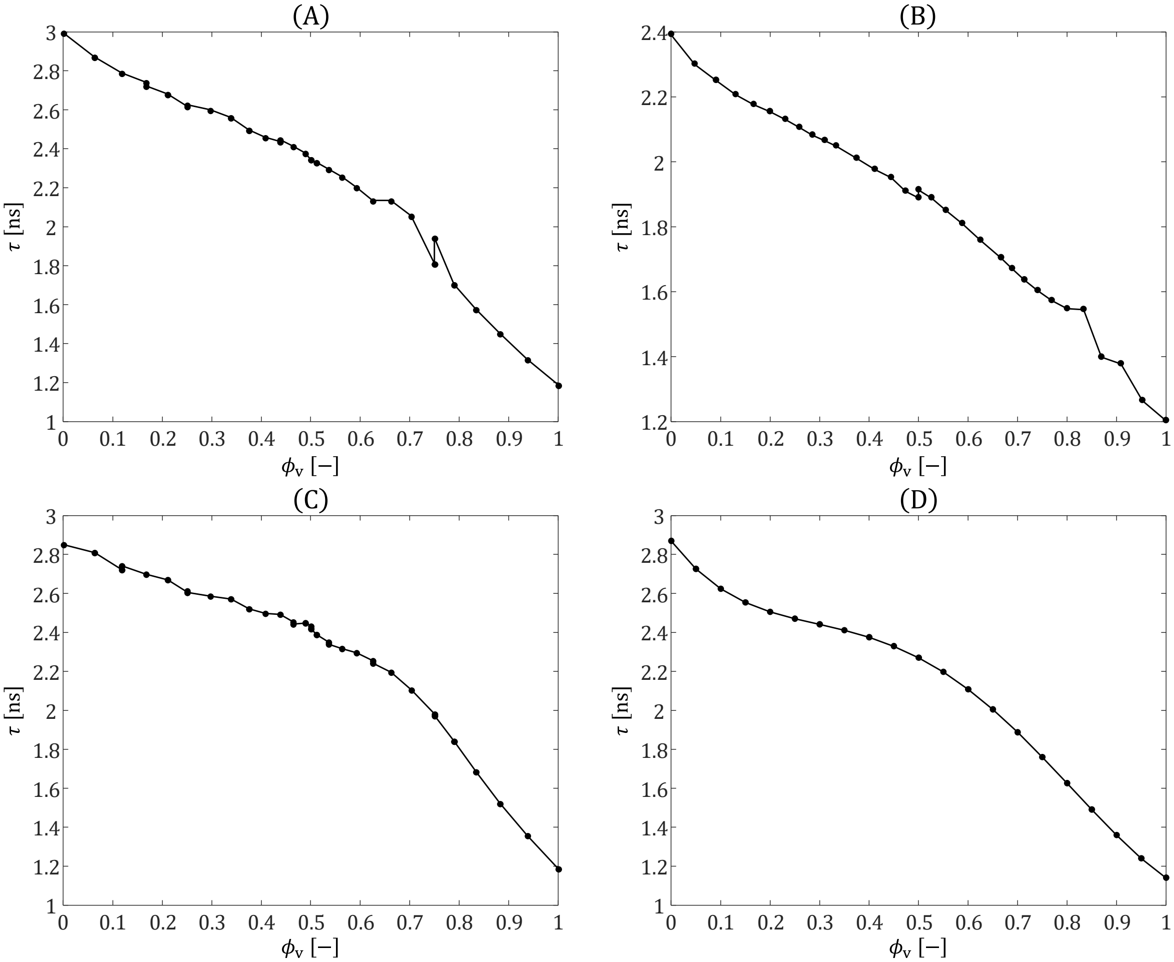

Figure 5-26 Calibration of the volume fraction measurements in for A) water/ethanol, B) water/ethylene glycol, C) water/propan-2-ol and D) water/propan-1-ol mixtures

Pure Water Droplet Measurement by Shadow imaging:

In addition to the measurements of the droplet composition, images of the droplets are recorded by a CCD camera (Prosilicate GT3300). The CCD camera had a resolution of 3000x3000 pixels and a zoom lens (OPTEM C-Mount) with an extension tube allows obtaining a resolution of about 8 µm/pxl. Shadow images, in which the droplet is black on a light background, are obtained by a backlighting. Light from a xenon flash lamp is delivered in the background of the droplet by means of a flexible waveguide. A condensing lens and a diffusing plate are used to ensure a uniform white background in the images. The duration of the lamp flashes is approximately 20 µs, which prevents motion blur on the image (if the droplet is not very stable). Images are acquired approximately every 10 seconds to follow the droplet evolution. Measurements of the fluorescence lifetime are performed in the time interval between the lamp flashes, while the lamp is switched off. Captures of shadow image and fluorescence lifetime measurements are alternating for several minutes until the droplet disappears. Collected images are then analysed to find the contour of the droplet.

The steps of the images processing are briefly presented below:

Step 1: The images of the droplet are first subtracted by an image in the absence of the droplet taken before or after the experiment. This subtraction allows obtaining a homogeneous background.

Step 2: Digital levels I are normalized between 0 for the minimum inside the droplet and 1 for the maximum in the background.

Step 3: The previously obtained image is segmented. Pixels inside the droplet are labelled using matlab's function “graythresh”, which implements the Otsu's method for finding a threshold value that minimizes the intraclass variance of the thresholded black and white pixels.

Step 4: The binary image obtained in the previous step is analysed with the Matlab function "regionprops". This function allows us to obtain several information about the droplet. First, it is used to determine the vertical position of the centre of mass. Regarding the droplet size, it is assumed that the droplet is only weakly deformed by the acoustic radiation pressure and thus its shape can be assimilated to an ellipse in the side view images. The same function is also used to retrieve the major and minor axes of the ellipse, denoted respectively S_l and S_s. Then the volume equivalent diameter D_{eq} and the aspect ratio r_a are computed as:

$$D_{eq} = (S_l^2\, S_s)^{\frac{1}{3}} \qquad (5-33)$$

$$r_a = S_l/S_s \qquad (5-34)$$

Figure 5-27 shows a sequence of images recorded during the evaporation of a round water droplet. Changes in the round droplet from 0 minute to 55 minutes were recorded. It can be seen that round droplets are slowly shrinking due to evaporation.

Round droplets over time

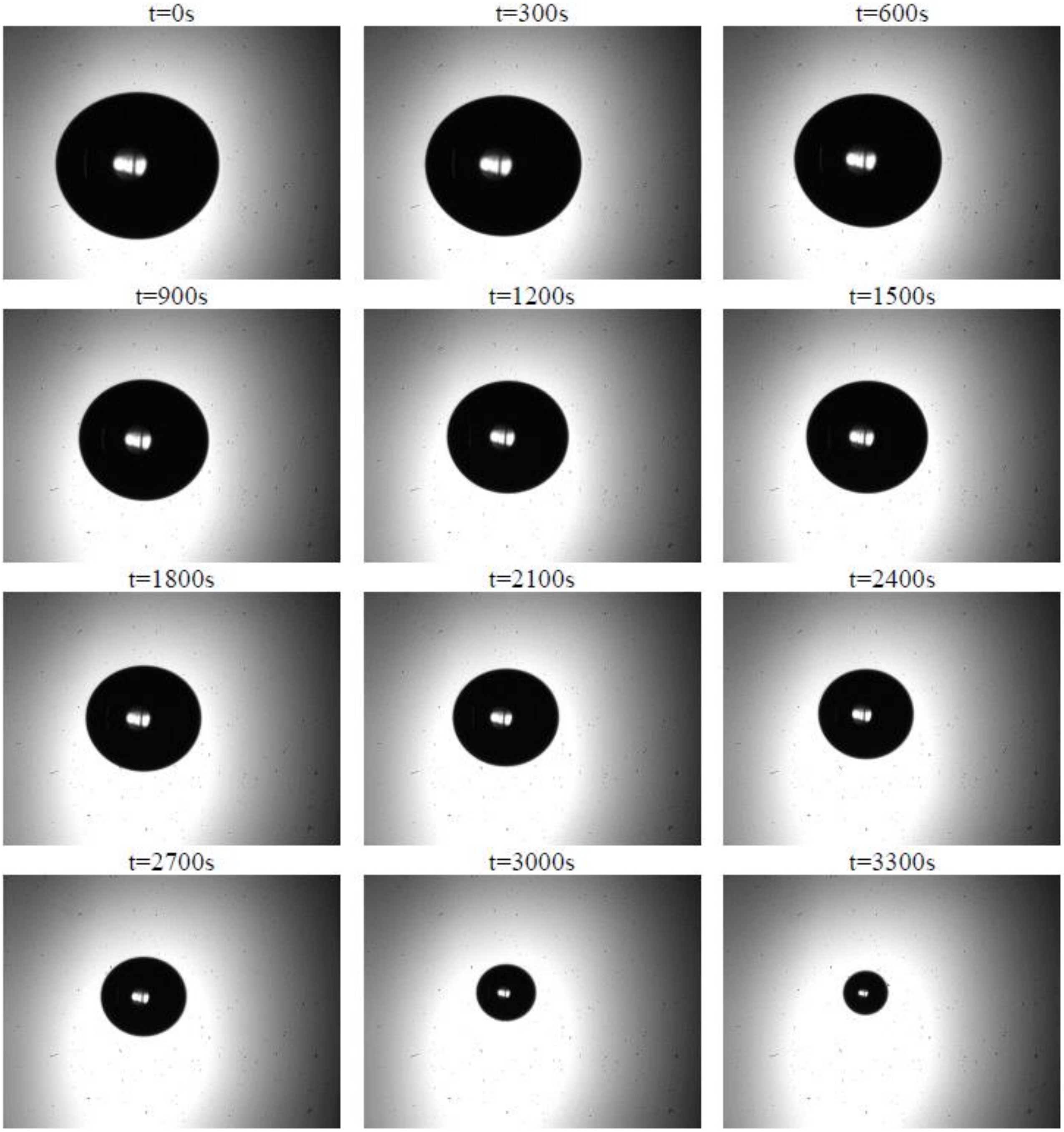

Figure 5-27 Case of a round water droplet evaporating in air at $T_\infty = 20°\mathrm{C}$ and H=42%(Relative Humditiy). The initial diameter of the drop is 2.0 mm.

Figure 5-28 and **Figure 5-29** are the analyse of the variation of equivalent diameter (normalized diameter square ratio) and aspect ratio. It can be seen that the evolution of the squared equivalent diameter follows a linear decrease with time. The behaviour is typical of an evaporating droplet under steady-state ambient conditions. As expected, the droplet gradually rises to approach the pressure node. The aspect ratio is fluctuating and gradually close to 1.05. As the droplet gets smaller, the capillary pressure increases which retains the droplet in a more spherical shape.

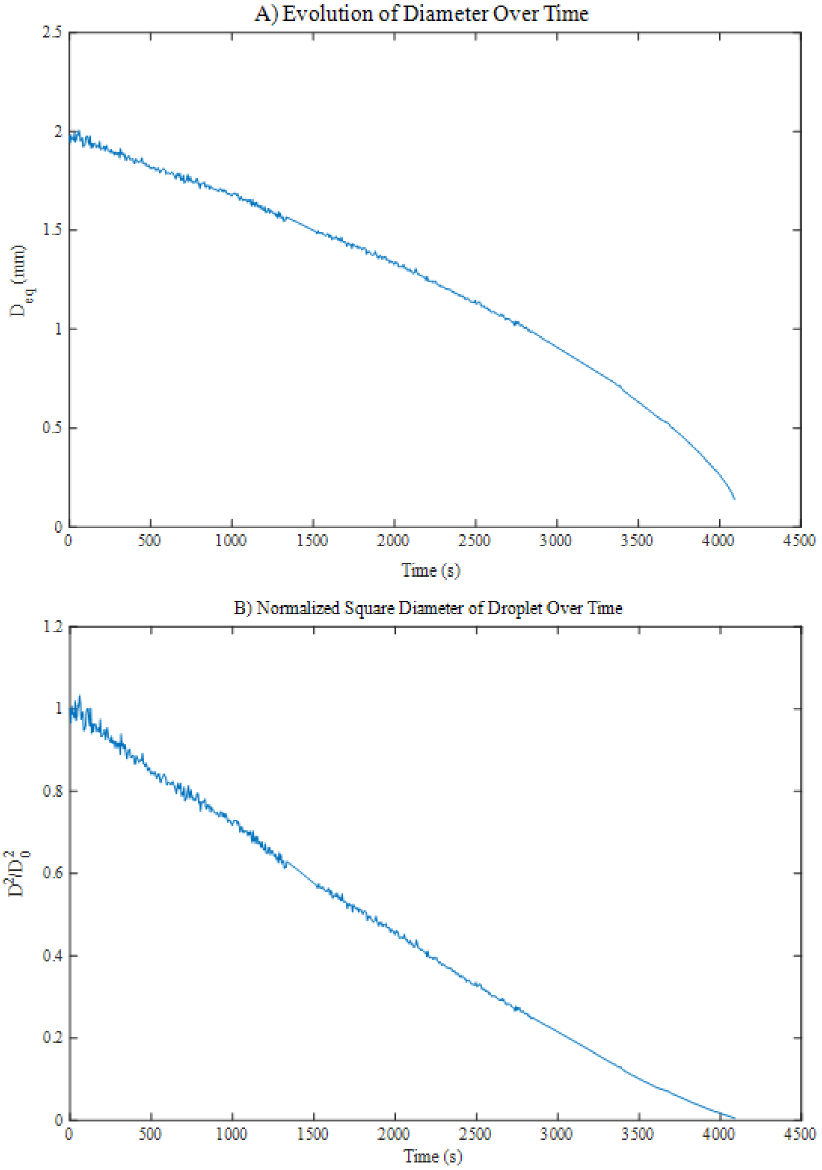

Figure 5-28 Evolution of the round droplet A) Equivalent diameter B) Normalized square diameter.

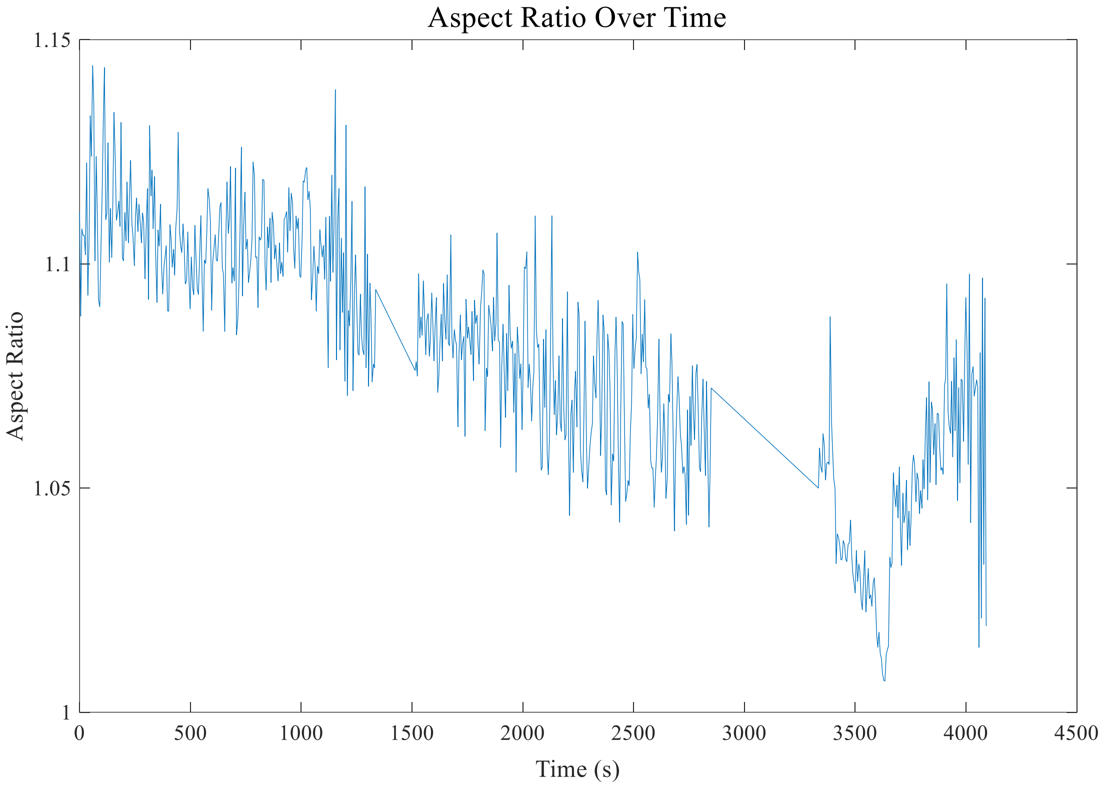

Figure 5-29 Evolution of the round droplet aspect ratio

Correspondingly, **Figure 5-27** shows a sequence of images recorded during the evaporation of an elliptic water droplet. Changes in an elliptic droplet from 0 minute to 55 minutes were recorded.

Figure 5-28 and **Figure 5-29** are the analyse of the variation of equivalent diameter (normalized diameter square ratio) and aspect ratio. The evolution of the squared equivalent diameter follows a linear decrease with time, also in the elliptic droplet. The behaviour is typical of an evaporating droplet under steady-state ambient conditions.

As expected, the droplet gradually rises to approach the pressure node. The aspect ratio is fluctuating and gradually close to 1.0. As the droplet gets smaller, the capillary pressure increases which retains the droplet in a more spherical shape.

Elliptic droplet over time

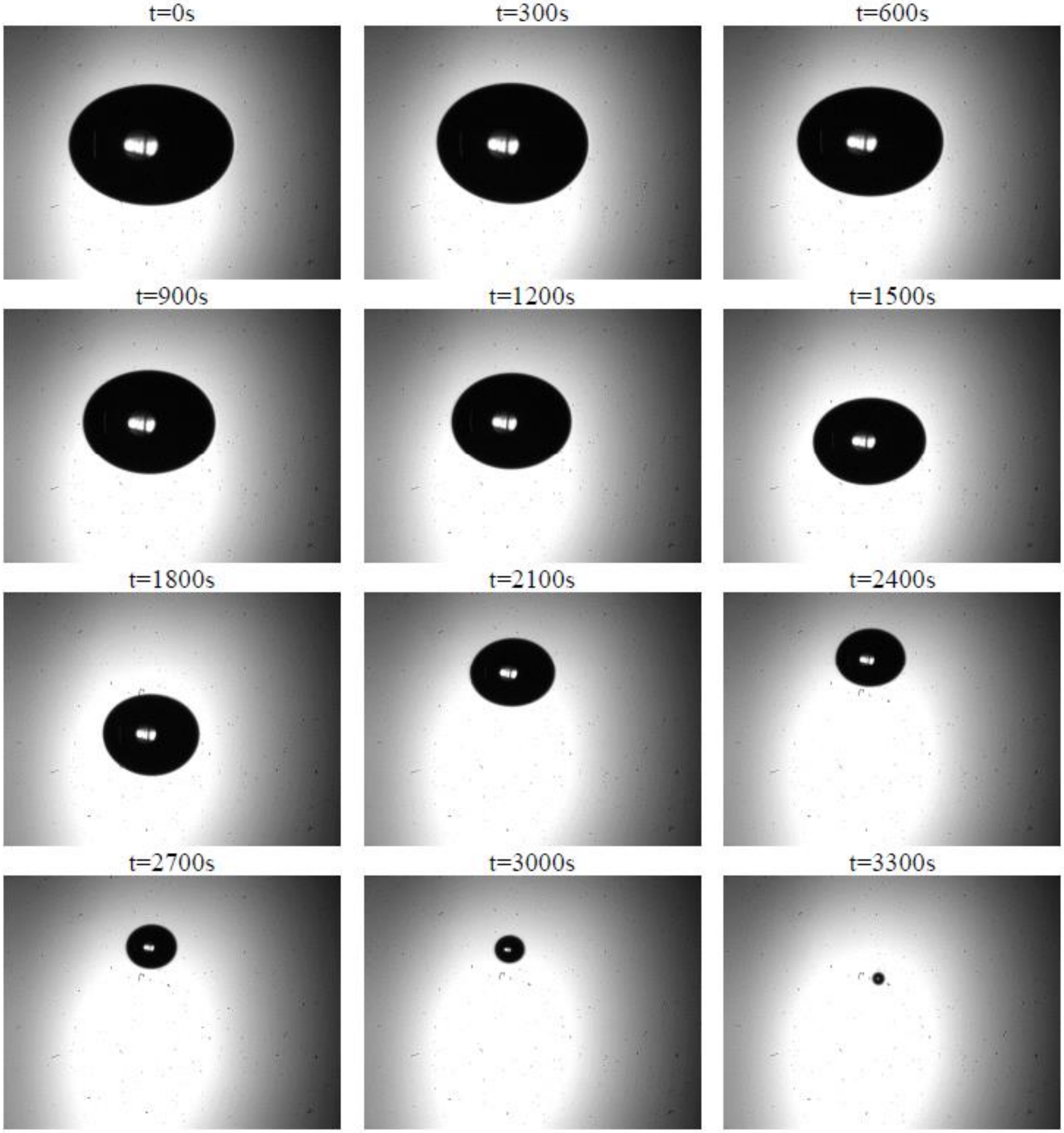

Figure 5-30 Case of a elliptic water droplet evaporating in air at $T_\infty = 20°\mathrm{C}$ and H=40%(Relative Humditiy). The initial diameter of the drop is 1.8 mm.

A) Evolution of Equivalent Diameter

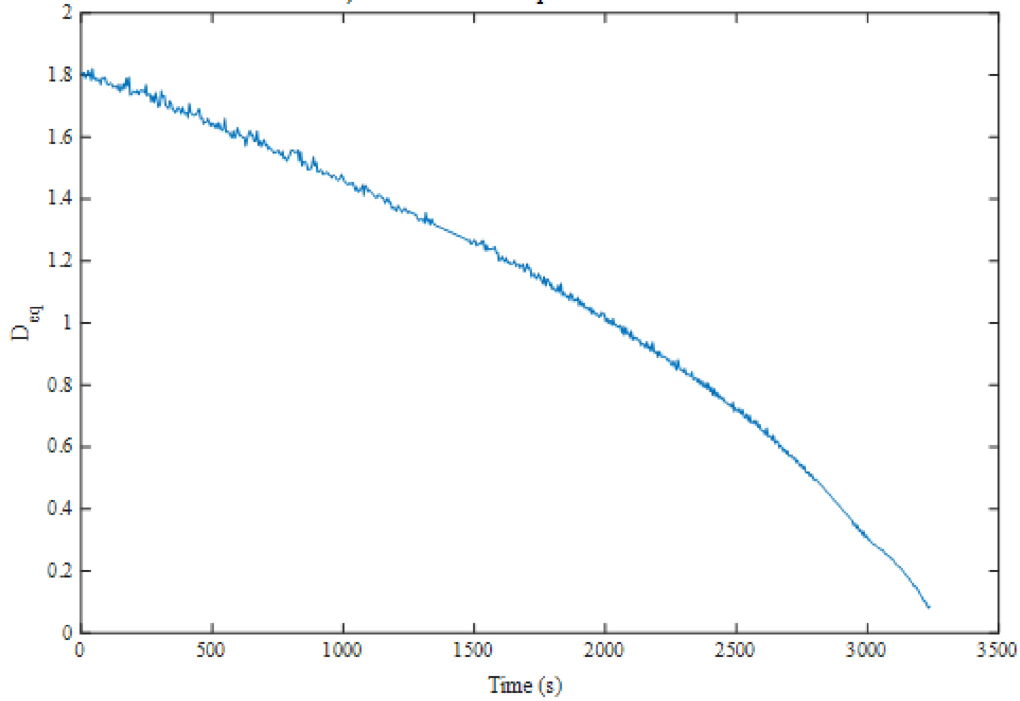

B) Normalized Square Diameter of Droplet Over Time

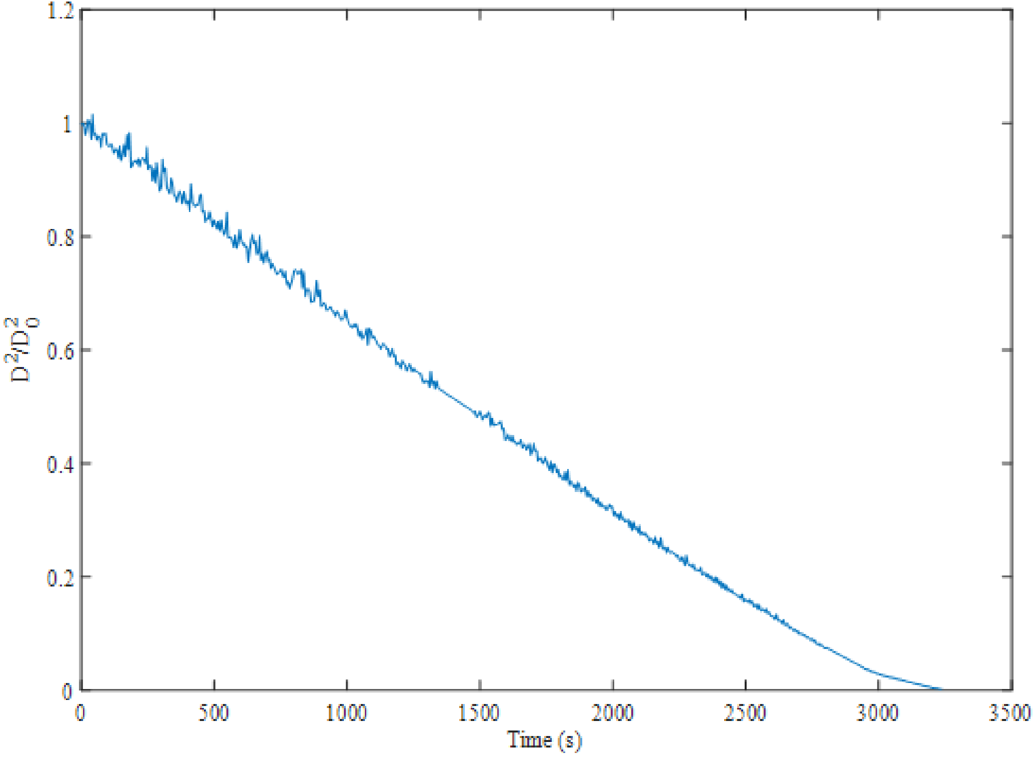

Figure 5-31 Evolution of the elliptic droplet A) Equivalent diameter B) Normalized square diameter.

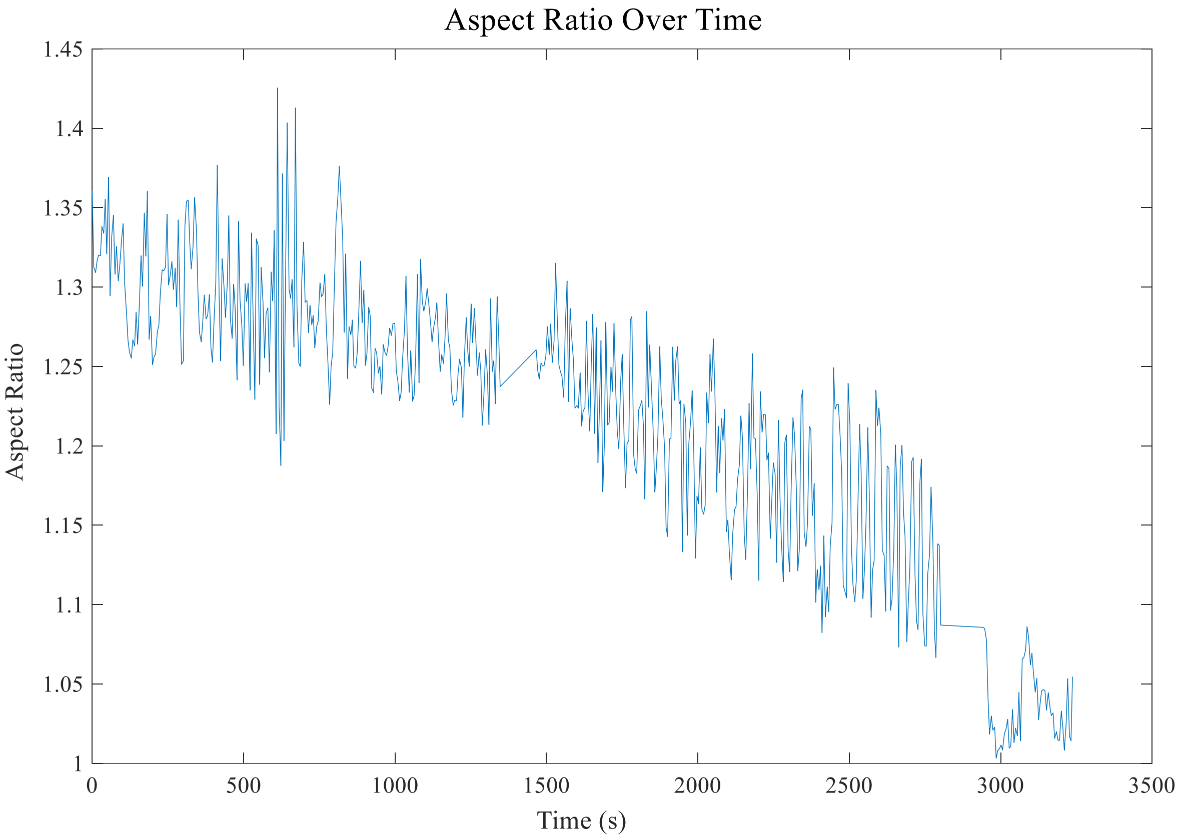

Figure 5-32 Evolution of the elliptic droplet aspect ratio

The loss of volume by evaporation means that the incident sound wave is less scattered. The interaction of the levitated droplet with the ultrasound field. Using the model developed by Yarin, it is possible to evaluate the sound pressure level (SPL) at any time during the droplet evaporation. As observed, SPL is almost constant. It slightly decreases over time as the droplet diameter gets lower than 0.7 mm.

This method of calculating the SPL can be used without difficulty because the droplet is mono-component. Surface tension and liquid density do not change during the evaporation process. In the case of a multicomponent droplet, the method is not reliable since the liquid properties are constantly changing and the composition must be known at the droplet surface where the surface tension must be calculated.

5.4 Modeling of the Evaporation of Multicomponents Droplets

A realistic model for the heat and mass transport processes across the liquid/gas interface of a vaporizing multicomponent droplet will be needed to interpret the measurements that will be obtained in the acoustic levitator. The problem of modelling droplet heating and evaporation is a long-standing one and has been widely discussed in the literature[35][36]. Classically, heat and mass transfer processes in the gas phase surrounding a vaporizing droplet are described using the quasi-steady approximation [36][37]. Quasi-steadiness means that the distribution of temperature and vapor concentration in the gas phase immediately adjusts to the local boundary conditions and the droplet size at each instant of the evaporation process. The evaporation models developed in the 50's have been progressively extended to the case of multicomponent liquid mixtures ([38][39][40][41][42][43][44]). The acoustic levitation has several effects. The sound radiation pressure leads to a flattening of the droplet. The acoustic field is also associated with an acoustic streaming in the vicinity of the droplet. Forced convection results in a substantial increase of the heat and mass transfers at the droplet surface. Hence, an acoustically levitated droplet evaporates faster than a droplet suspended in quiescent air.

A) Heat and Mass Transfer to the Gaseous Phase

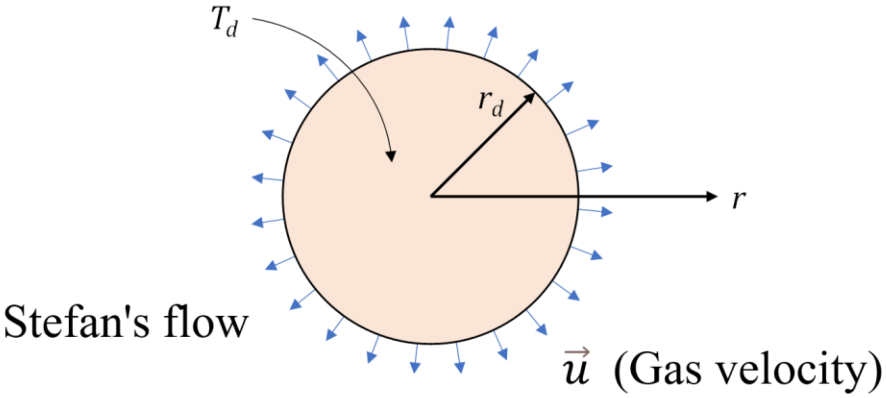

Figure 5-33 Schematic of an evaporating droplet. Overview of some notations

In the classical model of droplet evaporation, it is usually assumed that [36]:

1. The droplet remains spherical all the time,
2. The gas phase is in a quasi-steady state,
3. The solubility of air into the liquid is negligible,
4. The droplet evaporates in an inert environment without chemical reactions

5. Mass diffusion due to temperature and pressure gradients is negligible,

6. The effects of gravity are neglected (no buoyancy force in both liquid and gas phases).

The gas flow relative to an evaporating droplet is in principle unsteady due to the temporal evolution of the droplet size d. However, the characteristic time for the transfer in the gas phase is in all practical cases much smaller than the lifetime of the droplet, leading to the above assumption.

In the spherical coordinates (r, θ, φ), the continuity equation provides an expression for the gas velocity (Stefan flow):

$$u(r) = \frac{\dot{m}}{4\pi r^2 \rho_g} \qquad (5-35)$$

where r is the distance to the centre of the droplet and ρ_g is the density of the gas. $\dot{m}$ is the mass flow of vapor released over the droplet surface. Vapor is composed of the different species:

$$\dot{m} = \sum_i \dot{m}_i \qquad (5-36)$$

where the suffix i corresponds to the i^{th} species in the mixture. Fourier and Fick laws are used to describe the conductive heat and diffusional mass transfer in the gas phase:

$$\dot{m}\,\frac{dY_{vi}}{dr} = \frac{d}{dr}\left(4\pi r^2 \rho D_v \frac{dY_{vi}}{dr}\right) \qquad (5-37)$$

$$\dot{m}\,\frac{d}{dr}(Cp_g T) = \frac{d}{dr}\left(4\pi r^2 \kappa_g \frac{dT}{dr}\right) \qquad (5-38)$$

In the above equations, the subscript v indicates the vapour species. In principle, vapor species diffuse at different rates in the gas. Because of the Stefan flow, the evaporation rate of one of the species is affected by the evaporation rate of other species. Our analysis assumes that all the species in the vapor phase have the same mass diffusion coefficients[35], meaning that $D_{vi} = D_v$. It considers that the mixture of vapour species can be treated as a separate gas, similar to treating the mixture of nitrogen, oxygen and carbon dioxide as air. With the appropriate boundary conditions, the expression for the vapor mass flow rate:

$$\dot{m} = 4\pi\, \rho_{tot} D_v\, r_d\, Sh\, B_M \qquad (5-39)$$

where $r_d(t)$ is the droplet radius, Sh represents the ratio of the convective mass transfer to the rate of diffusive mass transport and B_M is the mass transfer Spalding number which can be defined by:

$$B_M = \frac{\sum_i Y_{vis} - \sum_i Y_{vi\infty}}{1 - \sum_i Y_{vis}} \qquad (5-40)$$

Subscripts s and ∞ relate to the conditions at the surface and in the ambient far away from the droplet, respectively.

The integration with the appropriate boundary conditions, on the other hand, leads to a second expression for the vapor mass flow rate $\dot{m}$:

$$\dot{m} = 4\pi \frac{\kappa_g}{Cp_v} r_d \, Nu \, B_T \qquad (5-41)$$

where B_T is the heat transfer Spalding number defined as:

$$B_T = \frac{Cp_v \, (T_\infty - T_s)}{L_{eff}} \qquad (5-42)$$

L_{eff} is the effective latent heat calculated by:

$$L_{eff} = \sum_i \epsilon_i \, Lv_i + Q_L / \sum_i \dot{m}_i \qquad (5-43)$$

In this expression, Q_L denotes the heat flux entering the drop and contributing to the temperature variation of the liquid phase. The coefficient ϵ_i represents the fraction of the vapor mass flow rate that is generated by the i^{th} species:

$$\epsilon_i = \dot{m}_i / \dot{m} = \dot{m}_i / \sum_i \dot{m}_i \qquad (5-44)$$

Assuming that species concentrations in the ambient gas are equal to zero ($Y_{vi\infty} = 0$), ϵ_i can be evaluated as follows:

$$\epsilon_i = Y_{vis} \Big/ \sum_i Y_{vis} \qquad (5-45)$$

The dimensionless numbers Nu and Sh correspond to the Nusselt and Sherwood numbers. The Nusselt number (Nu) is the ratio of convective to conductive heat transfer at the droplet surface.

$$Nu = \frac{2r_d \, h}{\lambda_g} \qquad (5-46)$$

where h is the heat transfer coefficient. The Sherwood number (Sh) is a dimensionless number analog to the Nusselt number but for the mass transfer:

$$Sh = \frac{2r_d\, h_m}{D_v} \tag{5 – 47}$$

where h_m is the mass transfer coefficient.

Nusselt and Sherwood numbers are of great importance for the modelling of the heat and mass transfers. Many efforts were devoted to the effects of forced convection in the case of a droplet motion relative to the gas phase.

- **Case of a motionless droplet in quiescent air**

This is the classic isolated drop model developed in the 1950s ,such as CK Law.

$$Nu = 2\,\frac{ln(1 + B_T)}{B_T} \tag{5 – 48}$$

$$Sh = 2\,\frac{ln(1 + B_M)}{B_M} \tag{5 – 49}$$

- **Case of a moving droplet**

Based on the film theory, Abramzon and Sirignano (1989)[45] derived an expression of Nu and Sh for the case of a droplet moving relatively to the surrounding gas phase:

$$Nu = \frac{ln(1 + B_T)}{B_T} \cdot \left[2 + \frac{Nu_0 - 2}{F(B_T)}\right] \tag{5 – 50}$$

$$Sh = \frac{ln(1 + B_M)}{B_M} \cdot \left[2 + \frac{Sh_0 - 2}{F(B_M)}\right] \tag{5 – 51}$$

Here, F is a function defined by:

$$F(B) = (1 + B)^{0.7}\,\frac{\ln\,(1 + B)}{B} \tag{5 – 52}$$

Nu_0 and Sh_0 are the Nusselt and Sherwood numbers in the case where the Stefan flow is negligible. This corresponds to low values of B_M and B_T (typically less than 0.1). Nu_0 and Sh_0 are function of the Reynolds number (Re), the Prandtl number (Pr) and the Schmidt number (Sc).

$$Re = \frac{\rho_g\, V_d\,(2r_d)}{\mu_g}, \qquad Pr = \frac{\rho_g\, \nu_g Cp_g}{\kappa_g}\ and\ Sc = \frac{\nu_g}{D_v} \tag{5 – 53}$$

In this expression, V_d is the droplet velocity. Several correlations are available from literature. A well-known empirical correlation was suggested by Ranz and Marshall:

$$Nu_0 = 2 + 0.6\, Re^{1/2}\, \mathrm{Pr}^{1/3}\, , 0 \leq Re \leq 200 \text{ and } 0 \leq Pr \leq 250 \qquad (5-54)$$

A similar correlation was found by Frössling:

$$Nu_0 = 2 + 0.552\, Re^{1/2}\, Pr^{1/3}\, , 0 \leq Re \leq 200 \text{ and } 0 \leq Pr \leq 250 \qquad (5-55)$$

A more specific correlation is provided by [46]. It is mainly recommended for lower values of the Reynolds number:

$$Nu_0 = 1 + (1 + \, Re\, Pr)^{1/3} \cdot f(Re) \qquad (5-56)$$

where $f(Re) = 1$ at $Re \leq 1$ and $f(Re) = Re^{0.077}$ at $Re \leq 400$. Correlations for the Sherwood number can be obtained from the above equations by replacing the Prandtl number with the Schmidt number (the analogous dimensionless number for mass transfer).

- **Case of an acoustically levitated droplet**

In the case of a levitated droplet, the acoustic field affects the heat and mass transfer by inducing a so-called “acoustic streaming” or “acoustically induced secondary streaming” whose time-averaged velocity is not equal to zero. The acoustic streaming is responsible for a steady transport of heat and mass in the vicinity of the droplet surface. This streaming can be divided in two regions: the inner and the outer acoustic streaming. The inner acoustic streaming is present in a narrow boundary layer of thickness $\delta \sim (\nu_g/\omega)^{1/2}$ close to the droplet surface. Viscous stresses are responsible for a steady flow, which takes the form of a hemispherical symmetric pattern with closed streamlines. The inner acoustic streaming is outlined in red in **Figure 5-34**. It plays a very important role on the steady heat and mass transports from the droplet surface [47] given that it can effectively accelerate the vapour and heat removal from the droplet surface. The thickness of the acoustic boundary layer δ is of the order of a few microns, which explains that it is very difficult to observe experimentally the inner acoustic streaming. The outer boundary of the acoustic boundary layer practically coincides with the droplet/particle surface, whereas heat and mass diffusion length scales are much larger.

A steady velocity also persists at a larger radial distance from the droplet surface corresponding to the outer acoustic region. The outer acoustic streaming, outlined in black in **Figure 5-34**, is a system of large-scale toroidal vortices around the levitated droplet. Without any additional blowing in the levitator, these vortices could be evidenced experimentally by several authors[48].

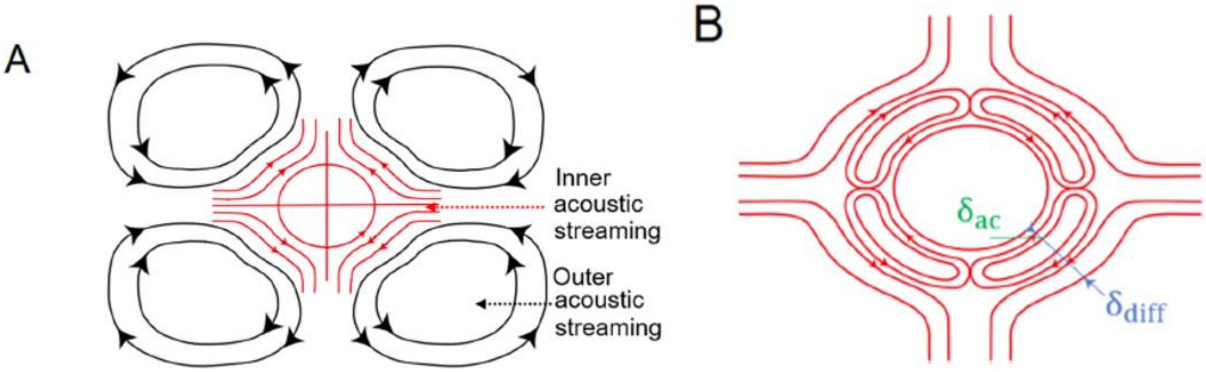

Figure 5-34 the inner acoustic streaming is positioned directly at the acoustic boundary layer, whereas the outer acoustic streaming (outer toroidal vortices) surrounds the droplet at further distance. (A) outer acoustic streaming. (B) inner acoustic streaming. Adapted from [50].

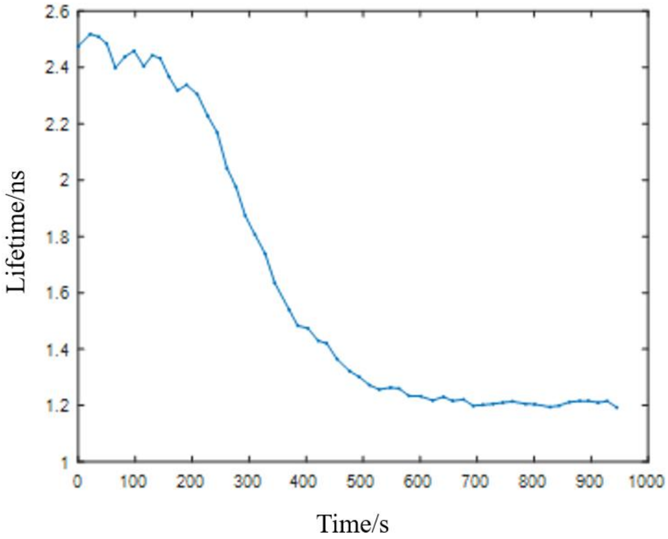

Figure 5-35 Time evolution of the fluorescence lifetime in the case of an ethanol/water (75%/25% by volume) droplet which is exposed to an air flow (q_v=0.1 L/min).

It is not totally clear to what extent the outer acoustic streaming affects heat and mass transfers at the droplet surface. [49] argued that vapor could stagnate in the vortices of the outer acoustic streaming, and thus suggested to apply a blowing air to expel this vapor from the droplet's surroundings. However, according to them, ventilation must be carefully controlled. If blowing is too small, the effect of blowing is insufficient. If too large, the inner acoustic streaming is affected, and the situation will resemble to the case of a moving droplet described above. Although it was implemented in our experimental setup, air blowing was not used during most of the experiment to avoid the risk of disturbing the droplet. Air is injected through small holes drilled in the reflector. The case of a droplet placed in an air flow rate of 0.1 L/min. It was observed that small movements of the droplet lead to fluctuations in the measurement results. Fluctuations in the values of the fluorescence lifetime can be observed at the beginning of the evaporation (until t=600 s) when the droplet is predominantly composed of ethanol. Fluctuations become less visible when the ethanol/water droplet has turned into a water droplet. Fluctuations can occur even without air blowing when the droplet is not stable. However, an air flow usually intensifies the phenomenon.

Attempts have been made to estimate (even roughly) the magnitude of the time-averaged velocity in the inner acoustic streaming. The amplitude velocity of gas particles is known to scale as:

$$B = \frac{A_{0e}}{\rho_g c_0} \qquad (5-57)$$

where A_{0e} denotes the pressure amplitude of the incident acoustic field, which depends on the acoustic resonance, i.e. the distance between the reflector and the transducer. A characteristic scale of the acoustic streaming velocity B_s is given by:

$$B_s = \frac{B^2}{\omega r_d} \qquad (5-58)$$

Based on this definition, the acoustic Reynolds number Re_a can be calculated as:

$$Re_a = \frac{B_s\ (2\, r_d)}{\nu_g} = \frac{2B^2}{\nu_g \omega} \qquad (5-59)$$

Transport phenomena in the inner acoustic streaming were examined both experimentally and numerically in several studies. The time averaged Nusselt (Nu) and Sherwood (Sh) numbers can be expressed by:

$$\begin{aligned} Nu &= K\, Re_a\, Pr^{\beta} \\ Sh &= K\, Re_a\, Sc^{\beta} \end{aligned} \qquad (5-60)$$

where K is a parameter that depends on the droplet shape, the droplet displacement relative to the pressure node and the sound pressure level (SPL). Yarin [47]examined theoretically the case of a small droplet ($r_d \ll \lambda$) located at the pressure node. Solving the transport equation of the vapor in the inner acoustic streaming, they found $\beta = 1$ and $K =$1.892. Yarin [47]extended their theory to droplets of larger size ($r_d \approx \lambda$) whose shape is not spherical and the position is distant from the pressure node. The expression they obtain for K is quite complex and depends on the deformation of the droplet, the amplitude of the acoustic pressure, and the droplet volume. The value of K significantly increases with the SPL. In practice, however, experimental results indicate that a value of K close to 1.9 (formally valid for the small droplet) remains a good approximation. Gopinath and Mills [51] experimentally obtained $K = 1.858$ and $\beta = 0.667$. It is expected to be valid for $Re_a \gg 1$ (Pr and Sc being close to 1), as the predominant mechanism of transport is the convection by the acoustic streaming. If $Re_a \ll 1$, heat and mass diffusion prevail over convection, and Nu and Sh should take a value close to 2 Brenn et al (2007) decided to use the Frössling correlation by replacing the Reynolds number Re by the acoustic Reynolds number Re_a. Surprisingly, they did not find it necessary to modify the coefficient 0.552 for their comparisons with their experimental results.

B) Model for the Heat and Mass Transfer Inside the Droplet

A steady circulation also exists within the droplet. It results from liquid entrainment at the droplet/gas interface by the steady acoustic streaming in the gas phase. **Figure 5-36**, extracted from Yarin [47], reveals two toroidal vortices inside the droplet. The lens effect induced by the droplet surface distort the actual shape of the streamlines. Nevertheless, it seems that the two vortices do not have the same size, the separation point being shifted towards the top of the droplet and the pressure node.

An estimate of the velocity on the liquid side can be obtained from the continuity of the shear stresses at the droplet surface. This calculation was done rigorously by Yarin et al. in the limiting case of a small spherical drop ($r_d \ll \lambda$) centred at the pressure node. The whole flow field inside the acoustically levitated droplet could be described by an analytical solution in the spherical coordinate system (R, θ, ϕ):

$$v_R = \frac{E'}{14\,\mu_l}(2\cos^2\theta - \sin^2\theta)(r^3 - r_d^2 r) \qquad (5-61)$$

$$v_\theta = \frac{E'}{28\,\mu_l}\sin 2\theta\,(3r_d^2 r - 5r^3) \qquad (5-62)$$

Here the parameter E' can be obtained by assuming that:

$$\frac{|v_\theta(R = r_d)|}{|u_\infty|} = \frac{\sqrt{2}}{25}\left(\frac{r_d}{\mu_l}\sqrt{\rho_g \mu_g \omega}\right) \qquad (5-63)$$

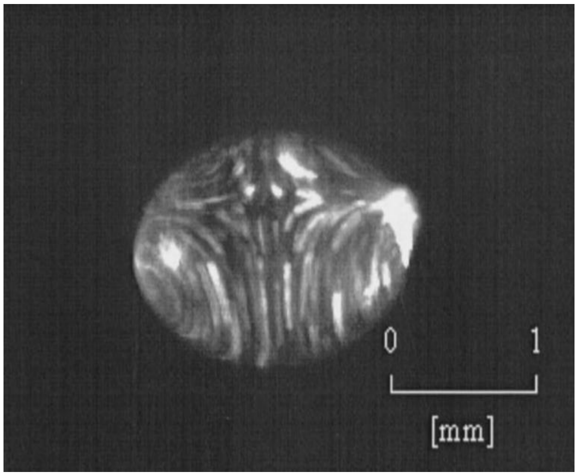

Figure 5-36 Visualized section of the flow field inside a µL methanol droplet with an aspect ratio of 1.5. The image is extracted from Yarin et al. (1999). It was obtained using a long exposure time not mentioned by the authors.

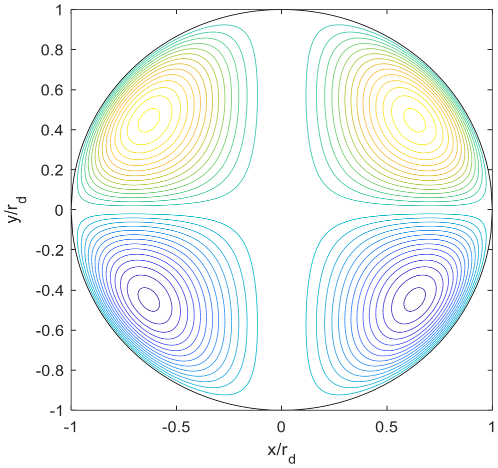

Figure5-37 Streamlines of the circulation flow in a spherical droplet centered at the pressure node

The acoustic streaming velocity in the gas at the outer boundary of the acoustic boundary layer (u_∞) is approximately equal to B_s in equation $(5-56)$. More precisely, Yarin et al. (1999) gives the following expression:

$$u_\infty(\theta) = -\frac{45}{32}\, B_s\, sin2\theta \qquad (5-64)$$

Using equations $(5-61)$to $(5-64)$, we obtain:

$$E' = \frac{63\sqrt{2}}{80} B_s \frac{\sqrt{\rho_g \mu_g \omega}}{r_d^2} \qquad (5-65)$$

Assuming a SPL of 160 dB and a water droplet of radius $r_d = 1$ mm, $\omega = 2\pi \cdot 58000$ rad/s, the pressure amplitude is $A_{0e} \approx 2000$ N/m^2 and the velocity amplitude of the sound is $B = 4.5$ m/s. The characteristic velocity B_s of the steady acoustic streaming is of the order of 6 cm/s. Taken $\mu_g = 1.8 \times 10^{-5}$ Pa·s, $\mu_l = 10^{-3}$ Pa·s, ρ_g=1.28 kg/m^3, equation $(5-63)$ yields a velocity ratio equal to 0.164. The surface velocity $v_\theta(R = r_d)$ is of the order of 1 mm/s. To get an idea of the temperature and composition distributions, dimensionless numbers can be used:

The Péclet number is the ratio of the rate of advection by the flow inside the droplet to the rate of diffusion. The thermal and mass Péclet number can be defined by:

$$Pe_{th} = \frac{(2\, r_d) \cdot v_\theta(R = r_d)}{a_l} \text{ and } Pe_m = \frac{(2\, r_d) \cdot\ v_\theta(R = r_d)}{D_l} \qquad (5-66)$$

The thermal diffusivity $a_l = \kappa_l/\rho_l\, Cp_l$ is close to 1.4 10^{-7} m^2/s. In the liquids, typical values for the mass diffusion coefficient D_l is of the order of 10^{-9} m^2/s. Assuming $v_\theta(R = r_d) \approx 1$ mm/s, Pe_{th} is expected to be of the order of 10 while Pe_m is about 1000. In the case of the mass transfer, convection plays a more important role. Given the high values of Pe_m, concentration gradients are expected to be superimposed on the streamlines of the liquid flow.

The Biot number is the ratio of the heat or mass diffusion to the resistance for convection at the surface of the droplet.

$$Bi_{th} = \frac{h\,(2r_d)}{\kappa_l} \text{ and } Bi_m = \frac{h_m}{D_l} 2r_d \qquad (5-67)$$

Assuming $Nu \approx 4$, $r_d = 1$ mm, $\kappa_g = 26 \times 10^{-3}$ W/mK, Equation $(5-46)$ gives a value of the heat transfer coefficient h equal to 50 W/m^{2}K. Considering that $\kappa_l = 0.6$ W/m K, the thermal Biot number Bi_{th} of about 0.17. This small value (compared to 1) allows to consider that temperature gradients are negligible inside of the droplet. For the "mass transfer Biot number", h_m is the mass transfer coefficient with the gas at the droplet surface. Assuming $Sh \sim 4$, $r_d \sim 1$ mm, $D_v \sim 2.5 \times 10^{-5}$ m^2/s, h_m is about 0.05 m/s according to equation $(5-47)$. For $D_l \approx 10^{-9}$ m^2/s, Bi_m is found to be of the order of 105. This high value compared to unity indicates that mass gradients are significant inside the droplet.

The **Fourier number** is the ratio of time, t, to the characteristic time scale for heat diffusion t_{th} and mass diffusion t_m. These characteristic times of diffusion can be obtained as follows:

$$t_{th} = r_d^2/a_l \text{ and } t_m = r_d^2/D_l \qquad (5-68)$$

For $r_d = 1$ mm, t_{th} is about 7s, while t_m is close to 1000 s. The value of t_m is comparable (and even longer) than the evaporation time of a droplet. This suggests that mass gradients maintain for the total duration of the evaporation process. In contrast, a uniform temperature is achieved in a few seconds.

Based on the previous description, the following model was adopted for heat and mass transfer within the droplet.

For heat transfer, it will be assumed that the temperature inside the droplet is spatially uniform but can vary in time (infinite conduction). The evolution of the temperature of the droplet is determined as follows:

$$m\, Cp_l\, T_d(t+dt) = m\, Cp_l\, T_d(t) + Q_L \qquad (5-69)$$

where Q_L is the heat flow entering the droplet and m is the mass of the droplet at time t. The heat flow Q_L must be deduced from an energy balance. At the droplet surface, the heat supplied from the gas phase is transformed for one part into latent heat, while the rest penetrates the droplet and changes the liquid temperature. From equation $(5-39)$, we can write that:

$$Q_L = \dot{m}\left(\frac{Cp_v\,(T_\infty - T_s)}{B_T} - Lv\right) \qquad (5-70)$$

Here $L_v = \sum_i \epsilon_i\, Lv_i$ and $\dot{m} = \sum_i \dot{m}_i$. B_T is calculated as follows:

$$B_T = (1 + B_M)^\phi - 1 \qquad (5-71)$$

where $\phi \approx \frac{1}{Lev}\frac{Cp_v}{Cp_g}$ [52] and B_M is obtained using equation $(5-39)$.

For the transfer of the species inside the droplet, several degrees of complexity can be considered in the modelling. To our knowledge, most of the studies have tried to simplify the problem by making excessive assumptions. Several studies assumed a uniform but time-varying composition, i.e. a rapid mixing inside the droplet. This approach allows rapid calculations but completely neglects the fact that composition gradients are present inside the droplet. Another simplifying approach relies on the assumption of a purely mass diffusion process inside the droplet. This approach, referred after as diffusion limited model, leads to a spherical symmetry in the distribution of the species, so the effect of the internal convection is neglected. A more accurate model would be to consider the velocity field inside the droplet, but it is more complex to implement. This approach is analogous to the Hill vortex model sometimes used to describe the evaporation of a moving droplet.

1) Rapid mixing model

At every time step of the resolution, the composition is determined as follows:

$$m_i(t + dt) = m_i(t) - \dot{m}\,\epsilon_i\,dt \qquad (5-72)$$

$$Y_{li}(t + dt) = m_i(t + dt)\Big/\sum_j m_j(t + dt) \qquad (5-73)$$

To obtain the vapor mass flow rate $\dot{m}$, equation $(5-36)$ is used. This implies to know the values of Y_{vis} to evaluate ϵ_i and B_M.

2) Diffusion limited model

Although the levitating droplet is flattened, it has been assumed a sphere. At each time step, the following mass diffusion equation is solved:

$$\frac{\partial Y_{li}}{\partial t} = \frac{D_l}{r^2}\frac{\partial}{\partial r}\left(r^2 \frac{\partial Y_{li}}{\partial r}\right) \qquad (5-74)$$

This equation is transformed to consider the moving droplet surface. By introducing $\xi = r/r_d(t)$, ones obtain:

$$\frac{\partial Y_{li}}{\partial t} - \xi \frac{\dot{r}_d}{r_d}\frac{\partial Y_{li}}{\partial \xi} = \frac{D_l}{\xi^2}\frac{\partial}{\partial \xi}\left(\xi^2 \frac{\partial Y_{li}}{\partial \xi}\right) \qquad (5-75)$$

with the following boundary conditions:

$$\partial Y_{li}/\partial \xi = 0 \text{ at } \xi = 0 \qquad (5-76)$$

$$-4\pi r_d^2 D_l \frac{\partial Y_{li}}{\partial \xi} = \dot{m}\cdot(\epsilon_i - Y_{lis}) \quad \text{at } \xi = 1 \qquad (5-77)$$

This equation is solved numerically using a Crank-Nicolson numerical time derivative scheme. A finite difference spatial discretization is applied for the right-hand side of equation $(5-74)$.

3) The vortex model (VM)

This model consists in solving the transport equations of the species within the droplet. The velocity field are used, even though these are essentially valid for the case where the droplet radius r_d is small in comparison with the wavelength of the acoustic field. A more detailed study of the velocity field would be necessary to improve this model. It is assumed that the mass fraction of species is uniform at the droplet surface but can vary over time. This model is therefore consistent with the description of heat and mass transfer to the gaseous phase described at the beginning of section. More details on the numerical implementation of this model can be found in **Appendix**. The distribution of the mass fraction essentially that depends on the mass Péclet number Pe_m shows several evolutions that the concentration field can follow. These results correspond to a special case where the mass fraction Y_{lis} is kept constant and equal to 1 at the surface of the droplet, while initially $Y_{li} = 0$.

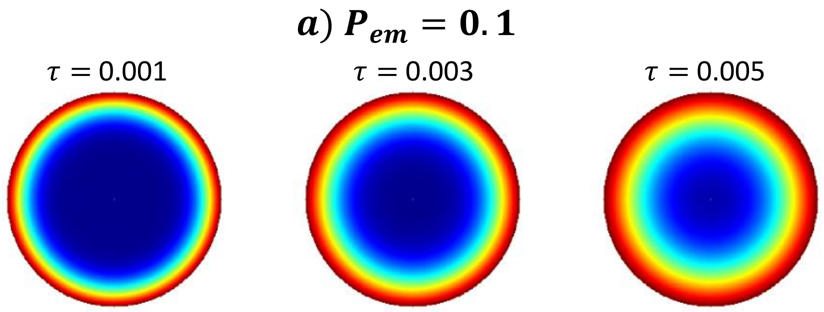

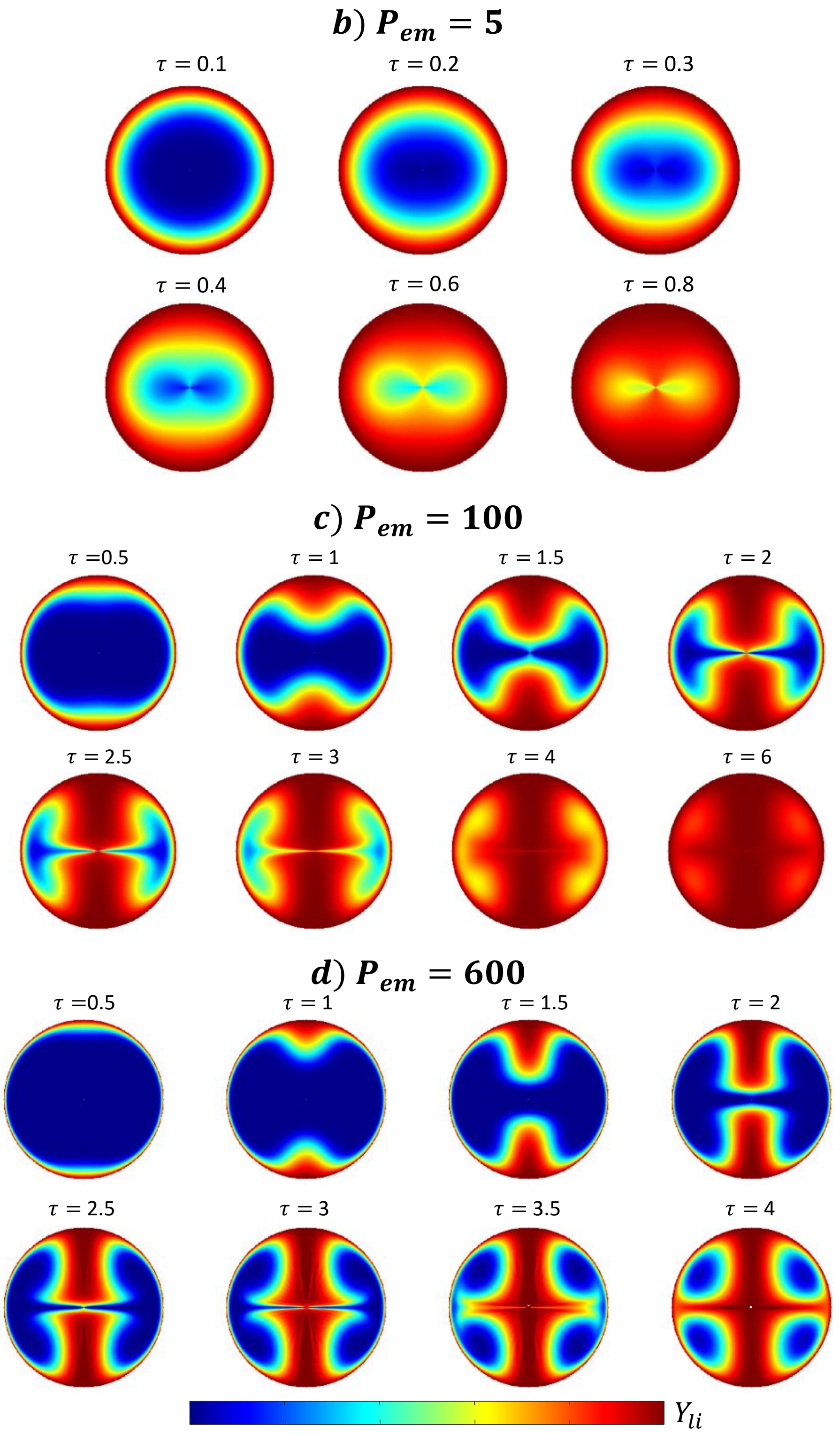

Figure 5-38 Time evolution of the mass fraction field in the vortex model (VM). Calculations are performed with different values of the mass Péclet number.

It shows different patterns that the concentration field can take:

Case of $\boldsymbol{Pe_m = 0.1}$: the field of mass fraction has a spherical symmetry. Mass transfer is dominated by diffusion. Therefore, the result obtained with the VM model is the same as using the DLM model.

Case of $\boldsymbol{Pe_m = 5}$: A region of lower concentration is positioned in the center of the droplet for most of the transfer process. This region is elongated in the horizontal direction and eventually divide in two. The effects induced by convection and diffusion are of roughly equal importance. Most of the transfer has been completed when $\tau = Ut/r_d$ is approaching 1 (i.e. when the liquid has almost completely circulated around the droplet).

Case of $\boldsymbol{Pe_m = 100}$: Mass transfer is dominated by convection. During the transient phase, two jets that are concentrated, meet at the center of the droplet. The region of low mass fraction is squeezed and splits in two. At the end of the transfer process (about $\tau = 6$), the vortex structure becomes apparent. Four zones of slightly lower mass fraction can be pointed out at the vortices' location.

Case of $\boldsymbol{Pe_m = 600}$: The rotational speed is higher than in the previous case. Mass diffusion has had no time to operate before the iso-concentration lines have adopted their final position. Gradients of mass fraction are perpendicular to the vortex streamlines. Four regions of low mass fraction maintain for a very long time.

1) The effective diffusion model (EDM)

This model is similar to the limited diffusion model (DLM) described before, except that the diffusion coefficient D_l is increased by a factor χ which depends on the rotational speed within the vortices. Thus, Equation is replaced by:

$$\frac{\partial Y_{li}}{\partial t} = \chi(Pe_m)\, D_l\, \frac{1}{r^2}\, \frac{\partial}{\partial r}\left(r^2 \frac{\partial Y_{li}}{\partial r}\right) \qquad (5-78)$$

The problem is solved with the same initial and boundary conditions. To set the value of χ however, it is necessary to refer to the VM, which considers the mass transport inside the vortices induced by the acoustic field. As the solutions of VM are essentially dependent on Pe_m, the same is assumed for the factor χ. To compare the rate of mass transfer inside the droplet to the case of pure diffusion, the average mass fraction Y_{lim} is first calculated and its evolution is plotted as a function of the diffusive time $t_D = t\, D_{li}/r_d^2$. The flow circulating inside the droplet greatly enhances the rate of mass transfer, as Y_{lim} grows faster with increasing Pe_m.

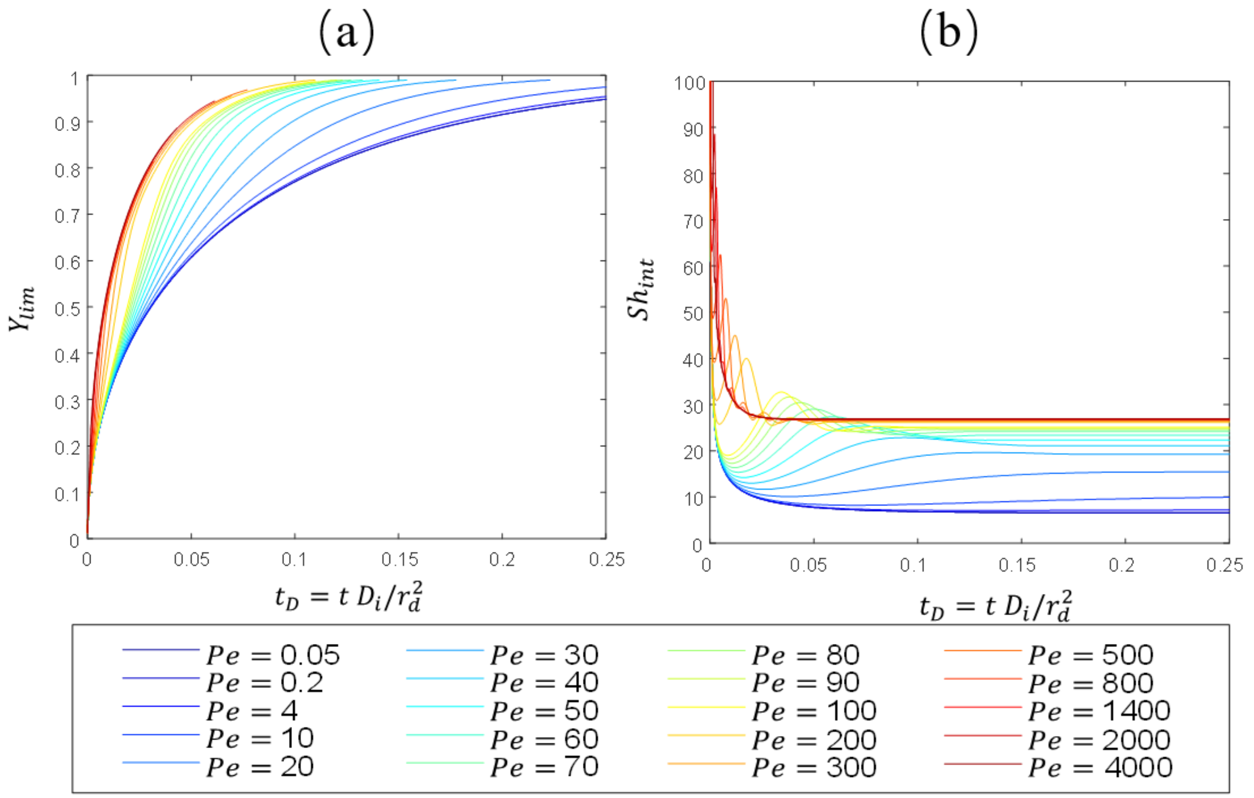

Figure 5-39 Time evolution of the volume average mass fraction Y_{lim} and the internal Sherwood number $\overline{Sh}_i$

To quantify more precisely the effect of the mixing inside the droplet, it is useful to calculate the internal Sherwood number:

$$\overline{Sh}_i = 2\,\frac{(\partial\overline{Y_{li}}/\partial\xi)_{r=r_d}}{1-Y_{lim}} \qquad (5-79)$$

where $\overline{Y_{li}}$ is the angular average of Y_{li} over the droplet surface along the θ coordinate, and Y_{lim} is the volume average of Y_{li}. The time evolution of $\overline{Sh}_i$ is presented in **Figure 5-39**.b) In the very first instants, the mass transfer is extremely rapid because the mass gradient is infinite at the surface. The pattern of the mass fraction field gradually builds up inside the droplet, and $\overline{Sh}_i$ eventually converges to an asymptotic limit at the long times. The oscillations that precede the horizontal asymptote are the result of the mixing inside the vortices. The oscillation period is related to the rotation speed of the vortices. In the range 4<Pe_m<100, the asymptotic value of $\overline{Sh}_i$ increases with the mass Péclet number. The parameter $\chi(Pe_m)$ introduced in Equation $(5-78)$ can be seen as the increase factor of $\overline{Sh}_i$ compared to the case of a pure diffusion inside the droplet ($Pe_m = 0$). It depends solely on the mass Péclet number in the long times,

$$\chi(\mathrm{Pe_m}) = \lim_{\tau\to+\infty} \frac{\overline{\mathrm{Sh_i}}(\mathrm{Pe_m},\tau)}{\overline{\mathrm{Sh_i}}(\mathrm{Pe_m}=0,\tau)} \qquad (5-80)$$

Figure 5-40 shows the evolution of χ as a function of Pe_m. The red curve is a proposed fitting for the results obtained based on the simulations with the vortex model. It corresponds to the following expression:

$$\chi(Pe_m) = 2.52 + 1.53\tanh(1.97\log_{10}(Pe_m/23)) \qquad (5-81)$$

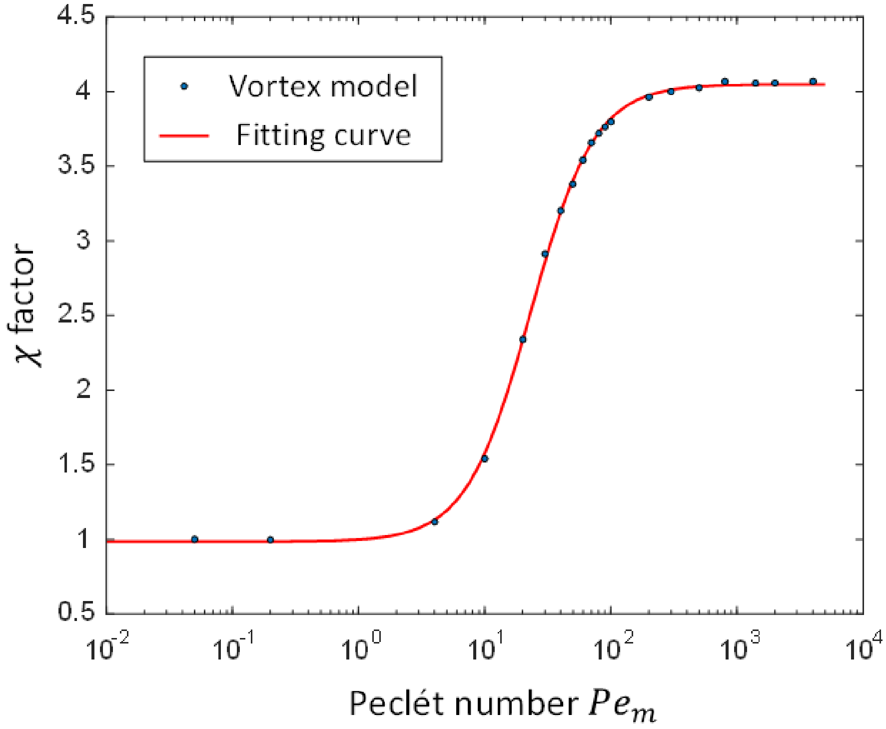

Figure 5-40 Influence of the Péclet number on the χ parameter

Given the high values of the mass Péclet number in our experimental conditions, it seems acceptable to assume that:

$$\chi(Pe_m) \approx 4.05 \qquad (5-82)$$

1）Modeling of the liquid/Vapor equilibrium at the droplet surface

At the surface of the levitated droplet, it is assumed an equilibrium between the vapor and the liquid phase. In the case of an ideal mixture, Raoult's law applies for a single component i as:

$$P_i = x_{liS}\,P_{sat}(T_S) \qquad (5-83)$$

where P_i is the partial pressure of the component in the gaseous mixture above the solution, x_{liS} is the mole fraction of the component in the liquid solution at the droplet surface, P_{sat} is the vapor pressure of component i. The Antoine equation provides an expression of the relation between the vapor pressure and the temperature of pure liquids. To account for the deviation from the ideal behavior, it is modified by introducing the activity coefficient γ_i which provides a correction for the interactions between the different molecules in the liquid phase:

$$P_i = x_{lis}\,\gamma_i\,P_{sat}(T_S) \qquad (5-84)$$

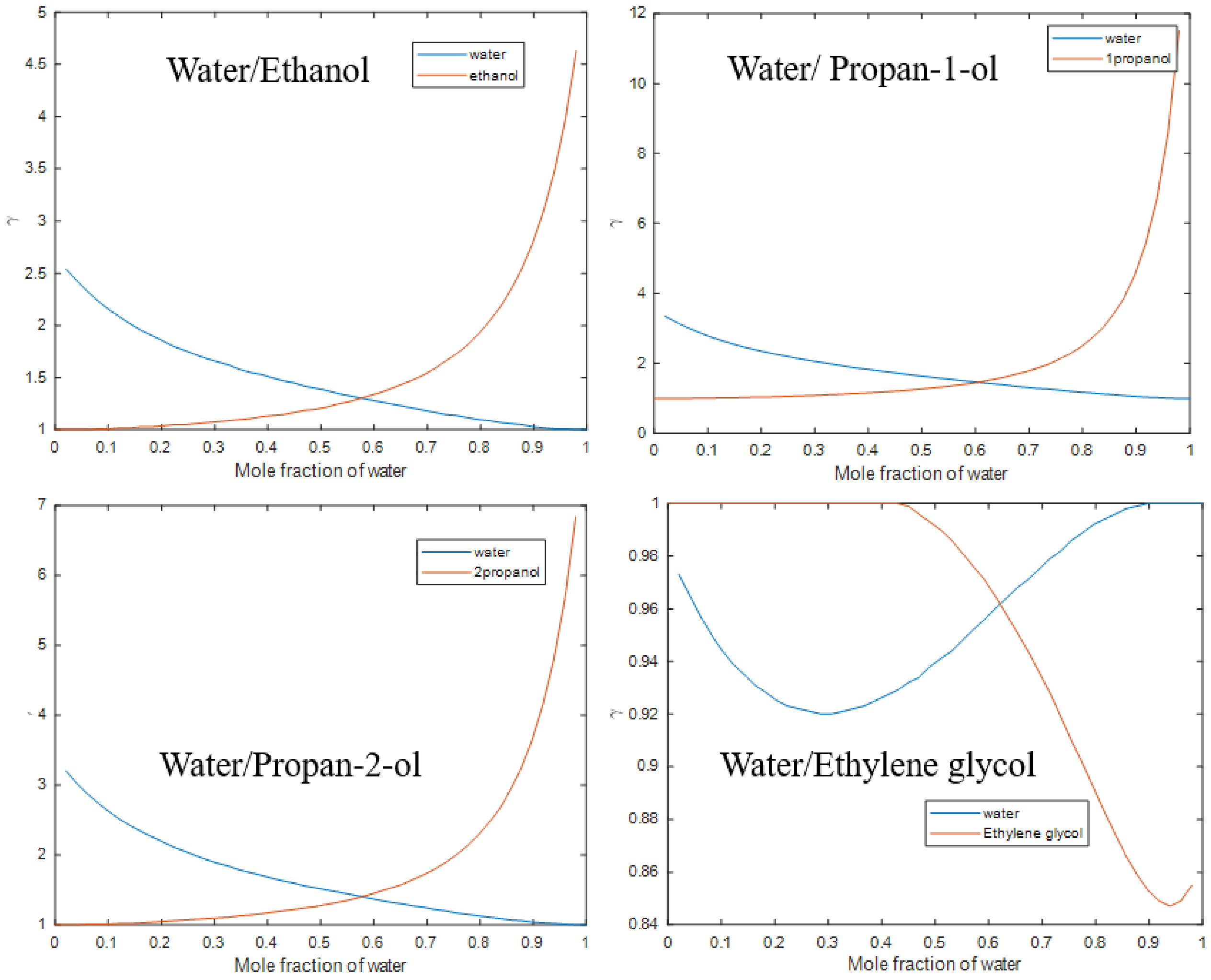

Figure 5-41 Chemical activity coefficient $\boldsymbol{\gamma i}$ in different binary mixtures

Presently, deviations from the ideal-gas law can be ignored in the gaseous phase. As a result,

$$x_{vis} = \gamma_i\,x_{lis}\,\frac{P_{sat}(T_S)}{P} \qquad (5-85)$$

The UNIFAC method was employed to determine the value of the activity coefficient γ_i. Details about the UNIFAC model and its parameterization can be easily found in the literature[53].

In the UNIFAC method, the liquid mixture is described as a "solution of groups". Molecules are segmented into "functional" groups and the specific properties of these functional groups are considered in the calculations. The UNIFAC model splits up the activity coefficient γ_i for each species in the system into a combinatorial nd a residual component. The residual component of the activity γ r is due to interactions between "functional" groups present in the system. The combinatorial component of activity is dependent on the type and number of the functional groups contained within the considered molecule. The effect of temperature on the interaction between groups is accounted for using an Arrhenius type equation. Interaction energy between groups, group surface area and volume contributions Q are usually tabulated for evaluating the activity coefficient. To illustrate, **Figure 5-41** shows the chemical activity coefficient of the several mixture at room temperature. Deviation from the ideal mixture is very noticeable.

2）Numerical resolution of the evaporation problem

The numerical resolution of the droplet evaporation is based on the equations presented above. Assuming the temperature and the composition of the droplet are known at time t, the algorithm used to determine the temperature and composition at time $t + dt$ is described in the paragraph below:

Step 1: The properties of the liquid phase (ρ_l, κ_l, Cp_l, μ_l, D_l) are calculated considering the volume average properties of the mixture.

Step 2: Equation $(5-85)$ is used to evaluate the mass fraction Y_{vis} of the vapor at the droplet surface. The 1/3 law[54] is used to evaluate the properties of the gaseous phase at a reference state defined by:

$$T_{ref} = \frac{2}{3}\,T_s + \frac{1}{3}T_\infty \text{ and } Y_{vi,ref} = \frac{2}{3}Y_{vis} + \frac{1}{3}Y_{vi\infty} \qquad (5-86)$$

Properties (ρ_{tot} , μ_g , κ_g and D_v) are calculated assuming that the gas mixture has a temperature and a composition (T_{ref}, $Y_{vi,ref}$).

Step 3: $B_M$can be calculated and B_T is evaluated using equation.

Step 4: Knowing the acoustic Reynolds number Re_a, it is possible to calculate Nu and Sh_i.

Step 5: $\dot{m}$ and the heat flow Q_L.can be calculated then. The mass flow rate $\dot{m}_i$ of the various species is obtained.

Step 6: Then, $T_m(t + dt)$ is determined.

Step 7: The composition at $t + dt$ is determined using DLM, RM, VM or EDM.

Step 8: The updated droplet radius is obtained from the expression below:

$$\frac{4\pi}{3}\,\rho_l(t+dt)\,r_d^3(t+dt) = \frac{4\pi}{3}\,\rho_l(t)\,r_d^3(t) - \sum_i \dot{m}_i dt \qquad (5-87)$$

Comparison of the different models of mass transfer inside the droplet

The previous paragraphs described the possible options for a modelling of the mass transfer inside the acoustically levitating droplets. Here, we compare these models for a case study that is typical of the conditions observed in the experiments inside the acoustic levitator. The droplet is made up of ethanol/water (50%/50% by volume), and has an initial diameter of 2 mm. The ambient air is at room temperature ($T_\infty = 20\,°\mathrm{C}$) and has a relative humidity $RH = 30\%$. The sound pressure amplitude A_{0e}=162 dBe, induces an acoustic streaming velocity B_S valued at about 18 cm/s. The acoustic Reynolds number Re_a is about 19, while the mass Péclet number Pe_m ranges from 26,000 to 36,000. Nusselt and Sherwood numbers are calculated based on Equations, using $K\ = 1.858$ and $\beta\ = 0.667$. The non-ideality of the water/ethanol mixture is account for, using the chemical activity coefficient displayed. Although the droplet is deformed by the acoustic pressure, for the modelling, it is assumed that it remains spherical. Also, inside the droplet, temperature is spatially uniform but time varying. Then it displays the time evolutions of the diameter, volume fraction of water, and temperature simulated by using the different models for mass transfer inside the droplet. The volume fraction of ethanol in the mixture progressively decreases as ethanol is more volatile than water. After about 500s, the binary mixture has been totally transformed into pure water. In the first seconds of the evaporation process, latent heat consumed for evaporation leads to a substantial decrease in the droplet temperature to reach approximately 7°C. After ethanol has been completely evaporated, the evaporation rate gets reduced, but the droplet temperature substantially remains below the room temperature at a value close to 11°C. This final equilibrium temperature represents the wet bulb temperature of water under conditions of 20°C and a relative humidity of 30%.

As observed in **Figure 5-42**, the models considered for the mass transfer yield relatively similar evolutions for the size, temperature, and composition of the droplet. The vortex model (VM) is a priori the most reliable model, but it is also the one that consumes the most time to run the simulation. A noticeable difference with VM can be observed with the diffusion limited model (DLM). In DLM, mass transfers from the center to the surface are considerably reduced which means that it takes more time for ethanol to be replaced at the droplet surface. The evaporation rate is reduced (**Figure 5-42** A) and the droplet undergoes less cooling at the beginning (**Figure 5-42**

C), while a longer time is required for the conversion into a pure water droplet (**Figure 5-42** B). The other two models, namely the rapid mixing model (RMM) and the effective diffusion model (EDM) gives results that are almost indistinguishable from VM.

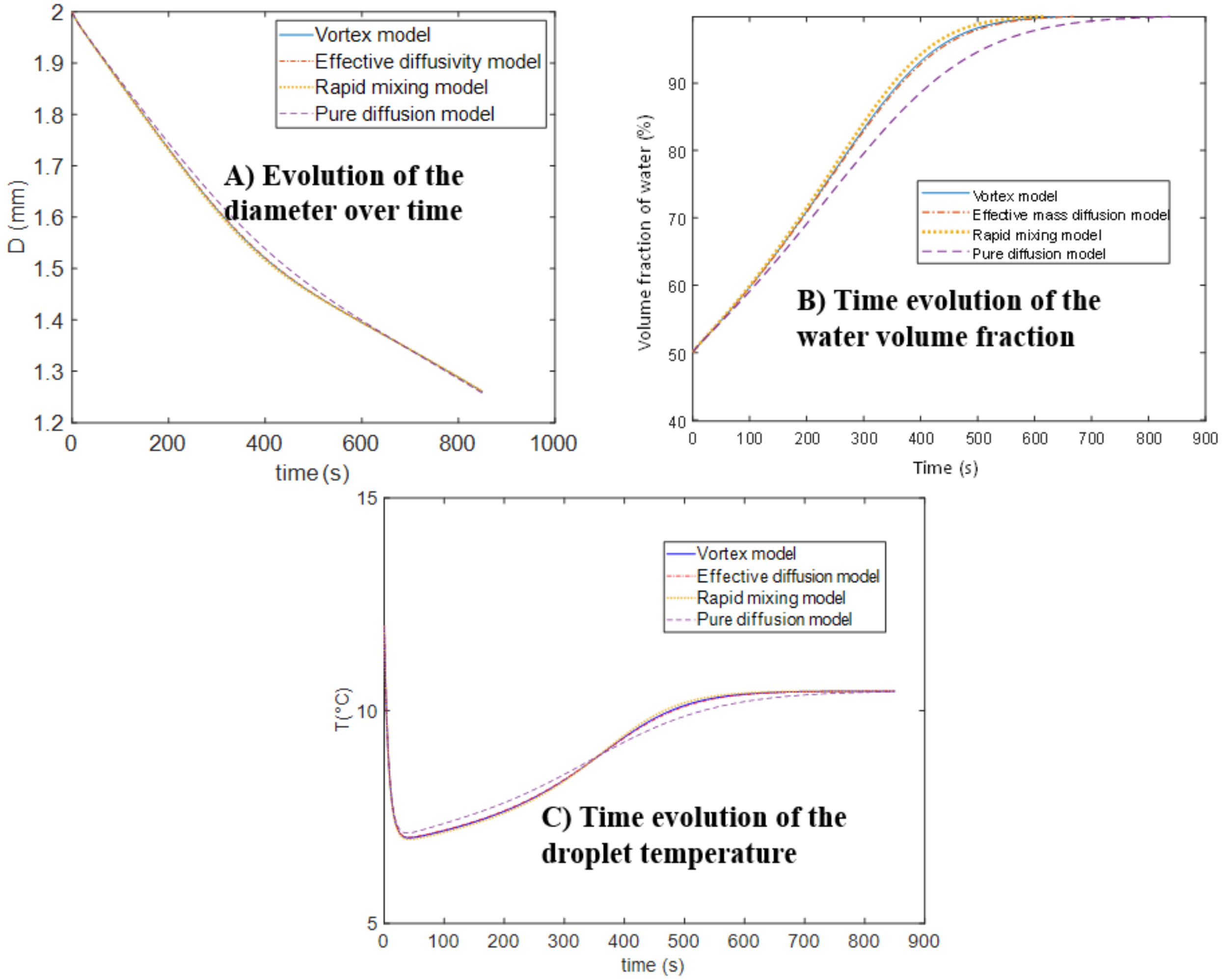

Figure 5-42 Time trends in diameter, water volume fraction and temperature for an ethanol/water drop, initially 2 mm in size and composed of 50% water by volume, placed in ambient air (T=20°C and RH=30%) t in a sound field of 162 dB

Simulations based on RMM are characterized by a faster increase of the water content inside the droplet, but the difference appears to be very small in the present case (far below the uncertainty limits of fluorescence-based composition measurements). These three models (RMM, EDM and VM) are therefore equivalent for a comparison with experiments. Once again, it's worth noting the presence of 2 contrarotating vortices inside the acoustically levitated droplet, instead of one for a droplet moving in translation. This results in a value of χ much larger than in the classical Hill vortex (4.05 against 2.72). The presence of two vortices inside the acoustically levitated droplet considerably increases the mixing rate, which in turn improves the relevance of the RMM. In the following, RMM will be used to describe the droplet evolution given its ease and rapidity of computation.

C） Discussion of experimental results obtained in the acoustic levitator

Numerical resolution of the evaporation problem

The focus was placed on binary mixtures containing water, as the fluorescence lifetime of EY is the lowest in water compared with other solvents. Also, in the absence of an enclosure housing the levitator, it's not possible to avoid water condensation on the droplet's surface as discussed later.

In practice, the room temperature and the relative humidity are recorded by sensors before, during and after the experiments. This ensures that ambient conditions are steady during the measurement. Averaged values are taken as parameters in the simulations of the droplet evaporation. Values of the ambient temperature and relative humidity are expected to be determined with a respective accuracy of ±1°C and ± 1%. The initial droplet volume is not precisely controlled, as it depends on the droplet detachment from the syringe needle. The sound pressure level is not perfectly controlled as well as it would require introducing a microphone in the acoustic cavity. Fundamentally, it is not possible to maintain a constant SPL when changing droplet composition. For instance, the SPL must be significantly increased for a water droplet to levitate compared to an ethanol droplet of the same volume, as liquid water has significantly higher density. And for a SPL value which makes it possible to levitate a water droplet, an ethanol droplet is highly flattened and breaks up easily because of ethanol lower surface tension. In general, the SPL couldn't be maintained. Either the voltage applied to the transducer or the distance between the reflector and the transducer had to be readjusted to ensure an acceptable aspect ratio (typically less than 1.5) and limit the risk of a droplet fallout. An estimate of the SPL is obtained from a shadow image taken a few seconds after the droplet has been placed in the levitator. If the composition and temperature have not changed, the density and surface tension of the liquid mixture are known with a good accuracy. The method developed by Yarin et al. can be used to estimate the SPL based on the aspect ratio and volume of the droplet. The procedure described above is successful if the droplet is big enough to observe a significant deformation when the droplet is subjected to a given pressure difference between the top and bottom sides of the droplet. The variation in density and surface tension for the binary mixtures of water/ethanol are given in **Appendix**. It is also assumed that the sound pressure level does not vary significantly as a function of time while the droplet is evaporating. In principle, when the droplet evaporates, the sound scattered by the droplet decreases, which leads to an increase in SPL, however it was observed that the phenomenon is rather limited.

The evaporation model was implemented for the ethanol/water mixture, as is relatively easy to obtain the physical properties of liquid and vapor as a function of temperature and composition. Further work is needed to find the same for physical properties of the other products (propan1ol, isopropanol and ethylene glycol) also considered in the levitator experiments.

The theoretical model of evaporation described previously has been implemented only in the case of the ethanol/water mixture, for which it proves to be relatively straightforward to obtain the physical properties as a function of temperature and composition for both the liquid and gaseous phases. Further work would be necessary to do the same for the physical properties of the other mixtures considered in our experiments in the acoustic levitator.

Water/ethanol mixtures

This first series of measurements was carried out under the conditions summarized in the table below.

Table 5-4 Experimental conditions for the study of droplets made up of water/ethanol mixtures of different initial volume fraction of water

Water initial volume fraction $\emptyset_v$	d_0 [mm]	T_{amb} $[°C]$	RH [%]	Axis Ratio	SPL $[dB]$
1	1.951	19.8	35	1.41	161.3
0.75	1.716	21.6	41	1.35	161
0.5	1.660	19.8	35	1.58	161.4
0.25	1.499	20.9	41	1.32	161.3
0	1.730	21.3	41	1.27	163.6

The time evolution of the normalized square diameter $(d/d_0)^2$ and that of the water volume fraction as a function of the reduced time t/d_0^2 have been shown, where d_0 is the diameter of the droplet at the time origin $t = 0$ (corresponding to the first measurement point). This choice seemed to be appropriate for comparing these different experiments. Indeed, in the case of a pure liquid droplet, the square diameter follows the d^2 law once the droplet has reached a thermal equilibrium, which generally occurs within a few seconds:

$$d^2 = d_0^2 - K\,t \qquad (5-88)$$

where K is the evaporation rate, whose value can be determined as below:

$$K = 2\pi \, B_M \, Sh \, D_v \frac{\rho_{tot}}{\rho_l} \qquad (5-89)$$

K is clearly a constant because there is a thermal equilibrium (B_M constant) and the acoustic Reynolds number Re_a does not depend on the drop size, which implies that Sh is constant.

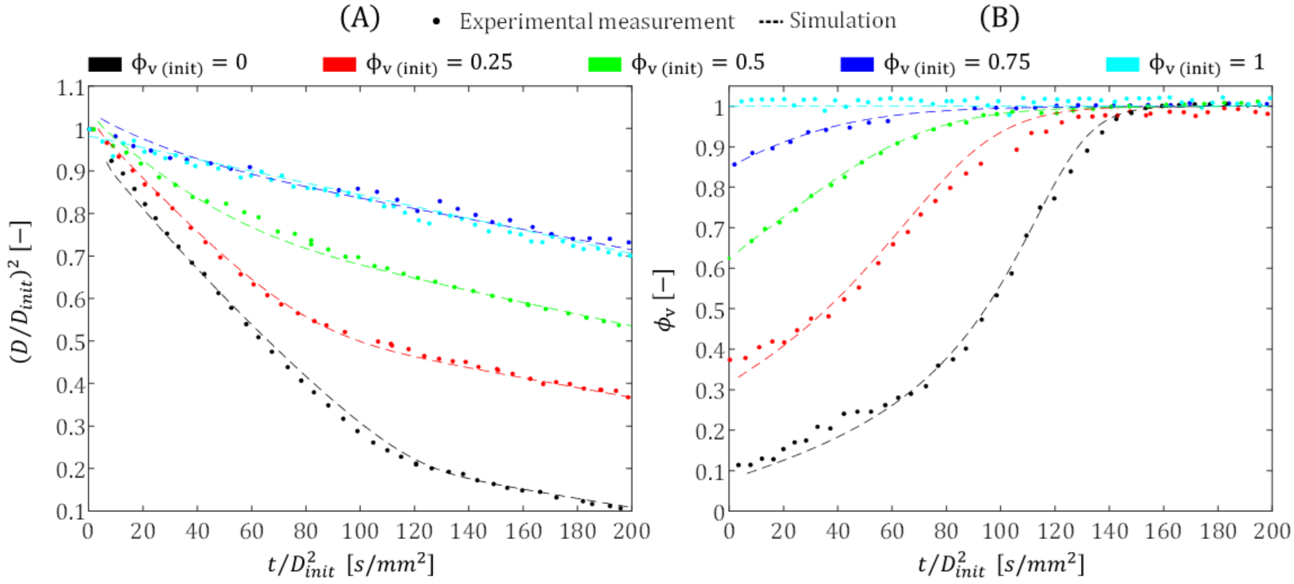

Figure 5-43 Time evolution of the A) normalized square diameter $(d/d_0)^2$ and B) the volume fraction of water as a function of the reduced time (t/d_0^2) for the experimental conditions summarized in **Table 5-4**.

Several comments can be made about these results. As expected, the evaporation rate slows down considerably as the amount of water initially present within the droplet is increased. Measurements show that there is systematically a higher value of the water volume fraction at $t = 0$ (first measurement point) than in the mixture which was prepared prior to the experiment. This can be explained by the fact that it takes about 30 s to insert the droplet inside the levitator, stabilize it (as there is an oscillation phase after the droplet detachment), then adjust the SPL and the droplet position relative to the optics. During this period, which is difficult to reduce, the droplet has already partially evaporated, and its composition has evolved towards a higher volume fraction of water.

It's interesting to note that a droplet of pure ethanol is progressively transformed into a pure water droplet. This is due to the condensation of the water moisture contained in the air (RH=35%) which occurs as the surface temperature of the droplet falls to temperatures as low as 6°C according to the modeling. The evaporation model described in the previous paragraphs is, in principle, well-suited to take condensation into account, since the saturation of water vapor at the droplet surface is incorporated. When the partial pressure of water vapor exceeds the saturation limit, the Spalding mass number (and thus the vapor mass flow rate $\dot{m}$) becomes negative, leading to condensation.

The dotted lines in **Figure 5-43** Time evolution of the A) normalized square diameter $(d/d_0)^2$ and B) the volume fraction of water as a function of the reduced time (t/d_0^2) for the experimental conditions summarized in **Table 5-4**. correspond to the predictions of the evaporation model. Given the difficulty of knowing the droplet evolution in the first few seconds following its introduction into the levitator, the initial conditions were adjusted in these calculations so that the simulation would start at approximately the same diameter and composition as the first measurement point. There is a rather good agreement between the theoretical model and the experimental data. The discrepancies between the experimental points and the simulation are generally of the same order as the measurement uncertainty, which is represented here with error bars. The uncertainty in the measurement of the droplet size was estimated around 4%, assuming a possible error of 2 pixels for the long and small axes (S_l) and (S_s). Yet it's not exactly true that the droplet has the shape of an ellipsoid, or even that it's asymmetrical, since it can be subject to slight oscillations, particularly after it's formed. Composition measurements are also very close to the prediction of the models. All in all, there is no apparent contradiction between measurements of droplet size and volume fractions.

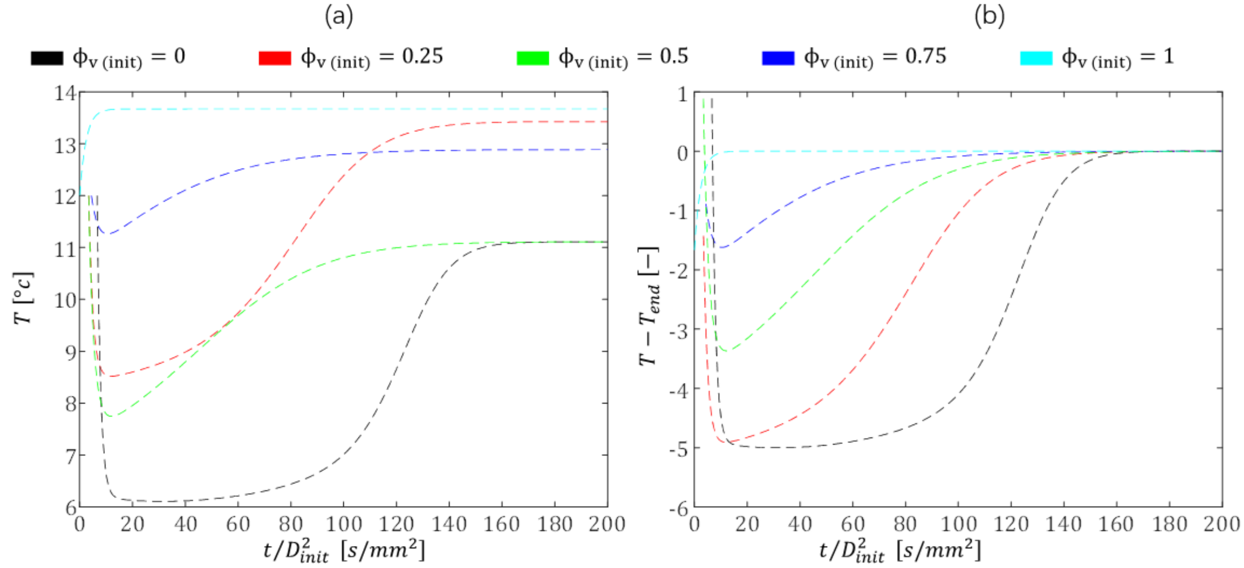

Figure 5-44 Evolution of the droplet temperature (a) and the difference between the droplet temperature and the wet bulb temperature (b).

Figure 5-44 (a) shows the evolution of the droplet temperature calculated for the 5 cases. At the beginning of the evaporation process, the temperature decreases extremely fast within a few seconds and reaches a minimum. Then, the volume fraction of water increases due to water condensation onto the droplet surface, and evaporation slows down. The droplet's temperature progressively rises until it finally stabilizes when only water remains inside the droplet. This equilibrium temperature corresponds to the wet bulb temperature, which is a function of the ambient temperature and humidity only. The temperature difference with the wet bulb temperature is shown in **Figure 5-44** (b). It can be clearly seen that the cooling of the droplet increases with the ethanol volume fraction.

Table 5-5 Experimental conditions corresponding to the study of the evaporation of pure ethanol droplets in ambient air of different humidities.

Water initial volume fraction ϕ_v	d_0 $[mm]$	T_{amb} $[°C]$	RH [%]	Axis ratio	SPL $[dB]$
0	2.33	23.7	20	1.62	160.7
0	1.61	23.7	28	1.58	160
0	1.95	19.8	35	1.44	161.3

To illustrate the effect of air humidity, experimental conditions were changed as shown in **Table 5-5**. Even if the change of the humidity is moderate, the effects are noticeable on the measurement results of the water volume fraction. When the ambient air humidity is increased, a faster increase of the water volume fraction is observed at the beginning of the droplet evaporation. This change of composition can also be noted in the progressive separation of the curves of the squared diameter $(d/d_0)^2$. As shown in **Figure 5-45**, when ethanol has been almost totally removed, the remaining water droplet evaporates at a slower rate for a higher relative humidity. The evaporation rate K in the second half of the d^2 curve is higher for the driest air of the cases tested. Here again, there is a good agreement between simulation and experimental results. The model correctly reproduces the effect of changing humidity for these three examples.

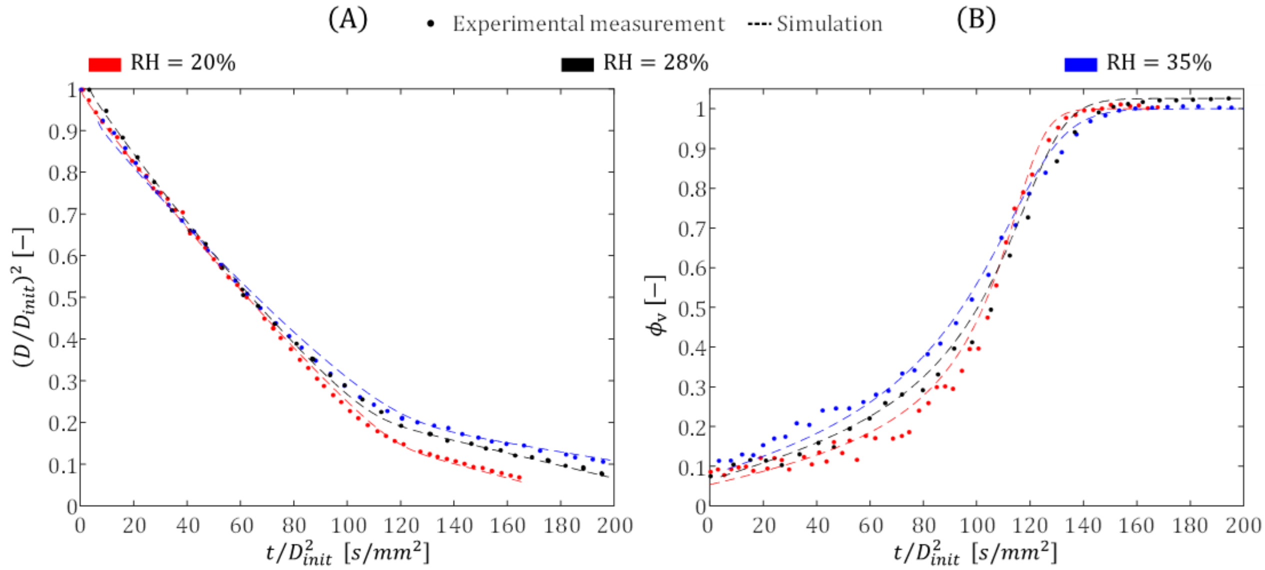

Figure 5-45 Time evolution of the A) normalized square diameter $(d/d_0)^2$ and B) the volume fraction of water as a function of the reduced time (t/d_0^2). Allowing to present the effect of the relative humidity on the water/ethanol droplet evaporation.

Finally, the effect of SPL was specifically tested in the case of an initial volume fraction of water equal to 50% and an ambient temperature of about 24°C, as shown in **Table 5-5**. As expected, the result can be seen in **Figure 5-45**, an increase in acoustic pressure leads to faster evaporation rate and composition change.

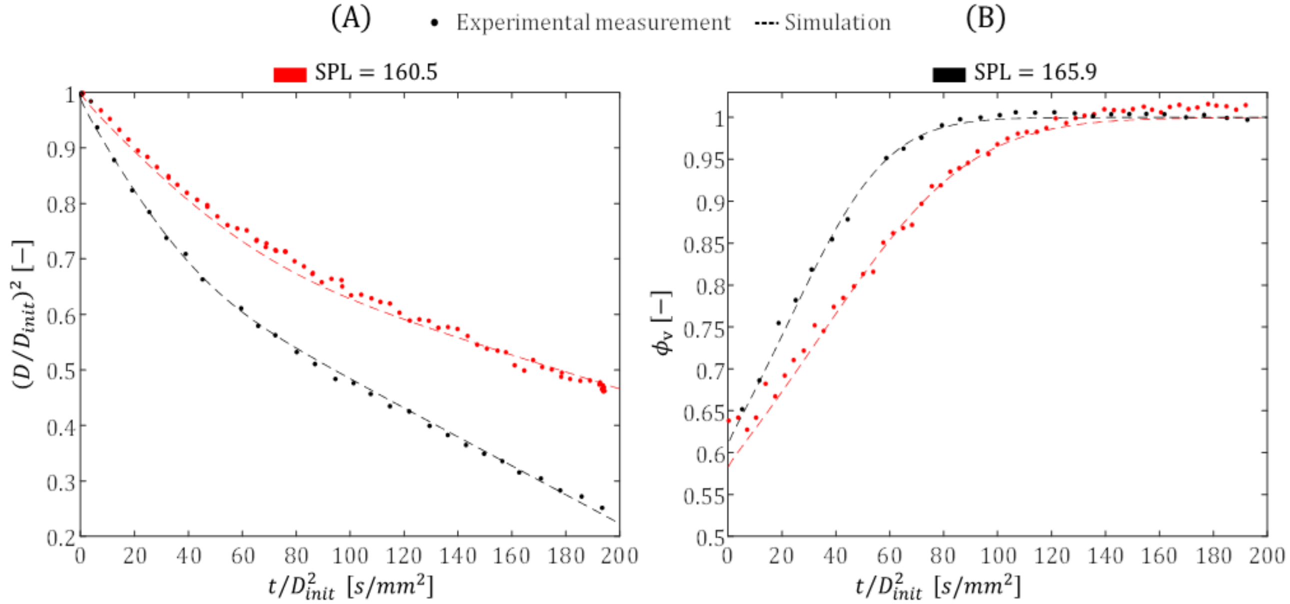

Figure 5-46 Time evolution of the A) normalized square diameter $(d/d_0)^2$ and B) the volume fraction of water as a function of the reduced time (t/d_0^2) for the experimental conditions summarized in **Table 5-6** allowing to present the effect of the Sound Pressure Level on the water/ethanol droplet evaporation.

Table 5-6 Experimental conditions employed for the study of the effect of SPL

Water initial volume fraction ϕ_v	d_0 $[mm]$	T_{amb} $[°C]$	RH [%]	Axis ratio	SPL $[dB]$
0.5	1.533	24.7	20	1.44	165.9
0.5	2.057	23.4	22.5	1.54	160.5

Water/propan-2-ol （Isopropanol）

The same approach was used to study water/propan-2-ol mixtures. Isopropanol has nearly the same properties as ethanol. Its boiling point is 82.5°C, compared with 78°C for ethanol. At first sight, the results obtained are therefore quite comparable to water/ethanol mixtures. The experimental conditions are summarized in **Table 5-7**.

Table 5-7 Experimental conditions for the study of droplets made up of water/isopropanol of different initial compositions

Water initial volume fraction ϕ_v	d_0 [mm]	T_{amb} [°C]	RH [%]	Axis ratio
1	1.53	22.4	26	1.53
0.75	1.79	22.2	26	1.19
0.5	1.05	21.6	27	1.33
0.25	1.16	22.1	26	1.44
0	1.45	22.2	26	1.24

For mixtures initially containing 0% and 25% of water in volume, the volume fraction of water increases moderately at the beginning of the evaporation process, then after about 120 s the droplet rapidly transforms into pure water. This change in composition seems to be faster than in the case of the ethanol/water mixture for comparable conditions. This could be related to the non-ideality of the propan-2-ol/water mixture, which is even more pronounced than that of water/ethanol. In **Figure 5-47**, it can be observed that the value of the chemical activity \gamma of other compound (ethanol or isopropanol) increases sharply as the molar fraction of water tends to 1. This increase is more abrupt in the case of isopropanol in the water/propan-2-ol mixture. The evaporation of propan-2-ol is therefore accelerated when the proportion of water becomes significantly close to 1. As expected, after the droplet completely transformed into water, the evaporation rate K appears to be roughly the same for all the cases studied, given that the temperature and relative humidity of ambient air are about the same for all the cases tested.

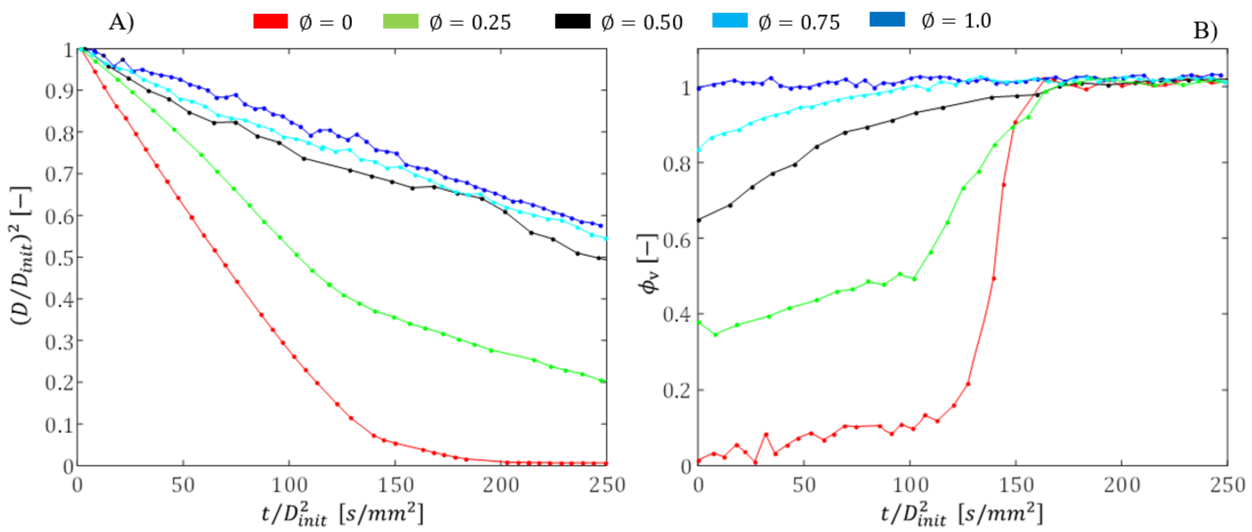

Figure 5-47 Time evolution of the A) normalized square diameter $(d/d_0)^2$ and B) the volume fraction of water as a function of the reduced time (t/d_0^2) for the experimental conditions summarized in **Table 5-7** for the evaporation of water/propan-2-ol droplets at various initial concentration.

Water/propan-1-ol mixtures

The water/propan1ol mixture differs from the previous two in that propan-1-ol is much less volatile than ethanol and propan-2-ol. The boiling temperature of propan-1-ol is 97°C. This species should therefore be about as volatile as water. **Table 5-8** Experimental conditions for the study of droplets made up of water/propan-1-ol mixtures shows the conditions of the measurements to study this mixture.

Table 5-8 Experimental conditions for the study of droplets made up of water/propan-1-ol mixtures

Water initial volume fraction ϕ_v	d_0 [mm]	T_{amb} [°C]	RH [%]	Axis ratio
1	1.72	22.1	26	1.73
0.75	1.98	22.1	26	1.18
0.5	1.52	21.6	26	1.59
0.25	1.74	22.1	26	1.46
0	1.70	22.1	26	1.41

The results are shown in **Figure 5-47**.

It is worth noting that the composition of a droplet containing pure propan-1-ol does not change with time. This means that water does not condense on the droplet surface as it does in the case of ethanol and propan-2-ol. In other words, the evaporation of a pure propan-1-ol droplet is not fast enough to cause a large enough decrease in temperature at the surface of the droplet. The temperature is not cold enough to trigger the condensation of the water moisture in air.

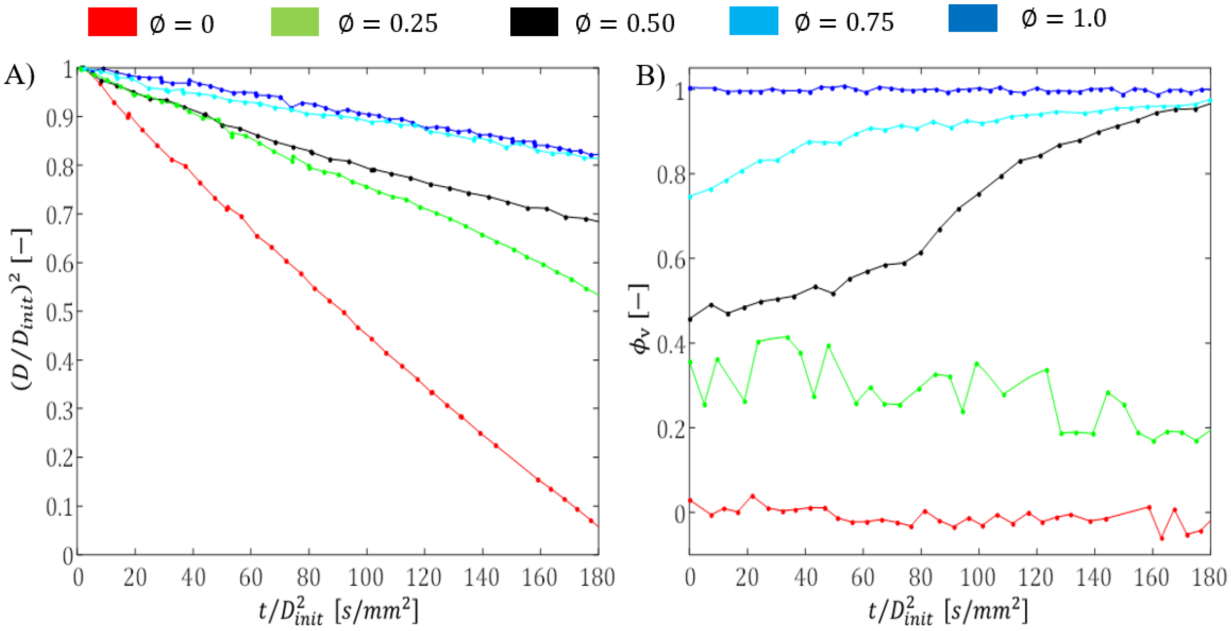

Figure 5-48 Time evolution of the A) normalized square diameter $(d/d_0)^2$ and B) the volume fraction of water as a function of the reduced time (t/d_0^2) for the experimental conditions summarized in **Table 5-9** for the evaporation of water/propan-1-ol droplets at various initial concentration.

The case of an initial volume fraction of water equal to 25% shows a singular evolution in comparison with previous mixtures. The composition remains unchanged over the time of the droplet evaporation. Fluctuations of the measured volume fractions are essentially due to measurement errors.

The evolution of the square diameter also confirms that there is no noticeable change in the evaporation rate K and therefore probably no change in composition of the droplet. Evaporation takes place as if the liquid inside the droplet was a single component. In fact, the mixture is azeotropic, and its main characteristics are summarized in the table below. An azeotrope is a mixture whose proportions cannot be altered or changed by simple distillation. This happens because when an azeotrope is boiled, the vapor has the same proportions of constituents in the liquid phase.

Ethanol and isopropanol can also form azeotropes with water but for lower water volume fractions (**Table 5-9**). In the case of propan-1-ol/water mixture, a major difference is that volatility of the azeotrope seems too low (boiling point= 88.24°C) for the droplet temperature to come close to the dew point of water and trigger a substantial water condensation. The absence of condensation allows the azeotropic mixture to maintain its composition throughout the whole evaporation process. This is not the same for water/ethanol and water/propan-2-ol azeotropic mixtures. Laser-induced fluorescence measurements reveal that condensation occurs, and the progressive addition of water disrupt the azeotropic composition. During its evaporation, the droplet composition crosses the azeotrope, but fails to remain.

Table 5-9 Azeotropes for binary mixtures of water/ethanol, water/propan-1-ol and water/propan-2-ol

Compound 1	Compound 2	BP az(°C)	BP 1 (°C)	BP 2 (°C)	Mass fraction of compound 1 (%)	Volume fraction of compound 1 (%)
Ethanol	water	78.29	78.44	100	95.68	96.6
Propan-1-ol	water	88.24	97.3	100	71.03	75
Propan-2-ol	water	80.4	82.5	100	87.7	90

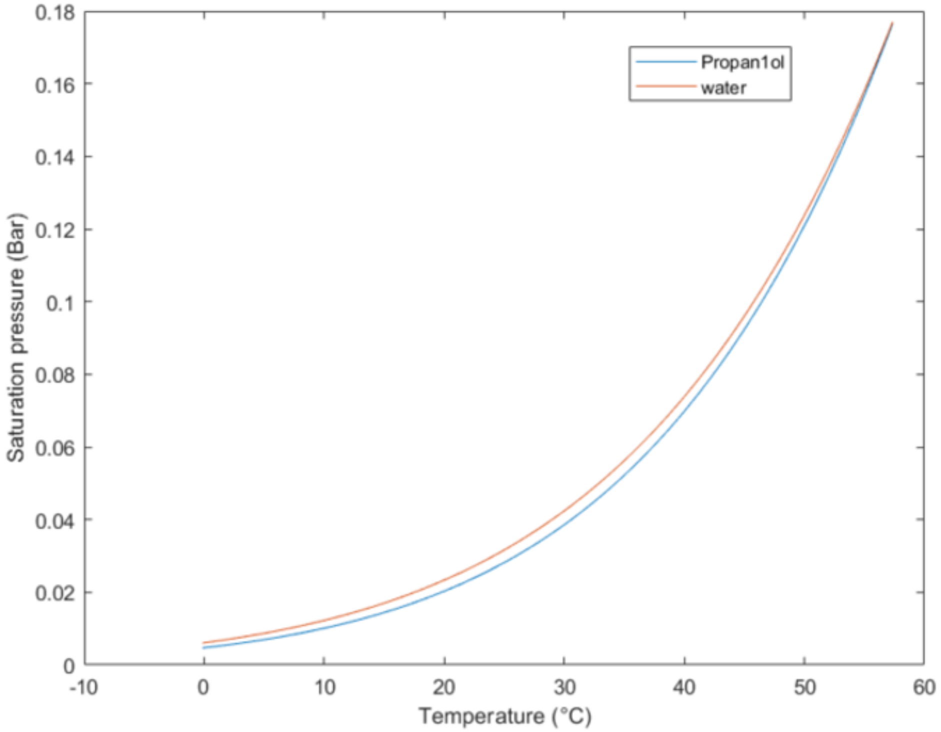

Figure 5-49: Saturation pressure of propan-1-ol and water according to [55][56]

When the initial volume fraction of water exceeds 25% (composition of the azeotropic mixture), the droplet slowly evolves to pure water. The tendency is thus the same as observed before for ethanol/water and isopropanol/water mixtures. The propan1ol compound evaporates faster. However, the saturation pressure of propan1ol is slightly lower than that of water, according to references cited in the NIST webbook of chemistry. At 20°C, P_{sat} is about 23 mBar for water and 20 mBar for propan1ol. We can infer that the faster evaporation rate of propan1ol compared with water is due to the ambient humidity (RH=28%), which slows down the evaporation of water unlike that of 1propanol. In our experimental conditions, the azeotrope is an attractor only when the initial volume fraction of water is greater than 0% but less than 25%. In contrast in a distillation at a temperature much closer to the boiling points of the compounds, the azeotrope is always an attractor. Further tests would be needed to confirm the role played by humidity in this singular behavior.

Water/ethylene glycol mixtures

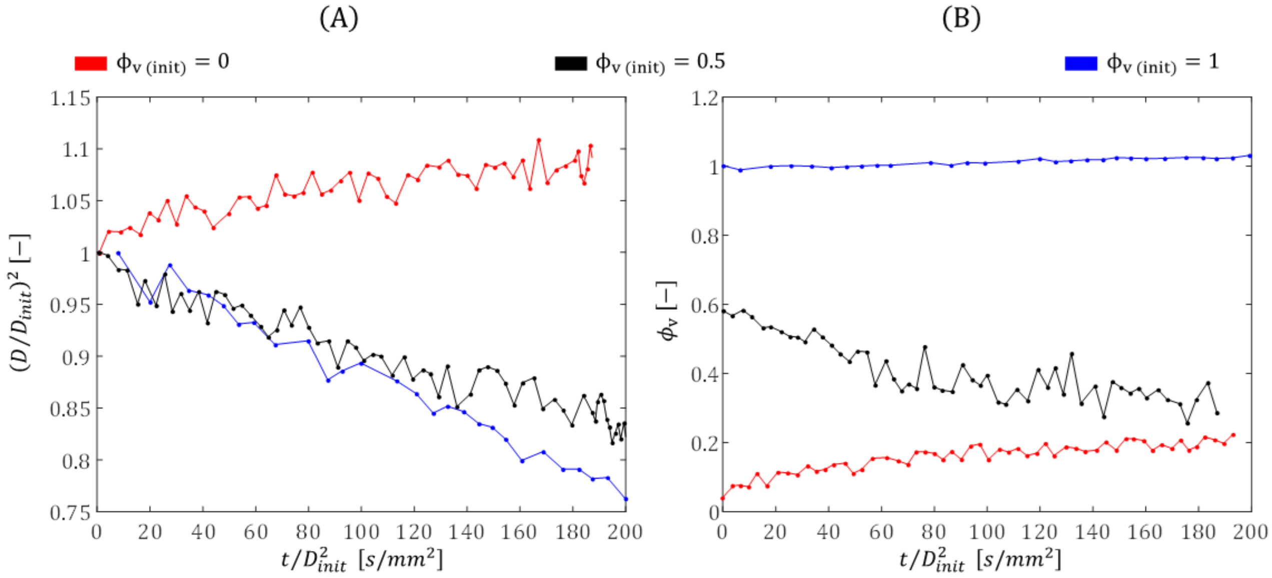

Figure 5-50 Time evolution of the A) normalized square diameter $(d/d_0)^2$ and B) the volume fraction of water as a function of the reduced time (t/d_0^2). For the evaporation of water/ethylene glycol droplets at various initial concentration.

Finally, the case of water/ethylene glycol mixture was considered. Ethylene glycol has a boiling point of 197.3°C, which means that its evaporation is negligible under normal temperature and pressure conditions. On the other hand, this chemical species is particularly hygroscopic. It can therefore naturally absorb moisture in air. Three experiments were carried out under the conditions shown in the table below. They involve a droplet of pure ethylene, a droplet initially composed of 50% by volume of water and ethylene glycol and a pure ethylene glycol droplet.

In the case of an initial pure ethylene glycol droplet, measurements reveal an increase in drop diameter by about 5%. This corresponds to an increase of the drop volume by 15%. This increase is explained by the hygroscopicity of ethylene glycol, which absorbs water from humid air. Measurements based on the fluorescence lifetime demonstrate an increase in water volume fraction of about 13%, which is consistent with the variation observed for the diameter (15/115≈13%) assuming that the size variation is only due to the addition of water.

Table 5-10: Experimental conditions for the study of droplets made up of water/ethylene glycol mixtures

Water initial volume fraction ϕ_v	d_0 [mm]	$\mathrm{T}_{\mathrm{amb}}$ [°C]	RH [%]	Axis ratio
1	2.14	20.6	37	1.32
0.5	1.69	21.5	36	1.29
0	2.17	22.2	36	1.27

For an initial volume fraction of water equal to 50%, the droplet diameter decreases over time due to the progressive evaporation of water that is initially contained in the mixture. The droplet diameter decreases by about 15%, corresponding to a loss of volume of about 40%. Over the same time period, measurements indicate a decrease of the water volume fraction approximately from 55% to 30%. Here again, there is a good agreement between size and composition measurements. At t=0, the initial droplet volume (v_0) is composed of water (55/100 v_0) and ethylene glycol (45/100 v_0). After evaporation of the water, only 15/100 v_0 of water and 45/100 v_0 of ethylene glycol remain. Thus, one expects to obtain a volume fraction of water equal to 15/45=0.33, which is approximately what is observed.

Remarks on composition measurements

Measurement uncertainties

To evaluate the measurement uncertainties, the derivative of f_v with respect to τ is used. The uncertainty can be determined by:

$$\Delta f_v = \left|\frac{df_v}{d\tau}\right| \Delta\tau \qquad (5-90)$$

where $\Delta\tau$ is the estimated error on the measurement of the lifetime of the fluorescence. This error depends on several parameters such as the number of photons collected and the signal to noise ratio. To get an approximate idea of $\Delta\tau$, repeated measurements were carried out levitated droplets.

These results indicate that $\Delta\tau$ is on the order of 0.04 ns under the conditions of the measurements performed in the levitator. Another possible method would consist in using the Monte Carlo type method as proposed in **Chapter 4**. **Figure 5-51** shows the uncertainty on the measured volume fraction Δf_v assuming that $\Delta\tau$ is equal to 0.04 ns for the three mixtures.

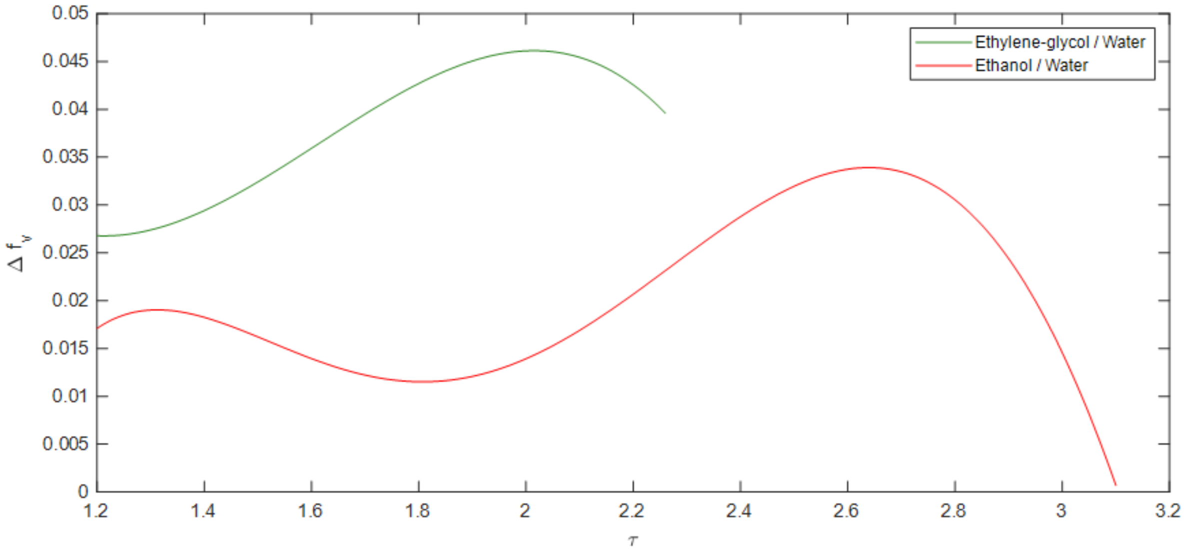

Figure 5-51 Estimate of the measurement uncertainties of the volume fraction assuming that Δτ is equal to 0.04 ns

Air blowing

To enhance the effect of convection, it is possible to inject a small stream of air close to the droplet by means of small holes that have been drilled into the reflector. Results obtained under such conditions turned out to be more difficult to interpret, because the position and shape of the droplet are considerably less stable. The disturbances easily affect the evaluation of the droplet size from the shadow images. Fluctuations in the lifetime measurements are also observed with an amplitude that is greater than a simple random error. These fluctuations are a priori not related to measurement errors, but probably to the fact that the droplet moves and deforms while the composition inside of it is not exactly uniform. Given the time for a measurement acquisition (typically 2s-3 s), it was not possible to correlate the droplet displacement and shape to the values of the fluorescence lifetime to gain insight into this phenomenon. We therefore decided not to blow air to obtain the steadiest conditions as possible.

Parameters estimation in the fluorescence decay model

When the measurement method was applied to levitating droplets, significant scattering of the measurements was sometimes observed. As previously explained, this scattering can be attributed mostly to the fact that the calibration curve relating the water volume fraction f_v to the fluorescence lifetime has a reduced slope for some ranges of composition. This is especially a problem when the volume fraction of water tends to 0 for the water/ethanol and water/propan-2-ol mixtures. The Scattering of the measurements is also due to the multi-exponential nature of the fluorescence decay, which is more pronounced when a small amount of water is present in the mixture. To improve measurement accuracy, data processing has been slightly modified. The fluorescence decay is still described by a biexponential function:

$$F(t) = \alpha\, e^{-\frac{t}{\tau_1}} + (1-\alpha)\, e^{-\frac{t}{\tau_2}} \qquad (5-91)$$

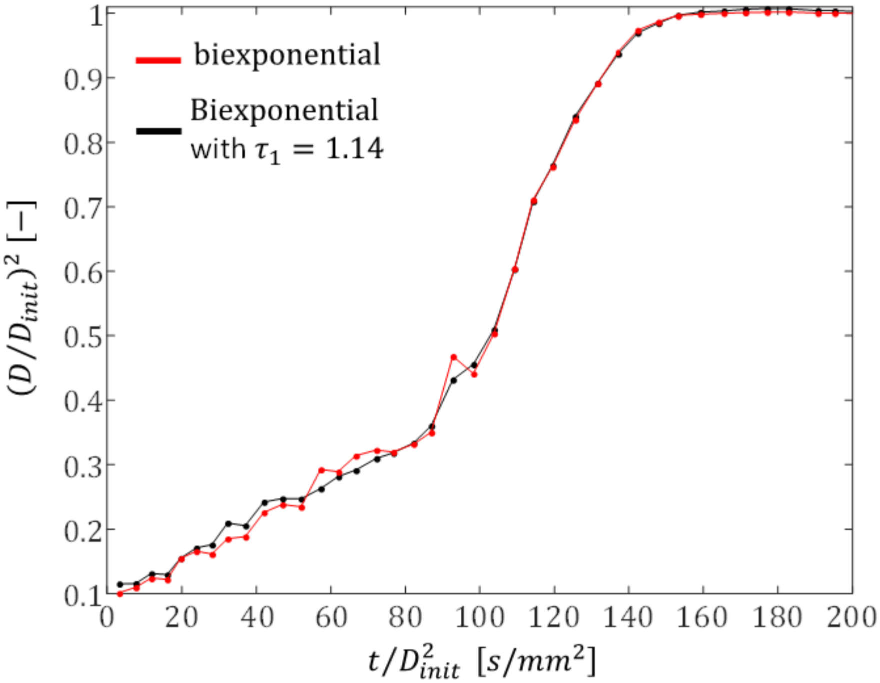

Figure 5-52 Comparison of Fitting Methods for Measuring the fluorescence lifetime. This figure illustrates the variance in measuring τ using different fitting methods, emphasizing the case of pure ethanol.

However, in order to limit the number of estimated parameters, τ_1 has been set at 1.14 ns (i.e. the fluorescence lifetime of EY in pure water). Only parameters α and τ_2 are estimated using the least squares method. Calibration data were processed again following the same methodology. **Figure 5-52** shows a comparison of the two approaches, the one with 3 free parameters (α, τ_1, τ_2) and the one with only two free parameters α et τ_2. With both methods, the average fluorescence lifetime $\tau = \alpha\,\tau_1 + (1-\alpha)\,\tau_2$ is used to derive the volume fraction of water in the mixture from the calibration curve.

5.5 Reference

[1]. Avedisian, C. T. (1994). Droplet Combustion and Soot Formation in Microgravity. National Aeronautics and Space Administration.

[2]. Sazhin, S. S. (2006). Advanced models of fuel droplet heating and evaporation. Progress in energy and combustion science, 32(2), 162-214.

[3]. Lemoine, F., & Castanet, G. (2013). Temperature and chemical composition of droplets by optical measurement techniques: a state-of-the-art review. Experiments in fluids, 54, 1-34.

[4]. Owen, J. F., Chang, R. K., & Barber, P. W. (1982). Morphology–dependent resonances in Raman scattering, fluorescence emission, and elastic scattering from microparticles. Aerosol Science and Technology, 1(3), 293-302.

[5]. J. Promvongsa, B. Fungtammasan, G. Gerard, S. Saengkaew, P. Vallikul, A Study on the Evaporation of Water–Ethanol Mixture Using Rainbow Refractometry, J. Energy Resour. Technol. 139 (2017).

[6]. Chiewudomrat, S. Saengkaew, G. Grehan, S. Leveneur, L. Estel, Evaluation of refractive index gradients in droplets by rainbow technique: application to CO2 capture by monoethanolamine aqueous spray, Exp. Fluids. 63 (2022) 153.

[7]. C. Maqua, V. Depredurand, G. Castanet, M. Wolff, F. Lemoine, Composition measurement of bicomponent droplets using laser-induced fluorescence of acetone, Exp. Fluids. 43 (2007) 979–992.

[8]. J. Coppeta, C. Rogers, Dual emission laser induced fluorescence for direct planar scalar behavior measurements, Exp. Fluids. (1998).

[9]. M. Koegl, M. Pahlevani, L. Zigan, A Novel Approach for Measurement of Composition and Temperature of N-Decane/Butanol Blends Using Two-Color Laser-Induced Fluorescence of Nile Red, Sensors. 20 (2020) 5721.

[10]. M. Koegl, M. Delwig, L. Zigan, Characterization of Fluorescence Tracers for Thermometry and Film Thickness Measurements in Liquid Coolants Relevant for Thermal Management of Electric and Electronic Components, Sensors. 22 (2022) 8892.

[11]. C. Maqua, G. Castanet, F. Lemoine, N. Doué, G. Lavergne, Temperature measurements of binary droplets using three-color laser-induced fluorescence, Exp. Fluids. 40 (2006) 786–797.

[12]. Mendels, D. A., Graham, E. M., Magennis, S. W., Jones, A. C., & Mendels, F. (2008). Quantitative comparison of thermal and solutal transport in a T-mixer by FLIM and CFD. Microfluidics and nanofluidics, 5, 603-617.

[13]. Lakowicz, J. R. (Ed.). (2006). Principles of fluorescence spectroscopy. Boston, MA: springer US.

[14]. Shakerizadeh-Shirazi, F., Hemmateenejad, B., & Mehranpour, A. M. (2013). Determination of the empirical solvent polarity parameter ET (30) by multivariate image analysis. Analytical Methods, 5(4), 891-896.

[15]. Ahmed, K., Auni, A., Ara, G., Rahman, M. M., Mollah, M. Y. A., & Susan, M. A. B. H. (2012). Solvatochromic and fluorescence spectroscopic studies on polarity of ionic liquid and ionic liquid-based binary systems. Journal of the Bangladesh Chemical Society, 25(2), 146-158.

[16]. Miao, W., Yu, C., Hao, E., & Jiao, L. (2019). Functionalized BODIPYs as fluorescent molecular rotors for viscosity detection. Frontiers in chemistry, 7, 825.

[17]. Mehdi, S., Yangpeng, L., Hadrien, C., Fabrice, L., Xishi, W., & Guillaume, C. (2021). Fluorescence lifetime measurements applied to the characterization of the droplet temperature in sprays. Experiments in Fluids, 62, 1-19.

[18]. Stiti, M., Castanet, G., Labergue, A., & Lemoine, F. (2020). Icing of a droplet deposited onto a subcooled surface. International Journal of Heat and Mass Transfer, 159, 120116.

[19]. Moog, R. S., Ediger, M. D., Boxer, S. G., & Fayer, M. D. (1982). Viscosity dependence of the rotational reorientation of rhodamine B in mono-and polyalcohols. Picosecond transient grating experiments. The Journal of Physical Chemistry, 86(24), 4694-4700.

[20]. Wang, M., Stiti, M., Chaynes, H., Becker, S., Berrocal, E., Lemoine, F., & Castanet, G. (2022). Two-photon fluorescence lifetime imaging applied to the mixing of two non-isothermal sprays: temperature and mixing fraction measurements. Experiments in Fluids, 63(11), 172.

[21]. Koegl, M., Delwig, M., & Zigan, L. (2022). Characterization of Fluorescence Tracers for Thermometry and Film Thickness Measurements in Liquid Coolants Relevant for Thermal Management of Electric and Electronic Components. Sensors, 22(22), 8892.

[22]. Koegl, M., Weiß, C., & Zigan, L. (2020). Fluorescence spectroscopy for studying evaporating droplets using the dye eosin-Y. Sensors, 20(21), 5985.

[23]. Mishra, Y. N., Yoganantham, A., Koegl, M., & Zigan, L. (2020). Investigation of five organic dyes in ethanol and butanol for two-color laser-induced fluorescence ratio thermometry. Optics, 1(1), 1-17.

[24]. Koegl, M., Weiß, C., & Zigan, L. (2020). Fluorescence spectroscopy for studying evaporating droplets using the dye eosin-Y. Sensors, 20(21), 5985.

[25]. Markides, C. N., Mathie, R., & Charogiannis, A. (2016). An experimental study of spatiotemporally resolved heat transfer in thin liquid-film flows falling over an inclined heated foil. International Journal of Heat and Mass Transfer, 93, 872-888.

[26]. Chakraborty, M., & Panda, A. K. (2011). Spectral behaviour of eosin Y in different solvents and aqueous surfactant media. Spectrochimica Acta Part A: Molecular and Biomolecular Spectroscopy, 81(1), 458-465.

[27]. Extracted from the website https://pradeepresearch.org/pdf-files/teaching-and-presentations/teaching/undergraduate%20courses/cy306-structure-and-energetics-of-biomolecules/presentations/H-%20and%20J-%20Aggregates.pdf

[28]. Enoki, M., & Katoh, R. (2018). Estimation of quantum yields of weak fluorescence from eosin Y dimers formed in aqueous solutions. Photochemical & Photobiological Sciences, 17, 793-799.

[29]. Yarin, A. L., Pfaffenlehner, M., & Tropea, C. (1998). On the acoustic levitation of droplets. Journal of Fluid Mechanics, 356, 65-91.

[30]. Hall, D. N., & Lamb, J. (1959). Measurement of ultrasonic absorption in liquids by the observations of acoustic streaming. Proceedings of the Physical Society, 73(3), 354.

[31]. King, L. V. (1934). On the acoustic radiation pressure on spheres. Proceedings of the Royal Society of London. Series A-Mathematical and Physical Sciences, 147(861), 212-240.

[32]. Leung, E., Jacobi, N., & Wang, T. (1981). Acoustic radiation force on a rigid sphere in a resonance chamber. The Journal of the Acoustical Society of America, 70(6), 1762-1767.

[33]. Lierke, E. G., Grossbach, R., Flogel, K., & Clancy, P. (1983, October). Acoustic positioning for space processing of materials science samples in mirror furnaces. In 1983 Ultrasonics Symposium (pp. 1129-1139). IEEE.

[34]. Lierke, E. G. (1996). Acoustic levitation–a comprehensive survey of principles and applications. Acta Acustica united with Acustica, 82(2), 220-237.

[35]. Sazhin, S. (2014). Droplets and sprays (Vol. 345). London: Springer.

[36]. Abramzon, B., & Sirignano, W. A. (1989). Droplet vaporization model for spray combustion calculations. International journal of heat and mass transfer, 32(9), 1605-1618.

[37]. Law, C. K. (1975). Asymptotic theory for ignition and extinction in droplet burning. Combustion and Flame, 24, 89-98.

[38]. J. Promvongsa, B. Fungtammasan, G. Gerard, S. Saengkaew, P. Vallikul, A Study on the Evaporation of Water–Ethanol Mixture Using Rainbow Refractometry, J. Energy Resour. Technol. 139 (2017).

[39]. J. Promvongsa, B. Fungtammasan, G. Gerard, S. Saengkaew, P. Vallikul, A Study on the Evaporation of Water–Ethanol Mixture Using Rainbow Refractometry, J. Energy Resour. Technol. 139 (2017).

[40]. S. Chiewudomrat, S. Saengkaew, G. Grehan, S. Leveneur, L. Estel, Evaluation of refractive index gradients in droplets by rainbow technique: application to CO2 capture by monoethanolamine aqueous spray, Exp. Fluids. 63 (2022) 153.

[41]. C. Maqua, V. Depredurand, G. Castanet, M. Wolff, F. Lemoine, Composition measurement of bicomponent droplets using laser-induced fluorescence of acetone, Exp. Fluids. 43 (2007) 979–992.

[42]. J. Coppeta, C. Rogers, Dual emission laser induced fluorescence for direct planar scalar behavior measurements, Exp. Fluids. (1998).

[43]. T. Lacassagne, S. Simoëns, M. El Hajem, J.-Y. Champagne, Ratiometric, single-dye, pH-sensitive inhibited laser-induced fluorescence for the characterization of mixing and mass transfer, Exp. Fluids. 59 (2018) 21.

[44]. L. Perrin, G. Castanet, F. Lemoine, Characterization of the evaporation of interacting droplets using combined optical techniques, Exp. Fluids. 56 (2015) 558–585.

[45]. Abramzon, B., & Sirignano, W. A. (1989). Droplet vaporization model for spray combustion calculations. International journal of heat and mass transfer, 32(9), 1605-1618.

[46]. Clift, R. (1978). Bubbles. Drops and Particles.

[47]. Yarin, A. L., Brenn, G., Kastner, O., Rensink, D., & Tropea, C. (1999). Evaporation of acoustically levitated droplets. Journal of Fluid Mechanics, 399, 151-204.

[48]. Lierke, E. G. (2002). Deformation and displacement of liquid drops in an optimized acoustic standing wave levitator. Acta Acustica United with Acustica, 88(2), 206-217.

[49]. Yarin, A. L., Brenn, G., Kastner, O., Rensink, D., & Tropea, C. (1999). Evaporation of acoustically levitated droplets. Journal of Fluid Mechanics, 399, 151-204.

[50]. Al Zaitone, B. A., & Tropea, C. (2011). Evaporation of pure liquid droplets: Comparison of droplet evaporation in an acoustic field versus glass-filament. Chemical Engineering Science, 66(17), 3914-3921.

[51]. Gopinath, A., & Mills, A. F. (1993). Convective heat transfer from a sphere due to acoustic streaming.

[52]. Kristyadi, T., Deprédurand, V., Castanet, G., Lemoine, F., Sazhin, S. S., Elwardany, A., ... & Heikal, M. R. (2010). Monodisperse monocomponent fuel droplet heating and evaporation. Fuel, 89(12), 3995-4001.

[53]. Fredenslund, A., Jones, R. L., & Prausnitz, J. M. (1975). Group-contribution estimation of activity coefficients in nonideal liquid mixtures. AIChE Journal, 21(6), 1086-1099.

[54]. Hubbard, G. L., Denny, V. E., & Mills, A. F. (1975). Droplet evaporation: effects of transients and variable properties. International journal of heat and mass transfer, 18(9), 1003-1008.

[55]. Kemme, H. R., & Kreps, S. I. (1969). Vapor pressure of primary n-alkyl chlorides and alcohols. Journal of Chemical and Engineering Data, 14(1), 98-102.

[56]. Bridgeman, O. C., & Aldrich, E. W. (1964). Vapor pressure tables for water.

Appendix: Mass Transport within the Levitated Droplet

In the spherical coordinate system (r, θ, ϕ), the species transport equation can be written as follows:

$$\frac{\partial Y_{li}}{\partial t} + v_r \frac{\partial Y_{li}}{\partial r} + \frac{v_\theta}{r} \frac{\partial Y_{li}}{\partial \theta} = \frac{D_l}{r^2} \left[\frac{\partial}{\partial r} \left(r^2 \frac{\partial Y_{li}}{\partial r} \right) + \frac{1}{\sin\theta} \frac{\partial}{\partial \theta} \left(\sin\theta \frac{\partial Y_{li}}{\partial \theta} \right) \right] \qquad (5-92)$$

These equations can be rewritten in a dimensionless form by introducing $\xi = r \,/\, r_d$ and $\tau = \ U t / r_d$, where U is a characteristic velocity for the flow inside the droplet. For simplification, it is assumed that the droplet radius r_d is constant.

$$\frac{\partial Y_{li}}{\partial \tau} + v_r^* \frac{\partial Y_{li}}{\partial \xi} + v_\theta^* \frac{1}{\xi} \frac{\partial Y_{li}}{\partial \theta} = \frac{1}{Pe_m} \frac{1}{\xi^2} \left[\frac{\partial}{\partial \xi} \left(\xi^2 \frac{\partial Y_{li}}{\partial \xi} \right) + \frac{1}{\sin\theta} \frac{\partial}{\partial \theta} \left(\sin\theta \frac{\partial Y_{li}}{\partial \theta} \right) \right] \qquad (5-93)$$

where $v_r = U\, v_r^*$ et $v_\theta = U\, v_\theta^*$ and $Pe_m = \frac{U\, r_d}{D_l}$ is the mass Péclet number. Now introducing $x = \cos\theta$, it can be seen that:

$$\frac{d\blacksquare}{d\theta} = -\sin\theta \frac{d\blacksquare}{d\, cos\theta} = -\sqrt{1 - x^2}\, \frac{d\blacksquare}{dx} \qquad (5-94)$$

Equation $(5-93)$ can be rewritten as follows:

$$\frac{\partial Y_{li}}{\partial \tau} + v_r^* \frac{\partial Y_{li}}{\partial \xi} - \sqrt{1 - x^2}\, v_\theta^* \frac{1}{\xi} \frac{\partial Y_{li}}{\partial x} = \frac{1}{Pe_m} \frac{1}{\xi^2} \left[\frac{\partial}{\partial \xi} \left(\xi^2 \frac{\partial Y_{li}}{\partial \xi} \right) + \frac{\partial}{\partial x} \left((1 - x^2) \frac{\partial Y_{li}}{\partial x} \right) \right] \qquad (5-95)$$

This problem is now solved in the orthogonal basis of Legendre polynomials assuming that:

$$Y_{li}(\xi, x, \tau) = \sum_{n=0}^{\infty} f_n(\xi, \tau) P_n(x) \qquad (5-96)$$

where P_n is the n^{th} Legendre polynomial and f_n functions are spherical harmonics that depend only on the variable ξ and τ.

$$\sum_{n=0}^{\infty} \left[\left(\frac{\partial f_n}{\partial \tau} + v_r^* \frac{\partial f_n}{\partial \xi} \right) P_n(x) - \sqrt{1 - x^2}\, \frac{v_\theta^*}{\xi} P_n'(x)\, f_n \right]$$

$$= \frac{1}{\xi^2\, Pe_m} \sum_{n=0}^{\infty} \left\{ \frac{\partial}{\partial \xi} \left(\xi^2 \frac{\partial f_n}{\partial \xi} \right) P_n(x) + f_n \cdot \frac{d}{dx} \left((1 - x^2) \frac{dP_n}{dx} \right) \right\} \qquad (5-97)$$

Legendre polynomial $P_n(x)$ is defined as the solution of the differential equation:

$$(1-x^2)P_n''(x) - 2xP_n'(x) + n\,(n+1)P_n(x) = 0 \qquad (5-98)$$

This allows us to write:

$$\frac{d}{dx}\left((1-x^2)\frac{dP_n}{dx}\right) = (1-x^2)P_n''(x) - 2xP_n'(x) = -n\,(n+1)P_n(x) \qquad (5-99)$$

Equation can be rewritten as:

$$\sum_{n=0}^{\infty}\left[\left(\frac{\partial f_n}{\partial \tau} + v_r^*\frac{\partial f_n}{\partial \xi}\right)P_n(x) - \sqrt{1-x^2}\,\frac{v_\theta^*}{\xi}P_n'(x)\,f_n\right]$$

$$= \frac{1}{Pe_m\,\xi^2}\sum_{n=0}^{\infty}\left\{P_n(x)\cdot\left[\frac{\partial}{\partial \xi}\left(\xi^2\frac{\partial f_n}{\partial \xi}\right) - n\,(n+1)\,f_n\right]\right\} \qquad (5-100)$$

Legendre polynomials are orthogonal for the scalar product:

$$\int_{-1}^{1} P_n(x)P_m(x)dx = \begin{cases} 0 & \text{if } n \neq m \\ C_n & \text{if } n = m \end{cases} \qquad (5-101)$$

$$C_n = \frac{1}{n+\frac{1}{2}} \qquad (5-102)$$

Multiplying Equation by $P_m(x)$, then integrating along x between -1 and 1:

$$C_m\frac{\partial f_m}{\partial \tau} + \sum_{n=0}^{\infty}\left[\frac{\partial f_n}{\partial \xi}\,A - f_n\,B\right] = \frac{C_m}{Pe_m\,\xi^2}\left(\frac{\partial}{\partial \xi}\left(\xi^2\frac{\partial f_m}{\partial \xi}\right) - m\,(m+1)\,f_m\right) \qquad (5-103)$$

where $A = \int_{-1}^{+1} v_r^*(\xi, x)\,P_n(x)\,P_m(x)\,dx$ and $B = \int_{-1}^{+1}\sqrt{1-x^2}\,\frac{v_\theta^*(\xi,x)}{\xi}P_n'(x)\,P_m(x)\,dx$. The velocity component v_r can be formulated as :

$$v_r = \frac{E'r_d^3}{14\,\mu_l}(3\cos^2\theta - 1)\left(\frac{r^3}{r_d^3} - \frac{r}{r_d}\right) = \frac{E'r_d^3}{14\,\mu_l}(3x^2-1)(\xi^3-\xi) \qquad (5-104)$$

$\sin 2\theta = 2\sin\theta\cos\theta$ and $\sin\theta = \sqrt{1-x^2}$, equation becomes:

$$v_\theta = \frac{E'r_d^3}{28\,\mu_l}2\sin\theta\cos\theta\left(3\frac{r}{r_d} - 5\frac{r^3}{r_d^3}\right) = \frac{E'r_d^3}{14\,\mu_l}\left(x\sqrt{1-x^2}\right)\cdot(3\,\xi - 5\,\xi^3) \qquad (5-105)$$

Defining $U = \frac{E'\,r_d^3}{14\,\mu_l}$, one obtains:

$$v_r^* = (3x^2 - 1)(\xi^3 - \xi) \qquad (5-106)$$

$$v_\theta^* = \left(x\sqrt{1-x^2}\right) \cdot (3\,\xi - 5\,\xi^3) \qquad (5-107)$$

Finally, Equation leads to:

$$\frac{\partial f_m}{\partial \tau} + \frac{1}{C_m}\sum_{n=0}^{\infty}\left[(\xi^3 - \xi)\frac{\partial f_n}{\partial \xi}\,A_{nm} - (3\, - 5\,\xi^2)\,f_n\,B_{nm}\right]$$
$$= \frac{1}{Pe_m\,\xi^2}\left(\frac{\partial}{\partial \xi}\left(\xi^2\frac{\partial f_m}{\partial \xi}\right) - m\,(m+1)\,f_m\right) \qquad (5-108)$$

$$A_{nm} = \int_{-1}^{+1}(3x^2 - 1)\,P_n(x)\,P_m(x)\,dx \text{ et } B_{nm} = \int_{-1}^{+1} x\,(1 - x^2)\,P_n'(x)P_m(x)\,dx \qquad (5-109)$$

Finally, it is possible to consider the time variation of the droplet radius r_d. It is equivalent to add a velocity transport $(\xi\,\dot{r_d}/r_d)$ in the radial direction. Then it becomes:

$$\frac{\partial f_m}{\partial \tau} + \frac{1}{C_m}\sum_{n=0}^{\infty}\left[(\xi^3 - \xi)\frac{\partial f_n}{\partial \xi}\,A_{nm} - (3\, - 5\,\xi^2)\,f_n\,B_{nm}\right] + \frac{1}{C_m}\xi\frac{\dot{r_d}}{r_d}\frac{\partial f_m}{\partial \xi} = \frac{1}{Pe_m\,\xi^2}\left(\frac{\partial}{\partial \xi}\left(\xi^2\frac{\partial f_m}{\partial \xi}\right) - m\,(m+1)\,f_m\right) \quad (5-110)$$

Coefficients A_{nm} and B_{nm} have some interesting properties which allow further simplifications. They are null except in the case where $n = m, m+2$ and $m-2$.

$$\sum_{n=0}^{\infty}\left[(\xi^3 - \xi)\frac{\partial f_n}{\partial \xi}\,A_{nm} - (3\, - 5\,\xi^2)\,f_n\,B_{nm}\right]$$
$$= (\xi^3 - \xi)\left(A_{mm}\frac{\partial f_m}{\partial \xi} + A_{m+2,m}\frac{\partial f_{m+2}}{\partial \xi} + A_{m-2,m}\frac{\partial f_{m-2}}{\partial \xi}\right)$$
$$- (3\, - 5\,\xi^2)\big(B_{mm}\,f_m + B_{m+2,m}\,f_{m+2} + B_{m-2,m}\,f_{m-2}\big) \qquad (5-111)$$

In practice, around twenty modes are sufficient to accurately simulate the distribution of the composition inside a droplet.

Numerical resolution:

Assuming that the evolution of the droplet composition is known until time τ_k, the Adams-Bashforth method is used for obtaining a numerical approximation to the solution at the next time step τ_{k+1}:

$$f_m(\tau_{k+1}, \xi_i) = f_m(\tau_k, \xi_i) + \frac{\Delta\tau}{2}\left(3\ \frac{\partial f_m}{\partial \tau}(\tau_k, \xi_i) - \frac{\partial f_m}{\partial \tau}(\tau_{k-1}, \xi_i)\right) \qquad (5-112)$$

In this expression, the term $\frac{\partial f_m}{\partial \tau}(\tau_k, \xi_i)$ is evaluated using an explicit method. This means that all the terms are calculated at time τ_k.The finite difference method is used for spatial derivatives.

for $2 \le \mathrm{i} \le N_r - 1$

$$\partial f_m/\partial \xi = \frac{\left(f_m(\tau_k, \xi_{i+1}) - f_m(\tau_k, \xi_i)\right)}{2\ d\xi^+} + \frac{\left(f_m(\tau_k, \xi_i) - f_m(\tau_k, \xi_{i-1})\right)}{2\ d\xi^-} \qquad (5-113)$$

for $2 \le \mathrm{i} \le N_r - 1$

$$\frac{\partial^2 f_m}{\partial \xi^2} = 2\ \frac{d\xi^- f_m(\tau_k, \xi_{i+1}) +\ d\xi^+ f_m(\tau_k, \xi_{i-1}) - (d\xi^- + d\xi^+) f_m(\tau_k, \xi_i)}{d\xi^- d\xi^+\ (d\xi^- + d\xi^+)} \qquad (5-114)$$

where $d\xi^+ = \xi_{i+1} - \xi_i$ and $d\xi^- = \xi_i - \xi_{i-1}$.

Initial condition

the numerical problem is solved with the condition that initially the mass fraction of the species is uniform.

$$Y_{li} = Y_{li_0}\ and\ \tau = 0 \qquad (5-115)$$

Given the orthogonality of Legendre polynomials, this implies that:

$$f_m(\xi, \tau = 0) = Y_{li_0}, \qquad \forall m \ge 0 \qquad (5-116)$$

Table 0-1 The first A_{nm} coefficients

m	A_{mm}	$A_{m+2,m}$	$A_{m-2,m}$
0	0	0.800000000000000	
1	0.533333333333333	0.342857142857143	
2	0.228571428571429	0.228571428571429	0.800000000000000
3	0.152380952380952	0.173160173160173	0.342857142857143
4	0.115440115440115	0.139860139860140	0.228571428571429
5	0.0932400932400933	0.117482517482517	0.173160173160173
6	0.0783216783216783	0.101357466063348	0.139860139860140
7	0.0675716440422323	0.0891640866873065	0.117482517482517
8	0.0594427244582043	0.0796107916850951	0.101357466063348

9	0.0530738611233967	0.0719189277541680	0.0891640866873065
10	0.0479459518361120	0.0655900621118012	0.0796107916850951
11	0.0437267080745342	0.0602898550724638	0.0719189277541680
12	0.0401932367149758	0.0557854406130268	0.0655900621118012
13	0.0371902937420179	0.0519095291064145	0.0602898550724638
14	0.0346063527376097	0.0485387804631409	0.0557854406130268
15	0.0323591869754272	0.0455802262253875	0.0519095291064145
16	0.0303868174835917	0.0429624429624430	0.0485387804631409
17	0.0286416286416286	0.0406296406296406	0.0455802262253875
18	0.0270864270864271	0.0385375995132093	0.0429624429624430
19	0.0256917330088062	0.0366508137353288	0.0406296406296406
20	0.0244338758235525	0.0349404424276801	0.0385375995132093

Table 0-2 The first B_{nm} coefficients

m	B_{mm}	$B_{m+2,m}$	$B_{m-2,m}$
0	0	0.800000000000000	
1	0.266666666666667	0.457142857142857	
2	0.114285714285714	0.380952380952381	0
3	0.0761904761904762	0.346320346320346	0.114285714285714
4	0.0577200577200577	0.326340326340326	0.152380952380952
5	0.0466200466200466	0.313286713286713	0.173160173160173
6	0.0391608391608392	0.304072398190045	0.186480186480187
7	0.0337858220211161	0.297213622291022	0.195804195804196
8	0.0297213622291022	0.291906236178682	0.202714932126697
9	0.0265369305616984	0.287675711016672	0.208049535603715
10	0.0239729759180560	0.284223602484472	0.212295444493587
11	0.0218633540372671	0.281352657004831	0.215756783262504
12	0.0200966183574879	0.278927203065134	0.218633540372671
13	0.0185951468710089	0.276850821900878	0.221062801932367
14	0.0173031763688048	0.275053089291132	0.223141762452107
15	0.0161795934877136	0.273481357352325	0.224941292794463

16	0.0151934087417958	0.272095472095472	0.226514308827991
17	0.0143208143208143	0.270864270864271	0.227901131126938
18	0.0135432135432135	0.269763196592465	0.229133029133029
19	0.0128458665044031	0.268772634059078	0.230234630234630
20	0.0122169379117763	0.267876725278881	0.231225597079256

Boundary conditions

The derivative $\partial Y_{li}/\partial \xi$ is null at the center of the droplet to avoid having a singular point. At the droplet surface, it is assumed that the mass fraction Y_{liS} remains uniform but can vary with time to satisfy the overall mass conservation. This means that:

$$f_m(\xi = 1, \tau) = 0, \text{for } m \neq 0 \qquad (5-117)$$

$$f_m(\xi = 1, \tau) \neq 0, \text{for } m = 0 \qquad (5-118)$$

This condition is not sufficient to close the problem. Assuming that the vapour mass fraction Y_{viS} of the species are known until time τ_k, the vapour mass flow rate $\dot{m}$ can be calculated Then, the mass flux $\dot{m}_i$ of the i^{th} species can be determined. A uniform mass flux at the droplet surface does not result in a uniform mass fraction. Vortices inside the droplet transport the compounds which affects the mass distribution at the surface. In practice, the solution is seen as the superposition of two easier-to-solve problems. Considering that $Y_{li}(\xi)$ is known until time τ_k, the evolution of Y_{li} during the next time interval $\Delta\tau$ is described by the following decomposition:
for $0 \leq t' \leq \Delta\tau$ and $0 \leq \xi \leq 1$

$$Y_{li}(\tau_k + t', \xi) = Y_{li}^1(t', \xi) + \alpha_i \, Y_{li}^2(t', \xi) \qquad (5-119)$$

Problem 1

In Equation (5-116), Y_{li}^1 is the solution to a problem where the mass fraction is kept constant and uniform at the surface of the droplet:

$$Y_{li}^1(t', \xi = 1) = Y_{liS}(\tau_k) \text{ at } \xi = 1 \qquad (5-120)$$

At $t' = 0$, the mass fraction Y_{li}^1 is identical to the mass fraction Y_{liS} calculated for the droplet at time τ_k:

$$Y_{li}^1(t' = 0, \xi) = Y_{li}(\tau_k, \xi) \text{ at } t = 0 \qquad (5-121)$$

Problem 2

Y_{li}^2 is the response to a unite increment of the mass fraction at the droplet surface:

$$Y_{li}^{2}(t', \xi = 1) = 1 \text{ at } \xi = 1 \qquad (5-122)$$

$$Y_{li}^{2}(t' = 0, \xi) = 0 \text{ at } t = 0 \qquad (5-123)$$

Finally, parameter α_i is adjusted to ensure the composition variation imposed by the mass flux $\dot{m}_i$ at the surface:

$$\alpha_i = \frac{\dot{m}_i \, \Delta\tau \; - m(\tau_{k+1}) \, \Delta Y_{lim}^{1}}{m(\tau_{k+1}) \, \Delta Y_{lim}^{2}} \qquad (5-124)$$

where $j = 1$ and 2, $\Delta Y_{lim}^{j} = Y_{lim}^{j}(\Delta\tau) - Y_{lim}^{j}(0)$, and Y_{lim}^{j} is the volume average of Y_{li}^{j}.

General Conclusion and Perspectives

Sprays play an important role in many industrial processes and technologies, for example: Fuel are used in combustion engines in propulsion systems (including aero-engines, rocket engine), transformation processes (production of powders by spray drying, spray coating for liquid film deposition, etc.), heat management (spray cooling of electronics and metal processing, etc.). Understanding the phenomena associated with heat and mass transfer is essential for designing and optimizing these applications and processes.

However, the development of optical measurement techniques, capable of characterizing heat and mass transfer in sprays remains a real challenge. While several techniques are commercially available for measuring droplet size and velocity, nothing really compares for droplet temperature and composition. The solutions, on which researchers are working, are mainly laser-induced fluorescence (LIF), rainbow refractometry and Raman spectroscopy, but each of these methods has its own strengths and weaknesses. Among the advantages of using LIF, there is a spectral shift of several nm between absorption and emission spectra of fluorescent molecules, which can ease the separation between the excitation light and fluorescence. Relatively low concentrations of dye molecules (typically a few µg/L) are generally sufficient for measurements.

So far, LIF measurements have been vastly based on the intensity of the fluorescence signal. The principle is to measure the variation in the intensity of the fluorescence signal to obtain quantitative measurements. However, the implementation in two-phase flows remains relatively complex. Using ratios of intensities measured in two detection bands is the most adopted solution. Preliminary studies, sometimes time-consuming, are required to select appropriate detection bands and fluorescent dyes to maximize the response of the intensity ratio to the examined parameter (temperature or composition) and the amount of signal.

In this research work, the possibilities offered by measurements of the fluorescence lifetime is assessed for the first time to characterize the temperature and composition of droplets. Lifetime-based measurements are now widespread in the field of microbiology in fluorescence microscopy applications (especially with its FLIM version, which involves scanning with a confocal or a multiphoton excitation microscope), but little was done in fluid mechanics, apart in the field of microfluidics in confined configurations such as microchannels. A well-established method for characterizing fluorescence lifetime is the so-called time-correlated single-photon counting technique (TCSPC). It involves measuring the arrival time of single fluorescence photons after the excitation by an ultrashort laser pulse (this latter must be significantly shorter than the time resolution of the time-stamping system, a few tens of ps). In addition, a high repetition rate is highly desirable to collect as fast as possible single photons and rapidly converge in the reconstruction of fluorescence decay. Ti:Sapphire oscillators operating at several tens of MHz are ideally suited for this purpose. Lifetime-based measurements are in principle not dependent on the excitation intensity. Its measurement is therefore less affected by light scattering and quenching phenomena than fluorescence intensity. This makes it advantageous when liquid/gas/solid interfaces alter the energy and transmission of light.

Multiple light scattering by the droplets in dense spray regions has several negative effects. It attenuates fluorescence excitation at the place where the laser beam is focalized. Droplets that are not normally directly exposed to laser light eventually receive laser light and emit some fluorescence in return. The lengthening of optical paths leads to a background noise that is difficult to get rid of. Fluorescence reabsorption can affect the fluorescence spectra emerging from the spray, which can pose problems for the two-color ratio metric approaches. Two-photon excitation is an elegant solution to mitigate the effects of multiple scattering. Due to the quadratic dependence of two-photon absorption on the excitation intensity, the laser light scattered by droplets is highly unlikely to induce two-photon fluorescence in a spray. At worst, if the laser beam is too strongly attenuated, no fluorescence is emitted.

In a first stage of this thesis, a new method for measuring droplet temperature is developed, based on the measurement of the fluorescence lifetime of some highly temperature-sensitive dyes, such as rhodamine B. Preliminary calibration is carried out in a cuvette to characterize the temperature evolution of the fluorescence lifetime for rhodamine B. Although fluorescence decays are commonly described by a first order kinetic, that of rhodamine B is more complex. As the temperature increases, the decay takes a more pronounced bi-exponential shape. This effect needs to be carefully accounted for to properly fit the experimental data and correctly estimate the average fluorescence lifetime.

Two-photon excitation for spray measurements requires the use of a long-distance microscope objective. A compromise has to be found. On the one hand, a working distance of several centimeters or more is preferred, so that droplets do not risk impacting the surface of the objective lens. On the other hand, it is important to have a two-photon volume that is not too elongated along the optical axis, and a large numerical aperture. Currently, commercially available microscope objectives are not very well suited to this new application in sprays. The choice of a working distance of only 25 mm is a clear limitation of the technique. It is hardly sufficient to observe the first few mm of the spray downstream the injector outlet.

A very high signal-to-noise ratio could be achieved under all the conditions which were tested in sprays. A dynamic range of about 3 decades for the decay curve can be retained in the spray, which is a bit lower than in a cuvette. This provides to the measurements, an accuracy and robustness which is probably unrivalled among the other temperature measurement techniques available in sprays. The absolute error typically does not exceed ±1°C in most cases and even reduces to about ±0.5°C if the uncertainty affecting the calibration coefficients are put aside. However, when measurements are carried out far from the spray axis, droplet concentration decreases considerably, and acquisition time must be increased beyond one minute to ensure a good statistical convergence and a high accuracy. This limitation is mainly due to the requirement to avoid the pile-up effect. The onset of the pile-up effect is not observed at the same laser power as in a liquid cuvette, so it can only be determined by in situ tests. This proved to be a problem during the spray experiments, as the pile-up effect had to be tested in advance at a few well-chosen locations in the spray to set the laser power and the concentration in fluorescent molecules.

The new measurement technique proved particularly useful when applied to the study of the mixing of two sprays injected at different temperatures. Fluorescence emissions of the droplets originating from the two sprays have different fluorescence lifetimes, which makes it possible to evaluate the temperature of both sprays separately but also their mixing fractions. The possibility of measuring the mixing fraction alone was first tested in the case of a mixture of two sprays seeded with eosin Y and rhodamine 6G separately, which are both insensitive to temperature and have very different fluorescence lifetimes. Combined measurements of temperature and mixing fractions alone are also possible using rhodamine B when there is a sufficient temperature contrast between the two sprays. The biexponential nature of the fluorescence decay of rhodamine B must be considered to obtain acceptable values of the mixing fraction. The volume fraction of a spray must exceed about 10% in the mix to measure its temperature with an acceptable accuracy of about 2°C-3°C. Mixing temperatures based either on the average fluorescence lifetime or on the mixing fraction (mixing temperature weighted by the liquid volume of the sprays) are always accurately measured with an accuracy of about 1°C. Nonetheless, these two definitions of the mixing temperature can differ by a few °C in the mixing zone.

The characterization of droplet composition was then examined. These measurements are not straightforward, regardless of how they are based on the fluorescence intensity or lifetime.

Temperature and chemical composition have an effect that is difficult to separate. Fluorescence intensity can be sensitive to the temperature through the absorption cross-section and the fluorescence quantum yield. The lifetime is only dependent through the quantum yield as these quantities are proportional. A study was therefore undertaken among a set of dyes to characterize the solvent effect on their fluorescence lifetime. Among the dyes we tested, eosin Y was found to be sensitive to solvent polarity. The fluorescence lifetime of eosin Y in the investigated solvents varies linearly with the solvent polarity scales ET (30). This scale is constructed by spectrophotometric measurements of the solvatochromism of Reichardt's pyridinium-N-phenolate betaine dye, e.g., the ET (30) dye dissolved in the solvent of interest. Another advantage of eosin Y is the very low temperature dependence of the fluorescence lifetime. The strongest effect of temperature was observed in water, with a variation of the fluorescence lifetime of less than 0.1 ns for a temperature change of more than 50°C. This makes it possible to measure the composition in conditions where temperature is changing by several tens of °C.

The new measurement technique was used to characterize the composition change of two-component droplets standing in an acoustic levitator. Droplet evaporation takes a few minutes, which is sufficiently long for measurements, as acquisitions take around 2s to ensure good statistical convergence. Furthermore, a theoretical analysis of the velocity field evidences the rapid mixing that takes place inside these acoustically levitated droplets. Two counter-rotating vortices ensure a rapid transport of species inside the droplet. The species concentration field can be assumed to be uniform when taking into account the relatively slow evaporation process undergone by the droplet. Based on this observation, composition measurements are permitted by performing a one-photon excitation in the entire droplet volume. Special care must be taken to avoid self-quenching, which eventually comes into play at the end of the droplet evaporation as the concentration of the fluorescent molecules increases. Self-quenching could be recognized as a FRET process for a few dyes, including eosin Y, rhodamine B and rhodamine 6G. It leads to a sharp shortening of the fluorescence lifetime when the dye concentration approaches 10^{-3} mol/L.

The focus was placed in particular on droplets made up of two components, one of which being water. These droplets evaporate in moist air at room temperature. In addition to the droplet composition, evolutions of the droplet size and shape were also monitored using shadow imaging. An estimate of the velocity of the acoustic streaming could be obtained by analyzing the shape deformation of the droplet.

Experimental results in the case of the ethanol/water mixture were compared with a theoretical evaporation model, taking into account the effect of the acoustic streaming on the species transport in the gaseous phase, the non-ideality of the mixture, the room temperature and humidity. Reasonably good agreements could be obtained for both size and composition measurements. For some other mixtures, noteworthy behaviors have been evidenced. In the case of the water/1propanol mixture, azeotropic behavior has been demonstrated for an initial composition of 25% water by volume. Indeed, the composition of this droplet remains almost constant as the droplet evaporates. Finally, the measurement technique was able to evidence the hygroscopic nature of ethylene glycol droplets, which spontaneously absorb moisture in air.

Perspectives

The possibilities offered by the new technique and the potential of this research work seem quite extensive.

The measurement techniques developed in this work, although it has some obvious limitations do not seem to introduce noticeable measurement biases and has an unrivaled dynamic range. Measurements could be therefore envisaged under more stringent conditions. In this respect, further research is needed to determine the range of conditions where the technique remains applicable in terms of droplet sizes, liquid concentration in a spray, light scattering. The measurement technique has some obvious limitations that may be addressed for applications demanding, for example, faster acquisition, a spatial scanning pattern or a longer working distance:

Currently, the working distance of the long-distance microscope used to generate two-photon excitation is limited to 25 mm. This distance proved to be sufficient to explore the first mm near the injector outlet. However, a great improvement would be to increase this working distance, without increasing the size of the two-photon fluorescence spot along the optical axis while maintaining about the same solid angle for the reception of the fluorescent photons. There would be a considerable advantage to an optical system with significantly wider lenses to achieve this goal even though it comes with the need of compensations to reduce dispersion.

Another limitation is the pointwise nature of these measurements. In addition, the photon counting system (detector and electronics) requires a "dead time" between detection events for the electronics to be reinitialized which makes the measurements even slower. In practice, it takes a few seconds or even minutes per acquisition to insure a satisfying statistical convergence. New solutions could be tested to suffer less from this issue while keeping some of the advantages that lifetime measurements and two-photons excitation can provide. To measure the lifetime in more locations at the same time, a first solution is to use a "streak" architecture of camera. These cameras give access to the temporal variation of the light intensity in only one direction. The incoming light is limited by a slit. Photoelectrons generated at the photocathode are deflected over time by an electric field produced by a pair of electrode plates, in a similar way to a traditional cathode ray tube of an oscilloscope. It is therefore still required to have a scanning approach in one direction to reconstruct the lifetime variation in a 2D domain. A less expensive but probably with lower performances is the use of intensified cameras to determine lifetime in the frequency domain. This method requires high-frequency intensity modulation of a CW laser for the excitation of fluorescence.

The femtosecond laser used in our study has an energy per pulse of the order of a few nJ. This energy is sufficient to generate two-photon fluorescence in a very small volume which is perfect for TCSPC applications in two-photon microscopy. It may be envisaged to use a much more powerful pulsed laser (including a nanosecond laser source provided it is powerful enough) to generate two-photon fluorescence inside a plane of a few mm2 or cm2. Intensity-based approaches based on two detection bands or previously mentioned streak and time-gated cameras for the lifetime could be used for the image acquisition. As for the pointwise measurements, the main advantage of a two-photon excitation sheet lies in the study of media where multiple light by liquid/gas interfaces poses difficulties (sprays, bubbles, suspensions…).

In the presented research work, we reported on a temperature measurement using rhodamine B and a composition measurement using eosin Y. Our initial plan was to combine these two measurements to simultaneously measure droplet temperature and composition. However, the emission spectra of these two dyes are not sufficiently shifted in wavelength, making it impossible to use beam splitters and chromatic filters to separate their emissions properly. Their lifetimes are also too close in water and several solvents to separate their response in the time domain as in Chapter 4 for rhodamine 6G and Eosin Y. A better pair of fluorescent dyes is still needed.

Obtaining temperature and composition measurements as close as possible to liquid/gas or liquid/liquid interfaces is one of the main challenges in the study of transfer phenomena in two-phase flows. The spatial resolution of the measurements is crucial to accurately evaluate heat and mass fluxes near a solid or a liquid surface. Fluorescence microscopy, especially two-photon fluorescence microscopy, has a clear potential for addressing this challenge. However, steady or slowly varying conditions are required to have time to scan the vicinity of an interface with a resolution in the micron range. When rapidly varying phenomena must be considered, periodic flows can give some solutions. It is possible to classify photon detection events according to the phase within the period of the studied phenomenon. Images in the space domain are obtained by doing a phase-locking reconstruction. Such a method was successfully tested in several studies, for example to study the mixing inside droplets moving in microchannels. Droplets can be generated in a perfectly periodic manner using a flow focusing geometry at the inlet of the microchannel. Similar studies could be carried out in a microchannel, such as the absorption of CO2 bubbles circulating in microchannels by an absorbent solution, or the cavitation in channel featuring a spray nozzle where flash boiling takes place. It would also be very interesting to study droplets moving in an open gaseous environment, using an injector capable of generating droplets periodically. These droplets can then be placed in a variety of environments affecting their temperature and compositions.

List of Publications

[1]. Wang, M., Stiti, M., Chaynes, H., Becker, S., Berrocal, E., Lemoine, F., & Castanet, G. (2022). Two-photon fluorescence lifetime imaging applied to the mixing of two non-isothermal sprays: temperature and mixing fraction measurements. Experiments in Fluids, 63(11), 172.